Proceedings Annual Meeting of the Austrian Society for Biomedical Engineering 2021

ÖGBMT 2021

Sept 30 - Oct 1, 2021
Graz University of Technology, Austria

Edited by
Gernot R. Müller-Putz, Christian Baumgartner

Österreichische Gesellschaft
für Biomedizinische Technik

Austrian Society for
Biomedical Engineering

TU Graz
Graz University of Technology

Verlag der Technischen Universität Graz 2021

DOI: 10.3217/978-3-85125-826-4-00

Verlag der Technischen Universität Graz
http://ub.tugraz.at/Verlag

ISBN 978-3-85125-826-4
DOI 10.3217/978-3-85125-826-4

Published by Verlag der TU Graz
Graz University of Technology

DOI: 10.3217/978-3-85125-826-4-00

Welcome Note

Dear conference participants!

We would like to welcome you to this year's Annual Meeting of the Austrian Society for Biomedical Engineering (ÖGBMT) at Graz University of Technology. Together with the Institute of Health Care Engineering with European Testing Center of Medical Devices and the Institute of Neurotechnology, we have organized this two-day event for you, which also appropriately honors "50 years of Biomedical Engineering in Graz". The scientific sessions will focus on biomedical imaging and signal processing, biomechanics, functional electrostimulation and neurorehabilitation, biomedical modeling and simulation, among others.
PD Dr. Rüdiger Rupp will give a keynote lecture on "Rehabilitation technology for people with spinal cord injury - hypes and hopes" and report on current developments in this field.

A total of 26 papers were finally accepted and are published "open access" in these “Proceedings Annual Meeting of the Austrian Society for Biomedical Engineering 2021” by the Verlag of Graz University of Technology.

In addition, prizes for the best master's theses and dissertations will be awarded by ÖGBMT, Graz University of Technology and industry in recognition of the outstanding achievements and high quality of the scientific work of our young researchers.

In particular, we would like to thank the Department for Computer Science and Biomedical Engineering, the HTS Cluster Styria, the Standortagentur Tirol and the City of Graz for their financial support of this annual conference. On behalf of the ÖGBMT and Graz University of Technology we wish you an exciting and inspiring stay at the ÖGBMT Annual Meeting 2021!

Gernot Müller-Putz

Christian Baumgartner

Published by Verlag der TU Graz
Graz University of Technology

DOI: 10.3217/978-3-85125-826-4-00

List of Authors I

List of authors in alphabetical order with start pages in their respective contributions.

Published by Verlag der TU Graz
Graz University of Technology

DOI: 10.3217/978-3-85125-826-4-00

List of Authors II

Published by Verlag der TU Graz
Graz University of Technology

DOI: 10.3217/978-3-85125-826-4-00

List of Authors III

Published by Verlag der TU Graz
Graz University of Technology

DOI: 10.3217/978-3-85125-826-4-00

List of Authors IV

Published by Verlag der TU Graz
Graz University of Technology

DOI: 10.3217/978-3-85125-826-4-00

Table of Contents I

Published by Verlag der TU Graz
Graz University of Technology

DOI: 10.3217/978-3-85125-826-4-00

Table of Contents II

Published by Verlag der TU Graz
Graz University of Technology

DOI: 10.3217/978-3-85125-826-4-00

Table of Contents III

Published by Verlag der TU Graz
Graz University of Technology

Proc. Annual Meeting of the Austrian Society for Biomedical Engineering 2021
DOI: 10.3217/978-3-85125-826-4-01

MODEL-BASED DEVELOPMENT OF A CLOSED-LOOP HEART RATE CONTROL STRATEGY USING VAGUS NERVE STIMULATION

M. Haberbusch[1,2], B. Kronsteiner[1,2], A. Kiss[2], F. Moscato[1,2,3]

[1]Center for Medical Physics and Biomedical Engineering, Medical University of Vienna, Vienna, Austria
[2]Ludwig Boltzmann Institute for Cardiovascular Research, Vienna, Austria
[3]Austrian Cluster for Tissue Regeneration, Vienna, Austria

max.haberbusch@meduniwien.ac.at

Abstract— *A previously developed numerical model of the cardiovascular system was applied to develop and compare two strategies for closed-loop heart rate control using vagus nerve stimulation in complete vagal-cardiac denervation. The strategies were also tested in a first pilot experiment in an anesthetized rabbit that underwent bilateral vagotomy. In-silico and ex-vivo experiment results were compared to evaluate the performance of the control strategies concerning* accuracy and settling time*. For both control strategies, the simulations led to performance indicators within the pre-defined requirements (10 bpm mean-squared error, 10% percentual overshoot, and 15 s settling time). In the in-vivo experiment, however, only one of the two control strategies could meet the requirements.*

Keywords— *numerical model, cardiac denervation, cardiovascular system, vagus nerve stimulation, closed-loop heart rate control.*

Introduction

In the past years, numerical models have gained increasing importance in the field of biomedical engineering. These models do not only help to better understand underlying mechanisms of human physiology and pathophysiology but also to develop novel treatment strategies and medical devices. Many successful examples of such computer simulations can be found in cardiovascular- [1],[2] and neural engineering [3],[4]. Although for long time models of both fields were typically separated representations of isolated physiological systems, in recent years, the interplay of the autonomic nervous- and the cardiovascular system is increasingly becoming a focus of interest, leading to integrated neuro-cardiovascular system models. Such models can not only improve our understanding of the autonomic control of the cardiovascular system in healthy individuals but also elucidate the hemodynamic and neurological changes associated with pathological conditions such as cardiac denervation resulting from e.g., diabetes mellitus or cardiac transplantation. From an engineering perspective, these models are of preeminent importance for the development of novel neuro-modulation-based treatment strategies for the conditions associated with cardiac denervation. Therefore, we applied a previously developed integrated numerical model [5],[6] that allows us to simulate the provoked acute cardiovascular effects of vagus nerve stimulation (VNS). This model was tuned and validated to reproduce the acute chronotropic response to VNS in rabbits that underwent bilateral vagotomy. The model was employed to develop two control strategies for closed-loop heart rate control using VNS in case of complete vagal-cardiac denervation. The model-based control strategies were evaluated in one pilot animal experiment.

Methods

Model overview: The developed model integrates a lumped-parameter representation of the cardiovascular system with its autonomic and intrinsic cardiac control and a model of cervical vagus nerve stimulation. In brief, the hemodynamic system model consists of modified Windkessel models representing the arterial and venous compartments of the systemic and pulmonary circulation. The atria and ventricles are realized as time-varying elastance models. The autonomic cardiac control is governed by the arterial baroreflex and the pulmonary stretch reflex. The intrinsic cardiac control is realized through a single-cell Hodgkin-Huxley-type sinoatrial node cell modeld. To simulate the acute cardiac effects of VNS, a multi-axon multi-compartment Chiu-Ritchie-Rogart-Stagg-Sweeney model [8] of an efferent vagal-cardiac nerve fiber population was implemented. Extracellular stimulation was realized by introducing an activation function as described by Rattay [9]. That model was coupled to a multi-compartment model of the ACh kinetics within the vagal-cardiac neuroeffector junctions [10]. The so-obtained ACh concentrations were then used to modulate the heart rate through changes in sinoatrial ion-channel gating behavior. The influence on atrioventricular conduction and ventricular contractility was implemented as a time-delay and first-order low-pass filter dynamics. An overview of the model can be found in Figure1.

Control Strategies: Two closed-loop heart rate control strategies were implemented using the previously described in-silico model: (a) unsynchronized VNS, and (b) cardiac-synchronized VNS. Briefly, in both control strategies, charge-balanced cathodic-anodic biphasic current pulses are delivered to the vagus

Published by Verlag der TU Graz
Graz University of Technology

DOI: 10.3217/978-3-85125-826-4-01

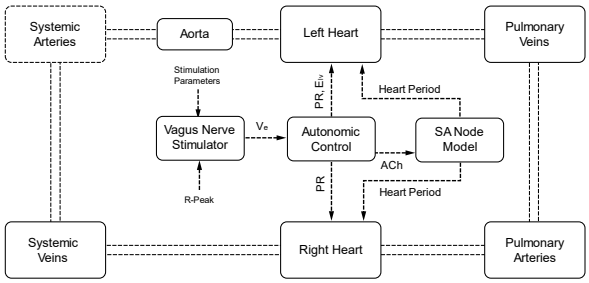

Figure 1: Overview of the integrated model (PR, atrioventricular conduction time; E_{lv}, left ventricular elastance, ACh, acetylcholine, V_e, extracellular potential).

nerve. In the unsynchronized control strategy, the stimulation is applied continuously without respect to the cardiac cycle. The shape of the pulses is determined by three main parameters: current amplitude (C), pulse width (PW), and frequency (F). In the synchronized strategy, a defined number of pulses (NP) is delivered with a specific delay (D) to the onset of left ventricular isovolumic contraction identified from the R-peaks in the electrocardiogram (ECG). A summary of the stimulation parameter values used is given in Table 1.

Table 1: Stimulation parameter values used in unsynchronized (U) and cardiac-synchronized (S) stimulation strategies.

Type	C (mA)	PW (µs)	F (Hz)	NP	D (ms)
U	0 – 2	200	30	-	-
S	0 – 2	200	30	8	0

The closed-loop control was implemented using a proportional-integral (PI) controller that minimizes the error between the measured instantaneous heart rate and a given reference heart rate. A previously performed sensitivity analysis highlighted the preeminent influence of the current amplitude on the provoked chronotropic responses [6], thus it was chosen as the control variable. The controller tries to minimize the perceived error by applying a correcting proportional and integrating term that are added to the current amplitude. The final form of the PI controller is given by Equation 1, where $P_c(t)$, is the controller output (current amplitude respectively), K_p is the proportional gain, K_i is the integral term, $e(t) = HR_{ref} - HR(t)$ is the error between the reference and the measured instantaneous heart rate.

$$P_c(t) = K_p e(t) + K_i \int e(t)dt \qquad (1)$$

Controller Gain Identification: The goal was to optimize the controller gains (K_p, K_i) concerning the accuracy and speed of convergence of the controller. Therefore, similar to the work of Ugalde et al. [11], the gains were optimized with regards to three performance indicators: (a) mean squared error (MSE) calculated from the last 10 s of the stimulation period, (b) percentual overshoot (%OS) corresponding to the overshoot amplitude expressed as a percentage of the final reference heart rate, and (c) the settling time (T_s) defined as the time that is required for the heart rate to go from baseline to 90% of the final value. Therefore, the cost function of the form:

$$F = \frac{1}{3}\left(\frac{MSE}{\widehat{MSE}} + \frac{\%OS}{\widehat{\%OS}} + \frac{T_s}{\widehat{T_s}}\right) \qquad (2)$$

was minimized using Bayesian optimization with 100 evaluations of the cost function. The cost function is defined as the arithmetic mean of the three performance indicators. The performance indicators were normalized to the respective requirements for the individual markers ($\widehat{MSE}$, $\widehat{\%OS}$, $\widehat{T_s}$). The predefined requirements were a maximum rise time of 15 s, a maximum relative overshoot of 10%, and a mean squared error below 10 bpm. For each optimization iteration, a step-response simulation was performed consisting of an initial phase of 100 seconds in which the controller is turned off to establish a baseline, followed by a phase of 100 seconds in which the controller is turned on, trying to reduce the heart rate by 35 bpm from baseline.

The optimization was carried out to meet the demands regarding the accuracy and settling time of the control strategy.

Hardware-in-the-loop implementation: Both control strategies were implemented using hardware-in-the-loop tools. The loop comprises an instrumentational amplifier (Warner DP-304A) to acquire the electrocardiogram (ECG) of the animal, a real-time prototyping system (DSPACE MicroLabBox) on which a binary of the control strategy is executed, a linear isolated stimulator (Biopac STMISOLA), and a bipolar cuff electrode used to deliver the stimuli to the animal's vagus nerve. A schematic overview of the hardware-in-the-loop chain is presented in Figure 2.

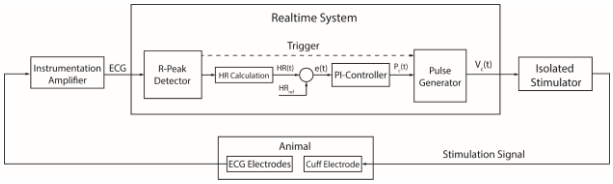

Figure 2: Schematic overview of the hardware-in-the-loop implementation of the control strategy.

Animal Preparation: One adult New Zealand white rabbit was used for initial evaluation of the control strategy under the approval of the Institutional Animal Care and Use Committee of the city of Vienna (BMBWF 2020-0.016.858 – GZ 2020-0.016.858).
The animal was premedicated with 0.1-0.2ml/kg ketamine (100mg/ml Ketasol®) and 0.2-0.3ml/kg dexme-

Published by Verlag der TU Graz
Graz University of Technology

DOI: 10.3217/978-3-85125-826-4-01

detomidine (Dexdomitor®, 1mg/ml) injected intramuscularly, followed by intravenous induction of the same mixture via the auricular vein 15-20 minutes after premedication was given. The animal then was endotracheally intubated allowing anesthesia to be maintained with sevoflurane vaporized in a 40:60 mixture of oxygen and medical air.
For electrode implantation, the carotid sheath on the left and the right were opened and the trio consisting of the cervical vagus nerve (CVN), the internal jugular vein, and the common carotid artery were dissected, followed by gentle isolation of the CVN. Once both, the right and left CVN were exposed, a bipolar cuff-electrode (Microprobes NC-3.5-2-250P-5-6-sut-300-TP) with a diameter of 0.75 mm and contact spacing of 3 mm was wrapped around the right CVN with the anode positioned cephalad. After electrode implantation, both vagus nerves were dissected cephalad to the stimulation cuff electrode using surgical clippers.
The ECG was acquired using needle electrodes with anode and cathode placed on right and left upper limb respectively, and the reference electrode on the right hindlimb. Arterial pressure was monitored from the right femoral artery and mean arterial pressure was maintained in a range of 60 to 80 mmHg.

Control Test Procedure: To evaluate the performance of the control strategies using the controller gains identified from the in-silico model, a step-response test was performed. The protocol consisted of a single step from baseline, reducing the heart rate by 35 bpm. For the in-vivo experiment results, the performance indicators were calculated and compared to the predictions of the computer simulation.

Results

The gains of the PI controller were automatically tuned concerning accuracy and settling time using the in-silico model. After optimization, for both control strategies, all three performance indicators were well below the pre-defined requirements of 10 bpm, 10% and 15 s for MSE, %OS and T_s, respectively (Table 2).

Table 2: Optimal PI gains found by automatic optimization for unsynchronized (U) and cardiac-synchronized (S) stimulation strategies.

Type	K_p	K_i	MSE	%OS	T_s
U	0.001	0.005	2.7 bpm	3.5%	5.8 s
S	0.01	0.05	0.7 bpm	0.2%	3.8 s

Using the identified values for the controller gains, both control strategies were tested in one acute pilot experiment in an anesthetized rabbit that underwent bilateral vagotomy. Therefore, a step response protocol consisting of a single step was performed, decreasing the heart rate, starting from baseline by 35 bpm. The results of the step response protocol in the in-vivo experiments and that of the in-silico model are presented in Figure 3 and Figure 4 for the synchronized and the unsynchronized control strategy, respectively.

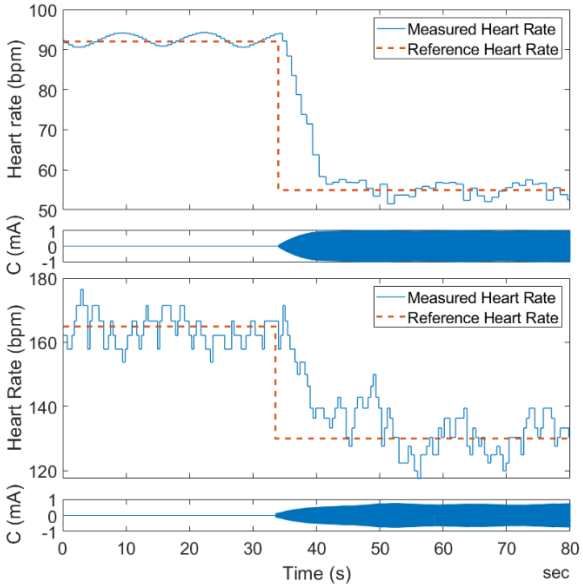

Figure 3: Step response using the unsynchronized control strategy in the in-silico model (top) and the in-vivo experiment (bottom).

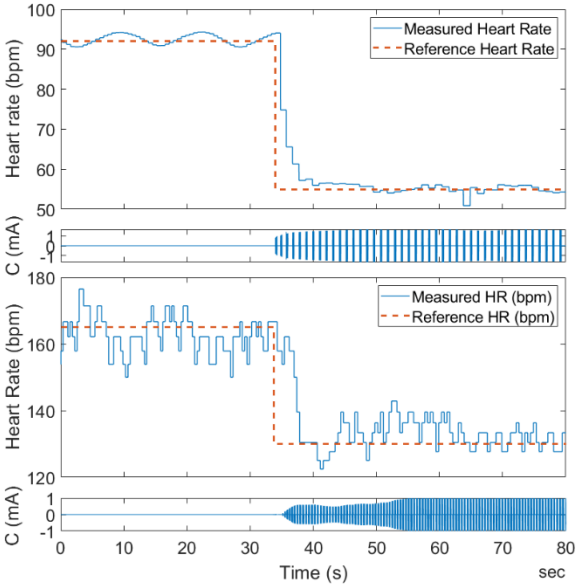

Figure 4: Step response using the cardiac-synchronized control strategy in the in-silico model (top) and the in-vivo experiment (bottom).

The three performance indicators (MSE, %OS, T_s) were also calculated for the in-vivo data. The results for the unsynchronized and the synchronized strategies are presented in Table 3. Both control strategies showed worse performance in the in-vivo experiments than predicted by the computer simulations. The synchronized control strategy however met all the pre-defined requirements while the unsynchronized type substantially exceeded the limits for the MSE.

Published by Verlag der TU Graz
Graz University of Technology

DOI: 10.3217/978-3-85125-826-4-01

Table 3: Performance indicators for in-vivo step response protocol using unsynchronized (U) and synchronized (S) stimulation strategies.

Type	MSE	%OS	T_s
U	22.9 bpm	2.3%	6.2 s
S	8.5 bpm	6.2%	4.3 s

Discussion

Numerical models have been proven to be viable tools to aid the development of medical devices and respective control strategies. In our work, we applied a previously developed numerical model that integrates the cardiovascular system and its autonomic control with a model of a vagal-cardiac nerve fiber population to develop two different control strategies for closed-loop heart rate control using VNS. These control strategies were then tested in a first pilot animal experiment.

The PI control was chosen over more sophisticated concepts as e.g., model predictive control due to its simplicity and straight-forward implementation. Although often a derivative term is added to the PI controller, it was omitted since previous studies suggest this leads to worse accuracy in closed-loop heart rate control [11].

The performance indicators calculated from the model predictions and the pilot in-vivo experiment for both control strategies lead to inconsistent results. Overall, the control strategies showed a substantially better performance in the computer simulations as compared to the pilot experiment. The discrepancies may be related to uncertain factors not considered in the numerical model such as anesthesia-related changes in dynamics of autonomic cardiovascular control. Thus, further investigations are needed to refine the computer model based on experimental results.

Although the performance of both control strategies was worse in the in-vivo experiment, the synchronized control strategy was markedly superior to the unsynchronized stimulation in terms of accuracy. Even though the performance was lower than predicted by the computer simulation, the synchronized control paradigm could meet all defined performance criteria suggesting it as a viable strategy for closed-loop heart rate control that should be pursued in future work.

Finally, we need to acknowledge limitations in our work. First, the baseline heart rate in the model was substantially different than that in the in-vivo experiments. This is because the intrinsic cardiac control of the model was realized as a human SA node model. We cannot exclude that using a sinoatrial node cell model of the rabbit would have improved the overall outcomes of the work. Moreover, the control strategy was only evaluated in a single animal. Therefore, we cannot draw any conclusions on the preservation of the control strategy performance for changed physiological conditions. Current work is focused on a refined tuning of the model for rabbit physiology and the evaluation of the control strategy in a virtual study population and later in a larger series of in-vivo experiments.

Overall, this work serves as a proof of concept of the capabilities of our model to aid the development and evaluation of novel VNS paradigms for the treatment of cardiovascular conditions associated with vagal-cardiac denervation.

Acknowledgments

This work was funded by the European Project H2020-EU.1.2.2. “A neuroprosthesis to restore the vagal-cardiac closed-loop connection after heart transplantation, NeuHeart” (Grant agreement ID: 824071).

References

[1] Y. Qian et al., “Computational hemodynamic analysis in congenital heart disease: simulation of the Norwood procedure,” Ann. Biomed. Eng., vol. 38, pp. 2302–2313, 2010.

[2] M. T. Politi et al., “The dicrotic notch analyzed by a numerical model,” Comput. Biol. Med., vol. 72, pp. 54–64, 2016.

[3] M. Sunshine et al., “Restoration of breathing after opioid overdose and spinal cord injury using temporal interference stimulation,” Commun. Biol., vol. 4, pp. 1–15, 2021.

[4] K. Aristovich et al., “Model-based geometrical optimisation and in vivo validation of a spatially selective multielectrode cuff array for vagus nerve neuromodulation,” J. Neurosci. Methods, vol. 352, pp. 109079, 2021.

[5] M. Haberbusch et al., ”Changes in Resting and Exercise Hemodynamics Early After Heart Transplantation: A Simulation Perspective,” Front. Physiol., vol. 11, pp. 1357, 2020.

[6] M. Haberbusch et al., “Towards Vagus Nerve Stimulation to Restore Heart Rate Control in Heart Transplant Patients: A Simulation Study,” in 18th Nordic Baltic Conference on Biomedical Engineering and Medical Physics, 2020.

[7] A. Fabbri et al., “Computational analysis of the human sinus node action potential: model development and effects of mutations,” J. Physiol., vol. 595, no. 7, pp. 2365–2396, 2017

[8] J. D. Sweeney et al., “Modeling of mammalian myelinated nerve for functional neuromuscular electrostimulation,” in IEEE 9-th ann. conf. Eng. Med. Biol., pp. 1577-1578, 1987.

[9] F. Rattay, Electrical Nerve Stimulation, Vienna, Austria: Springer-Verlag Wien, 1990.

[10] S. Dokos et al., "Vagal Control of Sinoatrial Rhythm: a Mathematical Model,” Journal of Theoretical Biology, vol. 182, pp. 21–44, 1996.

[11] H. M. R. Ugalde et al., “Model-Based Design and Experimental Validation of Control Modules for Neuromodulation Devices,” IEEE Trans. Biomed. Eng., vol. 63, no. 7, pp. 1551–1558, 2015

Published by Verlag der TU Graz
Graz University of Technology

Proc. Annual Meeting of the Austrian Society for Biomedical Engineering 2021
DOI: 10.3217/978-3-85125-826-4-02

MODELING THE DOUBLE LAYER FORMATION FOR ELECTRICAL NEUROSTIMULATION AT THE ORGANIC POLYMER - ELECTROLYTE INTERFACE

S.Stoppacher[1], C. Baumgartner[1], S. Scheruebel[2], M. Ücal[3], K. Kornmüller[2], R. Schindl[2] and T. Rienmüller[1]

[1]Institute of Health Care Engineering with European Testing Center of Medical Devices, Graz University of Technology, Austria
[2]Gottfried Schatz Research Center Division of Biophysics, Medical University of Graz, Austria
[3]Department of Neurosurgery, Medical University of Graz, Austria

stoppacher@tugraz.at

Abstract— *Electrical double-layer formation attracted significant interest more than a century ago and remains fundamentally involved in capacitive external stimulation of biological tissue. This work focuses on the study of the double layer characteristics at the interface formed between an electrolyte and polymer structures of organic photocapacitors for minimally invasive neurostimulation. Based on a combination of the Helmholtz and Gouy-Chapman methods, the Stern model is applied in COMSOL Multiphysics to investigate this electrical double layer formation. Simulations nicely highlight the importance of the electrolyte concentration and good cell adhesion.*

Keywords— *EDL, Stern model, photocap, organic photocapacitor, OEPC*

Introduction

Organic Photocapacitors (OEPCs)

Wireless light-sensitive semiconductors named organic electrolytic photocapacitor (OEPC) for cellular and tissue stimulation are currently attracting significant interest in the field of biomedicine [1][2]. This minimally invasive stimulation technique could be utilized to improve connectivity and tissue regeneration after peripheral or central nervous system injuries, such as cerebral injury. In using OEPCs for external stimulation of excitable cells, surpassing the threshold potential remains a major challenge, mainly due to an insufficient interface between the attached cell membrane and the electrode surface, which is caused by a small gap. This can electronically be described by an ideal capacitor acting in the intermediate layer [3]. The characteristic behavior within this cleft is essential to generate the required magnitude of stimulus to surpass the cells' threshold potential and can be described using models for the electrical double layer.

Double Layer Models

Many general studies have been published on the behavior of the electrolytic double layer (EDL). Helmholtz described the behavior of the electrolytic double layer for the first time in his seminal work in 1879 [4]**.** The model describes the linear potential curve across the "Helmholtz double layer", formed by ideally opposite charges between a metal electrode and the electrolyte. The double layer is bounded by the hydrate shells of the ions sitting on the electrode surface. The so-called outer Helmholtz plane (OHP) passes through the center of these ions. A major advance in the early 20th century was described by Louis Georges Gouy and David Leonard Chapman with the Gouy-Chapman double layer [5][6]. Their approach was an extended description of the Helmholtz theory, but Gouy and Chapman also considered the thermal motion and the ions forming a diffuse layer. Further findings from Otto Stern revealed that the electrolytic double layer can be described by a combination of the two previous models [7]. A rigid ion layer is assumed on the metal surface and an adjacent diffuse layer reaching deep into the electrolyte. Fig. 1 represents the double layer formed between the OEPC's surface and the electrolyte, where the OHP is limited by half of the K^+-hydrated shell size, shown in the inset of this picture. A diffusive layer is adjacent to the Helmholtz layer, where the potential decreases against zero.

Limitations are partially given by the Poisson-Boltzmann equation, where ions are treated as point charges and their physical size is ignored. Assumptions of point charges are mainly applicable for low ion concentrations and low electric potential changes. In other words, modeling EDL is often limited due to the simplification of the ionic structure.

Published by Verlag der TU Graz
Graz University of Technology

DOI: 10.3217/978-3-85125-826-4-02

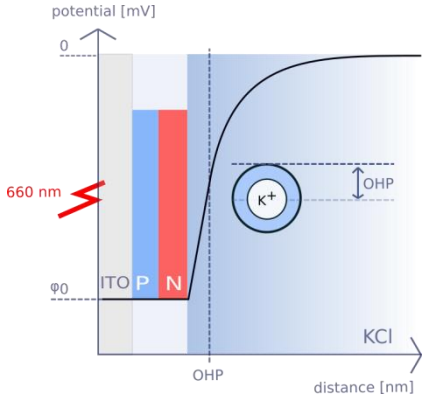

Figure 1: An electrochemical double layer schematic representing the OEPC-electrolyte interface illuminated with 660 nm light pulses. The initial surface potential φ_0 of the OEPC (ITO and PN layer) decreases against zero across the OHP and the diffusion layer. The OHP is limited by half of the K+-hydrated shell size, shown in the inset of this figure.

Methods

Double layer model

In order to describe the bilayer characteristics and subsequently evaluate whether optoelectronic neurostimulation is successful, it is necessary to take a detailed look at the mathematical descriptions of the double layer characteristics [8]-[13]. Focus is on the potential curve that arises between the electrode surface and the cell membrane. In this section, factors are pointed out essentially involved in the EDL formation. First, the linear Helmholtz potential distribution is described by Poisson's equation, shown in Eq. 1.

$$\frac{d^2\varphi}{dx^2} = -\frac{\rho(x)}{\varepsilon_r \cdot \varepsilon_0} \tag{1}$$

φ_0 … potential
$\rho(x)$ … charge density
ε_r … relative permittivity
ε_0 … electric field constant

Since there is a charge-free region between the metal surface and the ions, it follows for the Poisson equation that $\rho = 0$ at this point. The Helmholtz double layer capacity can be further calculated as shown in Eq. 2, where d equals the OHP distance.

$$C_H = \frac{\varepsilon_r \cdot \varepsilon_0}{d} \tag{2}$$

To explain the process in the diffusion layer, the Gouy-Chapman description is used. In addition, the Boltzmann distribution is considered in the Poisson equation for the potential field, see Eq. 3.

$$\rho(x) = \sum_i z_i \cdot e \cdot c_i \cdot \exp\left(-\frac{z_i \cdot e \cdot \varphi(x)}{k \cdot T}\right) \tag{3}$$

z_i … ion charge number
c_i … ion bulk concentration [M]
e … electron charge
k … Boltzmann constant
t … temperature [K]

For the calculation of the potential distribution, the linearized approach for solving the Poisson-Boltzmann equation is assumed as shown in Eq. 4, considering the Debye length κ^{-1}.

$$\varphi(x) = \varphi_0 \cdot \exp\left(-\frac{x}{\kappa}\right) \tag{4}$$

Hence, combining Eq. 1 and Eq. 3 yields the following expression, see Eq. 5:

$$\rho(x) = -\varepsilon_r \cdot \varepsilon_0 \frac{d^2\varphi(x)}{dx^2} = -\frac{\varepsilon_r \cdot \varepsilon_0 \cdot \varphi_0}{\kappa^2} \cdot \exp\left(-\frac{x}{\kappa}\right) \tag{5}$$

To describe the electrostatic ion interactions in electrolytes, the Debye-Hückel theory can be applied [14]. The thickness of the diffuse double layer, the so-called Debye length, can further be calculated considering the Avogadro constant (NA) and the ionic strength I_{str} see Eq. 6 and Eq. 7.

$$x_D = \kappa^{-1} = \sqrt{\frac{2 \cdot NA \cdot e^2 \cdot I_{str}}{\varepsilon_r \cdot \varepsilon_0 \cdot k \cdot T}} \tag{6}$$

$$I_{str} = \frac{1}{2}\left(\sum_i z_i^2 \cdot c_i\right) \tag{7}$$

The Gouy-Chapman bilayer capacitance is again related to the Debye length and is calculated as shown in Eq. 8, with σ representing the charge density.

$$C_{Gdiff} = \frac{d\sigma}{d\phi_0} = \frac{\varepsilon_r \cdot \varepsilon_0}{x_D} \cosh\left(\frac{z \cdot F \cdot \varphi_0}{2 \cdot R \cdot T}\right) \tag{8}$$

Finally, the Stern model combines both theories and can be described electrically by the sum of the Helmholtz capacity together with the Gouy-Chapman capacity, as shown in Eq. 9.

$$\frac{1}{C_{stern}} = \frac{1}{C_H} + \frac{1}{C_{Gdiff(\varphi_0)}} \tag{9}$$

Organic Photocaps

In this paper, an organic photocapacitor with the polymer layers H2Pc(p):PTCDI(n) is used. The OEPCs photo response is measured in a KCl electrolyte bath. For light stimulation, a 10 W LED with 660 nm is used.

Results

Analytical calculations were performed in MATLAB. Subsequently, both 1D and 2D models were set up in COMSOL Multiphysics using the AC/DC module.

Published by Verlag der TU Graz
Graz University of Technology

DOI: 10.3217/978-3-85125-826-4-02

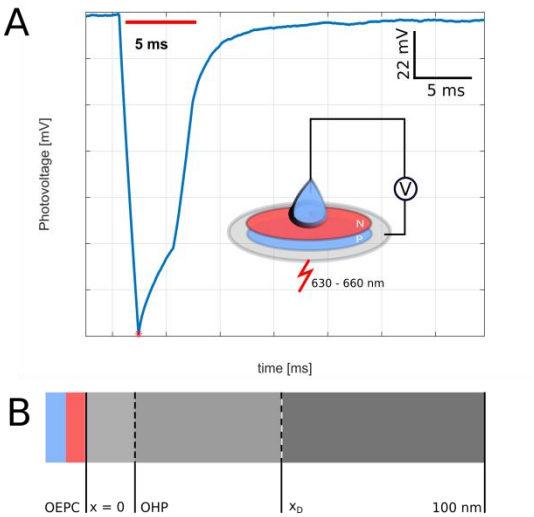

Figure 2: A. Electrical photo response measurement of an OEPC illuminated with a 5 ms light pulse, B. Model geometry with marked layer distances: x = 0, outer Helmholtz plane (OHP), Debye length (x_D) and the total length of 100 nm

The geometric model in COMSOL Multiphysics was set up as shown in Fig. 2 B, by inserting various layers with different thicknesses and distances, such as polymer-surface thickness, OHP, x_D and the total length.
A potential of -159 mV was set at the OEPC surface. The relative permittivity for the electrolyte was assumed with 78.4, the temperature with 293.15 K. The OHP is limited by the hydrated ion size of K^+ cations and was assumed with 0.315 nm [15]. The Debye length x_D was calculated with 3.01 nm for 0.01 M KCl and 0.95 nm for 0.1 M KCl. The total length was limited to 100 nm.

Fig. 2 A represents the measured photo response when illuminating the photocap for 5 ms. The inset part in Fig. 2 A represents the measurement setup for observing the photovoltage obtained from OEPCs using a KCl electrolyte. In the model, the potential decays to a steady-state starting from the polymer surface to a depth of about 100 nm into the electrolyte. Based on these assumptions and the equations listed in the methods section, the potential curves shown in Fig. 3 A are obtained for a temperature of 293.15 K. Furthermore, potentials maintained at prominent points within the double layer are represented in Tab. 1.

Table 1: Electrical potentials calculated within the double layer for different KCl concentrations.

	potential $\varphi(x)$ [mV]	
distance x	**0.01 [M]**	**0.1 [M]**
0	-159.00	-159.00
OHP	-122.19	-90.62
x_D	-58.06	-50.72

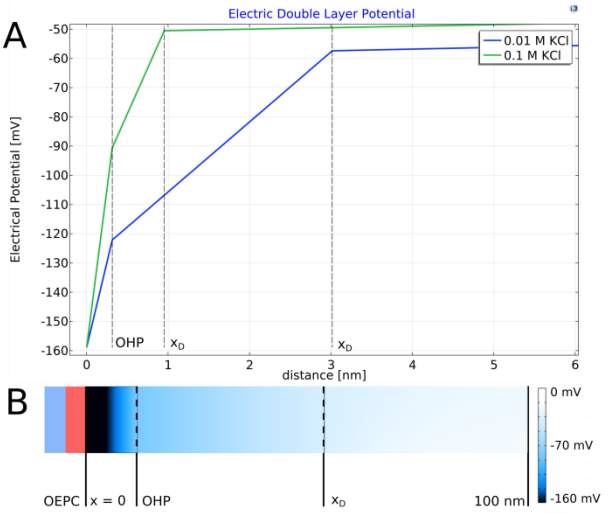

Figure 3: A. Electrical potential distribution for different electrolyte concentrations. The first dotted line represents the OHP distance, the second one the Debye length for 0.1 M KCl and the third one the Debye distance for 0.01 M KCl, B. Electrical potential distribution across the total length for 0.01 M KCl

The rapid potential drop between the OEPC surface and the OHP layer can be nicely seen in Fig. 3 B. In addition, the calculated capacities for various electrolyte concentrations are listed in Tab. 2.

Table 2: Calculated capacities for different electrolyte concentrations

	capacities [µF/cm²]	
	0.01 [M]	**0.1 [M]**
C_H	220.37	220.37
C_{Gdiff}	39.98	112.70
C_{stern}	33.84	74.56

Discussion

There are significant advantages associated with the use of EDL models, especially since experimental methods are complex and often difficult to implement. They can be used to effectively investigate the double layer characterization, which reveals the interaction between the stimulation electrode and the cell behavior. Key parameters such as ion concentration, ion size, electrical potential, geometries, and many other factors pertaining to double layer characteristics can be quickly investigated and indicate the best way to improve cell measurements.
The simulation results presented in this paper show the rapid potential decrease within the outer Helmholtz layer. Furthermore, a strong dependence on the electrolyte can be observed. Thus, both the conductive medium and coating of the stimulating device intended to enhance cell attachment and thus essential for successful neurostimulation should be

Published by Verlag der TU Graz
Graz University of Technology

DOI: 10.3217/978-3-85125-826-4-02

taken into account. The distance between the cell membrane and the OEPC surface is of enormous significance. Variations in temperature are not a major factor here.

Beside the constant assumptions in the Stern model mentioned at the beginning, the model limitations are given by the linearization of the Poisson-Boltzmann-equation. This approximation fits well for $\frac{\Delta\varphi}{kT} \leq 1$. Even though constraints arise with the linearized approach yielding the Debye-Hückel approximation, still good assumptions can be made with respect to a considerable number of cases. However, even in the case presented in this work, the approximation provides good assumptions despite small deviations. For larger potential changes improvements may be achieved by extending the Poisson-Boltzmann approach which can become complex quickly.

In conclusion, the model presented in this paper yields reasonable assumptions on parameters required to be adjusted to ensure successful external cell stimulation.

Acknowledgements

This work was funded by the FWF Zukunftskolleg Program as part of the project “LOGOS-TBI: Light-controlled Organic Semiconductor Implants for Regeneration after TBI” (Project ID: ZK-17). OEPCs were fabricated in the lab of the LOGOS-TBI collaboration partner Dr. Głowacki (Linköping University, Sweden).

References

[1] M. Jakešová, M. Silverå Ejneby, V. Đerek et al. Optoelectronic control of single cells using organic photocapacitors. Sci Adv. 2019; 5(4): eaav5265. doi:10.1126/sciadv.aav5265

[2] D. Rand, M. Jakešová, G. Lubin et al. Direct Electrical Neurostimulation with Organic Pigment Photocapacitors. Adv Mater. 2018; 30(25): e1707292. doi:10.1002/adma.201707292

[3] J. Kang, J. Wen, S. H. Jayaram et al. Development of an equivalent circuit model for electrochemical double layer capacitors (EDLCs) with distinct electrolytes. Electrochimica Acta. 2014; 115: pp. 587–598. doi:10.1016/j.electacta.2013.11.002

[4] H. Helmholtz. Studien über electrische Grenzschichten. Annalen der Physik. 1879; 243(7): pp. 337–382. doi:10.1002/andp.18792430702

[5] M. Gouy. Sur la constitution de la charge électrique à la surface d’un electrolyte. J. Phys. Theor. Appl. 1910; 9(1): pp. 457–468. doi:10.1051/jphystap:019100090045700

[6] D. L. Chapman. LI. A contribution to the theory of electrocapillarity. The London, Edinburgh, and Dublin Philosophical Magazine and Journal of Science. 1913; 25(148): pp. 475–481. doi: 10.1080/14786440408634187.

[7] O. Stern. ZUR THEORIE DER ELEKTROLYTISCHEN DOPPELSCHICHT. Zeitschrift für Elektrochemie und angewandte physikalische Chemie. 1924; 30: pp. 508-516. doi: 10.1002/bbpc.192400182

[8] M. A. Brown et al. Determination of Surface Potential and Electrical Double-Layer Structure at the Aqueous Electrolyte-Nanoparticle Interface. Phys. Rev. X. 2016; 6(1): p. 011007. doi: 10.1103/PhysRevX.6.011007.

[9] E. Gongadze, S. Petersen, U. Beck et.al. Classical Models of the Interface between an Electrode and an Electrolyte. COMSOL Conference 2009 Milan. 2009: p. 7.

[10] G. Spagnoli, T. Fernández-Steeger, H. Hu, et. al. Potential calculation according to the Gouy and the Stern model for kaolinite and smectite. Giornale di geologia applicata : rivista dell'AIGA. 2010; 13(1): pp.87-91. AIGA, 2010. doi: 10.1474/EHEGeology.2010-13.0-07.283

[11] M. A. Brown, A. Goel, Z. Abbas. Effect of Electrolyte Concentration on the Stern Layer Thickness at a Charged Interface. Angew. Chem. Int. Ed. 2016: p. 5

[12] T. Atouani, A. Saidane, A. Nouri, et. al. The Gouy-Chapman Capacitor of Double Layer in Dye Sensitized Solar Cells: Study and Simulation. International Journal of Renewable Energy Research. 2016; 6(1): pp. 164-170

[13] E. Partheniades. Forces between Clay Particles and the Process of Flocculation. Cohesive Sediments in Open Channels. Boston. 2009. doi: 10.1016/B978-1-85617-556-2.00003-2.

[14] P. Debye und E. Hückel. Zur Theorie der Elektrolyte. Physikalische Zeitschrift. 1923; 9: pp. 185–206.

[15] Tanganov B.B. ABOUT SIZES OF THE HYDRATED SALT IONS – THE COMPONENTS OF SEA WATER. European Journal of Natural History. 2013; 1: pp.36–37.

Published by Verlag der TU Graz
Graz University of Technology

Proc. Annual Meeting of the Austrian Society for Biomedical Engineering 2021
DOI: 10.3217/978-3-85125-826-4-03

SODIUM TRANSIENTS IN AN ASTROCYTE

K. Lenk[1], A. Tervonen[2], J. Hyttinen[2]

[1]Institute for Neural Engineering, Graz University of Technology, Austria
[2]BioMediTech, Faculty of Medicine and Health Technology, Tampere University, Finland

kerstin.lenk@tugraz.at

Abstract— *Astrocytes, a type of glial cells in the brain, are actively involved in neuronal information processing and memory formation. An astrocyte participates in neuronal activity by receiving neurotransmitters, e.g., glutamate, from an adjacent presynapse. This leads to the propagation of astrocytic intra- and intercellular calcium waves. In this study, we extend the computational model presented by Oschmann et al. (2017) to a finite element model of single astrocytes, including a realistic 2D geometry and* inositol 1,4,5-trisphosphate (*IP_3*) *and ion diffusion. Here, we conduct a parameter exploration of the sodium-calcium exchanger (NCX) and sodium-potassium-ATPase (NKA) rate constants. The calcium concentration directly depends on the amplitude of the glutamate stimulus. However, the sodium concentration instead relates only to the sodium-potassium pump activity.*

Keywords— *Astrocyte, simulation, sodium, calcium, diffusion*

Introduction

Astrocytes are a glial cell type that plays a major role in the ion and energy homeostasis of the brain. Astrocytes and neurons are in a ratio of 1:2 in rodents and even 1:1 in humans. A single astrocyte can connect between 270 000 and 2 million neuronal synapses [1]. Thus, astrocytes can functionally modulate neuronal activity and complex mammalian behavior. In a landmark paper [2], mice with transplanted human astrocytes showed improved long-term potentiation and performance in learning tasks, emphasizing the importance of human astrocytes for the unique human cognitive abilities. Experimental findings strongly indicate that astrocytes might be involved in various pathologies such as epilepsy, depression, Alzheimer's, and Huntington's disease [3], [4].

Computational modeling can aid experimental work by forming a theoretical framework to characterize the anatomy and function of neurons and astrocytes [5]. Thus, a well-planned theoretical study can guide experimentalists towards the most relevant experiments, and in this way, save time and resources. In our review paper [5], we summarized astrocyte models from subcellular to network level that have started to emerge.

Oschmann et al. [6] introduced an astrocyte model including two glutamate pathways which both induce calcium (Ca^{2+}) elevations (Fig. 1): activation of (1) the metabotropic glutamate receptors (mGluRs) and (2) the glutamate transporters (mGluT) at the plasma membrane. The mGluR pathway includes the uptake of glutamate from the extracellular space. Subsequently, inositol 1,4,5-trisphosphate (IP_3) followed by a Ca^{2+} release from the endoplasmic reticulum (ER) into the cytosol through IP_3 receptor channels. The increasing Ca^{2+} levels lead to an opening of further IP_3 channels and a Ca^{2+}-induced Ca^{2+} release (CICR). The second pathway includes the mGluTs, which transports potassium (K^+) out and sodium (Na^+) and glutamate into the cell. Furthermore, the sodium-calcium exchanger (NCX) exchanges Na^+ and Ca^{2+} ions. The Na^+-K^+-ATPase (NKA) transports Na^+ ions out and K^+ ions into the cell. Additionally, leak currents for Na^+ and K^+ are modeled.

The novelty of the model is the combination of those two pathways and their dependence on the surface-to-volume ratio (SVR) and ER amount in the respective cell section. The SVR is large in perisynaptic astrocytic processes that connect to the neurons and small in the soma of the astrocyte. The ER ratio behaves the opposite.

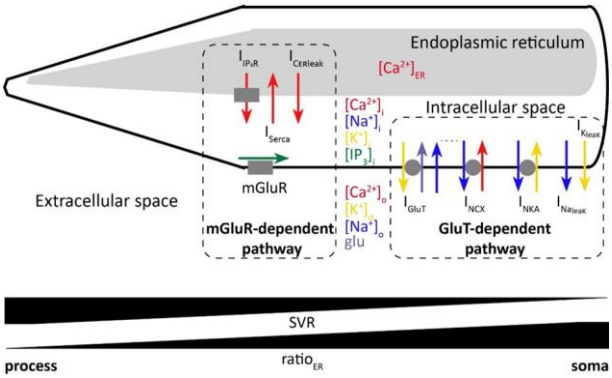

Figure 1: Scheme of the calcium dynamics within an astrocyte, including the mGluR- and the GluT-dependent pathway (adapted from [6]).

In this study, we combined the model by Oschmann et al. with a whole-cell astrocyte morphology [7]. Based on the width of a cell section, we automatically calculated the SVR. Furthermore, we added IP_3 and ion (Ca^{2+}, K^+, and Na^+) diffusion to the model.

Methods

We used the model and its parameters as described in Oschmann et al. [7] with the following additions: diffusion of IP_3, Ca^{2+}, K^+, and Na^+ with coefficients 300, 13, 1 960, and 1 330 µm²/s, respectively. Our model was implemented as a finite-

Published by Verlag der TU Graz
Graz University of Technology

DOI: 10.3217/978-3-85125-826-4-03

element method with a realistic geometry (Fig. 2 top) in COMSOL Multiphysics version 5.6. The geometry is implemented in 2D as a tridomain model (i.e., ER, cytosol, and extracellular space). The SVR in the geometry required by the model was based on the width of the processes.

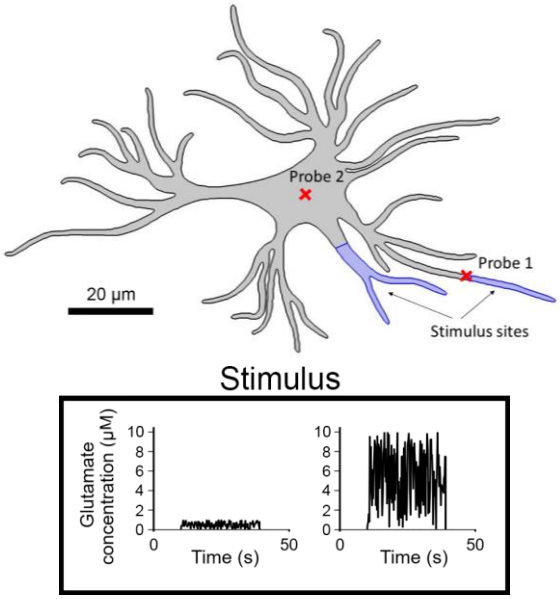

Figure 2: Top: Geometry of a single astrocyte with an indication of the stimulus sides (blue) and the locations of the two measurement probes (red crosses). Bottom: Random (uniform distribution) stimuli from 10 to 40 s with either 0.5 µM or 5 µM mean glutamate concentration.

We conducted a parameter exploration for the maximum pump current of NCX, I_{NCXmax}, with the values10^{-6}, 10^{-5}, 10^{-4}, 10^{-3}, 0.01, and 0.1 pA/µm², and for the maximal pump activity of NKA, I_{NKAmax}, with the values 10^{-6}, 0.1, 0.5, 1, 1.52, and 5 pA/µm². Similar parameter ranges have also been explored in Oschmann et al. [6]. Furthermore, we applied two different random glutamate stimuli with a mean of around 0.5 and 5 µM (Fig. 2 bottom) to two processes (Fig. 2 top).

For the different I_{NCXmax} and I_{NKAmax} values and the two glutamate input values, we measured the Ca^{2+} and Na^+ concentrations in one of the stimulated processes (Probe 1) and the soma of the astrocyte (Probe 2). Moreover, we counted the number of Ca^{2+} events (i.e., Ca^{2+} spikes with a full width at half maximum of maximally five seconds). We also determined the maximum values of the Na^+ concentration during the stimulation time as a function of the pump currents and the glutamate stimulus.

Results

Fig. 3 shows the Ca^{2+} concentrations in Probe 1 and 2 for the two applied glutamate concentrations. The higher stimulus led to more distinct Ca^{2+} spikes.

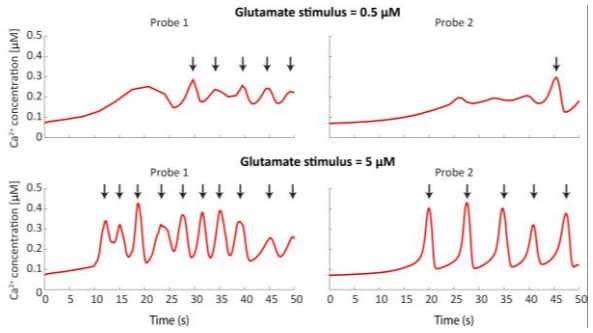

Figure 3: Ca^{2+} concentrations after stimulating the astrocyte with a glutamate concentration of 0.5 or 5 µM and applying I_{NCXmax} = 0.1 pA/µm² and I_{NKAmax} = 1 pA/µm². Rows: Glutamate stimulus of 0.5 (top) or 5 µM (bottom). Columns: Ca^{2+} concentrations in Probe 1 (left) or 2 (right) during the stimulation time. The arrows indicate the Ca^{2+} peaks. The x-axis depicts the time in seconds.

The maximum number of Ca^{2+} events was yielded with a glutamate stimulus of 5 µM and I_{NCXmax} = 0.1 pA/µm² and I_{NKAmax} = 1 pA/µm² (Fig. 4). As expected, the number of spikes was higher for a higher glutamate stimulus. For smaller I_{NKAmax} values and higher I_{NCXmax} values, the most number of Ca^{2+} oscillations were detectable.

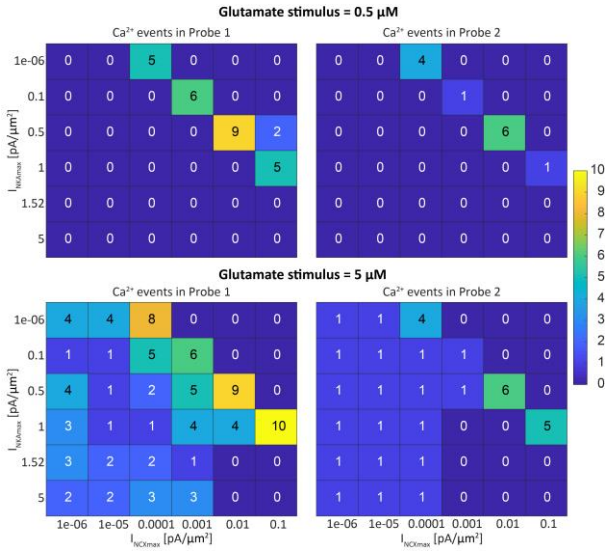

Figure 4: Number of Ca^{2+} events after stimulating the astrocyte with a glutamate concentration of 0.5 or 5 µM and different values for I_{NCXmax} and I_{NKAmax}. Rows: Glutamate stimulus of 0.5 (top) or 5 µM (bottom). Columns: Number of Ca^{2+} events (color bar) in Probe 1 (left) or 2 (right) during the stimulation time.

The maximum Na^+ concentration was clearly dependent on the values of I_{NKAmax} rather than on the values of I_{NCXmax} and the glutamate concentration (Fig. 5). The lower the values of I_{NKAmax} was the higher the Na^+ concentration.

Published by Verlag der TU Graz
Graz University of Technology

DOI: 10.3217/978-3-85125-826-4-03

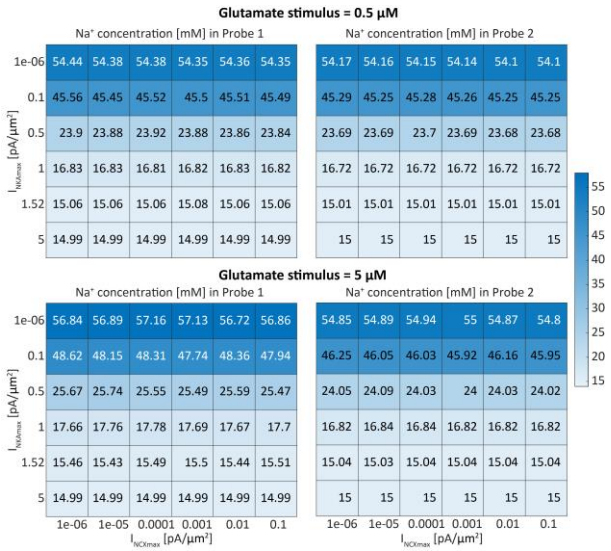

Figure 5: Na^+ concentrations after stimulating the astrocyte with a glutamate concentration of 0.5 or 5 µM and different values for I_{NCXmax} and I_{NKAmax}. Rows: Glutamate stimulus of 0.5 (top) or 5 µM (bottom). Columns: maximum Na^+ concentrations (color bar) in Probe 1 (left) or 2 (right) during the stimulation time.

Discussion

Our computational model investigates the intracellular calcium and sodium concentrations in dependence on the glutamate stimulus as well as the sodium-calcium exchanger, NCX, and the sodium-potassium-ATPase, NKA, pump rates. Therefore, we have extended the model by Oschmann et al. [7] by a realistic geometry and IP3 and ion diffusion.

There is a complex interplay between the calcium and sodium dynamics in the astrocyte. Calcium signals and oscillations may be triggered by activated mGluRs [8], [9] as well as by the NCX in reverse mode [10] and the inhibition of NKA [11]. In a study by Ziemens et al. [12], the authors used the equation of the NCX model as also used in [7]. They found that after glutamate-induced stimulation, the NCX switches from an inward mode to an outward/ reverse mode, which is connected to a calcium influx to the astrocyte. Furthermore, the model suggests that the calcium increase only weakly antagonizes the NCX in the processes but not in the soma.

Our study suggests that the intracellular sodium concentration is mainly driven by the NKA. A blockage of the NKA transporter by ouabain led to an increase of cytosolic sodium concentrations and thus seems to be the primary cause for sodium elevations in the astrocyte [10].

To conclude, our simulations showed that the calcium levels depend on the given glutamate concentrations and a balance of the sodium-calcium exchanger and the sodium-potassium-ATPase pump rates. The sodium levels rather relate only to the sodium-potassium pump activity.

Acknowledgements

K.L. received funding from the Academy of Finland (decision nos. 314647, 326452).

References

[1] T. Papouin, J. Dunphy, M. Tolman, J. C. Foley, and P. G. Haydon, “Astrocytic control of synaptic function,” *Philos. Trans. R. Soc. B Biol. Sci.*, vol. 372, no. 1715, p. 20160154, 2017, doi: 10.1098/rstb.2016.0154.

[2] X. Han *et al.*, “Forebrain engraftment by human glial progenitor cells enhances synaptic plasticity and learning in adult mice,” *Cell Stem Cell*, vol. 12, no. 3, pp. 342–53, Mar. 2013, doi: 10.1016/j.stem.2012.12.015.

[3] D. A. Coulter and C. Steinhäuser, “Role of Astrocytes in Epilepsy,” *Cold Spring Harb Perspect Med*, vol. 5, p. a022434, 2015, doi: 10.1038/clpt.2011.183.

[4] A. M. Wójtowicz, A. Dvorzhak, M. Semtner, and R. Grantyn, “Reduced tonic inhibition in striatal output neurons from Huntington mice due to loss of astrocytic GABA release through GAT-3.,” *Front. Neural Circuits*, vol. 7, no. November, pp. 1–12, Nov. 2013, doi: 10.3389/fncir.2013.00188.

[5] F. Oschmann, H. Berry, K. Obermayer, and K. Lenk, “From in silico astrocyte cell models to neuron-astrocyte network models: A review,” *Brain Res. Bull.*, vol. 136, pp. 1–9, Jan. 2017, doi: 10.1016/j.brainresbull.2017.01.027.

[6] F. Oschmann, K. Mergenthaler, E. Jungnickel, and K. Obermayer, “Spatial separation of two different pathways accounting for the generation of calcium signals in astrocytes,” *PLoS Comput. Biol.*, vol. 13, no. 2, pp. 1–25, 2017, doi: 10.1371/journal.pcbi.1005377.

[7] M. U. Khalid, A. Tervonen, I. Korkka, J. Hyttinen, and K. Lenk, “Geometry-based Computational Modeling of Calcium Signaling in an Astrocyte,” in *Proc. EMBEC’17 & NBC’17*, 2017, pp. 157–160, doi: 10.1007/978-981-10-5122-7_40.

[8] A. H. Cornell-Bell, S. M. Finkbeiner, M. S. Cooper, and S. J. Smith, “Glutamate induces calcium waves in cultured astrocytes: Long-range glial signaling,” *Science (80-.).*, vol. 247, no. 4941, pp. 470–473, Jan. 1990, doi: 10.1126/science.1967852.

[9] S. Kirischuk, F. Kirchhoff, V. Matyash, H. Kettenmann, and A. Verkhratsky,

Published by Verlag der TU Graz
Graz University of Technology

DOI: 10.3217/978-3-85125-826-4-03

"Glutamate-triggered calcium signalling in mouse Bergmann glial cells in situ: Role of inositol-1,4,5-trisphosphate-mediated intracellular calcium release," *Neuroscience*, vol. 92, no. 3, pp. 1051–1059, Jun. 1999, doi: 10.1016/S0306-4522(99)00067-6.

[10] R. C. Reyes, A. Verkhratsky, and V. Parpura, "Plasmalemmal Na + /Ca 2+ exchanger modulates Ca 2+-dependent exocytotic release of glutamate from rat cortical astrocytes," doi: 10.1042/AN20110059.

[11] X. L. Liu, A. Miyakawa, A. Aperia, and P. Krieger, "Na,K-ATPase generates calcium oscillations in hippocampal astrocytes," *Neuroreport*, vol. 18, no. 6, pp. 597–600, Apr. 2007, doi: 10.1097/WNR.0b013e3280b07bc9.

[12] D. Ziemens, F. Oschmann, N. J. Gerkau, and C. R. Rose, "Heterogeneity of Activity-Induced Sodium Transients between Astrocytes of the Mouse Hippocampus and Neocortex: Mechanisms and Consequences," *J. Neurosci.*, vol. 39, no. 14, pp. 2620–2634, 2019, doi: 10.1523/jneurosci.2029-18.2019.

Published by Verlag der TU Graz
Graz University of Technology

Proc. Annual Meeting of the Austrian Society for Biomedical Engineering 2021
DOI: 10.3217/978-3-85125-826-4-04

MODELING OF ION CHANNELS – A SIDE BY SIDE COMPARISON BETWEEN HODGKIN HUXLEY AND HIDDEN MARKOV APPROACH OF KV1.1

S. Langthaler[1], T. Rienmüller[1], J. Lozanovic Sajic[1,2] and C. Baumgartner[1]

[1]Institute of Health Care Engineering with European Testing Center of Medical Devices, Graz University of Technology, Austria
[2]Innovation Center of the Faculty of Mechanical Engineering, University of Belgrade, Serbia

s.langthaler@tugraz.at

Abstract— *Mathematical models of individual ion channels form the building blocks of complex in-silico tools, enabling the investigation of biophysical mechanisms and simulation of disease processes. We here propose a first simplified hidden Markov Model (HMM) for the voltage-gated potassium channel Kv1.1, taking into account the channels' specific activation and inactivation characteristics close to physiological temperature. The modeling approach and simulation results were compared with an existing Hodgkin Huxley model based on the same experimental data. The newly developed HMM shows a higher accuracy with regard to the activation and inactivation behavior compared to the Hodgkin Huxley approach.*

Keywords— *computational electrophysiology, Hodgkin-Huxley model, hidden Markov model*

Introduction

Single channel models constitute the basis of in-silico tools for simulation of ion current kinetics and action potential alterations in excitable cells. A variety of whole-cell models of different levels of complexity and abstraction have been introduced and have become an integral part in neuroscience and cardiac electrophysiology, enabling the investigation of biophysical mechanisms, simulation of disease processes as well as prediction of therapeutic interventions.[1–4] A high degree of biophysical detail considering the specific gating properties with, at the same time, low computational burden are the fundamental requirements and challenges for a successful integration and application of ion channel models in biomedical research.

Modeling of ion channel kinetics is commonly based on Hodgkin-Huxley (HH) or hidden Markov Model (HMM) descriptions.[4–7] The HH model offers a basic paradigm in which the channel can be either open or closed depending on a set of gates, controlled by a number of gating particles. The kinetic behavior of each gating particle between a permissive and non-permissive state is described as a first order process independent from the states of the other gates. Thus, a possible dependences between activation and inactivation of the channel is not considered.[4,6,8] However, although these models lack the underlying electrophysiological processes of channel gating, HH models closely reproduce the macroscopic currents with a small number of variables and low computational burden, and hence are still widely used in computational electrophysiology.[1,7]

In comparison, Markov Models specify channel states according to the protein conformation and thus take into account the channel-specific gating behavior, which enables a highly accurate and veritable modeling of the channel kinetics.[4,7–9] In particular the investigation of channelopathies or drug-specific effects on the gating behavior through targeted changes in certain conformational states requires the use of such a probabilistic method, where ideally each state would correspond to one protein conformation.[7,10] In practice, however, even complex Markov models are only approximations to the actual channel dynamics with reduced numbers of states in order to keep the computational burden as low as possible.[7]

In this work we present a newly developed hidden Markov based approach for modeling the macroscopic current of Kv1.1 channels, considering for the first time the slow and fast inactivation close to physiological temperature.[11] Kv1.1 (KCNA1) delayed rectifier channels are strongly expressed in the central and peripheral nervous system "regulating" neuronal subthreshold excitability and spike initiation. Mutations of the KCNA1 gene are primarily associated with neurological disorders such as epilepsy and cardiac dysfunctions, but also implicated in tumor development and progression.[12–16] For model parametrization experimental data from patch clamp measurements were used and the model results quantitatively evaluated and compared with an existing HH approach, based on the same experimental data. In addition, a qualitative comparison with regard to the advantages, disadvantages and limitations of the two methods was carried out.

Methods

Electrophysiological data: Comprehensive experimental data on Kv1.1 channels is provided via the ion channel knowledge base Channelpedia (https://channelpedia.epfl.ch).[11] Data used for model evaluation is based on the CHO_FT Rat KV1.1 35°C activation dataset (n = 66 individual cell measurements). Patch-clamp measurements were performed with the automated patch clamp system Nanion NPC-16 Patchliner Quattro (Nanion Technologies, Munich Germany) in whole-cell configuration.[11] Macroscopic currents

Published by Verlag der TU Graz
Graz University of Technology

DOI: 10.3217/978-3-85125-826-4-04

were recorded with activation protocols consisting of a 100 ms long initial- and re-pulse at -80 mV and test pulses starting at -90 mV to 80 mV (increment 10 mV) of 500 ms duration. The applied deactivation protocol consisted of an initial- and re-pulse of -80 mV for 100 ms, a depolarization pulse at 70 mV over 300 ms for activation, followed by 300 ms long deactivation pulses from -80 mV to +30 mV in 10 mV steps.

Hodgkin Huxley model: The Kv1.1 HH model by Ranjan et al. [11] for direct comparison comprises a single activation gate m and inactivation gate h. The macroscopic current is given by:

$$I_{Kv1.1} = \overline{g_{Kv1.1}} m^p h^q (V - E_K) \quad p = q = 1 \qquad (1)$$

with

$$\frac{dm}{dt} = \frac{m_\infty - m}{\tau_m} \quad \text{and} \quad \frac{dh}{dt} = \frac{h_\infty - h}{\tau_h} \qquad (2,3)$$

The model was implemented in the simulation environment MATLAB and differential equations for activation and inactivation gates solved numerically by the Forward Euler method. All model parameters and equations of gating variables can be found in Ranjan et al. [11].

Hidden Markov Model: Considering the specific knowledge on the protein structure and gating of Kv1.1 ion channels, demonstrating a fast activation in response to membrane depolarization and inactivation by both, a slow C and fast N-type inactivation [11,17], a 12-state HMM was defined and parametrized based on the activation curves. Fig. 1 illustrates the final HMM kinetic scheme consisting of 4 closed (C), 1 open (O), 4 inactivated states (I_C), representing the slow inactivation, which can only occur from a closed state, and 3 states depicting the fast inactivation path (I_N).

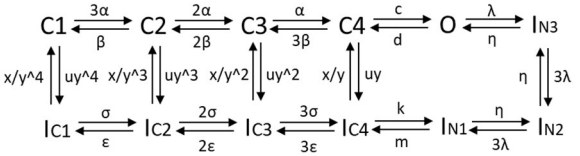

Figure 1: Kv1.1 hidden Markov Model, C: closed, O: open, IC: slow inactivation, IN: fast inactivation

Forward transition rates α, λ, σ and backward transitions β, η, ε are voltage-dependent and described by first order differential equations:

$$\alpha(V) = \alpha_1 . exp\left(\frac{V}{\alpha_2}\right) \qquad (4)$$

$$\beta(V) = \beta_1 . exp\left(\frac{-V}{\beta_2}\right) \qquad (5)$$

where α_i and β_i represent specific gating parameters and V the applied voltage. c, d, m, k and x, y and u denote constants without voltage-dependence. As P_o defines the probability of a channel being in the open state, the time evolution of the open probability is given by equation 6:

$$\frac{dP_O}{dt} = P_{C_4}(t).c + P_{I_{N3}}(t).\eta - P_O(t).(d + \lambda) \qquad (6)$$

where the first two terms represent all transitions entering the open state and the rightmost term all transitions leaving the open state.
The open probability P_o, the ion channel number N_c, the single channel conductance $g_{Kv1.1}$ and reversal potential E_K allow the calculation of the channels' macroscopic current:

$$I_{Kv\ .1} = g_{Kv1.1} N_c P_O (V - E_K) \qquad (7)$$

Parameterization of the rate constants is based on the averaged activation data (n = 66 single cell measurements) using a particle swarm optimization approach (MATLAB, Global Optimization Toolbox). Since the HMM approach models the current through a single ion channel, the number of ion channels has to be estimated for simulation of the macroscopic current. For the given dataset the channel number was determined to be N_c = 8987. The final model parameters are listed in Tab. 1.

Table 1: Parameters of the Kv1.1 HMM

Rate constants and parameters					
α_1	900 s^{-1}	λ_1	49.83 s^{-1}	σ_1	1049.7 s^{-1}
α_2	0.02 V	λ_2	2.94 V	σ_2	522.68 V
β_1	77.35 s^{-1}	η_1	51.18 s^{-1}	ε_1	1 s^{-1}
β_2	0.0441 V	η_2	1.1024 V	ε_2	944.2 V
c	108840 s^{-1}	k	3685 s^{-1}	x	78.04 s^{-1}
d	37851 s^{-1}	m	42310 s^{-1}	$g_{Kv1.1}$	10 pS
u	1*10^{-8} s^{-1}	y	181.39	E_K	0.065 V

Model evaluation: Accuracy of fitting results was quantified using the averaged root mean square error values (RMSE) over all voltage steps for both approaches, see Eq. 8.

$$RMSE = \sqrt{\sum (I_{\mathrm{Kv1.1\_model}}(t) - I_{\mathrm{measured}}(t))^2 / N} \qquad (8)$$

Results

Model simulation of activation protocols: Fig. 2a and 2b illustrate the simulated activation curves with the HMM and HH approach over all voltage-levels. Note that the figures represent the normalized currents, since the original HH model was derived from the normalized activation curves only. The newly developed HMM simulates the measured whole-cell currents with high accuracy. In particular, the fast inactivation can be modeled with high precision compared to the HH approach which demonstrates a too strong and prolonged inactivation ($RMSE_{HMM\_act}$ = 0.017 vs $RMSE_{HH\_act}$ = 0.0355). A comparison of both models is shown in Fig. 2c, revealing the normalized current at 50 mV with different fitting results ($RMSE_{HMM\_act}$ = 0.0145 vs $RMSE_{HH\_act}$ = 0.0287).

Published by Verlag der TU Graz
Graz University of Technology

DOI: 10.3217/978-3-85125-826-4-04

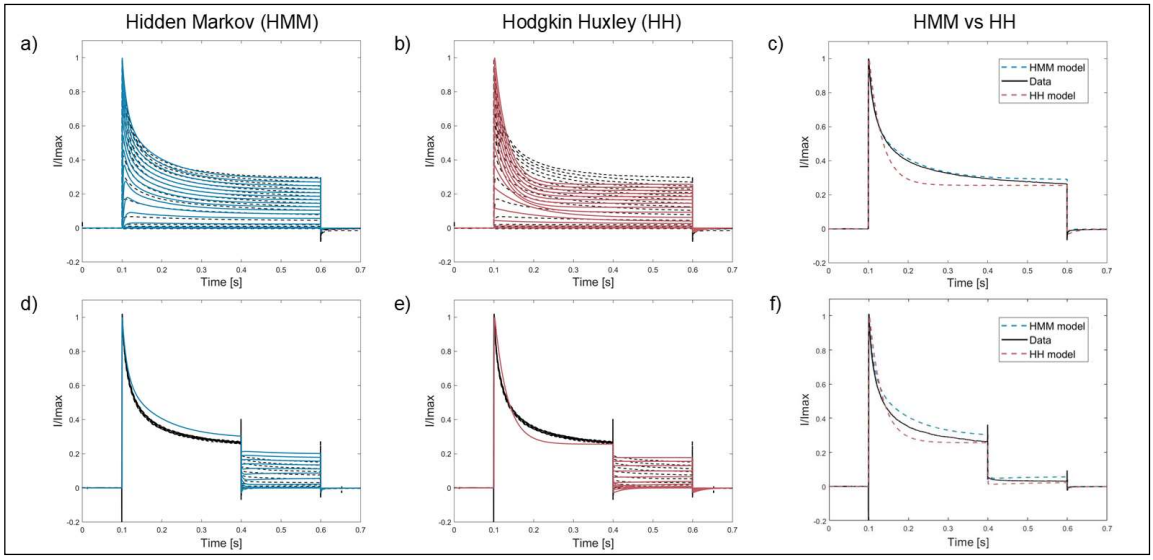

Figure 2: Normalized currents of the HHM and HH model over all voltage levels for a,b) activation $RMSE_{HMM\_act}$ = 0.017, $RMSE_{HH\_act}$ = 0.0355) and d,e) deactivation $RMSE_{HMM\_deact}$ = 0.0423, $RMSE_{HH\_deact}$ = 0.0425) measurements. Comparison of the normalized macroscopic current between HH and HMM for activation at +50 mV c) and for deactivation measurements at -30 mV f).

Model simulation of deactivation protocols: In addition, the measured deactivation curves were simulated and compared for model evaluation (see Fig. 2d-e). In contrast to the activation data, the deactivation currents cannot be simulated as precisely, showing greater deviations and an overestimation of the current especially at higher voltage levels (0 to 30 mV). However, fitting results of the HMM are comparable to the HH model with $RMSE_{HMM\_deact}$ = 0.0423 vs $RMSE_{HH\_deact}$ = 0.0425. Fig. 2f shows a comparison at -30 mV of both approaches ($RMSE_{HMM\_deact}$ = 0.0416 vs $RMSE_{HH\_deact}$ = 0.0423).

Qualitative comparison between the HH and HMM approach: The models represent completely different approaches in terms of model derivation, optimization and simulation. Tab. 2 outlines important modeling parameters and features that were taken into account and rated qualitatively, such as computational burden, model complexity or experimental data required for model parametrization.

Table 2: Comparison of the HH and HMM approach

	HH	HMM
model accuracy	(<<) +	+ (>>)
explainability of channel gating	+	+++
flexibility and adaptability	+	+++
model complexity	+	+++
comp. burden optimization	++	+++
comp. burden simulation	+	++
experimental data for model parametrization	+++	+++ (>>)

Assessment of methods: low (+) to high (+++) scores

Discussion

Single channel modeling constitutes a central part in computational electrophysiology. Extensive experimental investigations and the growing body of knowledge on ion channels enable the development of detailed models, simulating the specific gating behavior and bioelectric properties of ion channels.
We here proposed a new, simplified hidden Markov model of the voltage-gated potassium channel Kv1.1 close to physiological temperature (35°C) and compared the simulation results with a previously developed HH model. The developed HMM exceeds the accuracy of the HH model for the activation, inactivation and deactivation kinetics in terms of fitting the experimental data. However, the model showed less accuracy with regard to the deactivation characteristics. Thus, in a next step more focus should be taken on the deactivation path e.g. by consideration of deactivation protocols in model parametrization in order to further improve the validity of this initial model.
In general, by considering the protein structure and underlying gating mechanisms, HMMs provide a more accurate and reliable approach compared to HH. The kinetic schemes, depicting the transitions between different conformational states offer a better explainability and enable the investigation of specific modifications in the opening and closing behavior of the channel. Moreover, since HMM model the single channel dynamics they also offer a high degree of flexibility, allowing the application to different datasets with varying current amplitudes by adapting the number of ion channels. In contrast, HH models represent the macroscopic current and are only valid for a specific dataset. Hence, the adoption to other experimental data, sample populations or cells with varying ion channel composition, in particular without appropriate reparameterization is almost not possible.

Published by Verlag der TU Graz
Graz University of Technology

DOI: 10.3217/978-3-85125-826-4-04

Nevertheless, the high level of detail and complexity of HMM results in a huge number of parameters and a set of differential equations which increases the computational cost for both parametrization and simulation, and thus represents the major limitation of HMMs. Hence, various simplifications by reducing the number of states are proposed in order to keep the computational burden as low as possible, while maintaining the complex protein structure and accurately estimating the measured ion current. Such simplified models, as the one proposed, are rather phenomenological than representing the actual conformational states and are used, similar to HH models, to deterministically simulate the measured macroscopic currents from whole-cell measurements.[1,7]
In case of phenomenological modeling the experimental data required for model parametrization is comparable to that of HH models. However, in order to fully characterize the kinetic properties and improve the validity of HMMs, extensive experimental investigations are necessary including, for example, single channel patch clamp measurements, determination of fast and slow inactivation as well as possible cross links, or structural studies to gain a deeper knowledge on the actual protein conformation. All this together increases the experimental effort for HMM validation enormously compared to HH approaches.

We can summarize that both modeling approaches have strong advantages as well as disadvantages, and should always be selected with regard to the respective application. While HH models still represent the golden standard in neuroscience, offering a simple to use method with low computational burden and high integrability into complex cell models, HMMs are mainly considered in biomolecular and pharmacological research, better addressing the random nature of channel gating as the transitions of a channel between the different conformational states is represented by a stochastic process. Thus, HMMs implemented in whole cell applications with sufficient complexity and lower computational load have the potential to further improve the reliability and validity of such cell models and provide a valuable tool in the field of next generation in-silico electrophysiology.

References

[1] Andreozzi E, Carannante I, et al. Phenomenological models of Na V 1.5. A side by side, procedural, hands-on comparison between Hodgkin-Huxley and kinetic formalisms. Sci Rep. 2019;9: 17493. doi:10.1038/s41598-019-53662-9

[2] Yarov-Yarovoy V, Allen TW, et al. Computational Models for Predictive Cardiac Ion Channel Pharmacology. Drug Discov Today Dis Models. 2014;14: 3–10. doi:10.1016/j.ddmod.2014.04.001

[3] Beheshti M, Umapathy K, et al. Electrophysiological Cardiac Modeling: A Review. Crit Rev Biomed Eng. 2016;44: 99–122. doi:10.1615/CritRevBiomedEng.2016016454

[4] Nelson ME. Electrophysiological models of neural processing. Wiley Interdiscip Rev Syst Biol Med. 2011;3: 74–92. doi:10.1002/wsbm.95

[5] Maffeo C, Bhattacharya S, et al. Modeling and simulation of ion channels. Chem Rev. 2012;112: 6250–6284. doi:10.1021/cr3002609

[6] Sigg D. Modeling ion channels: Past, present, and future. J Gen Physiol. 2014;144: 7–26. doi:10.1085/jgp.201311130

[7] Sterratt D, Graham B, et al. Principles of Computational Modelling in Neuroscience. Cambridge University Press, New York. Jun 2011. ISBN 978-0-521-87795-4

[8] Carbonell-Pascual B, Godoy E, et al. Comparison between Hodgkin-Huxley and Markov formulations of cardiac ion channels. J Theor Biol. 2016;399: 92–102. doi:10.1016/j.jtbi.2016.03.039

[9] Fink M, Noble D. Markov Models for Ion Channels: Versatility versus Identifiability and Speed. Philosophical Transactions: Mathematical, Physical and Engineering Sciences. 2009;367: 2161–2179.

[10] Lampert A, Korngreen A. Markov modeling of ion channels: implications for understanding disease. Prog Mol Biol Transl Sci. 2014;123: 1–21. doi:10.1016/B978-0-12-397897-4.00009-7

[11] Ranjan R, Logette E, et al. A Kinetic Map of the Homomeric Voltage-Gated Potassium Channel (Kv) Family. Front Cell Neurosci. 2019;13. doi:10.3389/fncel.2019.00358

[12] D'Adamo MC, Liantonio A, et al. Kv1.1 Channelopathies: Pathophysiological Mechanisms and Therapeutic Approaches. Int J Mol Sci. 2020;21. doi:10.3390/ijms21082935

[13] Ovsepian SV, LeBerre M, et al. Distinctive role of KV1.1 subunit in the biology and functions of low threshold K(+) channels with implications for neurological disease. Pharmacol Ther. 2016;159: 93–101. doi:10.1016/j.pharmthera.2016.01.005

[14] Glasscock E. Kv1.1 channel subunits in the control of neurocardiac function. Channels. 2019;13: 299–307. doi:10.1080/19336950.2019.1635864

[15] Ouadid-Ahidouch H, Chaussade F, et al. KV1.1 K(+) channels identification in human breast carcinoma cells: involvement in cell proliferation. Biochem Biophys Res Commun. 2000;278: 272–277. doi:10.1006/bbrc.2000.3790

[16] Jang SH, Ryu PD, et al. Dendrotoxin-κ suppresses tumor growth induced by human lung adenocarcinoma A549 cells in nude mice. J Vet Sci. 2011;12: 35–40. doi:10.4142/jvs.2011.12.1.35

[17] Hasan S, Megaro A, et al. Electromechanical coupling of the Kv1.1 voltage-gated K+ channel is fine-tuned by the simplest amino acid residue in the S4-S5 linker. Pflugers Arch. 2020;472: 899–909. doi:10.1007/s00424-020-02414-0

Published by Verlag der TU Graz
Graz University of Technology

Proc. Annual Meeting of the Austrian Society for Biomedical Engineering 2021
DOI: 10.3217/978-3-85125-826-4-05

SIMULATION OF VESTIBULAR IMPLANT STIMULATION IN HUMAN INNER EAR ANATOMY WITH REGISTERED SYNTHETIC COCHLEA STRUCTURE

M. Handler[1], S. D'Alessandro[1], R. Saba[2], D. Baumgarten[1]

[1]Institute of Electrical and Biomedical Engineering, UMIT - Private University for Health Sciences, Medical Informatics and Technology, Hall in Tirol, Austria
[2]MED-EL GmbH, Innsbruck, Austria

michael.handler@umit-tirol.at

Abstract— *A human inner ear model was extended to include a synthetic cochlea model for analyzing unintended stimulation of the auditory nerve by a vestibular implant. Stimulation amplitudes for activation of the auditory nerve during monopolar vestibular stimulation were simulated as well as alterations in neural activation of other nerve branches due to the insertion of the synthetic cochlea. Only small deviations were found for stimulus amplitudes and neural activation in neighboring nerve branches, indicating a negligible effect on the overall stimulation result when including the synthetic cochlea model. A more complete picture of the stimulation outcome can be obtained by considering the synthetic cochlea instead of incomplete segmentations of the auditory nerve.*

Keywords— *Vestibular implant, virtual model, synthetic cochlea, human anatomy, nerve stimulation*

Introduction

Vestibular implants offer a potential treatment option for patients suffering from bilateral vestibular dysfunction to improve their sense of balance and spatial orientation. Human clinical studies and experimental evaluations considering animal models have been performed focusing on the improvement of vestibular implants and applied stimulation scenarios (e.g., [1]). In addition, also computer models have been used to analyze the effects of vestibular stimulation scenarios taking into account realistic inner ear anatomies of animals [2, 3] as well as human inner ear anatomies based on simplified synthetic models [4]. In our studies computer models based on µCT-scans of excised human specimen have been used to optimize selective vestibular nerve stimulation and minimize stimulation of nearby non-targeted nerves [5, 6]. For the evaluation of selective nerve stimulation and for considering anisotropic electrical properties in the computer models, 400 neurons were defined for each nerve branch in the models by paths starting from the most peripheral regions of the nerves and growing towards the central part of the inner auditory canal (IAC). For a detailed description of the nerve fiber generation algorithm, the reader is referred to [5, 6]. Neurons of the auditory nerve could not be considered in these computer simulations, because the domain of the auditory nerve could not be properly labeled due to insufficient spatial resolution and incomplete uptake of staining agent. However, the consideration of cochlear neurons in the simulations would allow for evaluating possible unintended stimulation of the auditory nerve caused by current spreads of a vestibular implant – a potential limiting factor for the selection of electrode and stimulation configurations.

In this work, a synthetic cochlear model was integrated in an existing human inner ear model to allow for the analysis of unintended stimulation of the auditory nerve by vestibular implants. A workflow is described for model preparation, replacement of the incompletely labeled cochlea by the synthetic model and nerve fiber generation. Finally, resulting nerve fiber activations after stimulation by monopolar electrode configurations are evaluated and compared between models with the originally labeled incomplete cochlea and the extended model.

Methods

The human inner ear model used in this study is based on a µCT-scan of a vestibular specimen of a donated body of a 78-year-old male. This model corresponds to Model 3 in [5]. For further details regarding the specimen preparation and segmentation, the reader is referred to our previous work [5]. Fig. 1 depicts the inner ear model focusing on the segmented structure of the auditory nerve. Due to the disconnected regions in the segmentation, nerve fibers could not be generated by our previously described algorithm [5] for this and similar models.

A CAD-model of a human auditory nerve and the combined scala tympani, scala vestibuli and scala media was created based on a human inner ear model. This model was used as synthetic cochlea to replace the incomplete structure of the originally labeled auditory nerve and cochlear scalas. In an initial registration step, a landmark-based registration approach was performed. Surface models of both the originally segmented auditory nerve and combined cochlear scalas were created. The surface models of the CAD geometry of the auditory nerve were registered to the originally segmented geometry by a landmark warping approach using ITK [7]. For both the original and synthetic cochlea model, 34 corresponding landmarks were defined manually on the most peripheral sections close to the organ of Corti and along the auditory nerve within the peripheral

Published by Verlag der TU Graz
Graz University of Technology

DOI: 10.3217/978-3-85125-826-4-05

section of the IAC as these structures could be identified best in the incomplete segmented data.
Additionally, six corresponding landmarks were defined manually on the surfaces of the cochlear scalas for both the original and synthetic cochlear model and a similarity transformation was performed in 3D Slicer [8]. After performing the registration based on manual landmarks, the preliminary result was improved by applying an automatic registration step using the BRAINSFit library [9] in 3D Slicer [8]. The result of the registration of the auditory nerve of the synthetic CAD model to the originally labeled auditory nerve is shown in Fig. 2.

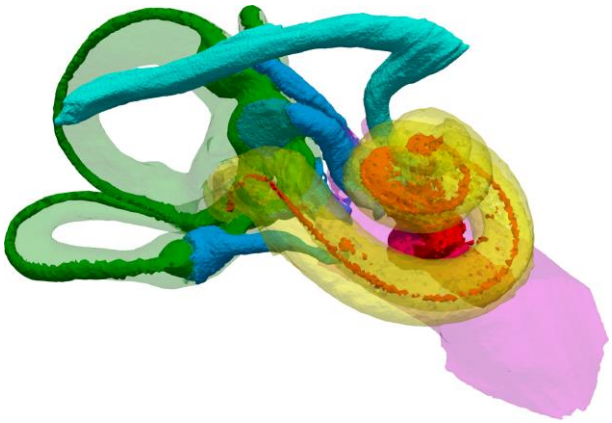

Figure 1: Human inner ear model with incompletely segmented auditory nerve, making the generation of an anisotropy field and virtual nerve fibers for the auditory nerve impossible for the algorithms described in our previous work [5].

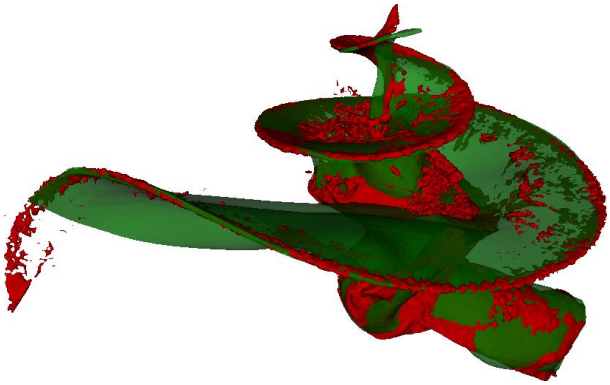

Figure 2: Original segmentation of auditory nerve (red) superimposed by the registered CAD model of the auditory nerve (green).

Next, the original segmentation result was smoothed to improve the quality of the meshing result in a later step. The segmented cochlea, all vestibular nerves and the facial nerve were removed from the model by replacing the corresponding labels in the segmentation by the label of the closest surrounding voxel. The registered cochlea was then inserted into the model by replacing the labels of the corresponding voxels by the registration result. After the insertion of the synthetic cochlea, the previously removed vestibular nerves and the facial nerve were also inserted again into the model. These additional steps for the vestibular nerves and the facial nerve were necessary to preserve their shapes in the model as the removal of the cochlea causes all neighboring structures to grow into the regions previously occupied by the original cochlea.
Two tetrahedra meshes were created for the original model with incomplete auditory nerve and the model considering the synthetic cochlea. The segmented components were surrounded by a spherical bone domain (diameter 5 cm) with low electric conductivity representing the temporal bone in the model, and the bone sphere was surrounded by a conductive layer of 1 cm thickness, similar to the work described in [4]. The model creation workflow is described in more detail in our previous work [5, 6]. Vector fields defining the fiber orientation for all nerves were created as explained in this previously described model creation workflow to consider anisotropic electrical conductivity tensors in the finite element model and to generate virtual nerve fibers for the evaluation of neural activation. For the auditory nerve of the model including the synthetic cochlea, a surface close to the organ of Corti was defined as the starting surface for the virtual nerve fibers, which grow from this starting surface towards the IAC.
Spherically shaped electrode contacts with a diameter of 300 µm were inserted in the ampullae of the anterior, lateral and posterior semicircular canals (SCCs) in both models to test for differences in the stimulation outcome between the models and for unintended neural activation of the auditory nerve caused by electrical stimulation of a vestibular implant. A biphasic stimulus current waveform (a 200 µs cathodic phase followed by a 200 µs anodic phase separated by a 30 µs interphase gap) was applied for each electrode contact separately at increasing amplitudes to evaluate active percentages of the different nerve branches in the model. The reference voltage and current sink electrode contact was considered at the outer boundary of the model. Fig. 3 depicts the model considering the registered synthetic cochlea, nerve fibers and electrode contacts in the ampullae.

Results

Fig. 4 shows the voltage distribution for the model considering the synthetic cochlea when applying a unit current (1 mA) via the electrode contact within the ampulla of the anterior SCC together with the voltage difference relative to the original model with incomplete auditory nerve. While the voltage distribution in the vestibular system is nearly unaffected by the insertion of the synthetic cochlea, slightly higher potentials are found at the auditory nerve and the IAC.
Fig. 5 depicts the fiber activation for every nerve branch in both models during stimulation by the electrode contact in the ampulla of the anterior SCC. First fibers of the auditory nerve (Cochlea) are activated

Published by Verlag der TU Graz
Graz University of Technology

DOI: 10.3217/978-3-85125-826-4-05

only at higher stimulus amplitudes of approximately 900 µA with an almost linear increase of activated fibers up to 3 mA, where more than 40 % of the nerve fibers of the cochlea are activated. A similar activation profile for the auditory nerve was also simulated when stimulating with the electrode contacts in the ampullae of the lateral and posterior SCCs (not shown).
Only minimal differences in the nerve fiber activation profiles were found for the other nerve branches when comparing the original model with the model considering the synthetic cochlea.

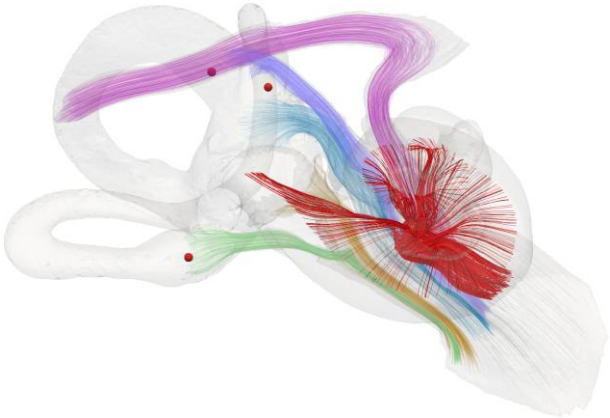

Figure 3: Human inner ear model with generated nerve fibers and inserted electrodes. The registered synthetic cochlea allowed for generating virtual auditory nerve fibers (red lines) for evaluation of unintended stimulation by electrode contacts of a vestibular implant (red spheres).

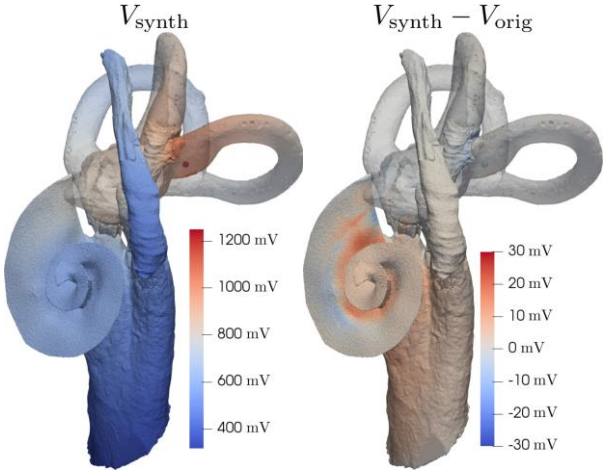

Figure 4: Voltage distribution at applied unit current (1 mA) via the electrode contact in the ampulla of the anterior SCC for the model with synthetic cochlea (V_{synth}) (left) and corresponding voltage difference ($V_{synth} - V_{orig}$) compared to the original model with incomplete auditory nerve (V_{orig}) (right).

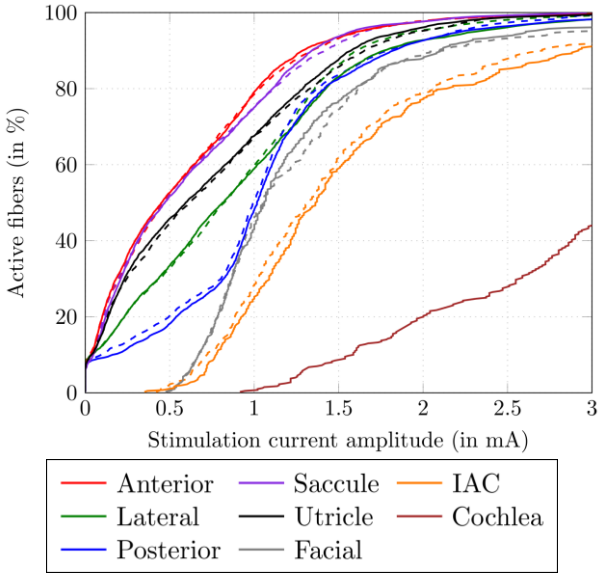

Figure 5: Comparison of neural activation for every nerve branch in the original model with incomplete auditory nerve (dashed lines) and the model with synthetic cochlea (solid lines) during stimulation by the electrode in the ampulla of the anterior SCC.

Discussion

In this work, previously described models of the inner ear were extended by a synthetic CAD model of the cochlea to allow for additionally evaluating unintended neural activation of the auditory nerve during targeted stimulation of vestibular nerve branches. A particular interest was in analyzing the effects of the replacement of the originally labeled cochlea by the synthetic model on the simulated stimulation outcome, as parts of the model were altered by the replacement procedure and also electrical properties were changed in the domain of the cochlea due to the consideration of anisotropic electrical conductivity for the auditory nerve instead of the previously considered isotropic conductivity.
In the described workflow, a CAD model of the cochlea based on a segmented µCT scan of a human inner ear was considered. To apply this model to specific segmented datasets, the CAD model of the cochlea needs to be deformed to match the shape of the auditory nerve and the combined cochlear scalas. Adapted CAD models of the cochlea are planned to consider significant variations in human cochlear anatomy in datasets we want to use in future simulation studies.
In the current implementation, the activation of the auditory nerve fibers is simulated by the same neural model as that for the vestibular nerve fibers considering adapted fiber diameters (2 µm) and without taking into account synaptic noise and afterhyperpolarization. For a detailed description of the neuron models and considered parameters see [6]. In future simulations it is planned to consider more accurate neural models (e.g., as summarized in [10]) for the auditory nerve to obtain a more reliable stimulation outcome.

Published by Verlag der TU Graz
Graz University of Technology

DOI: 10.3217/978-3-85125-826-4-05

The comparison of the voltage distributions during applied unit currents in the analyzed models showed that higher voltages are present in the IAC and the auditory nerve in the model considering the synthetic cochlea. This indicates that stimuli from the vestibular system result in higher voltage amplitudes for the model after the synthetic cochlea was applied, consequently leading to a higher chance of stimulation in these areas.

The resulting nerve fiber activation curves indicate that the stimulation outcome for vestibular nerve branches is not significantly influenced by replacing the incomplete cochlea model in the datasets by the registered CAD model of the cochlea. The small deviations in the results of the models depicted in Fig. 5 are mainly caused by differences in nerve fiber distributions within the corresponding nerve branches. On the one hand, these alterations in nerve fiber pathways derive from altered mesh resolutions caused by the replacement of the original cochlea by the synthetic cochlea. On the other hand, also different random seed distributions in both models for the nerve fiber generation slightly influence the computed nerve fiber pathways.

Additional analysis of unintended stimulation of auditory nerve fibers is possible by considering the synthetic cochlea in the human inner ear model during simulation of vestibular implant stimulation scenarios. In a next step it is planned to take into account anatomically more accurate surroundings of the inner ear in the simulations. Realistic human head models would allow for considering realistic reference electrode positions (e.g., below the scalp behind the auricle) and regions with heterogeneous electrical properties between stimulation and reference electrode contacts. Consequently, more realistic voltage distributions and stimulation outcomes can be simulated, leading to an improved reliability of answers to scientific questions provided by the performed in-silico experiments.

Acknowledgements

The authors wish to thank individuals who donated their bodies and tissues for the advancement of education and research. The authors would like to thank the Medical University of Innsbruck for providing labelled high-resolution µCT-scans of human vestibular anatomy. This work was supported by the federal state of Tyrol within the K-Regio program (project eVITA). This project is co-funded by the European Fund for Regional Development (EFRE).

References

[1] Crétallaz, C., Boutabla, A. et al.: Influence of systematic variations of the stimulation profile on responses evoked with a vestibular implant prototype in humans, *J. Neural Eng.*, vol. 17, pp. 036027, 2020

[2] Hayden, R., Sawyer, S. et al.: Virtual labyrinth model of vestibular afferent excitation via implanted electrodes: validation and application to design of a multichannel vestibular prosthesis, *Exp Brain Res*, vol. 210, pp. 623–640, 2011

[3] Hedjoudje, A., Hayden, R. et al.: Virtual Rhesus Labyrinth Model Predicts Responses to Electrical Stimulation Delivered by a Vestibular Prosthesis, *JARO*, vol. 20, pp. 313–339, 2019

[4] Marianelli, P., Capogrosso, M. et al.: A Computational Framework for Electrical Stimulation of Vestibular Nerve, *IEEE Transactions on Neural Systems and Rehabilitation Engineering*, vol. 23, pp. 897–909, 2015

[5] Handler, M., Schier, P.P. et al.: Model-Based Vestibular Afferent Stimulation: Modular Workflow for Analyzing Stimulation Scenarios in Patient Specific and Statistical Vestibular Anatomy, *Front. Neurosci.*, vol. 11, pp. 713, 2017

[6] Schier, P.P., Handler, M. et al.: Model-Based Vestibular Afferent Stimulation: Evaluating Selective Electrode Locations and Stimulation Waveform Shapes, *Front. Neurosci.*, vol. 12, pp. 588, 2018

[7] McCormick, M.M., Liu, X. et al.: ITK: enabling reproducible research and open science, *Front. Neuroinform.*, vol 8, pp. 13, 2014

[8] Fedorov, A., Beichel, R. et al.: 3D Slicer as an Image Computing Platform for the Quantitative Imaging Network, *Magn Reson Imaging*, vol. 30, pp. 1323–1341, 2012

[9] Johnson, H., Harris, G., and Williams, K.: BRAINSFit: mutual information rigid registrations of whole-brain 3D images, using the insight toolkit, *The Insight Journal*, vol. 57, 2007

[10] Bachmaier, R., Encke, J. et al.: Comparison of Multi-Compartment Cable Models of Human Auditory Nerve Fibers, *Front. Neurosci.*, vol. 13, pp. 1173, 2019

Published by Verlag der TU Graz
Graz University of Technology

Proc. Annual Meeting of the Austrian Society for Biomedical Engineering 2021
DOI: 10.3217/978-3-85125-826-4-06

AN APPROACH FOR VISUALIZATION OF THE INTERACTION BETWEEN COLLAGEN AND ELASTIN IN LOADED HUMAN AORTIC TISSUES

A. Pukaluk[1], H. Wolinski[2,3], C. Viertler[4], P. Regitnig[4], G.A. Holzapfel[1,5], G. Sommer[1]

[1]Institute of Biomechanics, Graz University of Technology, Austria
[2]Institute of Molecular Biosciences, University of Graz, Austria
[3]Field of Excellence BioHealth – University of Graz, Austria
[4]Institute of Pathology, Medical University of Graz, Austria
[5]Department of Structural Engineering, NTNU, Norway

pukaluk@tugraz.at

Abstract. *Knowledge of the interaction between the constituents of loaded aortic tissues is crucial to expand our understanding of load-bearing mechanisms in the aorta. We have therefore developed a procedure that enables simultaneous multi-photon microscopy imaging of collagen and elastin in human aortic tissue during the biaxial extension test. The microscopy images obtained were verified with the results of the histological staining. The mechanical response was also compared with findings from previously performed biaxial extension tests. The proposed pipeline has shown successful and has great potential for structural analysis of human aortic tissue.*

Keywords: *Human aorta, collagen, elastin, biaxial extension test, multi-photon microscopy*

Introduction

The healthy aortic wall consists of three layers, namely the intima, media and adventitia [1]. Each of the layers is characterized by its own structure and function. From a mechanical point of view, the main role is played by the media responsible for the aortic response to loading and the adventitia, which prevents the aorta from overstretching and possible rupture. Both media and adventitia owe their passive mechanical properties mainly to two proteins, namely collagen and elastin. Although the arrangement of these proteins in the aortic layers in the unloaded state has already been described [1,2], little is known about the changes caused by the load. Therefore, this study proposes a method for the efficient visualization of collagen and elastin in loaded aortic tissue.

Methods

The developed procedure was applied to one medial and one adventitial specimen from a non-atherosclerotic and non-aneurysmatic human abdominal aorta (52 yrs old, female). The aorta was received within 24 h of death and frozen at -20°C.

Sample preparation. The aortic tube was thawed at 4°C prior to preparation for testing and imaging. During preparation, all steps were carried out at room temperature and the samples were kept moist with phosphate buffered saline (PBS) at pH 7.4. Loose connective tissue was removed, and the intact aortic tube was cut open in the longitudinal direction. The intimal and adventitial layers were then carefully dissected from the media [3], and square samples measuring 20×20 mm were cut in order to obtain medial and adventitial patches. In addition, adjacent rectangular patches of dimensions of about 4×10 mm were cut for histological examinations. Particular care was taken to ensure that the edges of squares and rectangles match the anatomical longitudinal and circumferential directions of the aorta. The mean thickness of each sample was measured optically [3]. Each square sample was then pierced by four sets of hooks connected by sutures. A set of five hooks was used on each side [4].

Histology. Aortic specimens were embedded in paraffin and cut at 4 µm with the microtome Microm HM 335 (Microm, Walldorf/Baden, Germany). Next, the sections were stained with Picrosirius Red (PSR) to highlight fibrillar collagen and Elastica van Gieson (EvG) to highlight elastin fibers [5] to verify multi-photon microscopy images.

Multi-photon microscopy. The imaging took place at the IMB-Graz Optical Imaging Resource with a tunable picosecond laser (picoEmerald; APE, Berlin, Germany), which was integrated into a Leica SP5 confocal microscope (Leica Microsystems, Mannheim, Germany). The laser was tuned to 880 nm to induce both the second harmonic generation (SHG) signal from collagen and the two-photon excited (TPE) autofluorescence signal from elastin. A two-channel, non-descanned detector (NDD) in epi-mode was used to detect SHG and TPE signals simultaneously (SP 680 nm barrier filter, i.e., excitation light filter; BP 460/50 nm for SHG signal; BP 525/50 nm for TPE signal; beamsplitter RSP 495 for two-channel separation of SHG and TPE signals). *Z*-stacks were acquired with the HCX IRAPO L 25× NA 0.95 water immersion objective with a large working distance of 1.5 mm for imaging the deep tissue and a sampling interval of 0.6×0.6×5.0 µm.

As a compromise between image quality and acquisition time, four-fold line averaging was used to reduce image noise. A coverglass and water as the immersion medium could not be used with samples mounted on the biaxial test device, since the coverglass

Published by Verlag der TU Graz
Graz University of Technology

DOI: 10.3217/978-3-85125-826-4-06

could not be fixed horizontally and the sample quickly soaked up water. Alternatively, an aqueous eye gel Lac®-Ophtal® Gel (Dr. Winzer Pharma, Berlin, Germany) was used [6], and the lens was dipped directly into the gel.

Biaxial extension test. In order to carry out the planar biaxial extension test and the multi-photon imaging simultaneously, a biaxial testing device was constructed, which could be placed on the microscope stage, based on the design described in [7], but limited by the geometrical and environmental requirements of the microscope. The device integrates four high precision linear positioners SLC-2640 (SmarAct, Oldenburg, Germany) with the maximum travel range of 35 mm and 1 nm resolution while the maximum velocity is limited to 20 mm/s and the maximum blocking force to 3.5 N. Each positioner carries a bracket with an assembled load cell KM10z 25N (ME-Meßsysteme, Hennigsdorf, Germany) characterized by a maximum permissible force of 25 N and 1% accuracy class. The design of the device allows displacement and force measurements in two perpendicular directions (Fig. 1) with one set of sensors on each side.

The stretch-driven testing protocol was implemented with the LabView software (National Instruments, Austin, USA). All samples were loaded equibiaxially and quasi-statically at a speed of 3 mm/min. First, a sample was subjected to the pre-load of 10 mN, which was defined as the reference configuration at a stretch of 1. The pre-load was followed by cycles of preconditioning to obtain a reproducible response. The *z*-stack series of images was then taken in the center of the sample. After imaging was completed, the sample was stretched to 1.02 and imaged again. The experiment was repeated with 0.02 stretch increments until the stretch of 1.40 was reached.

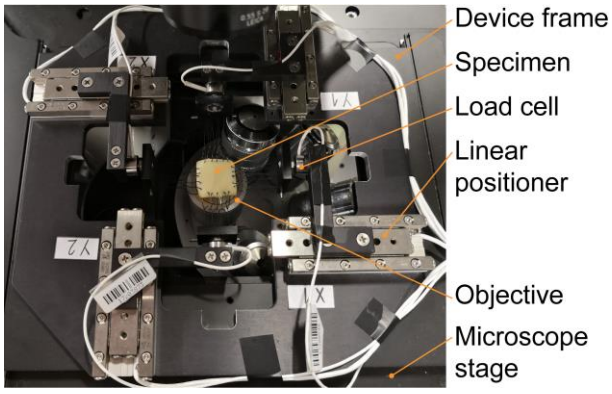

Figure 1: Biaxial testing device with a hooked specimen placed on the microscope stage.

Results

Histology. For the media, the histological staining showed crimpy collagen fibers embedded in a network-like arrangement of elastin fibers (Fig. 2). In contrast, the adventitia showed smooth, wavy collagen bundles accompanied by separate, either curly or straight, elastin fibers.

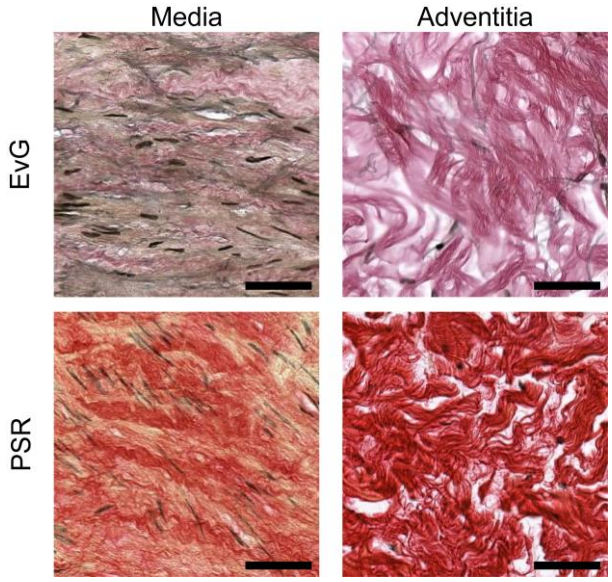

Figure 2: Histological staining of the aortic layers; scale bars denote 50 µm.

Multi-photon microscopy. The emission signal transmitted through the BP 460/50 nm and BP 525/50 nm filters was color-coded in green and red, respectively (Fig. 3). The red-colored channel, which was expected to reflect elastin, captured the network-like fibrillary structure in the media and individual fibers in the adventitia.

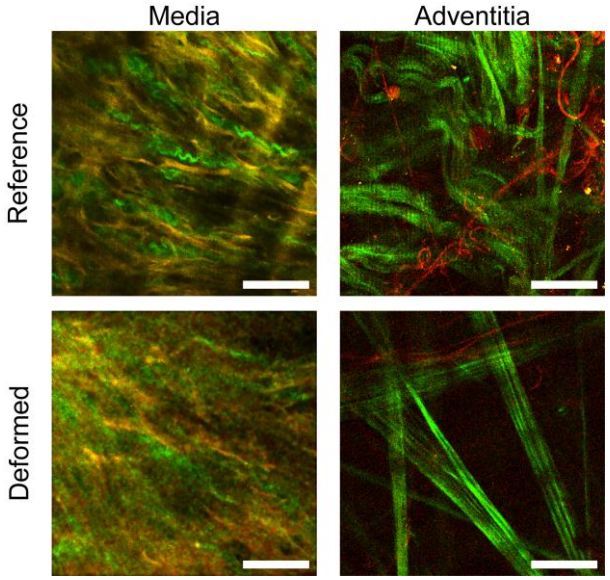

Figure 3: Multi-photon microscopy images of aortic layers at the reference and deformed (max stretch achieved) configurations; scale bars denote 50 µm.

Both images resembled the elastin shown by the EvG staining (Fig. 2). For the media, however, the green-colored channel contained not only the curly fibers corresponding to the histological analysis, but also the network-like structure of elastin. The spectral crosstalk of SHG signal from medial collagen and the TPE signal from elastin was observed as a yellow color in the merged images (Fig. 3). For adventitia, the green-colored channel contained fiber bundles

Published by Verlag der TU Graz
Graz University of Technology

DOI: 10.3217/978-3-85125-826-4-06

that were comparable to adventitial collagen as stained by EvG and PSR.

Biaxial extension test. The experiment was successfully carried out up to a stretch of 1.40 for the media, but has to be stopped at a stretch of 1.28 for the adventitia (Fig. 4) due to the overload of the linear positioners. In addition, tissue relaxation was observed as a decrease in Cauchy stress during imaging. Nevertheless, the characteristic mechanical response of both layers was recorded. Adventitia showed a stiffer response and more pronounced anisotropy than the media. In addition, a stiffer longitudinal response was observed for the adventitia while it was observed in the circumferential direction for the media.

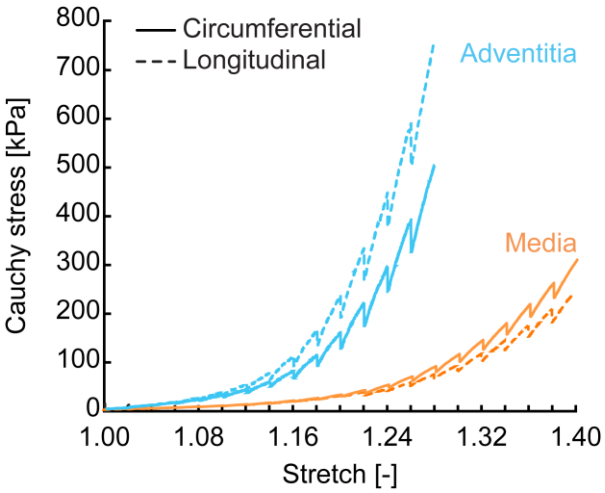

Figure 4: Cauchy stress vs stretch behavior obtained from equibiaxial mechanical tests.

Discussion

Multi-photon microscopy. In the course of this study, the importance of the correct setting of multi-photon microscopy and its validation was demonstrated. Although filters with an equivalent transmission range were used for divergent collagen examinations [8-11], this turned out to be unsuitable for imaging the untreated human aortic media without further processing, e.g., image subtraction.

The SHG signal from collagen can be observed to be induced by the laser excitation wavelength in the range from 730 to 940 nm [12,13]. The excitation wavelength commonly used is around 800 nm [10,14,15] as described by Zoumi et al. [12] or around 880 nm [8,9,11,16], which corresponds to near 900 nm, as reported by Chen et al. [17]. For this study, the emission wavelength 880 nm was chosen based on our previous studies on the human abdominal aorta [8,9], as the signal was observed to be optimal for this tissue in terms of the intensity of the emission. Differences in optimal values of the excitation and emission wavelengths can be caused by the sensitivity of the collagen SHG signal to the biochemical properties of the solution in which the fibrils are located. Although it proved to be insensitive to the pH value within the physiological range, it changes dramatically with the ionic strength of the solution [18].

The spectral crosstalk of medial collagen and elastin identified during this study was also observed for the human thoracic aortic media imaged by Koch et al. [19], who excited the tissue with a laser wavelength of 830 nm and used 400±50 nm and 525±25 nm bandpass filters to capture collagen and elastin, respectively. Interestingly, no prominent spectral crosstalk was reported by Phillippi et al. [20] when examining the human aortic media with the same settings. This discrepancy can be caused by using different gains for the distinct channels. In addition, van Zandvoort et al. [21] observed a spectral crosstalk of elastin TPE in the carotid arteries of mice using 410-490 nm bandpass emission filter. The presence of a TPE signal for elastin in this shorter wavelength range (410-490 nm) can be caused by a relatively higher intensity of this TPE signal compared to the SHG signal of collagen [22].

Biaxial extension test. During the test it was not possible to provide a physiologically similar environment (immersion with PBS at 37°C), resulting in noticeable drying of the tissue borders, which can affect the mechanical response. In addition, the Cauchy stress-stretch curves are affected by relaxation phenomena during imaging. Despite these limitations, our results are comparable with other studies.

Similar to our study, Niestrawska et al. [8] reported higher mean values of the Cauchy stresses in the circumferential than in the longitudinal direction for the medial layer of the human abdominal aorta. For the adventitia, too, a stiffer response in the longitudinal direction compared to the circumferential direction was reported in previous studies [8,23].

Further implications. The presented novel combination of multi-photon microscopy and biaxial extension tests provides an insight into the microstructure of the human aortic layers, which are exposed to increased equibiaxial stretch. The visualized collagen and elastin can be further analyzed and quantified in order to obtain important structural parameters such as orientation, dispersion, thickness and waviness of the fibers. Available material models are not yet able to take into account all of the structural parameters mentioned above. Therefore, combined microstructural and biomechanical data, as provided in the study, are essential to develop and calibrate novel material models to better reproduce and predict the mechanical behavior of aortic tissues in health and disease.

Acknowledgements

We would like to thank A. Donnerer from the Institute of Pathology, Medical University Graz, for his valuable support during tissue harvesting. Special thanks go to M. Triefhaider for his work on the biaxial testing device. We would also like to thank the Austrian Science Funds (FWF) for financial support with the grant no. P30260.

Published by Verlag der TU Graz
Graz University of Technology

DOI: 10.3217/978-3-85125-826-4-06

References

[1] Holzapfel, G.A. and Ogden, R.W.: Biomechanical relevance of the microstructure in artery walls with a focus on passive and active components, *Am. J. Physiol. Heart Circ. Physiol.*, vol. 315, pp. H540-H549, May 2018

[2] Sherifova, S. and Holzapfel, G.A.: Biochemomechanics of the thoracic aorta in health and disease, *Prog. Biomed. Eng.*, vol. 2, pp. 032002, Jul. 2020

[3] Sommer, G., Gasser, T.C. et al.: Dissection properties of the human aortic media: an experimental study, *J. Biomech. Eng.*, vol. 130, pp. 021007, Apr. 2008

[4] Eilaghi, A., Flanagan, J.G. et al.: Strain uniformity in biaxial specimens is highly sensitive to attachment details, *J. Biomech. Eng.*, vol. 131, pp. 0910031-0910037, Sep. 2009

[5] Weisbecker, H., Viertler, C. et al.: The role of elastin and collagen in the softening behavior of the human thoracic aortic media, *J. Biomech.*, vol. 46, pp. 1859-1865, Apr. 2013

[6] Bancelin, S., Lynch, B. et al.: Ex vivo multiscale quantitation of skin biomechanics in wild-type and genetically-modified mice using multiphoton microscopy, *Sci. Rep.*, vol. 5, pp. 17635, Dec. 2015

[7] Sommer, G., Haspinger, D.C. et al.: Quantification of shear deformations and corresponding stresses in the biaxially tested human myocardium, *Ann. Biomed. Eng.*, vol. 43, pp. 2234-2348, Oct. 2015

[8] Niestrawska, J.A., Viertler, C. et al.: Microstructure and mechanics of healthy and aneurysmatic abdominal aortas: experimental analysis and modeling, *J. R. Soc. Interface*, vol. 13, pp. 20160620, Nov. 2016

[9] Schriefl, A.J., Wolinski, H. et al.: An automated approach for three-dimensional quantification of fibrillar structures in optically cleared soft biological tissues, *J. R. Soc. Interface*, vol. 10, pp. 20120760, Dec. 2012

[10] Chow, M., Turcotte, R. et al.: Arterial extracellular matrix: a mechanobiological study of the contributions and interactions of elastin and collagen, *Biophys. J.*, vol. 106, pp. 2684-2692, Jun. 2014

[11] Krasny, W., Morin, C. et al.: A comprehensive study of layer-specific morphological changes in the microstructure of carotid arteries under uniaxial load, *Acta Biomater.*, vol. 57, pp. 342-351, May 2017

[12] Zoumi, A., Yeh, A., and Tromberg, B.J.: Imaging cells and extracellular matrix in vivo by using second-harmonic generation and two-photon excited fluorescence, *Proc. Natl. Acad. Sci. USA*, vol. 99, pp. 11014-11019, Aug. 2002

[13] Green, N.H., Delaine-Smith, R.M. et al.: A new mode of contrast in biological second harmonic generation microscopy, *Sci. Rep.*, vol. 7, pp. 13331, Oct. 2017

[14] Sugita, S. and Matsumoto, T.: Multiphoton microscopy observations of 3D elastin and collagen fiber microstructure changes during pressurization in aortic media, *Biomech. Model. Mechanobiol.*, vol. 16, pp. 763–773, Nov. 2017

[15] Timmins, L.H., Wu, Q. et al.: Structural inhomogeneity and fiber orientation in the inner arterial media, *Am. J. Physiol. Heart Circ. Physiol.*, vol. 298, pp. 1537-1545, Feb. 2010

[16] Di Giuseppe, M., Alotta, G. et al.: Identification of circumferential regional heterogeneity of ascending thoracic aneurysmal aorta by biaxial mechanical testing, *J. Mol. Cell Cardiol.*, vol. 130, pp. 205-215, Apr. 2019

[17] Chen, X., Nadiarynkh, O. et al.: Second harmonic generation microscopy for quantitative analysis of collagen fibrillar structure, *Nat. Protoc.*, vol. 7, pp. 654-669, Mar. 2012

[18] Williams, R.M., Zipfel, W.R. and Webb, W.W.: Interpreting second-harmonic generation images of collagen I fibrils, *Biophys. J.*, vol. 88, pp. 1377-1386, Feb. 2005

[19] Koch, R.G., Tsamis, A. et al.: A custom image-based analysis tool for quantifying elastin and collagen micro-architecture in the wall of the human aorta from multi-photon microscopy, *J. Biomech.*, vol. 47, pp. 935-943, Mar. 2014

[20] Phillippi, J.A., Green, B.R. et al.: Mechanism of aortic medial matrix remodeling is distinct in patients with bicuspid aortic valve, *J. Thorac. Cardiovasc. Surg.*, vol. 147, pp. 1056-1064, Mar. 2014

[21] van Zandvoort, M., Engels, W. et al.: Two-photon microscopy for imaging of the (atherosclerotic) vascular wall: a proof of concept study, *J. Vasc. Res.*, vol. 41, pp. 54-63, Jan. 2004

[22] Zoumi, A., Lu, X. et al.: Imaging coronary artery microstructure using second-harmonic and two-photon fluorescence microscopy, *Biophys. J.*, vol. 87, pp. 2778-2786, Oct. 2004

[23] Li, H., Mattson, J.M. and Zhang, Y.: Integrating structural heterogeneity, fiber orientation, and recruitment in multiscale ECM mechanics, *J. Mech. Behav. Biomed. Mater.*, vol. 92, pp. 1-10, Apr. 2019

Published by Verlag der TU Graz
Graz University of Technology

Proc. Annual Meeting of the Austrian Society for Biomedical Engineering 2021
DOI: 10.3217/978-3-85125-826-4-07

EFFECTS OF DISEASE PROGRESSION ON MECHANICAL STRESSES IN HUMAN ABDOMINAL AORTIC ANEURYSMS

E. Klimstein[1], M. Dalbosco[1], G.A. Holzapfel[1,2]

[1] Institute of Biomechanics, Graz University of Technology, Austria
[2] Department of Structural Engineering, NTNU, Norway

e.klimstein@student.tugraz.at, mdalbosco@tugraz.at, holzapfel@tugraz.at

Abstract — *The present study uses finite element (FE) simulations to investigate a three-stage theory on the pathogenesis of abdominal aortic aneurysms (AAAs). The effect of collagen growth and remodeling (G&R) on mechanical wall stresses during disease evolution is investigated. The results show that impaired remodeling during AAA growth leads to an increase in wall stress, indicating a more vulnerable vessel. Conversely, successful G&R of the collagen network results in less stress, suggesting a possible healing process promoted by vascular cells that sense the mechanical changes associated with AAA formation and growth. Overall, the results presented provide valuable insights into the pathogenesis of AAAs.*

Keywords — *Abdominal aortic aneurysm, finite element method, growth and remodeling*

Introduction

Abdominal aortic aneurysms (AAAs) are abnormal dilatations of the infrarenal aorta that are usually diagnosed when their diameter is greater than 30mm [1, 2]. If left untreated, AAAs can protrude to the point of rupture, an event that leads to death in up to 90% of cases [3, 4]. Elective surgery usually reduces the likelihood of rupture [1, 5]; however, the risk associated with the surgical procedure must also be considered. Even if other parameters such as growth rate or life expectancy are sometimes taken into account in this context [6], the decision for surgical intervention is usually made on the basis of the size of the AAA: patients are operated when the aneurysm diameter reaches 5.0cm (in females) or 5.5cm (in males) [6, 7].

However, reports of ruptured aneurysms smaller than these thresholds as well as stable larger aneurysms have raised questions about the suitability of this empirical standard [8]. Therefore, better criteria for aneurysm risk assessment are needed. To achieve this, a clearer understanding of the material behavior of the aortic tissue along the course of the disease is crucial. In this direction, Niestrawska et al. [9] proposed a three-stage biomechanical theory of AAA progression, in which aneurysm development is associated with intense G&R of the collagen fiber network. In short, stage 1 involves passive remodeling of the collagen fibers to the circumferential direction. This change is probably perceived by mechanotransduction mechanisms; hence cells react accordingly and remodel the collagen network, which leads to an increased compliance and the formation of a neo-adventitia on the abluminal side, which characterizes stage 2. As the disease progresses, this remodeling increases with considerable tissue stiffening and the build-up of the neo-adventitia (stage 3), which is characterized by a high degree of in-plane collagen isotropy.

The present work examines this newly developed mechanopathogenic model using FE simulations. For this purpose, the mechanical and histological constitutive parameters presented by Niestrawska et al. [9] are used for each stage to simulate four AAAs. The aim is to evaluate how the mechanical wall stresses change in the course of the disease and thus to shed light on biomechanical phenomena that are involved in the AAA pathogenesis.

Methods

Since Niestrawska et al. [9] found no correlation between aneurysm size and disease stage, 4 different AAA geometries, with diameters from 40 to 70mm, were examined. For each geometry, circumferential and axial wall stresses were calculated for stages 1 to 3, which resulted in a total of 12 simulations that were carried out in Abaqus 2017.

Geometry: The shape of the aneurysm is assumed to be axisymmetric (fusiform), described by the parametric equation [10, 11]

$$\mathrm{R(Z)} = \mathrm{R_a} + \left(\mathrm{R_{an}} - \mathrm{R_a} - \mathrm{c_3}\frac{\mathrm{Z}^2}{\mathrm{R_a}}\right)\exp\left(-\mathrm{c_2}\left|\frac{\mathrm{Z}}{\mathrm{R_a}}\right|^{\mathrm{c_1}}\right), \tag{1}$$

where $\mathrm{R(Z)}$ is the radius of the aneurysm in relation to the axial position Z, $\mathrm{R_{an}}$ denotes the maximum radius of the aneurysm, located at $\mathrm{Z} = 0$, and $\mathrm{R_a}$ represents the radius of the non-aneurysmatic region, taken as 15mm [1, 2]. The parameter c_1 is set to 5 and the geometric parameters c_2 and c_3 are given by Eqs. (2) and (3) [12], i.e.

$$\mathrm{c_2} = \frac{4.605}{(0.5\,\mathrm{L_{an}}/\mathrm{R_a})^{\mathrm{c_1}}}, \tag{2}$$

$$\mathrm{c_3} = \frac{\mathrm{R_{an}} - \mathrm{R_a}}{\mathrm{R_a}(0.8\,\mathrm{L_{an}}/\mathrm{R_a})^2}. \tag{3}$$

The ratio $\mathrm{F_L} = \mathrm{L_{an}}/\mathrm{R_{an}}$ has a value of 2.8 and determines the length of the aneurysmatic part L_{an} [13]. The length of the non-aneurysmatic part is chosen

Published by Verlag der TU Graz
Graz University of Technology

DOI: 10.3217/978-3-85125-826-4-07

to be 30% of L_{an}. Table 1 gives an overview of the values described above for the four AAA geometries.

Table 1: Overview of geometric parameters.

AAA radius R_{an} (mm)	AAA length L_{an} (mm)	Healthy length (mm)	Total length (mm)
20	56	16.8	98.6
25	70	21.0	112.0
30	84	25.2	134.4
35	98	29.4	156.8

The wall is modeled with a constant thickness of 1.5mm, which is a reasonable assumption for non-patient-specific geometries [12].

Material: The constitutive model of Gasser-Ogden-Holzapfel (GOH) [14] was used to characterize the material behavior of the AAA. It describes the tissue as an anisotropic hyperelastic material with a transversely isotropic fiber dispersion. While experimental evidence [15, 16] suggests that the amount of collagen dispersion in the circumferential-axial plane is usually higher than out-of-plane, the transversely isotropic GOH model has been used for simplicity, as it is readily available in Abaqus.

Niestrawska et al. [9] identified constitutive parameters for stages 1 to 3 by fitting the non-rotationally symmetric fiber dispersion model by Holzapfel et al. [15] to mechanical and histological data. In order to use these parameters with the GOH model, the transversely isotropic dispersion parameter was calculated by the relationship $\kappa = 1 - 2\kappa_{op}$ [13], where κ_{op} describes the out-of-plane dispersion [9]. The mean fiber angle α and the mechanical parameters c, k_1 and k_2, were taken directly from [9]. Table 2 summarizes the constitutive GOH parameters [14] for the three disease stages.

Table 2: Overview of constitutive parameters [9].

		Stage 1	Stage 2	Stage 3
c	[kPa]	0.95	1.83	3.78
k_1	[kPa]	1.30	0.46	8.96
k_2	[-]	98.6	112.0	156.8
κ	[-]	0.134	0.090	0.196
α	[°]	6.55	33.11	22.90

Mesh: Because of the axisymmetric nature of the problem, only one eighth of the aneurysm was modeled. For all four AAA geometries, the mesh consists of approximately 1100 C3D8H hybrid elements to take into account the assumption of incompressible behavior; the element size was selected after mesh convergence analyses (not shown here). Since there is no information about how the material parameters change in the radial direction, the mesh thickness consisted of a single element.

Boundary conditions: The displacements of the circumferential surfaces and the lower outlet surface were restricted according to (axi)symmetry. To the best of the authors' knowledge, there are no experimental data on pre-stretches in AAAs. In this study, an axial pre-stretching of 7% was applied to the upper outlet surface – a reasonable (healthy) value for an average patient age of 71 years [17] – while there was no pre-stretching in the circumferential direction. Finally, a pressure of 16kPa (120mmHg) was applied to the luminal surface, which resembled a (non-hypertensive) blood pressure load.

Results

Figure 1 shows the distribution of the circumferential Cauchy stresses σ_{circ} for all four AAA sizes and three disease stages. The simulation of the 70mm aneurysm did not converge for stage 1; however, we point out that such a large aneurysm is most likely not at the beginning of the disease and, therefore, the lack of this result should not affect the analysis.

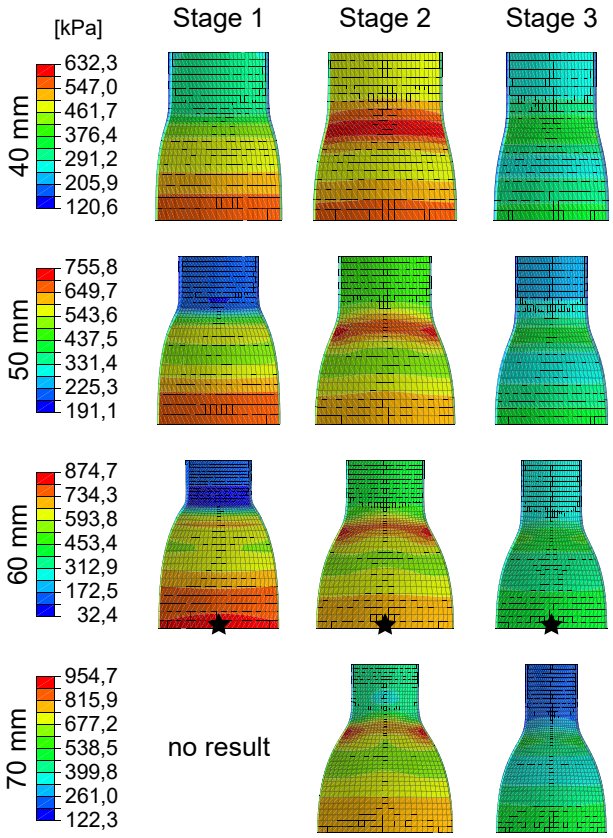

Figure 1: Distribution of the circumferential stress σ_{circ} on the luminal side of AAAs. Black stars identify the points used for plotting the stress-stretch curves of Fig. 4.

In Fig. 1, the maximum circumferential stress is always on the luminal side. In addition, the evolution of the circumferential stresses as the disease progression is similar for all aneurysm sizes: in stage 1 the maximum circumferential stress is in the sac (i.e. in the area of the maximum diameter); in stage 2 the stress value in the sac decreases slightly, but the maximum stress is now located in the neck area. In stage 3, the stresses decrease in

Published by Verlag der TU Graz
Graz University of Technology

DOI: 10.3217/978-3-85125-826-4-07

the entire domain, but the peak stress is still in the neck region.

Figure 2 shows the distribution of the axial Cauchy stresses σ_{axial} for all simulations. The maximum axial stress for all disease stages and all aneurysm sizes is always on the abluminal side of the sac. In general, the results of Figs. 1 and 2 agree well with earlier AAA simulations from the literature [12, 13], as well as with more recent *in vivo* measurements that identified, e.g., higher circumferential peak strain values on the neck of AAAs compared to the sac [18].

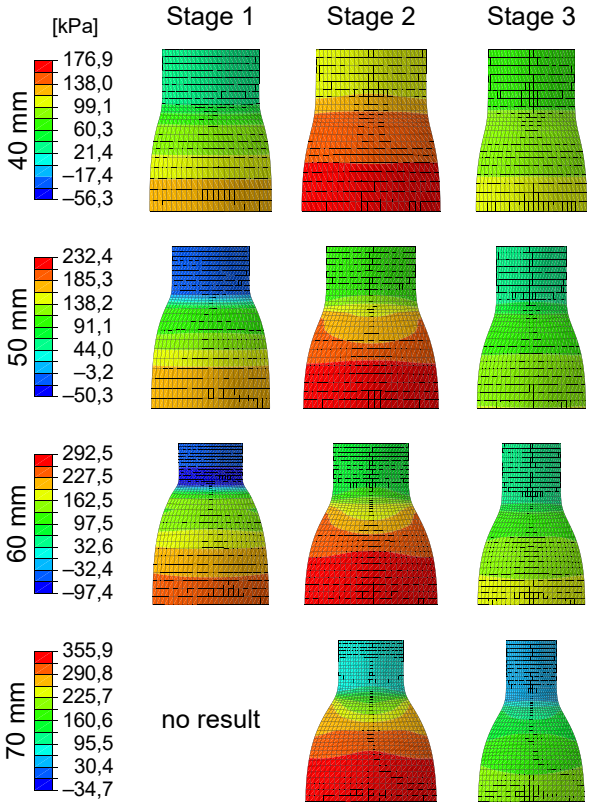

Figure 2: Distribution of the axial stress σ_{axial} on the abluminal side of the AAAs.

The maximum values of the stresses σ_{circ} and σ_{axial} for all simulations in Figs. 1 and 2 are summarized in Fig. 3, whereby it can be seen that the larger the aneurysm, the higher the stress values (in both directions), as expected. With regard to the development of the disease, the maximum stress values increase slightly from stage 1 to stage 2 (circumferential stress also changes location, see Fig. 1), while from stage 2 to stage 3 the maximum stresses in both directions decrease, which leads to stress values lower than stage 1. Interestingly, the percentage increase in the maximum circumferential stress (for the same stage) decreases with increasing size: for stage 2, e.g., the difference in maximum stress between the 40 and 50 mm AAAs is about 20%, while this increase is less than 10% between the 60 and 70mm AAAs. Although an idealized geometry is considered, this interesting result could in some way be related to the 5.5cm (empirical) threshold.

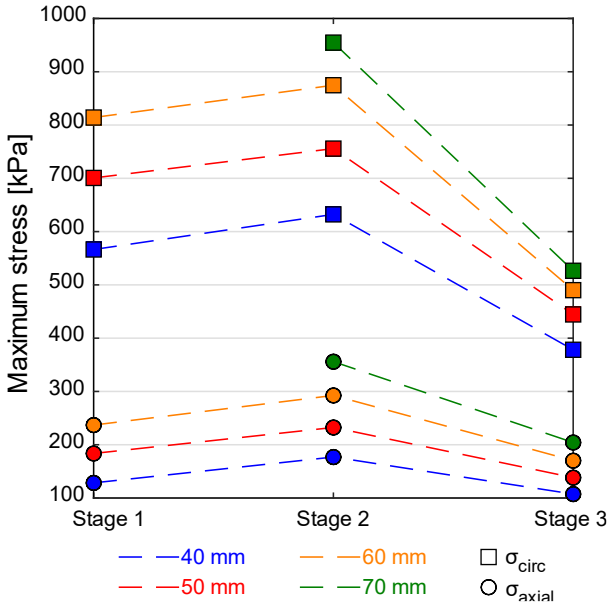

Figure 3: Maximum circumferential (squares) and axial stresses (circles) for different stages and aneurysm sizes.

Figure 4 shows circumferential stress-stretch curves for the three stages of the 60mm AAA, obtained from the same integration point located at the maximum AAA diameter (marked with black stars in Fig. 1). As expected, all curves are characterized by a linear slope (dominated by elastin) followed by a rapid increase in stress after collagen recruitment.

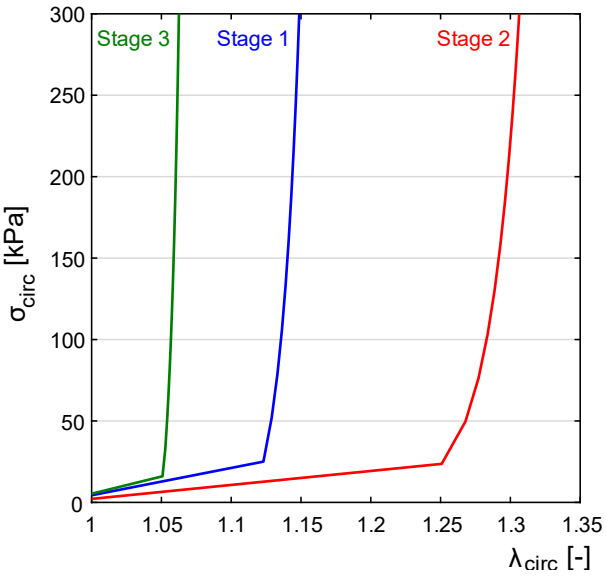

Figure 4: Circumferential stress-stretch curves for the three stages of the 60mm AAA.

The curves of Fig. 4 correspond to the definition of the disease stages by Niestrawska et al. [9], namely: the inflection point of stage 1 is between 1.1 and 1.15; stage 2 shows a more compliant behavior with an inflection point at $\lambda \geq 1{,}15$; and stage 3 shows a stiff behavior with an inflection point at $\lambda < 1{,}1$. These changes in the material stiffness of the tissue are also visible in Figs. 1 and 2, where the (compliant) stage

Published by Verlag der TU Graz
Graz University of Technology

DOI: 10.3217/978-3-85125-826-4-07

2 leads to the largest AAA diameter after pressurization, while the (stiff) stage 3 results in the smallest diameter. While the curves for the other AAA sizes are not shown here, the same behavior was observed.

Discussion

The clinical history of aortic aneurysms can be traced back to early descriptions by Roman and Greek doctors [19]; however, the pathogenesis of the disease has not yet been fully elucidated and decision-making criteria for assessing the risk of rupture are still predominantly empirical, based on diameter size [6, 7]. In this context, computer models such as the one presented here could contribute to a better understanding of the disease.

Numerical simulations of AAAs are not uncommon [12, 13]; in the present work, however, we have combined FE models with a more recent mechanopathogenic theory of development of aortic aneurysms, which was proposed by Niestrawska et al. [9]. Briefly, the authors identified three stages of the disease in which aneurysm development is associated with intense G&R of the collagen fiber network. It is believed that this G&R process consists of a reaction of mechanosensing vascular cells – particularly smooth muscle cells and fibroblasts – to (bio)mechanical changes related to the AAA pathogenesis in order to adapt the wall to the new configuration.

The results presented in Figs. 1 to 4 seem to support this hypothesis. First, by comparing stresses from the same column in Figs. 1 and 2, it can be seen that stopping the collagen remodeling process leads to increasing wall stresses, which, as expected, indicates an increasing risk of rupture in connection with aneurysm growth.

In the course of stage 1, on the abluminal side of the wall, Niewstrawska et al. [9] identified a passive reorientation of the mean fiber angle from the axial direction – characteristic of the healthy adventitia – to the circumferential direction, which is probably sensed by mechanotransducting cells (e.g., fibroblasts), which react accordingly and remodel the collagen network.

The associated changes (stage 2) lead to a slight decrease in the circumferential stresses on the aneurysm sac (Fig. 1), which is more pronounced in larger aneurysms. However, in this stage, axial stresses (Fig. 2) increase as well as the maximum circumferential stresses (Fig. 1), whose position is shifted from the sac to the AAA neck area. As the tissue also becomes more compliant (Fig. 4), greater dilatation due to blood pressure is clearly visible (Figs. 1, 2) and is likely to be perceived by the vascular cells.

Since the smooth muscle cells have largely disappeared at this stage [9], the further remodeling of the collagen network is promoted by fibroblasts, which increases the isotropy on the abluminal side of the wall (stage 3) [9]. Given the fusiform shape of most AAAs, it is worth noting that the shift towards a more isotropic (in-plane) fiber dispersion makes sense from a mechanical point of view. As a result, a considerable reduction in the stresses in both directions can be seen (Fig. 3). The decrease is more pronounced in the circumferential direction, where the maximum stress drops about 42% compared to stage 2 and by about 36% compared to stage 1. This is a direct result of the lower deformation (Figs. 1, 2) of the AAA resulting from the higher stiffness of the tissue (Fig. 4).

Disease progression (horizontal direction in Figs. 1, 2) and aneurysm growth (vertical direction in Figs. 1, 2) are simultaneous processes. Hence, a natural course of the disease would likely involve both. In this context, it is interesting to evaluate different stages combined with different diameters. The example of the circumferential stress (Fig. 1) shows that the maximum value initially rises from 566kPa (40mm, stage 1) to 756kPa (50mm, stage 2), but then drops to 490kPa (60mm, stage 3), i.e., below the initial value, which in turn suggests that collagen G&R could take place in an attemp to restore homeostasis.

It must be said, however, that these values are still much higher than those estimated for the healthy wall (~150kPa for the circumferential direction [13]), suggesting that if a healing process was actually in progress, either wall remodeling would persist or a new homeostatic state would have been established.

Conclusions and future work

There is a pressing need for better criteria for rupture risk assessment of AAAs that would enable the (bio)medical community to move forward from current empirical standards [8]. Using FE simulations to evaluate a recent three-stage theory for the development of AAAs [9], this study contributes to a better understanding of the pathogenesis of this disease.

The observed decrease in circumferential and axial stresses along disease progression (stages 1 to 3) appears to indicate an intentional healing process associated with collagen G&R promoted by vascular cells. As shown by Figs. 1 and 2, a lack of collagen remodeling leads to higher stresses during aneurysm growth, which indicates an increasing vulnerability of the vessel. Conversely, successful remodeling leads to significantly less stresses in the aortic wall (Fig. 3).

Future studies should use an appropriate non-rotationally symmetric fiber dispersion model [15] to validate these results, since arteries (both healthy and aneurysmatic) are known to be characterized by different amounts of in- and out-of-plane collagen fiber dispersion [16]. Furthermore, the effect of hypertension over the stability of the wall could be investigated by applying a pressure above 120 mmHg to the AAA.

Based on the histological state of the wall, Niestrawska et al. [9] identified two different stage 3 AAAs: vulnerable and potentially stable. Therefore, future work could also focus on differentiating these cases in order to gain better insights into a possible healing process in connection with the collagen remodeling.

Published by Verlag der TU Graz
Graz University of Technology

DOI: 10.3217/978-3-85125-826-4-07

References

[1] van der Vliet, J.A. and Boll, A.P.M.: Abdominal aortic aneurysm, *Lancet,* vol. 349, pp. 863-866, 1997.

[2] Sakahalisan, N., Limet, R. et al.: Abdominal aortic aneurysm, *Lancet,* vol. 365, pp. 1577-1589, 2005.

[3] Tillman, K., Lee, O.D. et al.: Abdominal aortic aneurysm: An often asymptomatic and fatal men's health issue, *Am. J. Men's Health,* vol. 7, pp. 163-168, 2013.

[4] Fleming, C., Whitlock, E.P. et al.: Screening for abdominal aortic aneurysm: A best-evidence systematic review for the U.S. Preventive Services Task Force, *Ann. Inter. Med.,* vol. 142, pp. 203-211, 2005.

[5] De Martino, R.R., Nolan, B.W. et al.: Outcomes of symptomatic abdominal aortic aneurysm repair, *J. Vasc. Surg.,* vol. 52, pp. 5-12, 2010.

[6] Brewster, D.C., Cronenwett, J.L. et al.: Guidelines for the treatment of abdominal aortic aneurysms: Report of a subcommittee of the Joint Council of the American Association for Vascular Surgery and Society for Vascular Surgery, *J. Vasc. Surg.,* vol. 37, pp. 1106-1117, 2003.

[7] Hirsch, A.T., Haskal, Z.J. et al.: ACC/AHA guidelines for the management of patients with peripheral arterial disease (lower extremity, renal, mesenteric, and abdominal aortic), *J. Vasc. Interv. Radiol.,* vol. 17, pp. 1383-1398, 2006.

[8] Vergaro, G., Del Corso, A. et al.: Biomarkers for growth prediction of abdominal aortic aneurysm: A step forward(?), *Eur. J. Prev. Cardiol.,* vol. 27, pp. 130-131, 2020.

[9] Niestrawska, J.A., Regitnig, P. et al.: The role of tissue remodeling in mechanics and pathogenesis of abdominal aortic aneurysms, *Acta Biomater.,* vol. 88, pp. 149-161, 2019.

[10] Elger, D.F., Blackketter, D.M. et al.: The influence of shape on the stresses in model abdominal aortic aneurysms, *J. Biomech. Eng.,* vol. 118, pp. 326-332, 1996.

[11] Roy, D., Holzapfel, G.A. et al.: Finite element analysis of abdominal aortic aneurysms: Geometrical and structural reconstruction with application of an anisotropic material model structural reconstruction with application of an anisotropic material model, *IMA J. Appl. Math.,* vol. 79, pp. 1011-1026, 2014.

[12] Rodríguez, J.F., Ruiz, C. et al.: Mechanical stresses in abdominal aortic aneurysms: Influence of diameter, asymmetry, and material anisotropy, *J. Biomech. Eng.,* vol. 130, p. 021023, 2008.

[13] Niestrawska, J.A., Haspinger, D.C. et al.: The influence of fiber dispersion on the mechanical response of aortic tissues in health and disease: a computational study, *Comput. Methods Biomech. Biomed. Engin.,* vol. 21, pp. 99-112, 2018.

[14] Gasser, T.C., Ogden, R.W. et al.: Hyperelastic modelling of arterial layers with distributed collagen fibre orientations, *J. R. Soc. Interface,* vol. 3, pp. 15-35, 2006.

[15] Holzapfel, G.A., Niestrawska, J.A. et al.: Modelling non-symmetric collagen fibre dispersion in arterial walls, *J. R. Soc. Interface,* vol. 12, p. 20150188, 2015.

[16] Niestrawska, J.A., Viertler, C. et al.: Microstructure and mechanics of healthy and aneurysmatic abdominal aortas: Experimental analysis and modelling, *J. R. Soc. Interface,* vol. 13, p. 20160620, 2016.

[17] Horny, L., Adamek, T. et al.: Analysis of axial prestretch in the abdominal aorta with reference to post mortem interval and degree of atherosclerosis, *J. Mech. Behav. Biomed. Mater.,* vol. 33, pp. 93-98, 2014.

[18] Derwich, W., Wittek, A. et al.: Comparison of abdominal aortic aneurysm sac and neck wall motion with 4D ultrasound imaging, *Eur. J. Vasc. Endovasc. Surg.,* vol. 60, pp. 539-547, 2020.

[19] S. G. Friedman, *A History of Vascular Surgery*, 2nd ed., Oxford: Blackwell Publishing, 2005.

Published by Verlag der TU Graz
Graz University of Technology

Proc. Annual Meeting of the Austrian Society for Biomedical Engineering 2021
DOI: 10.3217/978-3-85125-826-4-08

EFFECT OF ATRIAL INFLOW CONDITIONS ON VENTRICULAR FLOW PATTERN DURING LVAD SUPPORT: A SIMULATION STUDY

Ghodrati M.[1,2], Schlöglhofer T.[1,2,3], Maurer A.[1,2], Zonta F.[4], Moscato F.[1,2], Schima H.[1,2,3], Aigner P.[1,2]

[1] Center for Medical Physics and Biomedical Engineering, Medical University of Vienna, Austria
[2] Ludwig Boltzmann Institute for Cardiovascular Research, Vienna, Austria
[3] Department for Cardiac Surgery, Medical University of Vienna, Austria
[4]Institute of Fluid Dynamics and Heat Transfer, Technical University of Vienna, Austria

mojgan.ghodrati@meduniwien.ac.at

Abstract

Simulations of the ventricular flow patterns during left ventricular assist device (LVAD) support are mainly performed with straight inflow condition, neglecting the influence of the atrial vortex. In this study, the influence of the atrial inflow conditions – including rotation and asymmetric flow profiles – on the platelet behavior were investigated via Computational Fluid Dynamics (CFD) simulations.

Keywords

Left ventricular assist device, ventricular flow patterns, atrial inflow, computational fluid dynamics

Introduction

The use of LVADs as a treatment method for heart failure patients has been steadily increasing [1]. Despite the success of this treatment, there is still a high risk of thrombosis and consequently a high mortality rate from stroke [2], [3]. Therefore, there is an urgent need for intraventricular flow field investigation during LVAD support for a better understanding of the reasons for the high prevalence of thrombosis in these patients. Numerical simulations can be a useful tool for flow field analysis and for evaluation of the critical parameters at the location of depositions. However, the accuracy of the simulated flow fields is highly dependent on the defined inflow conditions [4].
Simulations of the ventricular flow patterns during LVAD support are mainly performed with perpendicular inflow conditions from the left atrium neglecting asymmetries arising due to uneven flow contribution of the pulmonary veins [5]–[7] as well as the atrial vortex. In this study, the influence of the atrial inflow conditions – including rotation and asymmetric flow profiles – on the flow patterns and the platelet behavior were investigated via numerical simulations.

Methods

The left ventricle (LV) and the pump of an LVAD patient were segmented from computed tomography (CT) images and used in this study.
The Navier-Stokes equations were solved using the finite-volume CFD solver (FLUENT, Ansys 19.1, Pennsylvania, USA). The blood was modeled as a non-Newtonian fluid with a density of 1060 kg/m3 and a dynamic viscosity of 0.0035 Pa·s. using Laminar model [8].
Three different inflow boundary conditions were considered to investigate the importance of the atrial inflow conditions; first, a simulation was performed with perpendicular velocity to the inflow (Straight, flow rate: 3.5 lit/min) to replicate the typical approach of intraventricular flow simulation. For the second simulation an additional rotational component at the inflow (Rotation: 35 rpm) was applied as a representative of the atrial vortex and a third simulation was performed with asymmetric inflow conditions (Asymmetric: 60%/40% left/right flow ratio to replicate physiologic uneven flow distribution of the pulmonary veins). The overview of boundary conditions can be seen in Fig1.

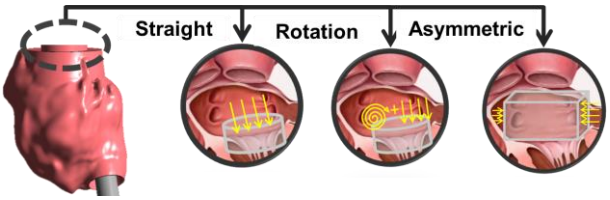

Figure 1: Patient specific LV geometry with atrial inflow conditions.

A Lagrangian approach was used to track 10 000 particles with a diameter of three micrometers. Particles were injected at the beginning of the simulation at the mitral annulus and tracked over 7s within the LV. The risk of platelet activation and aggregation was evaluated by analysis of particle trajectories inside of the LV. The Shear Stress Histories (SSH), (Eq. 1), and the Residence Times (RT) of the particles, (Eq. 2), were used as indicators for thrombogenicity [9]

$$SSH = \int_{t_0}^{t} \tau(X(t'), t')dt' \quad (1)$$

$$RT_i = T_i^{entrance} - T_i^{exit} \quad (2)$$

Published by Verlag der TU Graz
Graz University of Technology

DOI: 10.3217/978-3-85125-826-4-08

Results

Atrial inflow conditions affect the intraventricular flow patterns as well as particle trajectories significantly (Fig. 2).

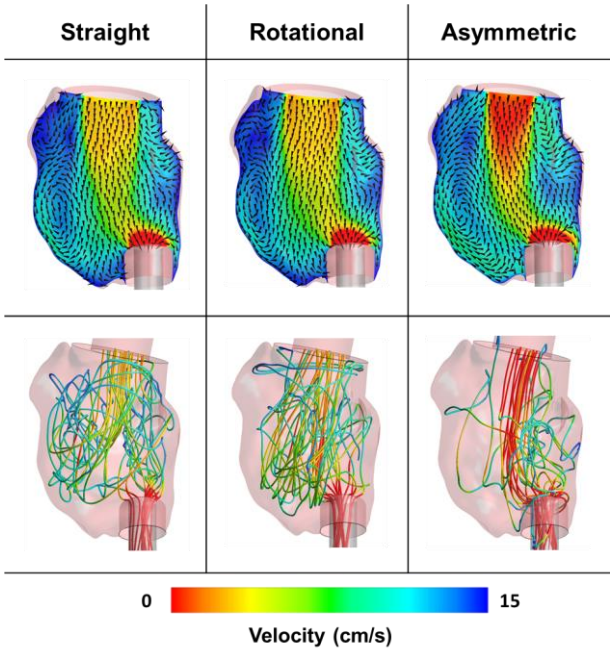

Figure 2: Top row: mean blood flow patterns at coronal plane; bottom row: Particle trajectories for straight, rotation, asymmetric inflow conditions colored with particle velocity magnitude.

Also stagnation regions was increased with rotational inflow (Straight: 13.62, Rotation: 15.83, Asymmetric: 7.33 cm^2) which can be seen in Fig. 3.

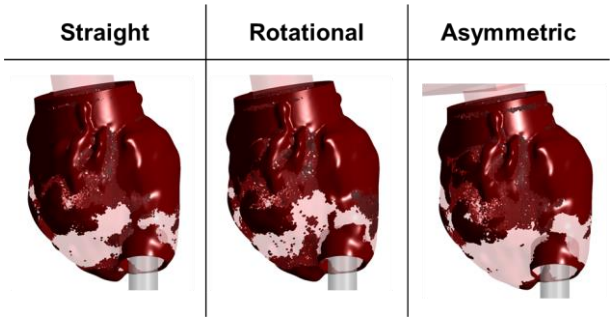

Figure 3: Iso-volume of stagnation volume defined by mean velocity magnitude < 0.5 cm/s.

The distribution of the particles in terms of RT and SSH is visualized by using box plots (Fig. 4 & Fig. 5).

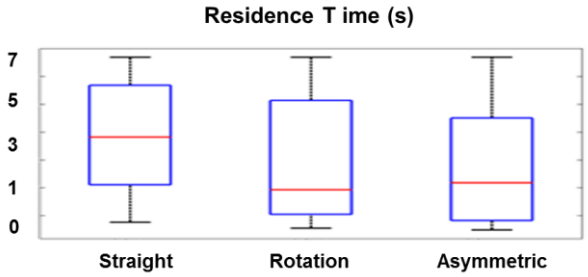

Figure 4: Box plots of particle residence time.

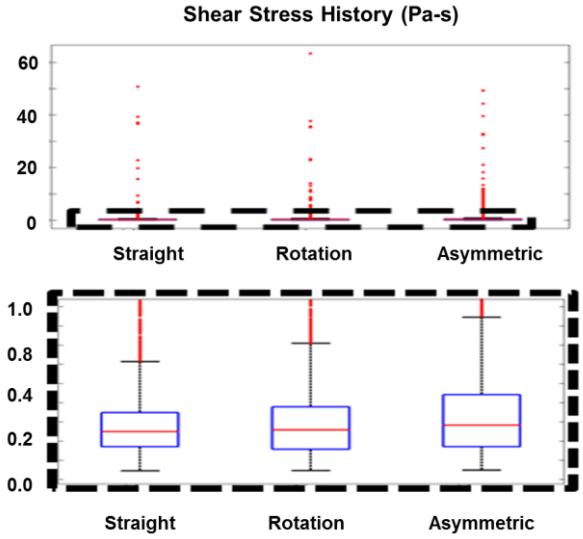

Figure 5: Box plots of shear stress history.

The percentage of the particles remaining within the LV after 7s of simulation was comparable for simulations with straight and rotation inflow, while it decreased significantly for asymmetric inflow. Moreover, particles experienced higher accumulative shear stresses with the asymmetric inflow (Table 1).

Table 1: Median and outlier information for RT and SH.

		Straight	Rotation	Asymmetric
RT (s)	Median	3.82	1.92	2.18
	Outliers (Max, %)	6.99, 19	6.99, 18	6.99, 13
SSH (Pa-s)	Median	0.25	0.26	0.29
	Outliers (Max, %)	50.78, 2	63.48, 3	49.46, 6

Published by Verlag der TU Graz
Graz University of Technology

DOI: 10.3217/978-3-85125-826-4-08

Discussion

The previously validated numerical simulation [8] was used in this study to investigate the effect of atrial boundary conditions on the ventricular flow pattern during LVAD support.

Consideration of the rotational boundary condition at the mitral annulus creates lower washout and consequently larger stagnation volume, mainly at the apex around the LVAD inflow cannula, compared to the conventional straight boundary conditions. While stagnation volume was associated with thrombus formation by previous studies [10], it was shown that inaccurate simulation of the blood stasis region could result in misprediction of these aforementioned regions of stagnation.

Further, inclusion of the asymmetric boundary conditions resulted in an overall significant increase in SSH values and a larger proportion of particles that experienced exposure to high RT, indicating elevated risk of platelet activation and thrombus formation [9].

Neglecting the atrial flow conditions could lead to inaccurate simulation of ventricular blood flow. Therefore reliable prediction of blood component's behavior and the evaluation of the risk of thrombosis demand careful consideration of the atrial inflow conditions.

Acknowledgements

This study was partially funded by the Jubiläumsfonds of the Austrian National Bank Project Nr. 17314 and the Austrian Research Promotion Agency (FFG): M3dRES Project Nr. 858060.All the simulations were performed on Vienna Scientific Cluster.

References

[1] J. K. Kirklin *et al.*, "Eighth annual INTERMACS report: Special focus on framing the impact of adverse events," *The Journal of Heart and Lung Transplantation*, vol. 36, no. 10, pp. 1080–1086, Oct. 2017, doi: 10.1016/j.healun.2017.07.005.

[2] D. Acharya *et al.*, "INTERMACS Analysis of Stroke During Support With Continuous-Flow Left Ventricular Assist Devices," *JACC: Heart Failure*, vol. 5, no. 10, pp. 703–711, Oct. 2017, doi: 10.1016/j.jchf.2017.06.014.

[3] A. D. DeVore and G. C. Stewart, "The Risk of Stroke on Left Ventricular Assist Device Support," *JACC: Heart Failure*, vol. 5, no. 10, pp. 712–714, Oct. 2017, doi: 10.1016/j.jchf.2017.08.002.

[4] Long Q., Merrifield R., and Yang G. Z., X. Y. Xu, P. J. Kilner and, and D. N. Firmin, "The Influence of Inflow Boundary Conditions on Intra Left Ventricle Flow Predictions," *Journal of Biomechanical Engineering*, vol. 125, no. 6, pp. 922–927, Jan. 2004, doi: 10.1115/1.1635404.

[5] S. Liao, M. Neidlin, Z. Li, B. Simpson, and S. D. Gregory, "Ventricular flow dynamics with varying LVAD inflow cannula lengths: In-silico evaluation in a multiscale model," *Journal of Biomechanics*, vol. 72, pp. 106–115, Apr. 2018, doi: 10.1016/j.jbiomech.2018.02.038.

[6] V. K. Chivukula *et al.*, "Left Ventricular Assist Device Inflow Cannula Angle and Thrombosis Risk," *Circulation: Heart Failure*, vol. 11, no. 4, p. e004325, Apr. 2018, doi: 10.1161/CIRCHEARTFAILURE.117.004325.

[7] M. Ghodrati *et al.*, "The influence of left ventricular assist device inflow cannula position on thrombosis risk," *Artif Organs*, vol. 44, no. 9, pp. 939–946, Sep. 2020, doi: 10.1111/aor.13705.

[8] M. Ghodrati *et al.*, "Validation of numerically simulated ventricular flow patterns during left ventricular assist device support," *Int J Artif Organs*, vol. 44, no. 1, pp. 30–38, Jan. 2021, doi: 10.1177/0391398820904056.

[9] C. Mahr *et al.*, "Intermittent Aortic Valve Opening and Risk of Thrombosis in Ventricular Assist Device Patients:," *ASAIO Journal*, vol. 63, no. 4, pp. 425–432, 2017, doi: 10.1097/MAT.0000000000000512.

[10] C. N. Bagot and R. Arya, "Virchow and his triad: a question of attribution," *British Journal of Haematology*, vol. 143, no. 2, pp. 180–190, Oct. 2008, doi: 10.1111/j.1365-2141.2008.07323.x.

Published by Verlag der TU Graz
Graz University of Technology

Proc. Annual Meeting of the Austrian Society for Biomedical Engineering 2021
DOI: 10.3217/978-3-85125-826-4-09

OPTIMIZATION OF PULSED CHEMICAL EXCHANGE SATURATION TRANSFER MRI BY OPTIMAL CONTROL

Clemens Stilianu[1], Christina Graf[1], Armin Rund[2], Rudolf Stollberger[1]

[1]Institute of Medical Engineering, Graz University of Technology, Graz, Austria
[2]Institute for Mathematics and Scientific Computing, University of Graz, Graz, Austria

stilianu@tugraz.at

Abstract— *The goal of this work was to design improved Chemical Exchange Saturation Transfer MRI RF pulses applicable to whole-body clinical scanners. Conventionally, CEST imaging requires a long continuous wave saturation pulse, however, due to hardware limitations, only pulsed saturation is practicable for in vivo scanners. Consequently, RF pulses with a duty cycle of 90% are designed by optimal control. The simulation results were compared to a 100% duty cycle Continuous-Wave pulse and a 90% Gaussian standard pulse. The optimal control pulse showed superior efficiency to the Gaussian pulse and comparable performance to the Continuous-Wave pulse, while transmitting less energy to the patient.*

Keywords—*CEST, Pulsed CEST MRI, Optimal Control, Optimization, Pulse Design*

Introduction

Chemical Exchange Saturation Transfer (CEST)-MRI is a specific imaging method that can efficiently detect various metabolites in the human body undetectable by conventional MRI [1]. This can be realized by applying a long, off-resonant Continuous Wave (CW) saturation radio frequency (RF) pulse. However, such pulses are not always feasible due to hardware limitations and Specific Absorption Rate (SAR) restrictions, especially on clinical scanners which require pulsed RF excitation which typically provide much lower saturation, [1]. Optimal Control (OC) is emerging as a promising tool to find Duty Cycled (DC) pulses that achieve high CEST-effects while accounting for hardware limitations of clinical scanners. OC CEST pulses with a DC of up to 90% are designed to challenge CW pulses and exceed state of the art pulses used on clinical scanners.

Theory and Methods

Bloch-McConnell equations are the basis for describing chemical exchange phenomena in MRI. Explicitly, they describe a six-dimensional inhomogeneous system of ODEs giving us the temporal evaluation of the magnetization vector $M(z,t)$:

$$\frac{dM}{dt} = A \cdot M + b, \qquad \frac{d\tilde{M}}{dt} = \tilde{A} \cdot \tilde{M} + b,$$

$$s.t. \quad M(t=0) = M_0, \qquad \tilde{M}(t=0) = \tilde{M}_0. \tag{1}$$

The Bloch-McConnell equations in this case include two proton pools, one pool for bulk water and one pool for the solute, which are connected via chemical exchange with exchange rate k_{sw} from solute pool to bulk water pool and exchange rate k_{ws} from the bulk water pool to the solute pool. Therein, M and A describe the system with chemical exchange and $\tilde{\mathrm{M}}$ and $\tilde{A}$ describe the system without chemical exchange. Each of the pools are defined individually by relaxation times T_{1w} and T_{2w} for bulk water and T_{1s} and T_{2s} for the solute pool.

The optimization problem is given as

$$\min_{B_1} J\left(B_1, M_z, \tilde{M}_z\right) = \frac{\alpha}{2}\int_0^T (B_1)^2\, dt - \\ -\beta\left|M_z(z_1) - \tilde{M}_z(z_1)\right| - \gamma \int_\Omega \mathrm{M}_z(z)\, dz. \tag{2}$$

The first integral of Eq. 2 corresponds to the transmitted energy in the B_1 field with the regularization parameter α. The second term maximizes the difference between the magnetization M_z with CEST and the magnetization $\tilde{M}_z$ without CEST at the saturation offset z_1, i.e. maximization of the corresponding CEST peak weighted with parameter β. The third term ensures the maximization of the area under the z-spectrum by integrating over the whole frequency space Ω weighted by the parameter γ. The design of this cost function was inspired by [2].

For OC, the DC of the RF-pulse is fixed to a value of 90% with an on time of $t_p = 100$ ms and subsequent off times of $t_d = 12.5$ ms (see Tab. 2). 90% DC is chosen to maximize the on time and therefore the dependent CEST effect as well as ensure the feasibility of measurements on clinical MRI scanners. For performance review, the simulation is also conducted for a CW pulse with a DC of 100% and a Gaussian standard pulse with the same t_p and t_d times as the OC pulse. The Gaussian standard pulse is a Gaussian function filtered with a cosine window which is directly taken from [3]. The amplitude of the CW pulse as well as the Gaussian standard pulse is optimized to yield a maximum CEST effect for this model, thus the best CW pulse and Gaussian standard pulse for a given saturation time are used within the following comparison.

Published by Verlag der TU Graz
Graz University of Technology

DOI: 10.3217/978-3-85125-826-4-09

The simulation and optimization process is demonstrated using the example of a creatine pool with a frequency offset of $\delta = 1.9$ ppm in chemical exchange with a bulk water pool with no offset (see Tab. 1). The simulation parameters are taken from [4].

Table 1: Simulation parameters for the creatine CEST model including a water pool and a solute pool.

Simulation Parameter	**Value**
Offset, δ [ppm]	1.9
Exchange rate solid-water , k_{sw} [Hz]	50
Exchange rate water-solid , k_{ws} [Hz]	1
B_0 [T]	3
Relaxation, T_{1w} [s]	1.08
Relaxation, T_{2w} [ms]	0.069
Relaxation, T_{1s} [s]	1.00
Relaxation, T_{2s} [ms]	0.160
Time discretization, Δt [ms]	0.1
Frequency discretization, Δz [ppm]	0.05

The RF pulse is optimized with a hybrid semismooth quasi-Newton method [5] which also allows the implementation of constraints prescribed by the clinical scanner (Amplitude: $B_{1max} \leq 2.5\ \mu T$ and Phase: $0 \leq \varphi \leq 2\pi$). The underlying Bloch-McConnell equations and their corresponding adjoint equations are solved numerically by symmetric operator splitting [6].

Results and Discussion

The optimized pulse can be seen in Fig. 2 on the top right and the corresponding spectrum underneath. There, the saturated spectrum without exchange $\widetilde{M}(z)$

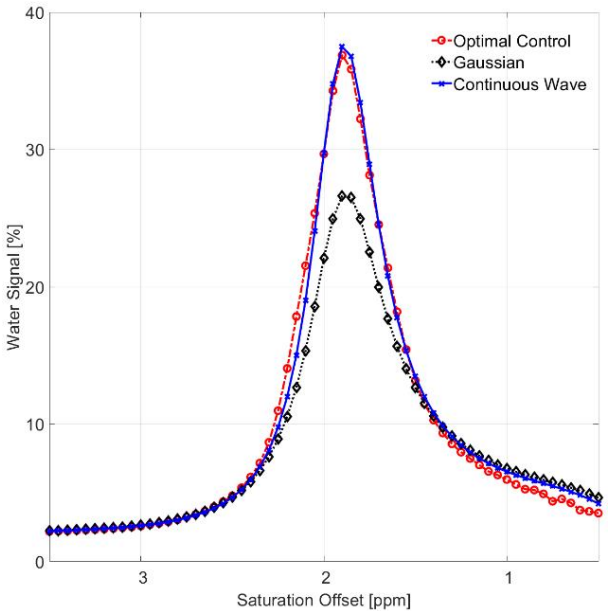

Figure 1 : Direct comparison of the CEST-Peaks for the CW- , OC- and Gaussian-pulse.

is shown in blue, the one with chemical exchange $M_z(z)$ in red, and the CEST effect is seen as difference $|M_z(z) - \widetilde{M}_z(z)|$. To compare the performance of the OC results the same model is tested with a CW pulse and a Gaussian standard pulse. CW pulses are broadly known as the most efficient pulses for generating high contrast CEST images, mainly used for NMR spectroscopic measurements. However these pulses are not applicable on clinical scanners due to

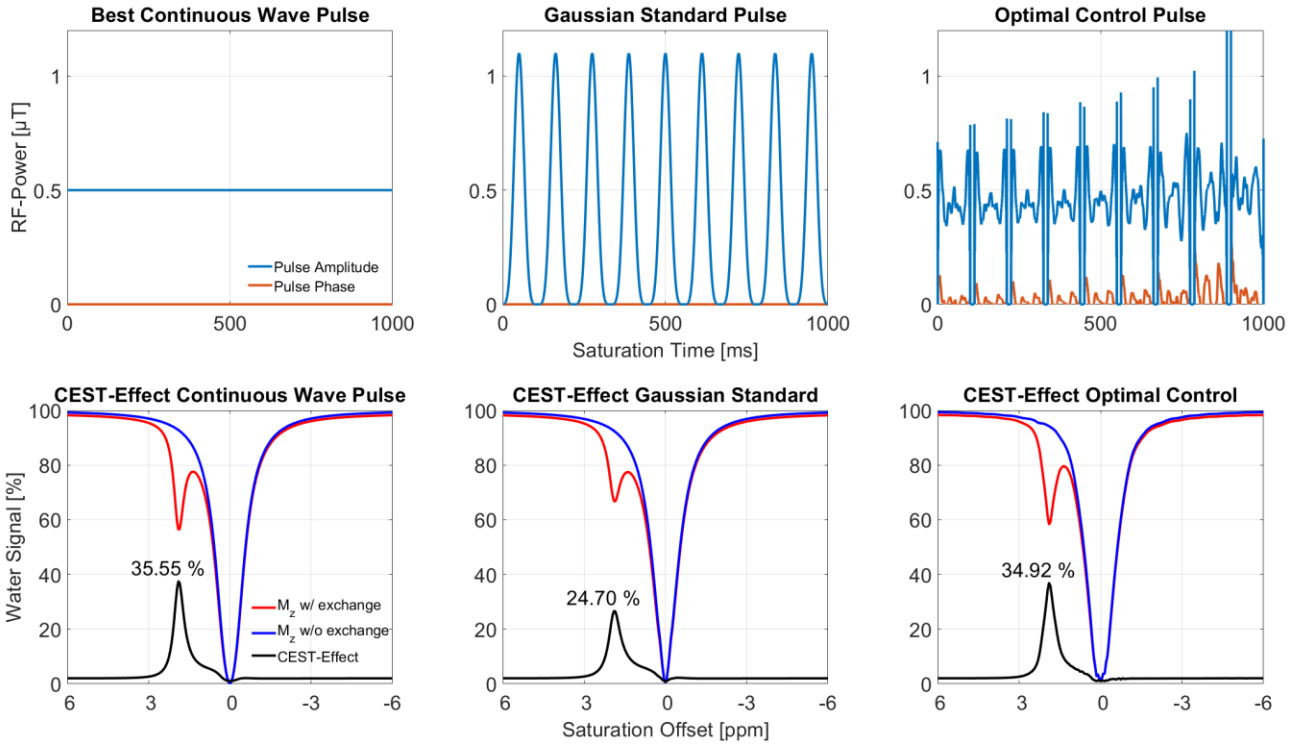

Figure 2: Comparison of the CW- , OC- and Gaussian-pulses and the corresponding z-spectra.

Published by Verlag der TU Graz
Graz University of Technology

DOI: 10.3217/978-3-85125-826-4-09

hardware limitations and SAR restrictions. That is why pulsed Gaussian standard pulses or pulsed truncated sinc pulses (not included in this work) are currently used as most efficient RF pulses for CEST imaging.

By comparing the spectra that are generated with the OC, CW and Gaussian pulses we can get an understanding of how efficient the pulses generate contrast in CEST images. Smooth and slim spectra potentially generate easy to distinguish CEST peaks for measurements. Therefore, minimizing the negative integral is a priority for the optimization process, as this on the one hand limits the energy that is put into the RF pulse, and on the other hand restrains broadening of the CEST peak and truncates artefacts in the resulting spectra. All pulses exhibit a comparatively small area as can be seen in Tab. 2. The CEST peaks of all pulses can be seen in greater detail in Fig. 1. The CEST peak maximum of the OC pulse reaches the CEST peak maximum of the CW within approximately 1.7 % and beats the maximum of the Gaussian pulse by about 30.5 %.

Furthermore, a restriction to a MRI RF pulse is the energy transferred to the human's body. The Integral of $(B_1(t))^2$ over the pulse duration is proportional to said energy, hence proportional to the SAR [7]. In Tab. 2 we observe that the Gaussian RF pulse train exhibits the highest energy, followed by the CW with OC showing the lowest energy among those three. This underlines that OC addresses those limitations successfully.

The presented RF pulse designed by means of optimal control showed to outperform state of the art pulses in terms of CEST effect and pulse energy. The next logical step would be the implementation on the MR scanner and comparison to both the CW and Gaussian RF pulse.

Table 2: Comparison of significant features of a CW pulse with a DC-OC pulse and a DC-Gaussian standard pulse. Total duration was set to 1 s.

Pulse feature	**CW**	**Gaussian**	**OC**
CEST-Effect [%]	35.55	24.70	34.94
Integral $(B_1(t))^2$ [(µT)^{2}s]	2500	2844	2094
Area [a.u.]	200	191	198
Duty Cycle, DC [%]	100	90	90

Conclusion

We implemented an optimal control framework for CEST RF pulse design. The optimized pulses were able to outperform state of the art Gaussian pulses by 30.5% and achieve almost the same efficiency as CW pulses while being applicable to clinical scanners.

References

[1] S. A. Smith, J. A. D. Farrell, C. K. Jones, D. S. Reich, P. A. Calabresi, and P. C. M. Van Zijl, "Pulsed magnetization transfer imaging with body coil transmission at 3 Tesla: Feasibility and application," *Magn. Reson. Med.*, vol. 56, no. 4, pp. 866–875, Oct. 2006, doi: 10.1002/mrm.21035.

[2] E. S. Yoshimaru, E. A. Randtke, M. D. Pagel, and J. Cárdenas-Rodríguez, "Design and optimization of pulsed Chemical Exchange Saturation Transfer MRI using a multiobjective genetic algorithm," *J. Magn. Reson.*, vol. 263, pp. 184–192, Feb. 2016, doi: 10.1016/j.jmr.2015.11.006.

[3] K. Herz *et al.*, "Pulseq-CEST: Towards multi-site multi-vendor compatibility and reproducibility of CEST experiments using an open-source sequence standard," *Magn. Reson. Med.*, vol. 00, pp. 1–14, 2021, doi: 10.1002/mrm.28825.

[4] M. Zaiß, B. Schmitt, and P. Bachert, "Quantitative separation of CEST effect from magnetization transfer and spillover effects by Lorentzian-line-fit analysis of z-spectra," *J. Magn. Reson.*, vol. 211, no. 2, pp. 149–155, Aug. 2011, doi: 10.1016/j.jmr.2011.05.001.

[5] A. Rund, C. S. Aigner, K. Kunisch, and R. Stollberger, "Magnetic Resonance RF Pulse Design by Optimal Control with Physical Constraints," *IEEE Trans. Med. Imaging*, vol. 37, no. 2, pp. 461–472, Feb. 2018, doi: 10.1109/TMI.2017.2758391.

[6] C. Graf, A. Rund, C. S. Aigner, and R. Stollberger, "Accuracy and Performance Analysis for Bloch and Bloch-McConnell Simulation Methods," *J. Magn. Reson.*, p. 107011, May 2021, doi: 10.1016/j.jmr.2021.107011.

[7] M. A. BERNSTEIN, K. F. KING, and X. J. ZHOU, "INTRODUCTION TO RADIOFREQUENCY PULSES," in *Handbook of MRI Pulse Sequences*, Elsevier, 2004, pp. 29–34.

Published by Verlag der TU Graz
Graz University of Technology

Proc. Annual Meeting of the Austrian Society for Biomedical Engineering 2021
DOI: 10.3217/978-3-85125-826-4-10

ELECTRICAL NEUROMODULATION DURING ROBOT-ASSISTED STEPPING IN HUMANS WITH SPINAL CORD INJURY

Matthias J. Krenn[1,2]

[1] Department of Neurobiology and Anatomical Sciences, University of Mississippi Medical Center, Jackson, MS, USA, [2] Center for Neuroscience and Neurological Recovery, Methodist Rehabilitation Center, Jackson, MS, USA

mkrenn@umc.edu

Abstract— *Electrical neuromodulation using transcutaneous spinal stimulation can modify the spinal motor output. In recent years, proof-of-principal studies have shown the benefits of this intervention to recover locomotor functions. Here, we assess changes of joint torques during stimulation over a wide range of stimulation frequencies (1 – 100 Hz). The presented example shows high susceptibility to the external input by modifying stepping patterns during robot-assisted treadmill training.*

Keywords—*Transcutaneous spinal stimulation, neuromodulation, sensorimotor integration, spinal cord injury, robot-assisted gait training*

Introduction

Spinal cord injury (SCI) is a devastating neurological condition that affects the interactions between supraspinal structures and the spinal cord below the lesion. It results in partial or complete loss of volitional and postural control of movements associated with impaired sensorimotor integration. The ensuing muscle weakness is often accompanied by spastic motor behaviors, such as increased muscle tone (hypertonia), hyperactive reflexes (hyperreflexia), and clonus, as well as involuntary muscle contractions (spasms) and improper muscle coordination (dyssynergia) [1, 2].

New developments in electrical neuromodulation with transcutaneous (TSS) spinal stimulation show promise for improving walking in people with SCI [3–5]. The underlying premise of TSS interventions is that the generated afferent input modifies the excitability of the lumbosacral network to either augment appropriate or suppress pathophysiologic spinal motor output [4, 6].

Here, we address the impact of TSS frequency from 1 up to 100 Hz on locomotor pattern in people with incomplete SCI.

Methods

Robot-assisted treadmill stepping

The participant was first instrumented for EMG recording and TSS stimulation (see below). After determining the stimulation thresholds, the subject was placed in the bodyweight support harness and fitted into the robotic gait orthosis (Lokomat Pro V4, Hocoma AG, Volketswil, CH). The Lokomat (Fig. 1A) was used in a research mode, which provided real-time analog data output. This device controls leg movement towards a predefined trajectory of a physiological gait pattern by controlling the hip and knee joint torques of the exoskeleton. A cascaded control system (Fig. 1B) integrates a first-order impedance controller (proportional-

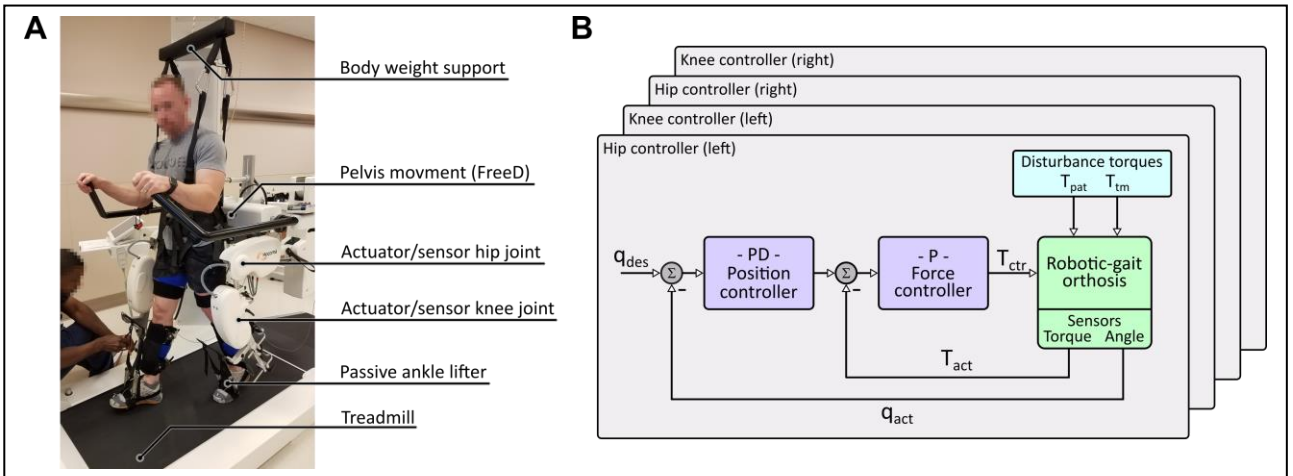

Figure 1. (A) Components of the robot-assisted gait exoskeleton, Lokomat Pro. (B) Cascaded control structure. Primary angle controller based on desired (q_{des}) and measured actual (q_{act}) angles; secondary torque control loop based generates the actuating torque (T_{ctr}) of the exoskeleton; actual torque (T_{act}) measured at the actuators. The disturbance torques by a participant (T_{pat}) and treadmill (T_{tm}). Modified from Jezernik et al. (2003) [7].

Published by Verlag der TU Graz
Graz University of Technology

DOI: 10.3217/978-3-85125-826-4-10

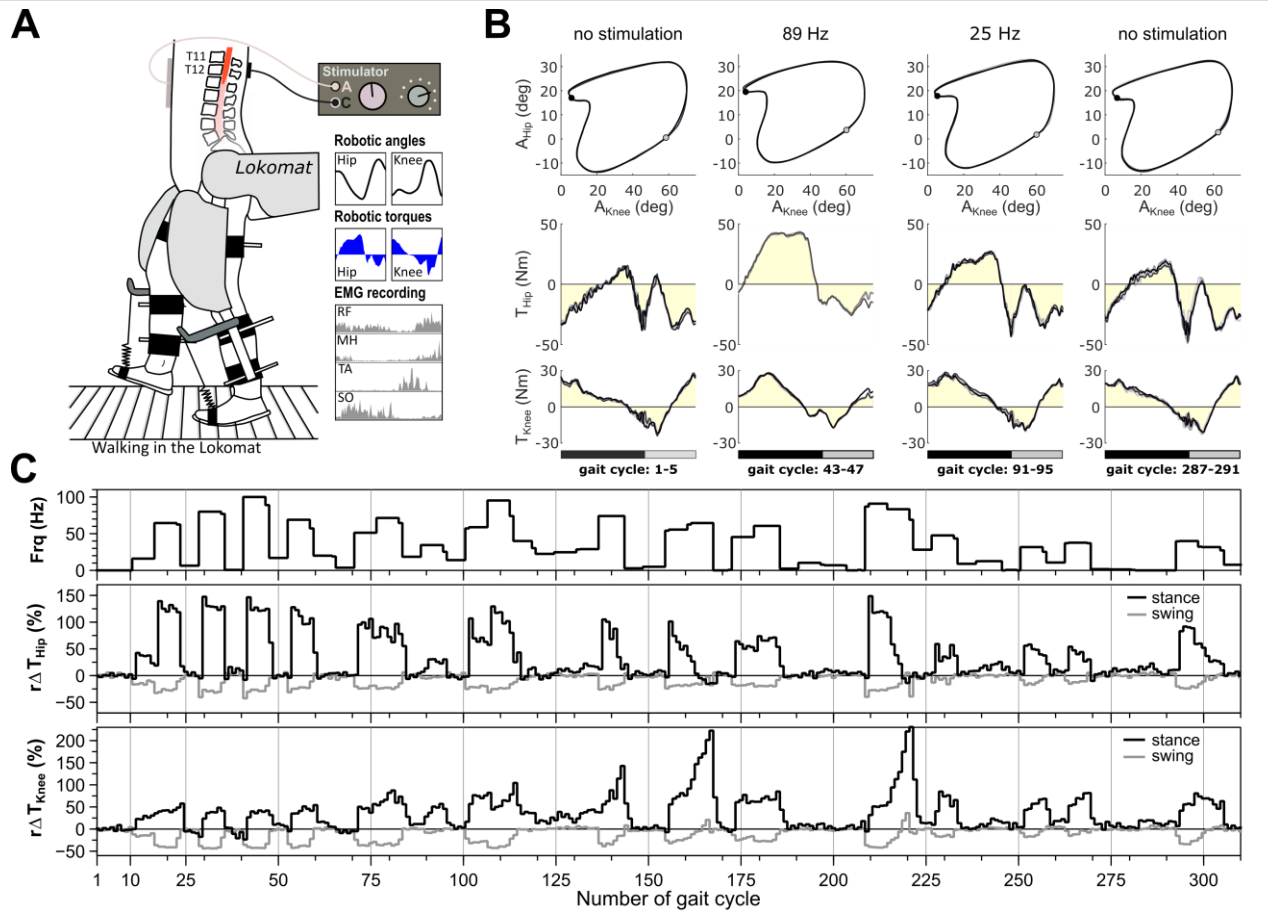

Figure 2. Recording setup and illustrative robotic torques and angles in participant S2 (left leg). A: Recording setup: The subject is placed in a robotic-assisted gait orthosis (Lokomat Pro, Hocoma, Inc.) on a treadmill with body-weight support. Robotic torques and angles in hip and knee joints were output using the Lokomat research setting. EMG signals were simultaneous recorded in the rectus femoris (RF), medial hamstrings (MH), tibialis anterior (TA), and soleus (SO) muscles. During stepping at constant treadmill speed and body weight support, continuous transcutaneous spinal stimulation was applied at various frequencies but the same intensity. B: Angle (A) and torque (T) signals for five superimposed consecutive gait cycles (duration 2.4 s) at different stimulation frequencies. Hip–knee cyclograms (top) present the gait trajectories of the robotic joints (beginning of stance, black circle; beginning of swing, grey circle). Robotic hip (middle) and knee (bottom) joint torques produced by the robotic actuators (stance phase, 62%, marked in black; swing phase, 38%, in grey). Note similar trajectories but changes in hip and knee torques at different stimulation frequency. C: Traces of stimulation frequency (top), hip (middle), and knee (bottom) robotic torques over 310 gait cycles for stance (black) and swing (gray). The stimulation frequency was randomized and kept constant for ten consecutive gait cycles. Hip and knee robotic torques are expressed relative to the first 10 gait cycles (no stimulation).

derivative, PD) for angle deviations and a second-order proportional (P) torque controller [7].

TSS intervention

Two self-adhesive hydrogel electrodes (5 cm, diameter) were placed on both sides of the T11/12 interspinous space and connected to act as a single cathode. The rectangular electrodes (7.5 x 10 cm) were placed over the lower anterior abdomen left and right of the umbilicus and connected as a single cathode [8]. The stimulation frequencies were randomized from 1 to 100 Hz, whereas the intensity was set individually to allow comfortable stepping across the applied frequency range.

Experimental procedure

After checking the proper orthosis fit and stepping pattern over ~30 gait cycles, the robotic torques and EMG were first recorded without stimulation (10 gait cycles). Then, the stimulation frequencies were randomly selected by custom-made software up to 100 and remained constant for ten consecutive gait cycles. The trigger signal provided by a data acquisition card (CompactRIO Systems) was used to synchronize the frequency change with the right heel-strike defined by the Lokomat. Stepping without stimulation was repeated at random throughout the recording. Data from 310 consecutive gait cycles were analyzed of which the first ten gait cycles without stimulation were used for normalization.

Published by Verlag der TU Graz
Graz University of Technology

DOI: 10.3217/978-3-85125-826-4-10

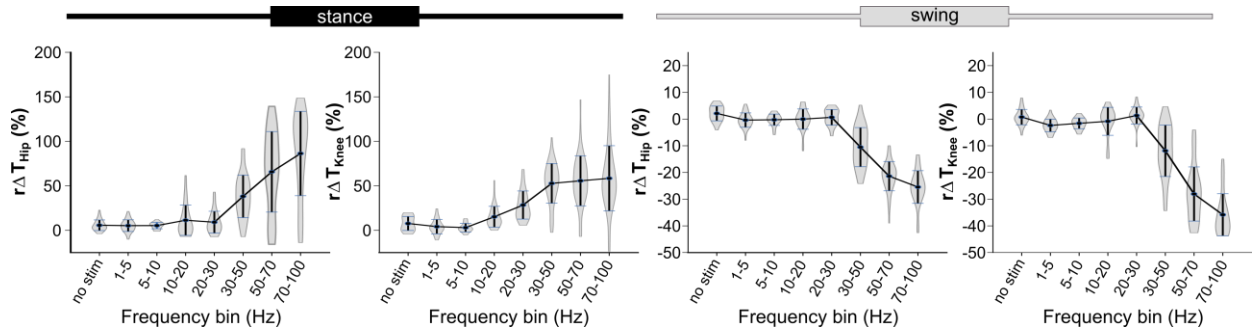

Figure 3. The violine plots for the relative changes in hip and knee torques for each stimulation frequency bin during stance and swing. The line graph presents the mean (avgT) and standard deviation of each frequency bin.

Data analysis

The subsequent heel identified a gait cycle–strike signals from the Lokomat output and divided it into the stance (62%) and swing (38%) phase. The robotic torques (T) generated by the Lokomat hip and knee actuators during stepping were calculated as the area under the curve (Fig. 1B), separately for stance and swing, hip and knee, and left and right sides. The relative change in torque ($r\Delta T_{gc}$, in %) was calculated as the normalized difference between the torque during each gait cycle (T_{gc}) and the averaged torque across the first ten gait cycles without stimulation ($T_{avg}[1:10]$) for each side, joint, and gait phase (Eq. 1).

$$r\Delta T_{gc} = \frac{T_{gc} - T_{avg[1:10]}}{T_{avg[1-10]}} \cdot 100\% \quad (1)$$

Results

An example of relative changes in the robotic torques (rΔT) are shown in Figure 2B-D for the entire recording session (310 gait cycles) with and without TSS applied at randomly selected stimulation frequencies in a participant (left leg). The robotic torques for no stimulation conditions (baseline), interspersed throughout the recording session, was stable (Fig. 2B, first and last columns). Administering the stimulation at different frequencies produced instantaneous changes in torque predominantly sustained in magnitude over multiple gait cycles or showed an incremental or decremental change (Fig. 2C). The changes in robotic torques during stimulation were largely in opposite directions between stance and swing in both hip and knee joints (Fig. 2B, middle columns; Fig. 2C). With frequency data aggregated in bins, it became apparent that the hip and knee robotic torques increased during stance and decreased during swing at higher frequencies in this participant (Fig. 3).

Discussion

In this study, we examined the immediate effect of TSS across different stimulation frequencies on robotic support of hip and knee kinematics and muscle activation patterns during treadmill stepping. We have found individually distinct patterns of changes in the robotic torques that differed in magnitude and direction depending mainly on the applied stimulation frequency and gait phase (Fig. 2).

Recently developed methods of transcutaneous posterior root stimulation have opened a new avenue to provide non-invasive, multi-segmental input to modify the motor output of the lumbosacral spinal cord. This study has presented that TSS has the potential to modify the state of the lumbosacral network during stepping. However, an injured spinal cord provides opportunities for more in-depth comparative studies to deduce the nature and scope of changes after SCI.

The study demonstrates that robotic torques and angle cyclograms can be informative for evaluating a patient's progress during gait training. Additionally, we raise the awareness for and establish the impact of Lokomat parameters on gait kinematics and robotic torques, which can enrich the knowledge of rehabilitation progression when used as an assessment tool in research and clinical settings.

Acknowledgments

This study was supported by the Wings for Life Research Foundation (WFL-US-07/19: 199).

References

1. Adams MM, Hicks AL (2005) Spasticity after spinal cord injury. Spinal Cord 43:577–86.
2. Dietz V, Sinkjaer T (2007) Spastic movement disorder: impaired reflex function and altered muscle mechanics. Lancet Neurol 6:725–733.
3. Hofstoetter US, Krenn M, Danner SM, et al (2015) Augmentation of Voluntary Locomotor Activity by Transcutaneous Spinal Cord Stimulation in Motor-Incomplete Spinal Cord-Injured Individuals. Artif Organs 39:E176-86.
4. Mayr W, Krenn M, Dimitrijevic MR (2016) Motor Control of Human Spinal Cord Disconnected from the Brain and Under External Movement. Adv Exp Med Biol 957:159–171.
5. Dimitrijevic MR, Danner SM, Mayr W (2015) Neurocontrol of Movement in Humans With Spinal Cord Injury. Artif Organs 39:823–833.
6. Bellew JW, Allen M, Biefnes A, et al (2018)

Published by Verlag der TU Graz
Graz University of Technology

DOI: 10.3217/978-3-85125-826-4-10

Efficiency of neuromuscular electrical stimulation: A comparison of elicited force and subject tolerance using three electrical waveforms. Physiother Theory Pract 34:551–558.
7. Jezernik S, Colombo G, Keller T, et al (2003) Robotic orthosis lokomat: a rehabilitation and research tool. Neuromodulation 6:108–15.
8. Mayr W, Krenn M, Dimitrijevic MR (2017) Neuroprosthetic Advances. In: Arle JE, Shils JL (eds) Innovative Neuromodulation. Elsevier, pp 209–234

Published by Verlag der TU Graz
Graz University of Technology

Proc. Annual Meeting of the Austrian Society for Biomedical Engineering 2021
DOI: 10.3217/978-3-85125-826-4-11

POLYSYNAPTIC RESPONSE ACTIVITY IS PREFERABLY ENGAGED BY SPINAL CORD STIMULATION WITH REPETITIVE PATTERNS

J.L. Vargas Luna[1], A. Pataraia[2], R. Crevenna[2], W. Mayr[1], M.R. Dimitrijevic[3,4]

[1]Center for Medical Physics and Biomedical Engineering, Medical University of Vienna, Austria

[2]Department of Physical Medicine, Rehabilitation and Occupational Medicine, Medical University of Vienna, Austria

[3]Department of Rehabilitation and Physical Medicine, Baylor College of Medicine, United States

[4]Foundation for Movement Recovery, Norway

joseluis.vargasluna@gmail.com

Abstract— *In the last couple of decades, Spinal Cord Stimulation (SCS), either epidural or transcutaneous, has become a strong research branch in neuromodulation. In an initial effort to understand the mechanisms behind SCS, the monosynaptic reflex loops have been well studied; however, very few studies focus on the polysynaptic responses, which appear after 50ms. Here we study how low repetition continuous stimulation promotes the appearance of such responses as well as basic characteristics of their behaviour. Although limited to a single case, it shows that the versatility of the polysynaptic responses might be a pivotal element to understand how polysynaptic circuitry can be engaged to help the restorative neurological process.*

Keywords—*SCS, monosynaptic reflex, polysynaptic reflex*

Introduction

Spinal Cord Stimulation (SCS) to treat paralysis, either with an epidural or transcutaneous approach, has become a strong research branch in neuromodulation in the last couple of decades. In an initial effort to understand the mechanisms behind SCS, the monosynaptic reflex loops have been well studied; however, very few studies focus on the polysynaptic responses, which appear after 50ms. On the other hand, the application of SCS already as a possible treatment had led to some promising results [1]–[3]. However, these reports remained a limited series of clinical cases, and the generalized application remains limited by the lack of information on how to identify responders from non-responders.

SCS relies on the selective activation of the posterior afferent branches of the spinal roots. After an electrical stimulus, axons in the posterior roots are activated, triggering the reflex circuits in the lumbosacral spinal cord. Multiple reports have helped characterize the output of such a circuit, but most of them have focused on the mono- and oligosynaptic phase only or in evoked EMG-like activity.

This report analyses the posterior root reflex activity at latencies between 50 and 400ms and how they evolve with increasing intensity and repetitive stimulation.

Methods

Low-frequency SCS stimulation was applied in a person with a motor discomplete Spinal Cord Injury (SCI).

SCS was applied non-invasively using a transcutaneous bipolar setup [4]. Briefly, the cathode was placed at the vertebral level T11-T12 and the anode 10cm below. The stimulation pulses consisted of biphasic current-controlled rectangular pulses of 1ms per phase. Stimulation was delivered by a STMISOLA stimulator (Biopac Systems Inc., USA). A custom programmed Labview (National Instruments Inc., USA) interface was used to control the stimulator via a D/A converter module (USB-6221 OEM, National Instruments Inc., USA).

SCS was applied in single pulses and continuous mode. For single pulses, 8s delay was allowed between pulses. Recruitment curves were acquired by a stepwise increase of amplitude, starting from 60mA until 100mA per pulse phase in increments of 5mA. For continuous mode, a rate of 2 pulses per second (pps) was used. In the present case, the maximum intensity applied was 95mA, the individual threshold for perceiving discomfort.

The response of the central nervous system was indirectly monitored via surface electromyography on the lower limb muscle groups. Specifically for this report, left Quadriceps (LQ), Hamstrings (LH) were chosen.

The monosynaptic responses were quantified as the peak-to-peak value (mVpp) of the short-latency re-

Published by Verlag der TU Graz
Graz University of Technology

DOI: 10.3217/978-3-85125-826-4-11

sponse, which appears between 5-50ms post-stimulus.

The polysynaptic responses were identified as bursts of activity higher than the noise level (15µV) that last for at least 3ms. If at least 5ms separated above-threshold activity, then they were considered part of different polysynaptic discharges.

Results

Consistent with other reports, the results show that SCS can elicit monosynaptic responses in all muscles (Fig. 1). These responses have an intensity-dependent amplitude, aligning with the concept that higher intensities synchronously recruit a higher number of afferent nerve fibres. Even at the low stimulation rate used in continuous mode, post-activation depression is already visible in the monosynaptic responses (Fig. 2).

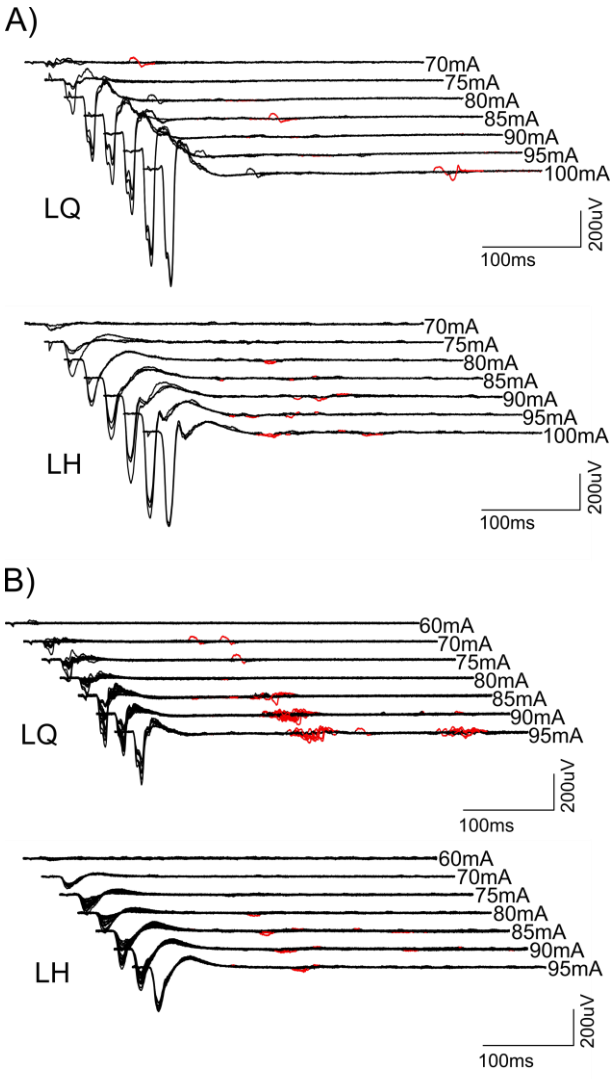

Figure 1: Responses elicited by A) single and B) 2pps repetitive stimulation. Red marks correspond to polysynaptic activity,

Polysynaptic responses are characterized by asynchronous motor unit discharges distributed in tens to hundreds of milliseconds.

Polysynaptic responses were observed mainly at 2pps stimulation and only at LQ and LH. Polysynapic responses had a higher stimulation threshold with 85mA and 80mA for LQ and LH, respectively, in contrast to their monosynaptic threshold of 75mA and 70mA.

On each muscle, the aspect and behaviour of the polysynaptic responses looked different in shape, latency, and duration. On the other hand, within the same muscle, the responses were consistent, at least regarding the latency.

Interestingly, in LQ, a second group of polysynaptic activity started to appear at 90mA and was fully established at 95mA.

Discussion

While intensity has a significant effect on the occurrence of polysynaptic responses, higher stimulation intensity does not necessarily lead to higher response amplitudes; but instead, other complex changes could be observed, like the grouping of spread discharges or triggering spasms-like activity [5].

Here is shown how, on the same subject, single and still low repetitive stimulation with 2pps produced an input to the central nervous system that resulted in entirely different behaviour. Since the electrode configuration and setup remain the same, the only explanation is the role of temporal variables evoked with continuous though slow repetition of stimulation. In this case, we report observations with 2pps only, since it allows us to observe the responses directly. However, it is expected that with higher stimulation rates, where the period between stimuli is shorter than the latency of the polysynaptic responses, the effects would be observed not as direct discharges but as modulation. Thus, while the post-activation depression is well studied and explains observed habituation of the monosynaptic reflexes, the control strategies for polysynaptic responses are still to be studied and understood in more detail.

This case report shows how the rhythmical activation of the same motor pool can facilitate the consistent activation of the polysynaptic circuitry. It also shows how the polysynaptic response amplitude is dependent on the intensity, but not in a linear way. Specifically, it appears that increasing the intensity facilitates the synchronization of all elicited responses. Moreover, the triggering of a completely new group of polysynaptic responses suggests complex interneuron processing, namely since in the presented example,

Published by Verlag der TU Graz
Graz University of Technology

DOI: 10.3217/978-3-85125-826-4-11

it appeared only in one of the four main lower extremity muscle groups.

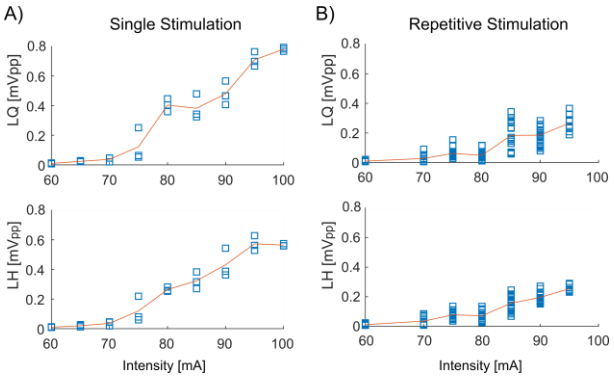

Figure 2: Recruitment curves of the monosynaptic reflexes evoked by A) single and B) 2pps repetitive stimulation. Squares represent the single points and continuous line the average.

Mono- and oligosynaptic reflex loops are essential to characterize the lumbosacral circuits. However, they remain just an artificial response to an unphysiological grouped sensory input, which does not exist in the same form in natural conditions and, therefore per se, are not enough to understand the engagement of deeper polysynaptic circuits involved in the volitional movement.

Further studies on the behaviour of these polysynaptic responses will be necessary to characterize individual functional profiles of spinal cord injury and understand how to gain reliably control over these reflex mechanisms, as well as to understand their role in coordinated interaction between multiple bilateral muscle groups and how to neuromodulate the motor behaviour as a whole, rather than just in limited reflex loops.

References

[1] M. R. Dimitrijevic, Y. Gerasimenko, and M. M. Pinter, “Evidence for a spinal central pattern generator in humans.,” *Ann. N. Y. Acad. Sci.*, vol. 860, pp. 360–76, Nov. 1998.

[2] G. Courtine *et al.*, “Transformation of nonfunctional spinal circuits into functional states after the loss of brain input.,” *Nat. Neurosci.*, vol. 12, no. 10, pp. 1333–1342, 2009.

[3] C. A. Angeli *et al.*, “Recovery of Over-Ground Walking after Chronic Motor Complete Spinal Cord Injury,” *N. Engl. J. Med.*, vol. 379, no. 13, pp. 1244–1250, Sep. 2018.

[4] M. J. Krenn, J. L. Vargas Luna, W. Mayr, and D. S. Stokic, “Bipolar transcutaneous spinal stimulation evokes short-latency reflex responses in human lower limbs alike standard unipolar electrode configuration.,” *J. Neurophysiol.*, vol. 124, no. 4, pp. 1072–1082, Oct. 2020.

[5] J. L. Vargas Luna *et al.*, “Neurophysiology of epidurally evoked spinal cord reflexes in clinically motor-complete posttraumatic spinal cord injury,” *Exp. Brain Res.*, Jul. 2021.

Published by Verlag der TU Graz
Graz University of Technology

Proc. Annual Meeting of the Austrian Society for Biomedical Engineering 2021
DOI: 10.3217/978-3-85125-826-4-12

ELECTRICAL STIMULATION METHODS FOR THE PRECLINICAL TREATMENT OF TBI SEQUELAE – AN OVERVIEW

D. Ziesel[1], M. Nowakowska[2], M. Üçal[2], C. Baumgartner[1], K. Kornmueller[3], S. Scheruebel[3], T. Rienmüller[1]

[1]Institute of Health Care Engineering with European Testing Center of Medical Devices, Graz University of Technology, Austria
[2]Department of Neurosurgery, Medical University of Graz, Austria
[3]Gottfried Schatz Research Center for Cell Signaling, Metabolism and Aging, Biophysics Division, Medical University of Graz, Austria

daniel.ziesel@tugraz.at

Abstract— *Electrical stimulation methods have been used in numerous studies to treat a variety of neurologic disabilities. Traumatic brain injury (TBI) may lead to several different complications, many of which can be treated with electrical stimulation. Only recently, the focus of researchers has shifted more towards preclinical studies to be able to investigate the underlying mechanisms of how these stimulation methods affect nervous tissue in greater detail. This article will give an overview of the most prominent electrical stimulation modalities, namely transcranial magnetic stimulation (TMS), transcranial direct current stimulation (tDCS), deep brain stimulation (DBS) and vagus nerve stimulation (VNS). Some preclinical studies will be highlighted to show the diverse range of possible applications of electrical stimulation for the treatment of TBI sequelae.*

Keywords— *traumatic brain injury, transcranial magnetic stimulation, transcranial direct current stimulation, deep brain stimulation, vagus nerve stimulation*

Introduction

Traumatic brain injury (TBI) may lead to a variety of different diseases and disabilities, ranging from neuropsychiatric changes to motor impairments [1]. Neuropsychiatric sequelae can be subdivided into cognitive disorders, such as attention, memory and executive deficits, and behavioral disorders like personality changes, depression, anxiety and posttraumatic stress disorder [2]. Post-TBI motor impairments include tremor, ataxia, paresis and postural instability [1]. TBI patients are also prone to headaches, dizziness, nausea, fatigue, sleep disturbances and seizures [2].

Over the years, many different therapeutic methods have been proposed to target neuronal damages caused by TBI at various stages post-injury. A modern approach is the stimulation of neurons with the help of electrical currents to mitigate further damage following the initial incident and help restore original function in the affected areas [3]. This article will give a brief overview of the most commonly used methods for electrical stimulation of nervous tissue and different stimulation protocols that can be applied. The aim is to provide a basis for finding new treatment modalities and an incentive to refine stimulation parameters of existing protocols for specific disabilities to achieve better treatment outcomes.

Effects of Electrical Stimulation

Nervous tissue can generate action potentials spontaneously based on the intrinsic properties of the neuronal cell membranes. The excitability of neuronal cells allows for the modulation of their activity through neurostimulation. The resulting activation or inhibition of excitable tissue may serve as an effective therapeutic method in many subfields of neurology, especially in neurotraumatology [4].

The effect of electrical stimulation depends on intrinsic features of the targeted brain tissue. On a neuronal level, it is generally easier to excite an axon than a soma, while myelinated axons are the most excitable part of the cell [3]. In almost all cell areas, except for some types of dendrites [3], action potentials can be elucidated easier with negative currents. Increasing the negative potential of the extracellular space drives depolarization within the neuron, which can ultimately lead to the induction of action potentials. Branching, bending and diameter changes of the axon lead to differences in the site and threshold of the stimulation [3].

Electrical stimulation influences brain electrophysiology on a deeper level through modulation of neuronal signaling. This effect is not only limited to short-term observations, but can also result in the facilitation or attenuation of long-term modifications on a cellular level. Activity-dependent synaptic plasticity may either strengthen or weaken the formation of synapses, which is crucial for post-traumatic regeneration and recovery of high-level cognitive abilities like learning and memory formation [5].

Since TBI may result in a lower threshold to seizures [4], the safety of electrical stimulation needs to be considered. Only very few studies, however, report seizures after stimulation of brain tissue of TBI patients, which may correlate with the severity of the injury [4].

Published by Verlag der TU Graz
Graz University of Technology

DOI: 10.3217/978-3-85125-826-4-12

Stimulation Methods

Transcranial Magnetic Stimulation (TMS)

TMS utilizes magnetic fields to induce electrical currents in cortical tissue with the aim to improve various neurologic conditions. A magnetic coil is positioned tangentially near the surface of the head of a subject, acting as the stimulating device. Discharging a large alternating electric current through the coil leads to a magnetic field perpendicular to the stimulating coil. This magnetic field is able to penetrate the skull and induce secondary electrical currents in the intracranial tissue [6]. Depending on the direction of the induced current, the change in membrane potential may result in the inhibition or excitation of neuronal activity, as well as the elicitation of action potentials when the cell membrane is depolarized above its threshold potential [6].
Since the induced electromagnetic field diminishes greatly over distance through the neuronal tissue, TMS is mainly used to stimulate structures near the surface of the brain such as the neocortex. Some of these structures project axons to deeper regions within the brain, allowing for indirect stimulation of functionally connected regions [7]. Different coil types achieve different penetration depths depending on their geometry, materials, and coil design. Circular coils achieve a higher depth penetration and are used to stimulate larger volumes of neuronal tissue since the entire region below the coil is affected similarly. A figure-of-eight shaped coil, where two circular coils are positioned next to each other with their currents flowing in different directions, allows for more selective stimulation of brain tissue at the cost of stimulation depth. The intersection of the two electromagnetic fields produced by this arrangement is characterized by an increased current density compared to the surrounding regions [6]. TMS can be applied in the form of single or repetitive pulses [8], leading to different treatment outcomes.

Transcranial Direct Current Stimulation (tDCS)

tDCS uses direct current, as opposed to the pulsed protocols of most other stimulation methods, to hyperpolarize or depolarize the membranes of neurons in desired cortical areas [9]. For that, two large pad electrodes are placed on the scalp of the patient near the area of interest and a current of several milliamperes is applied. Thereby, the current density is the decisive factor for the efficacy and localization of the induced stimulus [10]. The resulting excitation or inhibition of neurons can lead to neuromodulation [9].
This stimulation method is painless, noninvasive, and can be used as a treatment for depression and a variety of cognitive dysfunctions, including TBI sequelae [11]. Anodal tDCS increases the excitability of underlying cortical neurons, while cathodal tDCS inhibits neuronal activity [10].

Deep Brain Stimulation (DBS)

DBS involves the implantation of a stimulation electrode into a target brain region so that electrical stimuli can be delivered to specific brain areas. It is commonly used for the treatment of Parkinson's disease, essential tremor, obsessive compulsive disorder and epilepsy in humans [12]. Due to its versatility and accuracy, DBS has potential as a treatment for many different neurological diseases, including sequelae from TBI. The targeted area depends highly on the kind of condition to be treated. Current research focuses on neuromodulation and the neuroprotective effects of DBS, as well as its potential for neurogenesis [13].
DBS systems usually consist of a stimulation electrode that is implanted in the target area and a connected subcutaneous wire that forwards the stimuli from an external pulse generator. Stimulation electrodes are frequently implanted bilaterally and comprise four metal contacts, which can be used both as anodes and cathodes [13]. Bipolar configurations, where an electrical field is generated between two adjacent contacts, allow for a concentrated electric field and higher precision.
The brain area of interest is usually identified with the help of CT and MRI scans, which may also be used to guide the surgeon during implantation. During the procedure, electrical activity is continuously measured through the DBS microelectrodes to determine their relation to the target area and verify the position of the metal contacts. Afterwards, initial stimulation is carried out to confirm the efficacy of the implanted device. [14]

Vagus Nerve Stimulation (VNS)

VNS is an invasive stimulation method that uses a cuff electrode wrapped around the vagus nerve to indirectly stimulate distant brain regions. The United States Food and Drug Administration (FDA) has approved VNS for the treatment of drug-resistant epilepsy and refractory major depressive disorder. Several studies show that it may also be useful in the treatment of TBI sequelae. The exact mechanisms underlying VNS are still not fully understood, but several studies have revealed its potential for neuroprotection, which is achieved through a combination of anti-inflammatory effects, reduction of the permeability of the blood-brain barrier and the modulation of neurotrophins and neurotransmitters [15]. Preclinical research focuses on various applications for VNS and further investigations into its underlying mechanisms. It has been shown that it is able to mitigate TBI sequelae in animal models and is therefore a promising new treatment approach.
Most commonly, the stimulation is delivered to the left cervical vagus nerve [16], which is relatively easy to access through surgical means. Stimulation of the right vagus nerve is usually avoided since it has more projections to the cardiac atria and could therefore

Published by Verlag der TU Graz
Graz University of Technology

DOI: 10.3217/978-3-85125-826-4-12

affect the cardiac rhythm [16]. Helical electrodes, which can have a monopolar, bipolar or tripolar configuration, are implanted and wrapped around the vagus nerve. Monopolar electrodes are comparatively cheap but require an additional ground electrode. Bipolar configurations allow the induced current to flow between the two electrodes, enabling a much greater control of the current path. Tripolar electrodes are more expensive, but this configuration can prevent leakage currents by positioning the stimulating electrode between two common counter-electrodes.

Treatment Outcomes

The stimulation methods mentioned above are under preclinical investigation to treat a variety of conditions directly or indirectly related to TBI. Not just the modality of stimulus delivery, but also the stimulation protocol is of utmost importance to reach the desired outcome. Factors such as stimulation frequency, amplitude and signal shape have different effects on the affected tissue, and finding the optimal parameters is often an iterative process. Additionally, researchers are interested in the time frame of the treatment, which includes the optimal time for the onset of stimulation after TBI and the number of sessions per day, or whether the stimulation delivery is connected to a trigger during behavioral tests. This section highlights some examples of preclinical studies using electrical stimulation to treat TBI sequelae.

In [17], researchers use TMS together with environmental enrichment to facilitate recovery from TBI by increasing cortical excitability and reorganization. Rats are subjected to a controlled cortical impact (CCI) TBI model and stimulated for six days with custom 25 mm figure-eight TMS coils placed above the center of their head between the lambda and bregma. Stimuli are delivered once daily with the following protocol: 7 cycles of 4 s, 26 s interval between stimuli, 10 Hz pulses. After six weeks of behavioral and functional tests, the investigators concluded that the TMS group showed a significant improvement on the beam walk and challenge ladder tests, as well as increased primary somatosensory cortex local field potentials and biceps motor evoked potentials compared to an unstimulated control group.

As an example of a tDCS study, [18] describes a stimulation protocol to decrease impulsivity in a rat TBI model using CCI. Before CCI, the animals were trained on a five-choice serial reaction time task to measure their motor impulsivity and attention. After injury, rats were allowed to recover for 6 weeks before tDCS sessions began. While the rats were anesthetized, two Ag/AgCl hydrogel electrodes were placed on their heads for stimulation, with the cathode in front of the bregma and the anode between the scapulae. tDCS session were carried out daily over a period of 7 days in the form of cathodic stimulation for 10 min with 800 µA, resulting in a current density of 7.08 A/m². Two hours after stimulation, tests were started and the results compared to the post-injury baseline that was acquired after the recovery period. It was found that cathodal tDCS slightly decreased accuracy, but significantly reduced impulsivity in the reaction time task compared to the unstimulated baseline, with the greatest recovery in rats with more severe deficits.

Rajneesh et al. [19] demonstrate the effect of DBS on bladder function of rats with TBI induced by the weight-drop method. Four weeks post-injury, twisted bipolar DBS electrodes were implanted in the pedunculopontine tegmental nucleus (PPTg) of the animals. Thereafter, an initial urodynamic measurement was conducted to evaluate bladder function. Electrode positions were verified with the help of MRI studies. During experiments, the bladder contraction pressure was continuously measured. When it exceeded a given threshold, DBS with a frequency of 50 Hz, a pulse width of 182 µs and varying voltages between 1 and 2.5 V was applied for 10 s to augment bladder contractions. Urodynamic analyses showed that the DBS protocol with 2 V significantly improved the voiding efficiency of TBI rats from 39 to 69 %. They concluded that DBS in the PPTg is an effective treatment for bladder dysfunction.

In [20], the wake-promoting effects of VNS are investigated. Adult rats were subjected to a severe TBI model by free fall drop and their degree of consciousness was observed one hour later. Thereafter, the left vagus nerve was surgically exposed at the cervical level and a VNS electrode wrapped around it. Animals were then stimulated by a VNS protocol with a frequency of 30 Hz, an amplitude of 1 mA and a pulse width of 0.5 ms. Their consciousness was assessed again one hour after stimulation. Six hours after VNS, rats were euthanized and tissue from their prefrontal cortices extracted for further immunohistochemistry and western blot analysis. These findings were compared with observations from unstimulated rats, and the researchers concluded that VNS could promote alertness, with the primary mechanism being the upregulation of excitatory and the downregulation of inhibitory neurotransmitters.

Conclusion

From the examples shown above, it is apparent that electrical stimulation can be used to treat a wide variety of neurological impairments. Although electrical stimulation methods differ greatly in the way the stimuli are delivered, the underlying mechanisms to induce neuronal modulation are often quite similar. Investigating these mechanisms and comparing them between different stimulus delivery modalities could lead to new neurological insights and aid in the discovery of innovative concepts for electrical stimulation. The main objective is to find novel stimulation methods that are less invasive and more precise than current approaches.

Published by Verlag der TU Graz
Graz University of Technology

DOI: 10.3217/978-3-85125-826-4-12

Acknowledgements

This research was funded in whole by the Austrian Science Fund (FWF) [ZK 17].

References

[1] W. C. Walker and T. C. Pickett, “Motor impairment after severe traumatic brain injury: A longitudinal multicenter study,” *J. Rehabil. Res. Dev.*, 2007, doi: 10.1682/JRRD.2006.12.0158.

[2] S. Riggio and M. Wong, “Neurobehavioral sequelae of traumatic brain injury,” *Mt. Sinai J. Med.*, vol. 76, no. 2, pp. 163–172, 2009, doi: 10.1002/msj.20097.

[3] F. Rattay, “The basic mechanism for the electrical stimulation of the nervous system,” *Neuroscience*, vol. 89, no. 2, pp. 335–346, Mar. 1999, doi: 10.1016/S0306-4522(98)00330-3.

[4] E. Clayton, S. K. Kinley-Cooper, R. A. Weber, and D. L. Adkins, “Brain stimulation: Neuromodulation as a potential treatment for motor recovery following traumatic brain injury,” *Brain Research*. 2016, doi: 10.1016/j.brainres.2016.01.056.

[5] B. C. Albensi and D. Janigro, “Traumatic brain injury and its effects on synaptic plasticity,” *Brain Injury*, vol. 17, no. 8. Taylor and Francis Ltd., pp. 653–663, 01-Aug-2003, doi: 10.1080/0269905031000107142.

[6] S. Groppa *et al.*, “A practical guide to diagnostic transcranial magnetic stimulation: Report of an IFCN committee,” *Clinical Neurophysiology*. 2012, doi: 10.1016/j.clinph.2012.01.010.

[7] M. F. Villamar, A. Santos Portilla, F. Fregni, and R. Zafonte, “Noninvasive brain stimulation to modulate neuroplasticity in traumatic brain injury,” *Neuromodulation*, vol. 15, no. 4, pp. 326–337, Jul. 2012, doi: 10.1111/j.1525-1403.2012.00474.x.

[8] W. Klomjai, R. Katz, and A. Lackmy-Vallée, “Basic principles of transcranial magnetic stimulation (TMS) and repetitive TMS (rTMS),” *Annals of Physical and Rehabilitation Medicine*. 2015, doi: 10.1016/j.rehab.2015.05.005.

[9] A. R. Brunoni *et al.*, “Clinical research with transcranial direct current stimulation (tDCS): Challenges and future directions,” *Brain Stimulation*, vol. 5, no. 3. pp. 175–195, 2012, doi: 10.1016/j.brs.2011.03.002.

[10] S. Wiethoff, M. Hamada, and J. C. Rothwell, “Variability in response to transcranial direct current stimulation of the motor cortex,” *Brain Stimul.*, vol. 7, no. 3, pp. 468–475, 2014, doi: 10.1016/j.brs.2014.02.003.

[11] M. J. Begemann, B. A. Brand, B. C¨určić-Blake, A. Aleman, and I. E. Sommer, “Efficacy of non-invasive brain stimulation on cognitive functioning in brain disorders: A meta-Analysis,” *Psychological Medicine*, vol. 50, no. 15. Cambridge University Press, pp. 2465–2486, 01-Nov-2020, doi: 10.1017/S0033291720003670.

[12] I. S. Khan, E. N. D’Agostino, D. R. Calnan, J. E. Lee, and J. P. Aronson, “Deep Brain Stimulation for Memory Modulation: A New Frontier,” *World Neurosurgery*. 2019, doi: 10.1016/j.wneu.2018.12.184.

[13] T. M. Herrington, J. J. Cheng, and E. N. Eskandar, “Mechanisms of deep brain stimulation,” *Journal of Neurophysiology*, vol. 115, no. 1. American Physiological Society, pp. 19–38, 08-Jan-2016, doi: 10.1152/jn.00281.2015.

[14] C. O. Oluigbo, A. Salma, and A. R. Rezai, “Deep brain stimulation for neurological disorders,” *IEEE Rev. Biomed. Eng.*, 2012, doi: 10.1109/RBME.2012.2197745.

[15] Y. Wang *et al.*, “Vagus nerve stimulation in brain diseases: Therapeutic applications and biological mechanisms,” *Neurosci. Biobehav. Rev.*, vol. 127, pp. 37–53, 2021, doi: 10.1016/j.neubiorev.2021.04.018.

[16] C. M. Noller, Y. A. Levine, T. M. Urakov, J. P. Aronson, and M. S. Nash, “Vagus Nerve Stimulation in Rodent Models: An Overview of Technical Considerations,” *Frontiers in Neuroscience*, vol. 13. Frontiers Media S.A., 04-Sep-2019, doi: 10.3389/fnins.2019.00911.

[17] S. S. Shin *et al.*, “Transcranial magnetic stimulation and environmental enrichment enhances cortical excitability and functional outcomes after traumatic brain injury,” *Brain Stimul.*, vol. 11, no. 6, pp. 1306–1313, Nov. 2018, doi: 10.1016/j.brs.2018.07.050.

[18] K. M. Martens, K. M. Pechacek, C. G. Modrak, V. J. Milleson, B. Zhu, and C. Vonder Haar, “Cathodal Transcranial Direct-Current Stimulation Selectively Decreases Impulsivity after Traumatic Brain Injury in Rats,” *J. Neurotrauma*, vol. 36, no. 19, pp. 2827–2830, Oct. 2019, doi: 10.1089/neu.2019.6470.

[19] C. P. Rajneesh, J. C. Liou, T. H. Hsieh, H. Y. Chin, and C. W. Peng, “Efficacy of deep brain stimulation on the improvement of the bladder functions in traumatic brain injured rats,” *Brain Sci.*, vol. 10, no. 11, pp. 1–13, Nov. 2020, doi: 10.3390/brainsci10110850.

[20] X. Dong, E. Papa, H. Liu, Z. Feng, F. Huang, and C. Liao, “Vagus nerve stimulation causes wake-promotion by affecting neurotransmitters via orexins pathway in traumatic brain injury induced comatose rats,” 2018.

Published by Verlag der TU Graz
Graz University of Technology

Proc. Annual Meeting of the Austrian Society for Biomedical Engineering 2021
DOI: 10.3217/978-3-85125-826-4-13

ANALYSIS OF SOMATOSENSORY EVOKED POTENTIALS AFTER NON-INVASIVE ELECTROCUTANEOUS STIMULATION OF FOOT AND THIGH

V. Mondini[1*], P. Tumfart[1*], G.R. Müller-Putz[1]

[1]Institute of Neural Engineering, Graz University of Technology, Graz, Austria

[*]These authors contributed equally.

E-mail: gernot.mueller@tugraz.at

Abstract *— Following major amputations and the consequent truncation of nerves, up to 45-85% of patients are left with a neuropathic pain condition known as phantom limb pain (PLP). Recent research has shown that the addition of somatosensory feedback to daily use prostheses has the potential to alleviate the phenomenon of PLP, as long as a natural sensation, "as if" it was coming from the missing limb, is restored. One approach to evaluating how natural a sensation is perceived, is by studying the neural correlates of somatosensory stimulation, known as somatosensory evoked potentials (SEPs). Source localization techniques such as dipole modeling may be used to reconstruct the neural sources of SEPs, thus mapping the origin of each sensation within the somatosensory homunculus. Source localization of SEPs has already been demonstrated to discriminate stimulations in the upper-limb/mouth corners and between left/right side of the body, however, no evidence so far is present for the lower limb and same body side. In this work, the discriminability of SEPs relative to foot vs. thigh stimulations on the same body side is being studied. The spatiotemporal evolution of SEPs is analyzed, and preliminary source localization results are presented.*

Keywords*— Electroencephalography (EEG), somatosensory evoked potentials (SEP), source localization, dipole fitting, phantom limb pain*

Introduction

Following major amputations and consequent truncation of nerves, up to 45-85% of patients experience a chronic neuropathic pain known as phantom limb pain (PLP) [1]. Among the identified causes of PLP, there is the loss of sensory input from the missing (i.e. phantom) limb [1]. A consistent body of literature suggests that somatosensory feedback has the potential not only to improve the functional performance of prostheses [2] and to enhance the sense of embodiment [3], but also to reduce phantom limb pain [4]–[6].

Somatosensory feedback can be given through both invasive and non-invasive techniques [7], such as the (invasive) electrical stimulation of the peripheral nerves with implanted electrodes [4], [5], the (non-invasive) electrocutaneous stimulation of the sensory nerves [3], or the non-invasive mechanical stimulations such as vibrotactile stimulation on the stump [8], with the aim being, in all cases, to restore a sensation as natural as possible, as if it was coming from the missing limb.

One of the main limitations when studying somatosensory feedback is the lack of objective evaluation methods, i.e., the findings are usually indirect and mostly based upon the patients' perceptions. One opportunity for objectification may come from quantitative neurophysiological recordings such as electroencephalography (EEG), i.e., the non-invasive recording of the brain's electrophysiological activity using a set of electrodes placed on the scalp.

When a somatosensory stimulus is applied, e.g., with electrical or vibrotactile stimulation, the EEG can capture the corresponding neural response known as somatosensory evoked potential (SEP) [9]. EEG source localization techniques such as dipole modeling (as in [10]) may then be used to reconstruct the 3-dimensional sources of neural activity related to the SEP, and therefore give information on where the sensation is mapped and felt.

Being able to discriminate the stimuli at more proximal or distal areas of the same limb, would give us insights into the efficacy of a prosthesis wishing to restore a sensation from the amputated limb; by mapping indeed the stimulation with respect to the somatosensory homunculus [11], it would be possible to assess whether a realistic sensation from the missing limb is restored.

The efficacy of SEPs source localization to discriminate stimuli applied to the fingers or mouth corners, and between left and right side of the body, has already been demonstrated [12]–[14]; however, whether and to which extent it is possible to discriminate stimuli in the lower limb, and on the same side of the body, has not yet been explored.

In this work, the neural correlates and mapping of somatosensory stimuli elicited in the foot vs. thigh area of the same leg are being studied. Given the exploratory nature of the study, a cohort of healthy participants is enrolled.

Methods

Participants and experimental paradigm: Twenty healthy volunteers (ten females and ten males), aged 28.43 ± 9.7 years (mean ± std), took part in the study which was approved by the local ethical committee from Medical University Graz. All participants had right leg dominance, as assessed by the Waterloo

Published by Verlag der TU Graz
Graz University of Technology

DOI: 10.3217/978-3-85125-826-4-13

Footedness Questionnaire Revised test (WFQ-R) [15]. The data from one participant were excluded due to technical problems.
The experiment was organized into three blocks, of which two stimulation blocks (for the foot and the thigh area) and one final resting block.
In each stimulation block, 500 biphasic, single-pulse, square electrical current pulses of 300us were delivered every 1.5-2s, through a certified functional electrical stimulation device (Motionstim 8, Medel, Hamburg). Breaks of 3 to 4.5 seconds were inserted every four stimulations, and a fixation cross was displayed in front of the participants to avoid blinks and saccadic eye movements. The electrical stimuli were delivered through a pair of round, 3.2cm electrodes (Axelgaard Manufacturing Co., Ltd., Fallbrook, USA) applied to the skin surface (Figure 1a-b).
For the foot area, the electrodes were placed behind the malleolus, so to target the *suralis* nerve (Figure 1b-c). For the thigh area, the electrodes were placed above the knee (Figure 1a), so to target the *sciatic* nerve (Figure 1c).

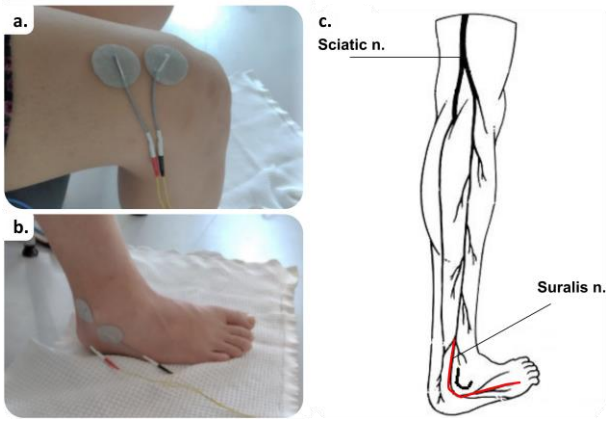

Figure1. Stimulation sites in the thigh (a) and foot (b) area, targeting the *sciatic* and *suralis* nerve (c).

The stimulation intensity was tailored to each participant, so as to elicit a clear but tolerable sensation (sensory threshold) but no muscle twitch. We defined the stimulation intensity in the foot area, and then kept the same for the thigh area. The applied current was 11.48 ± 2.58 mA (mean ± standard deviation). All stimulations were delivered on the right leg.
The order of stimulation blocks (foot or thigh) was randomized across participants. Each stimulation block lasted for approximately ~20mins, while a final resting block collected approximately 200s of resting-state EEG.

Data recording: We collected the 64 channel EEG signal at 512Hz with an eego™ sports amplifier and a waveguard™ electrode cap (ANT Neuro, Hengelo, Netherlands). Reference and ground electrodes were CPz and FPz, respectively. We digitized the exact positions of EEG electrodes with an ultrasonic position-measuring device (ELPOS, Zebris Medical GmbH, Germany).

Data analysis: We analyzed the EEG signals using Matlab (Mathworks Inc., Natick, USA) and EEGLAB (Swartz Center for Computational Neuroscience, La Jolla, USA), with a similar pipeline as in previous work from our group [10]. The raw EEG was zero-phase bandpass filtered between 0.5 and 100Hz (with a 10^{th} order Butterworth), the bad channels were interpolated, and the data were re-referenced to their common average (CAR). The continuous EEG was epoched [-0.2 0.5]s with respect to the stimulus onsets, and the trials with an abnormal probability distribution (based on standard deviation and kurtosis) were rejected. An independent component analysis (ICA) [16] was used to separate the data into components (IC) that are maximally statistically independent. The ICs were used to fit source dipoles in the brain (with the DIPFIT toolbox [17]), and only the ICs explaining more than 90% of the variance of their scalp projection, were considered for further analysis. The remaining ICs were additionally visually inspected, and the ones related to artifacts (e.g. eye movement, or electrical noise) were excluded from further analysis. Reconstruction of the signal with the so-selected IC components and mixing matrix, led us to obtain the clean EEG data. The epoched and clean data were finally split into the two stimulation conditions, i.e. foot vs. thigh stimulation.
The relevant SEP components were isolated by further epoching of the data between [0 115]ms with respect to the stimulus onset [12]–[14]. An additional ICA was finally run for each stimulation condition, and the resulting IC components were used to fit the equivalent current dipoles. All fitted dipoles were visually inspected, and the ones lying in the sensorimotor areas were identified as corresponding to the SEPs. For each participant, only one dipole for each SEP was identified. For visualization purposes, the x/y/z coordinates of the dipoles were averaged across participants. A Wilcoxon signed-rank test was used to evaluate statistical differences in the x/y/z position distributions of the foot vs thigh.
The spatiotemporal distribution of SEP components of foot vs. thigh was further inspected. A Wilcoxon rank-sum test was used to reveal statistical differences in signal amplitudes, for each electrode and time-point, between the foot and thigh stimulations. A post-hoc Bonferroni correction was applied to the significance level, to control for the type I error.

Results

Spatiotemporal evolution of SEPs:
The temporal evolution of the SEP at a selected location (Cz) is depicted in Figure 2, showing the grand-averaged amplitude of the EEG signal, in both foot and thigh stimulation conditions, with respect to the stimulus onset. Statistically significant differences between the two stimulation conditions (alpha=0.01, Bonferroni corrected) were revealed in the first [0 110]ms after stimulus onset. Within this period, both foot and thigh SEPs share the same shape (i.e.,

Published by Verlag der TU Graz
Graz University of Technology

DOI: 10.3217/978-3-85125-826-4-13

sequence of positive and negative deflections), but with a delay of ~10ms for the foot with respect to the thigh stimulation condition. For example, while the larger negative component peaks at ~95ms for the thigh, it peaks at ~105ms for the foot.

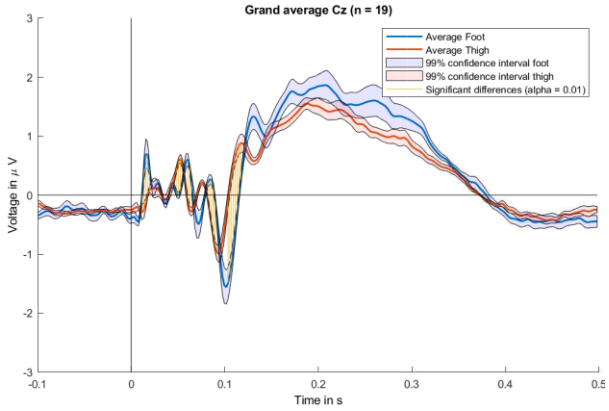

Figure 2: Grand-average amplitude of the EEG signal at location Cz, for both stimulation conditions, with respect to the stimulus onset. The variability among subjects is displayed in the confidence intervals (alpha=0.01). The time-points with statistically different SEP responses (alpha=0.01, Bonferroni corrected) are highlighted in yellow.

The spatiotemporal evolution of the SEPs for both stimulations is also displayed in Figure 3, showing the topographical representation of average scalp potential, at different time points after the stimulus onset. A small positivity at 55ms in the central electrodes, followed by a negativity at 95ms, can be seen for the thigh stimulation condition (upper row). A similar positivity at 65ms, followed by a negativity at 105ms, is visible in the foot stimulation condition (middle row). When contrasting the two conditions (lower row), it appears that the SEP components for the thigh are more frontally located than the foot.

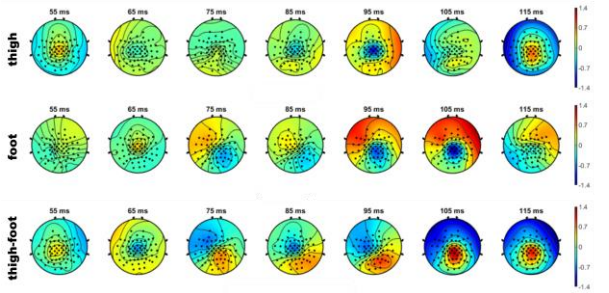

Figure 3: Topographical representations of average scalp potentials for the thigh (upper row), foot (middle row) and difference thigh-foot (lower panel), at selected time points with respect to the stimulus onset.

Source localization: The results of source localization, i.e., the estimated positions for the foot vs. thigh dipoles, averaged across participants, are depicted in Figure 4. The average difference in (x,y,z) position between foot and thigh was (-0.05, 7.8, 1.8) arbitrary units. No statistical difference in the (x,y,z) coordinates distributions between foot and thigh was found, however, a tendency (p-value = 0.08) of the foot component being located more frontally than the thigh component was highlighted.

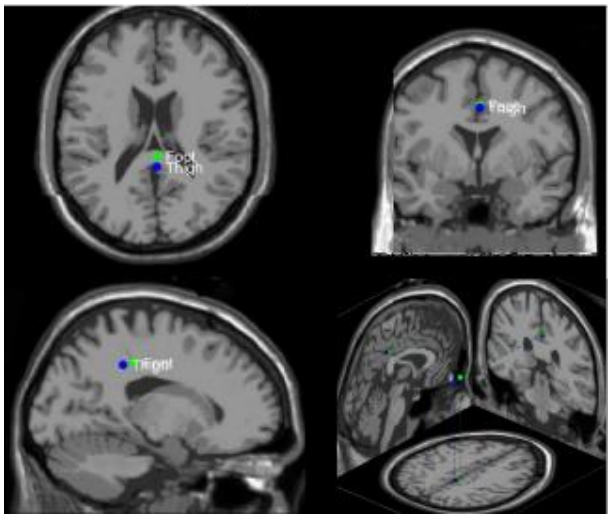

Figure 4. Estimated positions for the foot vs. thigh dipoles, averaged across participants.

Discussion

In this study, we investigated whether and to which extent the neural correlates of somatosensory stimulations applied to more proximal and distal areas of the lower limb, could be discriminated.
To do so, we analyzed the spatiotemporal evolution of somatosensory evoked potentials (SEPs) elicited by non-invasive electrocutaneous stimulation of foot vs thigh area, and additionally projected the SEPs to source space, to identify their cortical origin.
When looking at the SEPs in the time domain we could observe that, despite sharing a similar shape, the responses to stimulations in the foot vs. thigh were delayed from each other by approximately ~10ms. A delayed response coming from the foot area with respect to the thigh area can be easily explained, if considering the more distal location, and therefore longer distance to be traveled in the ascending sensory pathways, with respect to the collection point.
When looking at the spatiotemporal evolution of the SEPs, we could also find differences between foot and thigh stimulations, with the thigh SEP components being more frontally located than the foot SEP components.
When finally projecting the SEPs to source space, we could observe a tendency for the foot dipoles to be estimated more anteriorly with respect to the thigh dipoles; however, due to the dispersion of data, the difference was not significant. One approach to improve the localization of dipoles could be to increase the number of stimuli per condition. While indeed, in literature, typically 500 to 1000 stimulations are delivered [12]–[14], using only 500 stimuli per condition,

Published by Verlag der TU Graz
Graz University of Technology

DOI: 10.3217/978-3-85125-826-4-13

and further reducing this number when cleaning the data and rejecting artifactual trials, might not be sufficient to achieve the desired signal-to-noise. A second aspect that might have affected our recordings, is the potential presence of cross-talk between the foot and thigh stimulation condition, and so the effect of different stimulation setups could be explored in the future. As a final way to improve the reliability of source localization, the subject-specific anatomical data from MRI scans could be incorporated.
Altogether, this study could show that somatosensory stimulations even at proximal and distal locations of the same leg, produce SEPs with distinct spatiotemporal evolutions. Additional preliminary results for projecting the SEPs to source space are encouraging, however, further investigation needs to be carried out to improve the reliability of the technique.

Acknowledgments

This research was supported by funding from Saphenus Medical Technology GmbH in the project “Evoked”.

References

[1] D. P. Kuffler, ‘Origins of Phantom Limb Pain’, *Mol. Neurobiol.*, vol. 55, no. 1, pp. 60–69, 2018, doi: 10.1007/s12035-017-0717-x.

[2] D. Rusaw, K. Hagberg, L. Nolan, and N. Ramstrand, ‘Can vibratory feedback be used to improve postural stability in persons with transtibial limb loss?’, *J. Rehabil. Res. Dev.*, vol. 49, no. 8, pp. 1239–1254, 2012.

[3] M. R. Mulvey, H. J. Fawkner, H. E. Radford, and M. I. Johnson, ‘Perceptual embodiment of prosthetic limbs by transcutaneous electrical nerve stimulation’, *Neuromodulation Technol. Neural Interface*, vol. 15, no. 1, pp. 42–47, 2012.

[4] P. M. Rossini *et al.*, ‘Double nerve intraneural interface implant on a human amputee for robotic hand control’, *Clin. Neurophysiol.*, vol. 121, no. 5, pp. 777–783, 2010.

[5] D. W. Tan, M. A. Schiefer, M. W. Keith, J. R. Anderson, J. Tyler, and D. J. Tyler, ‘A neural interface provides long-term stable natural touch perception’, *Sci. Transl. Med.*, vol. 6, no. 257, pp. 257ra138-257ra138, 2014.

[6] C. Dietrich *et al.*, ‘Sensory feedback prosthesis reduces phantom limb pain: Proof of a principle’, *Neurosci. Lett.*, vol. 507, no. 2, pp. 97–100, Jan. 2012, doi: 10.1016/j.neulet.2011.10.068.

[7] C. Antfolk, M. D’Alonzo, B. Rosén, G. Lundborg, F. Sebelius, and C. Cipriani, ‘Sensory feedback in upper limb prosthetics’, *Expert Rev. Med. Devices*, vol. 10, no. 1, pp. 45–54, Jan. 2013, doi: 10.1586/erd.12.68.

[8] P. D. Marasco, K. Kim, J. E. Colgate, M. A. Peshkin, and T. A. Kuiken, ‘Robotic touch shifts perception of embodiment to a prosthesis in targeted reinnervation amputees’, *Brain*, vol. 134, no. 3, pp. 747–758, 2011.

[9] A. Macerollo, M. J. Brown, J. M. Kilner, and R. Chen, ‘Neurophysiological changes measured using somatosensory evoked potentials’, *Trends Neurosci.*, vol. 41, no. 5, pp. 294–310, 2018.

[10] J. Wagner, T. Solis-Escalante, P. Grieshofer, C. Neuper, G. Müller-Putz, and R. Scherer, ‘Level of participation in robotic-assisted treadmill walking modulates midline sensorimotor EEG rhythms in able-bodied subjects’, *NeuroImage*, vol. 63, no. 3, pp. 1203–1211, Nov. 2012, doi: 10.1016/j.neuroimage.2012.08.019.

[11] W. Penfield and E. Boldrey, ‘Somatic motor and sensory representation in the cerebral cortex of man as studied by electrical stimulation.’, *Brain J. Neurol.*, 1937.

[12] M. Schaefer, W. Mühlnickel, S. M. Grüsser, and H. Flor, ‘Reliability and Validity of Neuroelectric Source Imaging in Primary Somatosensory Cortex of Human Upper Limb Amputees’, *Brain Topogr.*, vol. 15, no. 2, pp. 95–106, Dec. 2002, doi: 10.1023/A:1021468423831.

[13] Y. Lyu, X. Guo, Z. Wang, and S. Tong, ‘Resting-state EEG network change in alpha and beta bands after upper limb amputation’, in *2016 38th Annual International Conference of the IEEE Engineering in Medicine and Biology Society (EMBC)*, 2016, pp. 49–52.

[14] P. Montoya *et al.*, ‘The cortical somatotopic map and phantom phenomena in subjects with congenital limb atrophy and traumatic amputees with phantom limb pain’, *Eur. J. Neurosci.*, vol. 10, no. 3, pp. 1095–1102, 1998, doi: 10.1046/j.1460-9568.1998.00122.x.

[15] L. J. Elias, M. P. Bryden, and M. B. Bulman-Fleming, ‘Footedness is a better predictor than is handedness of emotional lateralization’, *Neuropsychologia*, vol. 36, no. 1, pp. 37–43, 1998.

[16] A. Delorme and S. Makeig, ‘EEGLAB: an open source toolbox for analysis of single-trial EEG dynamics including independent component analysis’, *J. Neurosci. Methods*, vol. 134, no. 1, pp. 9–21, Mar. 2004, doi: 10.1016/j.jneumeth.2003.10.009.

[17] A. Delorme, J. Palmer, J. Onton, R. Oostenveld, and S. Makeig, ‘Independent EEG Sources Are Dipolar’, *PLOS ONE*, vol. 7, no. 2, p. e30135, Feb. 2012, doi: 10.1371/journal.pone.0030135.

Published by Verlag der TU Graz
Graz University of Technology

Proc. Annual Meeting of the Austrian Society for Biomedical Engineering 2021
DOI: 10.3217/978-3-85125-826-4-14

MODEL-BASED RECONSTRUCTION FOR MULTI-FIELD T_1 QUANTIFICATION

O. Maier[1], M. Bödenler[1,2], L.M. Broche[3], H. Scharfetter[1], R. Stollberger[1,4]

[1]Institute of Medical Engineering, Graz University of Technology, Austria
[2]Institute of eHealth, University of Applied Sciences FH JOANNEUM, Graz, Austria
[3]Aberdeen Biomedical Imaging Centre, University of Aberdeen, Aberdeen, UK
[4]BioTechMed-Graz, Austria

oliver.maier@tugraz.at

Abstract

The recent introduction of in-vivo field cycling MRI systems enables the exploration of new contrast mechanics at different field strength. The present work explores changes in T_1 for main magnetic field from 200 mT down to 2 mT. The problem of inherent low SNR with such low fields is overcome by using a joint regularization approach in space and exploiting shared information between different parameter maps. This strategy enables preservation of fine details while effectively suppressing noise in the reconstructed T_1 maps. Especially in-vivo data showed huge improvements of visual quality compared to reference methods.

Keywords *fast field-cycling, MRI, multi-field T_1 quantification, ultra-low field imaging*

Introduction

Fast field cycling (FFC) MRI is a technique that allows the modulation of the main magnetic field during an imaging experiment and thus gives access to new, unexploited contrast mechanisms [1]. Recent work on MR hardware enabled the construction of the first whole-body FFC system with fields ranging from 50 µT to 200 mT [2]. The ramping of the main magnetic field can be utilized to explore the field dependency of the longitudinal (T_1) and transverse relaxation (T_2) times, also referred to as Nuclear Magnetic Relaxation Dispersion (NMRD) [3]. The controlled change of the main field allows to quantify these relaxation time constants at various field strengths. Especially T_1 shows promising potential for imaging with novel contrast in region affected by a stroke [2]. However, the small fields lead to a decreased SNR [4] which complicates evaluation and quantification of the results.

In the context of quantitative MRI in high field applications, model-based reconstruction was proven to improve SNR in the final parameter maps while simultaneously preserving quantitative accuracy [5,6,7]. Dedicated regularization functionals can exploit spatial similarity between neighboring pixels to stabilize the fitting procedure. Further, features in individual parameter maps, such as tissue boundaries, can be assumed to correlate well throughout all unknown parameter maps. To this end, we propose to incorporate the T_1 quantification process for multi-field FFC imaging in a model-based reconstruction framework [8]. Specifically, the redundancies between T_1 maps from multiple fields will be exploited by means of a total generalized variation (TGV) functional [9] in conjunction with a Frobenius norm. This type of regularization promotes spatially smooth structures but also allows for discontinuities, i.e., edges between tissue, leading to an overall improved image impression and avoids the known stair casing artifacts from total variation. The proposed approach is compared to standard non-linear fitting techniques on simulated numerical data and in-vivo stroke patients.

Theory

The MRI signal for an inversion-recovery FFC sequence [10] can be described by

$$M_z\left(t^{evo}\right)=\left[-\alpha M_0 - M_0^E\right] e^{\frac{-t^{evo}}{T_1^E}} + M_0^E, \quad (1)$$

with $M_z\left(t^{evo}\right)$ being the signal after an evolution time t^{evo}. M_0 refers to the equilibrium magnetization for the detection field and M_0^E refers to the magnetization at the evolution field. α accounts for imperfections of the inversion pulse, incomplete polarization, and field ramping effects [11]. A schematic sequence diagram is given in Fig. 1.

Introducing a proportionality constant C to relate evolution B_0 field and detection field B_0^E with the corresponding magnetization, one ends up with

$$S(u) = \mathcal{F}\left\{C\left[-\alpha B_0 e^{\frac{-t^{evo}}{T_1^E}} + B_0^E\left(1 - e^{\frac{-t^{evo}}{T_1^E}}\right)\right]\right\}. \quad (2)$$

This equation is valid for one evolution time and field strength and incorporates the sampling and Fourier transformation operator $\mathcal{F}$. The signal equation resembles the well known behavior of the

Published by Verlag der TU Graz
Graz University of Technology

DOI: 10.3217/978-3-85125-826-4-14

inversion recovery sequence but relaxation takes place at the evolution field B_0^E. The unknowns u consist of C, α^E, and T_1^E and are identified from measurement data d using a regularized non-linear least squares problem given by

$$\min_{u,v} \quad \frac{1}{2}\|S(u) - d\|_2^2 + \gamma(\beta_0\|\nabla u - v\|_{1,2,F} + \beta_1\|\|\mathcal{E}v\|_{1,2,F}) \tag{3}$$

The regularization parameter γ is used to balance between data and a prior knowledge. The terms in bracket after the regularization parameter reflect the TGV Frobenius functional, with v being an auxiliary variable, enabling a weighting between first and higher order derivatives. The ratio of parameters β_0/β_1 balances the optimization costs between first and second derivatives, respectively, and is chosen as $1/2$. The derivatives a realized via finite differences for the gradient ∇ and symmetrized gradient $\mathcal{E}$. The optimization itself is carried using PyQMRI, a recently proposed Python toolbox for quantitative MRI [8]. Regularization parameter γ is chosen based on visual inspection of the results.

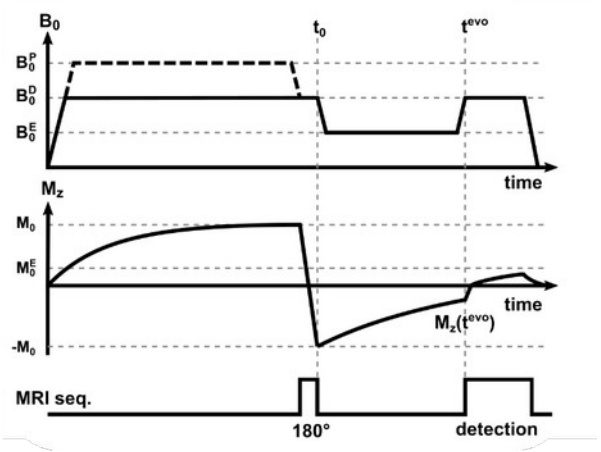

Figure 1: Exemplary sequence diagram for an inversion recovery FFC acquisition. After the inversion pulse, the main magnetic field is ramped to the evolution field where relaxation takes place. Prior to data acquisition the field is ramped back.

Methods

Numerical brain phantoms were simulated using eq. (2) and three simulated field strengths. Simulated evolution times and T_1 values were chosen similar to expected in-vivo values. Image resolution was chosen as 128x128 pixels, similar to the resolution of the acquired stroke images. To account for in-vivo SNR levels, complex Gaussian noise was added to the simulated data to achieve an SNR of 8.3 in white matter and 16.7 in gray matter, directly after inversion. The simulated ground truth is given in the top of Fig. 2.

Acquired stroke images are part of an ongoing study at University of Aberdeen and were acquired using an inversion-recovery spin-echo FFC sequence with a 128x128 matrix and at 3 field strengths. The proposed method is applied to an exemplary data set of this study to show its applicability for in-vivo applications.

The reference methods consisted of non-linear fitting for each field separate with Tikhonov regularization, a field-combined approach with Tikhonov regularization and a field-combined method using H1 regularization, i.e., penalizing the 2-norm of the gradient of the parameter maps [12].

Results

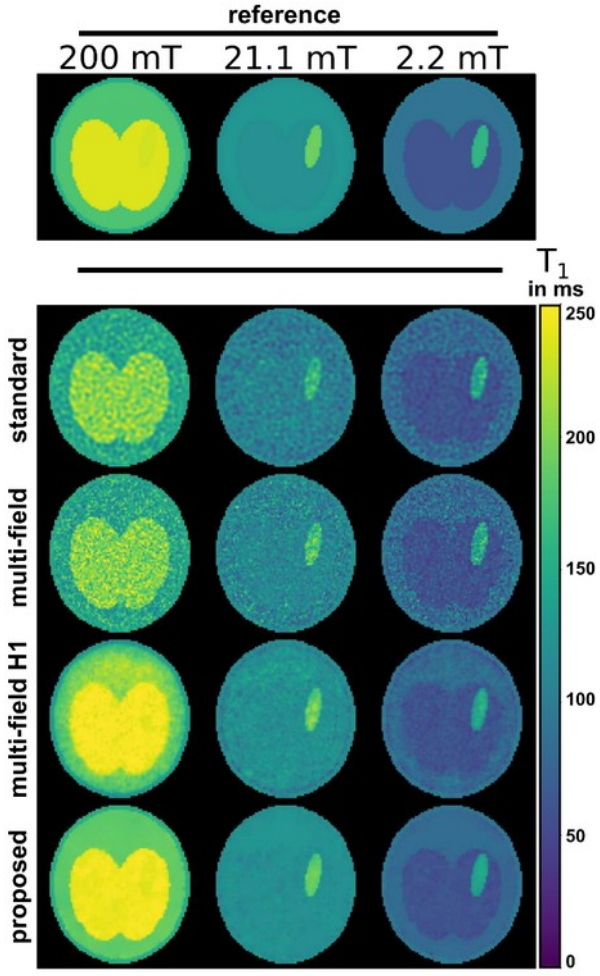

Figure 2: Ground truth phantom T_1 maps and reconstruction results using different fitting algorithms. The proposed method is visually closest to the reference.

Published by Verlag der TU Graz
Graz University of Technology

DOI: 10.3217/978-3-85125-826-4-14

Numerical simulations, given in Fig. 2, show the reduced noise using spatial regularization compared to Tikhonov based methods. Further, edges are best preserved using the proposed approach. Quantitative evaluation (Fig. 3) shows good accordance to the ground truth values. The proposed method shows least residual noise and best relative absolute difference for low field strength. At 200 mT a small bias to the ground truth can be observed.

Application to in-vivo measurements show a similar picture (Fig. 4). Standard methods without spatial regularization show poor SNR which might even hide the lesion. Both spatially regularized approaches are able to recover high quality T1 maps, enabling a clear delineation of the stroke. The proposed approach shows the best suppression of noise while maintaining sharp edges between different tissue.

Discussion

This work demonstrates that spatial regularization in combination with fitting all data in a combined fashion can hugely improve the quality of T_1 maps obtained from multiple fields using FFC imaging techniques. The best results could be achieved using the proposed TGV-Frobenius prior, preserving sharp edges and effectively suppressing noise.

The improved noise suppression could be achieved by leveraging spatial information in combination with redundant information at different field strength. A limitation of such an approach might be the possibility of cross contamination from one map to the other. Although such an effect is theoretically possible, it could not be observed in practice [13, 14]. Still, care should be taken when choosing the regularization parameters as too much regularization might introduce such effects.

As the proposed method is posed as reconstruction problem from k-space, it could further be leveraged to reduce the acquisition time of the measurement, enabling either faster scanning or the acquisition of multiple additional fields in the same scan time.

Especially in-vivo applications benefit from the proposed fitting approach, showing a vast improvement in image quality. This improvement of image quality enables the exploration of the underlying contrast mechanics and is subject of an ongoing study at the University of Aberdeen. The proposed method is freely available at: https://github.com/IMTtugraz/PyQMRI

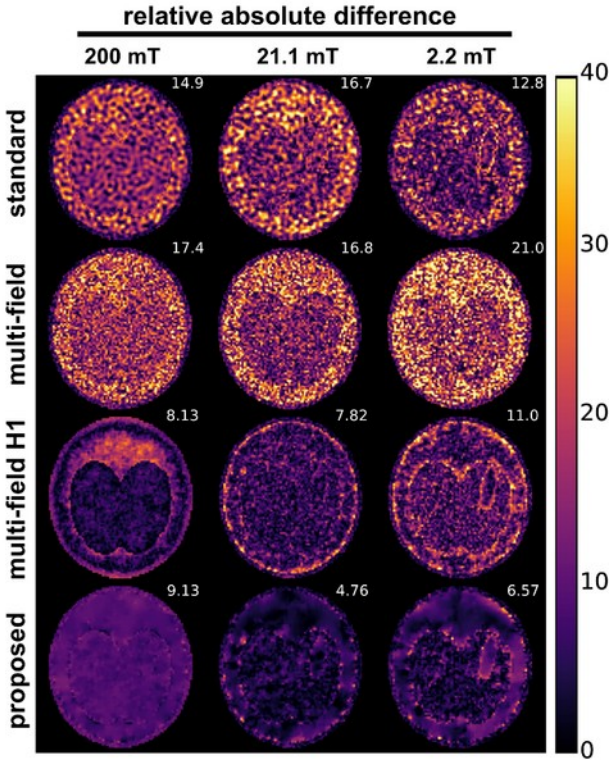

Figure 3: Relative absolute difference to the ground truth for the used fitting algorithms. Mean difference within the object is given in the top right corner of each map. The proposed method shows improved edge preservation and noise suppression, especially for maps at lower field strength.

Acknowledgements

This article is based upon work from COST Action CA15209, supported by COST (European Cooperation in Science and Technology). Oliver Maier is a Recipient of a DOC Fellowship (24966) of the Austrian Academy of Sciences at the Institute of Medical Engineering at TU Graz. The authors would like to acknowledge the NVIDIA Corporation Hardware grant support. The authors would like to thank Dr. Mary-Joan Macleod for data acquisition and patient recruitment.

Published by Verlag der TU Graz
Graz University of Technology

DOI: 10.3217/978-3-85125-826-4-14

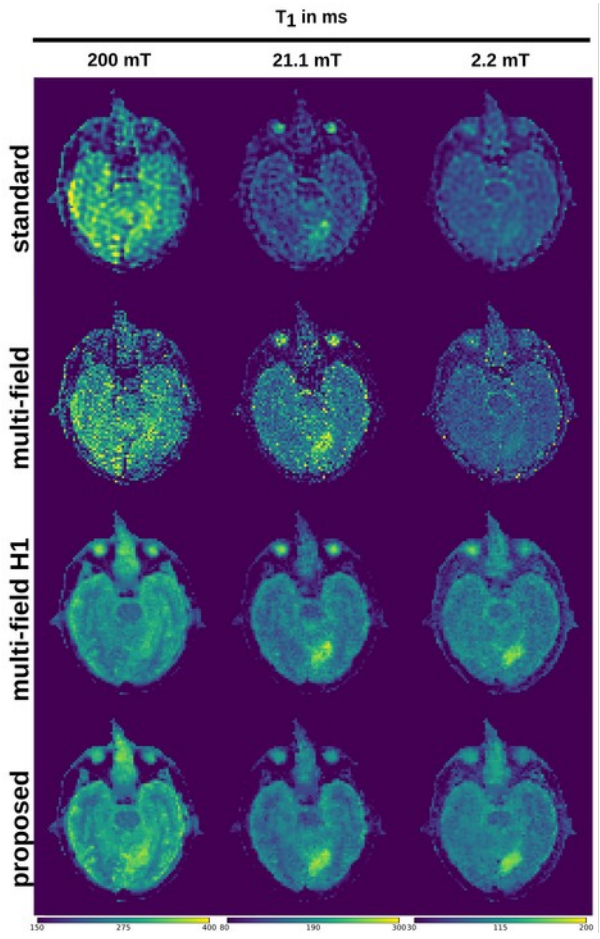

Figure 4: Exemplary in-vivo results for a patient suffering from a stroke. The stroke area can be clearly delineated in T_1 maps from lower fields and in approaches using spatial regularization and all fields combined for fitting. Results using the proposed method show the least residual noise in the T_1 maps.

References

[1] Lurie DJ, Aime S, Baroni S, Booth NA, Broche LM, Choi CH, et al. Fast Field-Cycling Magnetic Resonance Imaging. *Comptes Rendus Physique* 2010;11(2):136–148.

[2] Broche LM, Ross PJ, Davies GR, MacLeod MJ, Lurie DJ. A whole-body Fast Field-Cycling scanner for clinical molecular imaging studies. *Scientific Reports* 2019;9(1):10402.

[3] Steele RM, Korb JP, Ferrante G, Bubici S. New applications and perspectives of fast field cycling NMR relaxometry. Magnetic Resonance in Chemistry 2016;54(6):502–509.

[4] Bödenler M, Basini M, Casula MF, Umut E, Gösweiner C, Petrovic A, et al. R1 dispersion contrast at high field with fast field-cycling MRI. *Journal of Magnetic Resonance* 2018;290:68–75.

[5] Sumpf TJ, Uecker M, Boretius S, Frahm J. Model-based nonlinear inverse reconstruction for T2 mapping using highly undersampled spin-echo MRI. *Journal of Magnetic Resonance Imaging* 2011;34(2):420–428.

[6] Wang X, Roelo_s V, Klosowski J, Tan Z, Voit D, Uecker M, et al. Model-based T1 mapping with sparsity constraints using single-shot inversion-recovery radial FLASH. *Magnetic Resonance in Medicine* 2018;79(2):730–740.

[7] Maier O, Schoormans J, Schloegl M, Strijkers GJ, Lesch A, Benkert T, et al. Rapid T1 quanti_cation from high resolution 3D data with model-based reconstruction. *Magnetic Resonance in Medicine* 2019;81(3):2072–2089.

[8] Maier O, Spann SM, Bödenler M, Stollberger R. PyQMRI: An accelerated Python basedQuantitative MRI toolbox. *Journal of Open Source Software* 2020;5(56):2727.

[9] Knoll F, Bredies K, Pock T, Stollberger R. Second order total generalized variation (TGV) for MRI. *Magnetic Resonance in Medicine* 2011;65(2):480–491.

[10] Ross PJ, Broche LM, Lurie DJ. Rapid _eld-cycling MRI using fast spin-echo. *Magnetic Resonance in Medicine* 2015;73(3):1120–1124.

[11] Hógáin DÓ, Davies GR, Baroni S, Aime S, Lurie DJ. The use of contrast agents with fast _eld-cycling magnetic resonance imaging. *Physics in Medicine and Biology* 2010;56(1):105–115.

[12] Rudin LI, Osher S, Fatemi E. Nonlinear total variation based noise removal algorithms. *Physica D: Nonlinear Phenomena* 1992;60(1):259–268.

[13] Knoll F, Holler M, Koesters T, Otazo R, Bredies K, Sodickson DK. Joint MR-PET Reconstruction Using a Multi-Channel Image Regularizer. *IEEE Transactions on Medical Imaging* 2017;36(1):1–16.

[14] Bredies K. Recovering Piecewise Smooth Multichannel Images by Minimization of Convex Functionals with Total Generalized Variation Penalty *BT - Efficient Algorithms for Global Optimization Methods in Computer Vision.* Berlin, Heidelberg: Springer Berlin Heidelberg; 2014. p. 44–77.

Published by Verlag der TU Graz
Graz University of Technology

Proc. Annual Meeting of the Austrian Society for Biomedical Engineering 2021
DOI: 10.3217/978-3-85125-826-4-15

ADVANCING ARTERIAL SPIN LABELING TOWARDS CLINICAL USE

I. Middelhoff[1], S. M. Spann[1], O. Maier[1], R. Stollberger[1]

[1]Institute of Medical Engineering, TU Graz, Austria

i.middelhoff@tugraz.at

Abstract
Arterial Spin Labeling is an MR imaging method to non-invasively and quantitatively measure perfusion. Problems like long scan times and motion sensitivity prevent it as of yet from being in clinical use. We present a novel data acquisition sequence and reconstruction method for ASL to overcome these challenges. The introduced 3D GRASE sequence with time-dependent CAIPIRINHA undersampling pattern allows faster, single-shot imaging. The novel second—order, spatio-temporal TGV constraint in the reconstruction produces a better Signal-to-Noise ratio from fewer measurements by denoising the images. Both novel methods improve upon the motion sensitivity of ASL. Given all this progress, ASL becomes closer to being in clinical use.

Keywords— *MRI, Arterial Spin Labeling, Quantitative Imaging*

Introduction

MR Imaging is an invaluable tool in today's clinical environment. In many situations, an MR scan is the optimal path towards diagnosis or disease monitoring. Novel MRI methods are capable of measuring additional physiological parameters for supporting clinical diagnosis or treatment decisions. One of these techniques is Arterial Spin Labeling (ASL) which allows the non-invasive quantification of perfusion in organs. In contrast to other perfusion measurements (e.g. PET, DSC, DCE), ASL does not use an exogenous tracer, but magnetically labels blood flowing into the organ. The non-invasiveness of the procedure and the possibility of absolute quantification of perfusion makes it highly suitable for repeated measurements and longitudinal studies.
ASL works by acquiring a set of two images, a so-called 'label image' where the inflowing blood of the organ is magnetically labeled with special preparation pulses and a 'control image' without preparation. By calculating the difference between these two images, the signal from the static tissue cancels while the signal from the inflowing labeled blood remains. Through a physiological model, quantitative perfusion values can be calculated [1]. ASL was shown to yield promising results in stroke, arteriovenous malformation and tumor studies as early as 2000 [2]. The continued importance of ASL is shown by a recent consensus paper from the ISMRM study group summarizing state-of-the-art methods and recommending imaging procedures [3].
However, ASL faces many challenges before it can be adopted as a routine tool for clinical diagnosis. The perfusion signal is relatively small, leading to inherently low SNR. The intuitive solution, measuring multiple times and averaging, results in clinically unfeasible scan times and makes the scans prone to physiological noise (e.g. motion).

Methods

In this work we present and combine two novel methods that bring ASL beyond its current limitations and one step further into clinical routine. The first aspect to be addressed is the image acquisition. ASL images are commonly acquired with a multi-shot Gradient and Spin Echo (GRASE) or Stack-of-Spiral (SoS) sequence, where different parts of the data are acquired over several brief acquisition periods called 'shots' [3]. While this technique provides good SNR and image quality it is very susceptible to inter-shot motion which is a main source of physiological noise (see figure 1 below) [4].

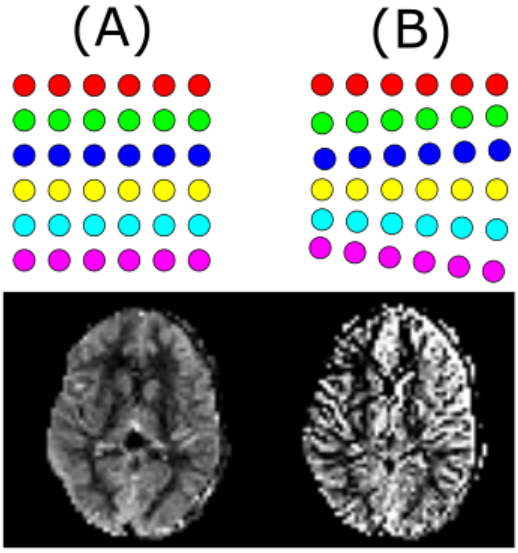

Figure 1: (A) A fully sampled, multi-shot acquisition of a 3D k-space of a stationary patient. Each dot represents one k-space line and each color represents one shot. (B) In case of motion between shots (here, rotation), the true coordinates of the acquired data do not align with the expected k-space coordinates [4]. Below the result of image acquisition of a stationary and a moving subject.

Published by Verlag der TU Graz
Graz University of Technology

DOI: 10.3217/978-3-85125-826-4-15

To reduce the influence of inter-shot motion current recommendations [3] propose parallel imaging with acceleration factors of up to 3. This allows the acquisition of the k-space in two shots, which improves motion robustness but is insufficient for patients (e.g. stroke) who often move involuntarily. To overcome this limitation we developed a GRASE [6] sequence (see figure 4) whose acceleration can be increased up to 6 by using a time-dependent CAIPIRINHA undersampling pattern [5] (see figure 2), allowing a single-shot acquisition of each time frame. [11]

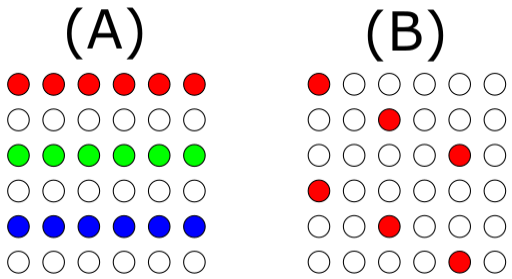

Figure 2: Comparison of GRAPPA and CAIPIRINHA undersampling patter: (A) 2x1 GRAPPA acceleration. (B) 1x6 CAIPIRINHA acceleration with a shift of 2

The developed time-dependent CAIPIRINHA pattern brings together the acceleration of common parallel imaging techniques like GRAPPA or SENSE while introducing additional spatial and temporal incoherence which is advantageous in the reconstruction. Also, over the course of several images a full dataset is acquired allowing easy calculation of coil sensitivities (see figure 3) which are needed in the reconstruction process.

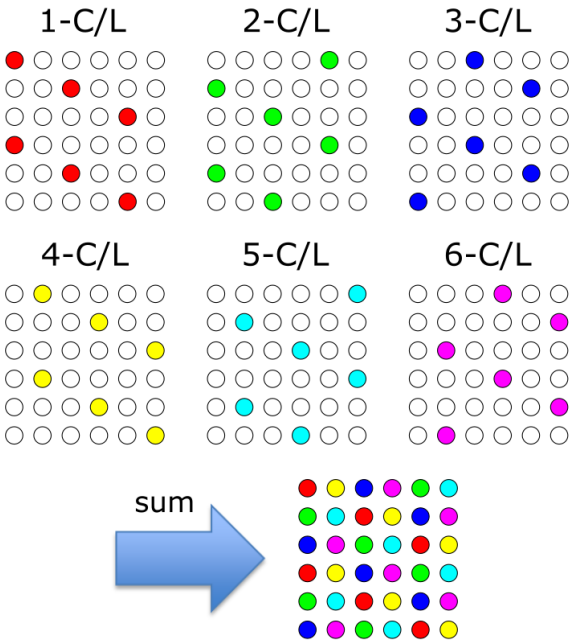

Figure 3: A time-series of 6 k-spaces with a 1x6(2) time-dependent CAIPIRINHA acceleration. Over the course of the series a full k-space is acquired. Still, a full image can be reconstructed from each undersampled k-space.

The readout sequence, GRASE, improves upon Echo-Planar Imaging (EPI). Over the course of any MR data readout, the signal decays due to T2 relaxation. The longer the readout lasts, the stronger is the decay. This decay leads to blurring in the image [7]. During an EPI readout, the signal decay happens with time constant T2*. In a GRASE sequence, EPI is combined with a Turbo-Spin Echo (TSE). This leads to a signal decay with a mix of time-constants T2* and T2, which is longer than T2*. This allows more data to be acquired while keeping the blurring at the same level.

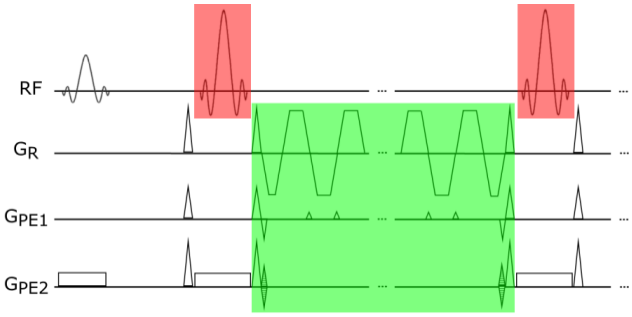

Figure 4: The GRASE readout of the sequence diagram. Prior to the shown section, a pulsed Continuous Arterial Spin Labeling (pCASL) [8] labeling module is applied in combination with background suppression pulses to improve SNR. In the shown section, a 3D slab is excited. Then, the TSE refocusing pulses reverse signal losses due to field inhomogeneities (red). In between two refocusing pulses, an EPI readout occurs (green). The shown section is repeated several times. The number of refocusing pulses and the length of the EPI readout determine how many lines of k-space are measured per shot.

The second aspect of the ASL process to be improved is the image reconstruction. As a baseline, the new, accelerated sequence necessitates parallel imaging reconstruction algorithms. In theory, this would suffice to get the images. Here, a second-order, spatio-temporal Total Generalized Variation (TGV) [9] regularization is added to constrain the reconstruction process for the control, the label and the difference images simultaneously [11]. TGV is a powerful regularization tool which enforces piecewise smooth images which has been shown to be an appropriate choice for MR image reconstruction [10]. All images are reconstructed simultaneously. Sparsity in both the spatial and temporal dimensions are exploited with TGV which inherently denoises the reconstructed images. The full reconstruction problem is stated in equation (1):

Published by Verlag der TU Graz
Graz University of Technology

DOI: 10.3217/978-3-85125-826-4-15

$$(c^*, l^*) \in \operatorname{argmin}_{c,l} \frac{\lambda_c}{2}||Kc - d_c||_2^2 + \frac{\lambda_l}{2}||Kl - d_l||_2^2 + \gamma_1(w)TGV(l) + \gamma_1(w)TGV(c) + \gamma_2(w)TGV(c - l) \quad (1)$$

In equation (1) λ and ɣ are weighting parameters, *c* and *l* are the control and label images, K is the forward Operator from image space to the measurement space and *d* refers to the measured data. The definition of TGV can be found in [9].

To test this novel acquisition and reconstruction method data was acquired in-vivo to compare it to fully sampled multi-shot acquisitions. 5 healthy, consenting volunteers were measured on a 3T MR system (Prisma, Siemens Healthcare, Germany). All measurements were done using a pCASL sequence with a 3D-GRASE readout, once using 6 shots for a fully sampled acquisition and once using the above described CAIPIRINHA acceleration for single-shot acquisition. The parameters were: FOV: 200x200 mm^2, matrix: 64x64x38 voxels, 3.1x3.1x3 mm^3 resolution, 20% slice oversampling, TE/TR: 15/4100, EPI-factor: 21, Turbo-factor: 23, 180° refocusing pulses, labeling duration: 1800 ms, Post-Labeling Delay: 1800 ms. This results in an acquisition time of 4.5 min for 5 control/label pairs and one proton density image for the fully segmented acquisition. All scans were done with the patients being asked to remain still. For two volunteers the procedure was repeated with the subjects cued to move their head in a predetermined manner. All data was then reconstructed using equation (1). In post-processing, all images for each subject were registered to reduce motion artifacts in the averaging process, the perfusion weighted images were calculated and Cerebral Blood Perfusion (CBF) maps were created according to [3].

Results

Figure 5 shows a comparison between the motion-affected and the motion free data acquired with the standard multi-shot approach and the proposed single-shot method. The figure clearly shows visually that the multi-shot acquisition is much more prone to motion-induced errors than the accelerated single-shot sequence.

In figure 6, there is a comparison between the different acquisition types for different number of averages in. Visually, a significant noise increase is evident for the fully sampled image between 30 and 12 averages, especially in the white matter. For the novel acquisition and reconstruction method nearly the same image quality can be achieved although the acquisition time is reduced by more than half.

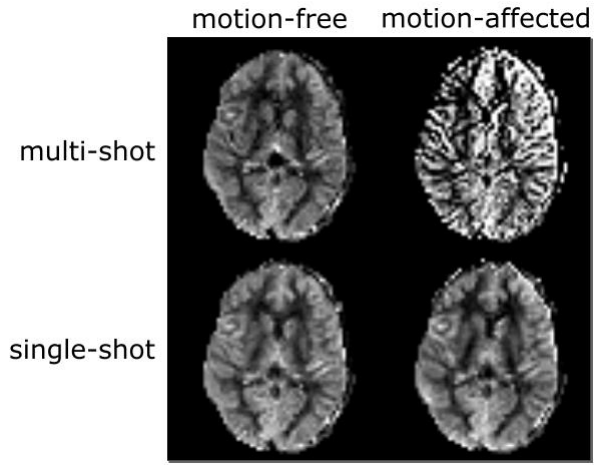

Figure 5: Comparing the effects of motion onto the CBF maps for the two tested acquisition methods.

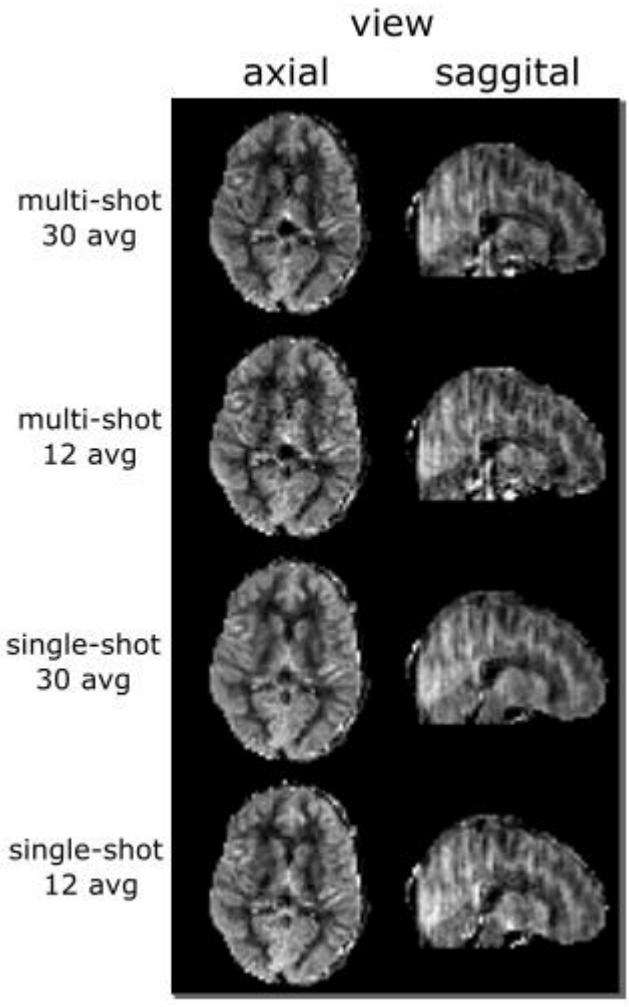

Figure 6: Comparison for a different number of averages for the two tested acquisition methods.

Published by Verlag der TU Graz
Graz University of Technology

DOI: 10.3217/978-3-85125-826-4-15

A quantitative comparison confirms the visual analysis. The novel method increases temporal signal-to-noise ratio over the whole brain by 16% compared to the full acquisition. In addition the acquisition time can be reduced by a factor of 3 without the loss of information or image quality.

Discussion

The results show a clear improvement of the GRASE sequence with a time-dependent CAIPIRINHA pattern and TGV-constrained reconstruction compared to the recommended ASL acquisition as described by Alsop et al [3]. With this, the motion problem as well as the SNR problem are addressed.

With this new approach the current motion problems are reduced due to two factors. First, the single shot acquisition completely circumvents the problem of inter-shot motion. The only motion that can impact the data for one image is during the < 300 ms acquisition period. Second, the TGV constraints enforces smoothness in spatial and temporal directions. Thus, slight inconsistencies between subsequent images may be smoothed out in the reconstruction process.

The TGV constraint also reduces the problem of low SNR. Additionally, it allows the acquisition of less averages while maintaining details and image quality.

The proposed method is currently evaluated in simulations and patients with neurovascular diseases and compared to current gold standard methods.

Measuring perfusion non-invasively can be a great step forward in the clinical routine as well as in brain research areas e.g. for studying the neuronal activity in the human brain or for real-time interoperative guidance. Also, having increased the time resolution by a factor of 6, real-time ASL for psychological and neurological research becomes a possibility.

With the presented improvements ASL has come one step closer to a clinically, viable tool.

References

[1] Ho, M.L.: Arterial Spin Labeling: Clinical Applications, *Journal of Neuroradiology*, vol. 45, no. 5, pp. 276-289, 2018.

[2] Chalela, J.A., Alsop, D.C. et. al.: Magnetic resonance perfusion imaging in acute ischemic stroke using continuous arterial spin labeling, *Stroke*, vol. 31, no. 3, pp. 680-687, 2000.

[3] Alsop, D.C., Detre, J.A. et. al.: Recommended implementation of arterial spin-labeled perfusion MRI for clinical applications: A consensus of the ISMRM perfusion study froup and the European consortium for ASL in dementia, *Magnetic Resonance in Medicine,* vol. 73, no. 1, pp. 102-116, 2015.

[4] Zaitsev, M., Maclaren, J. et. al.: Motion Artifacts in MRI: a complex problem with many partial solutions, *Journal of Magnetic Resonance Imaging*, vol. 42, no. 4, pp. 887-901, 2015.

[5] Breuer, F.A., Blaimer, M. et. al.: Controlled Aliasing in Volumetric Parallel Imaging (2D CAIPRINHA), *Magnetic Resonance in Medicine*, vol. 60, no. 6, pp. 1488-1497, 2008.

[6] Feinberg, D.A., Oshio, K.: GRASE (Gradient and Spin-Echo) MR Imaging: a new fast clinical imaging technique, *Radiology,* vol. 181, no. 2, pp. 597-602, 1991.

[7] Johnson, G., Hutchison, J.M.: The limitations of NMR recalled echo imaging techniques, *Journal of Magnetic Resonance*, vol. 63, no. 1, 14-30, 1985.

[8] Dai, W., Garcia, D. et. al.: Continuous flow-driven inversion for arterial spin labeling using pulsed radio frequency and gradient magnetic fields

[9] Bredies, K., Holler, M.: A TGV-based framework for variational image decompression, zooming and reconstruction. Part II: Numerics, *SIAM Journal on Imaging Sciences*, vol. 8, no. 4, pp. 2851-2886, 2015.

[10] Knoll, F., Bredies, K. et. al.: Second order total generalized variation (TGV) for MRI. *Magnetic Resonance in Medicine*, vol. 65, no. 2, pp. 480–491, 2011.

[11] Spann, S.M., Shao, X. et. al.: Robust single-shot acquisition of high resolution whole brain ASL images by combining time-dependent 2D CAIPIRINHA sampling with spatio-temporal TGV reconstruction, *NeuroImage*, vol. 206, p

Published by Verlag der TU Graz
Graz University of Technology

Proc. Annual Meeting of the Austrian Society for Biomedical Engineering 2021
DOI: 10.3217/978-3-85125-826-4-16

Relevance-guided Deep Learning for Feature Identification in R2* Maps in Alzheimer's Disease Classification

C. Tinauer[1], S. Heber[1], L. Pirpamer[1], A. Damulina[1], M. Soellradl[2], M. Sackl[1], E. Hofer[1], M. Koini[1], R. Schmidt[1], R. Stollberger[2], S. Ropele[1], C. Langkammer[1]

[1]Department of Neurology, Medical University of Graz, Austria

[2]Institute of Medical Engineering, Graz University of Technology, Austria

christian.tinauer@medunigraz.at

Abstract- *When using deep neural networks to separate Alzheimer's disease patients (n=119) from normal controls (n=131) by using MR images, heat mapping revealed that the image preprocessing is introducing misleading features used by the classifier. Therefore we systematically investigated the influence of registration and brain extraction on the learned features by heat mapping. Results were compared to a novel relevance-guided training method, focusing on brain tissue. The relevance-guided configurations yielded highest classification accuracies and also confirmed histopathologically relevant regional iron deposition.*

Keywords- *Deep convolutional neural networks, heat mapping, relevance guidance, Alzheimer's disease*

Introduction

Deep learning techniques are increasingly utilized in medical applications, including image reconstruction [1], segmentation [2], and classification [3,4]. However, despite the good performance those models are not easily interpretable by humans [5]. Especially medical applications require verification that the high accuracy of those models is not the result of exploiting artifacts in the data [6]. Our previous experiments on Alzheimer's disease (AD) classification showed that Deep Neural Networks such as Convolutional Neural Networks (CNNs) might learn from features introduced by the brain extraction algorithm [7]. Therefore, in this work we investigated how preprocessing steps including registration and brain extraction determine which features in the R2* maps are relevant for the separation of patients with AD from normal controls. MR-based R2* mapping enables the in vivo detection of iron. Brain iron accumulates during aging and has been associated with neurodegenerative disorders including AD.

Methods

Dataset: We retrospectively selected 252 MRI datasets from 119 patients with probable AD (mean age=72.4±9.0 years) from our outpatient clinic and 133 MRIs from 131 age-matched healthy controls (mean age=70.3±9.1 years) from a local community dwelling study. Patients and controls were scanned using a consistent MRI protocol performed at the same scanner at 3 Tesla (Siemens TimTrio) including a T1-weighted MPRAGE sequence (1mm isotropic resolution) and a spoiled FLASH sequence (0.9x0.9x2mm³, TR/TE_1=35/4.92ms, 6 echoes, 4.92ms echo spacing, 64 slices). The AD data was randomly split up into 178 training, 37 validation and 37 test scans and the normal control data was randomly split up into 95 training, 19 validation and 19 test scans, creating 1 partition.

Preprocessing: Binary brain masks from each subject were obtained using FSL-SIENAX [8] and subsequently used for brain extraction (BET) to isolate the brain tissue from the skull. R2* maps were calculated voxelwise using a numerical correction model [9] and nonlinearly registered to the 1mm MNI152 template using FSL fnirt [10].

Classifier network: We utilized a 3D classifier network, combining a single convolutional layer (kernel 8x8x8, 8 channels) with a down-convolutional layer (kernel 8x8x8, 8 channels, striding 2x2x2) as the main building block. The overall network stacks 4 of these main building blocks followed by two fully connected layers (16 and 2 units) (Figure 1). Each layer is followed by a Rectified Linear Unit (ReLU) nonlinearity, except for the output layer where a Softmax activation is applied.

Published by Verlag der TU Graz
Graz University of Technology

DOI: 10.3217/978-3-85125-826-4-16

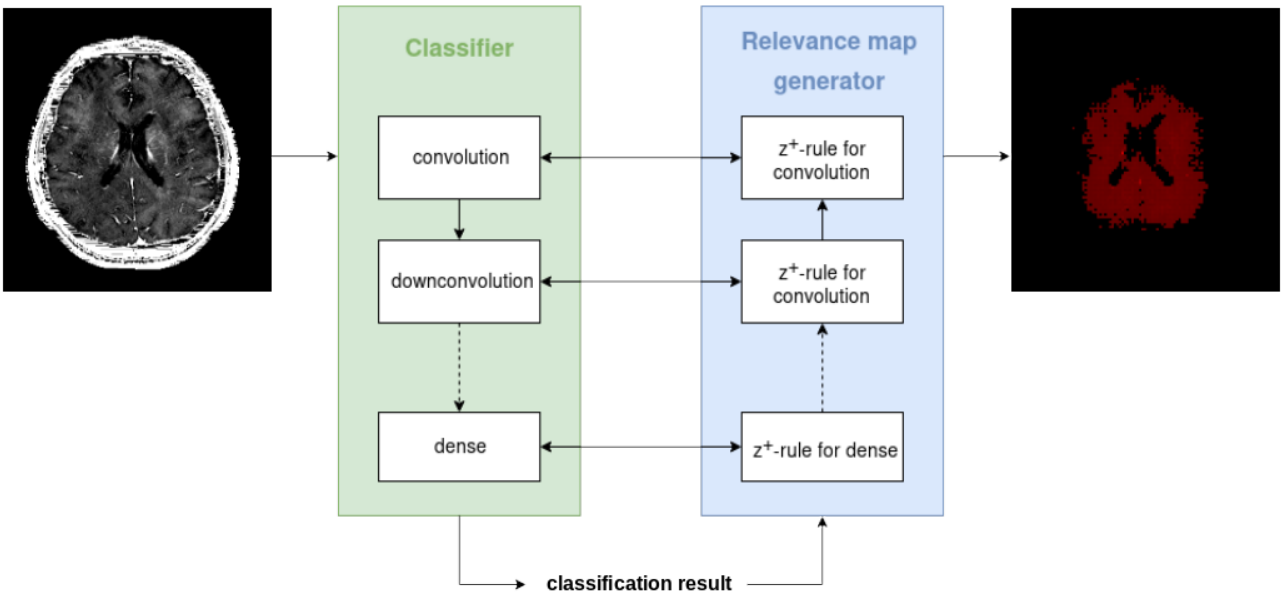

Figure 1: Overview of the used relevance-guided classifier network. We extend a default classifier network (green) with a relevance map generator (blue). For every layer of the classifier network a corresponding relevance redistribution layer is added to the generator network. The output relevance map of the generator has the same resolution as the R2* map used as input for the classifier and allows to guide the training of the classifier network by adding a term that sums relevance values outside a given brain mask to the categorical cross entropy loss.

Relevance-guided classifier network: To focus the network on "relevant features", we propose a relevance-guided network architecture that extends the given classifier network with a relevance map generator (Figure 1). To this end we implemented the deep Taylor decomposition (z^+-rule) [11] to generate the relevance maps of each input image depending on the classifier's current parameters.

Training: We trained models for two differently preprocessed types of R2*:

- R2* images in native subject space
- R2* images nonlinearly registered to the 1mm MNI152 template

For each type we compare the two standard classifier networks (unmasked and masked) with the outcome of our relevance-guided method. Each model was trained using Adam optimizer [12] for 60 epochs with a batch size of 8. The difference in the class sizes was accounted for using a class weighting in the loss function.

Heat map presentation: Besides qualitatively comparing individual heat maps, we compared average heat maps by accumulating the bin contents of each averaged heat map histogram from top until we reached 20 % of all relevance within the heat map overlaid on an MNI152 1mm template.

Results

The resulting balanced classification accuracy between normal controls and AD shows increased performance on the test set for the relevance-guided models (Table 1). However, the obtained relevance maps (Figure 2) show that using unmasked images or brain masking yield highly relevant features for AD/normal control classification at the respective outer boundaries (left and center column). In contrast, relevance-guided training identifies regions within brain tissue, with the highest feature density in the basal ganglia. The corresponding receiver operating characteristics (ROC) curves for all six models are shown in Figure 3.

Published by Verlag der TU Graz
Graz University of Technology

DOI: 10.3217/978-3-85125-826-4-16

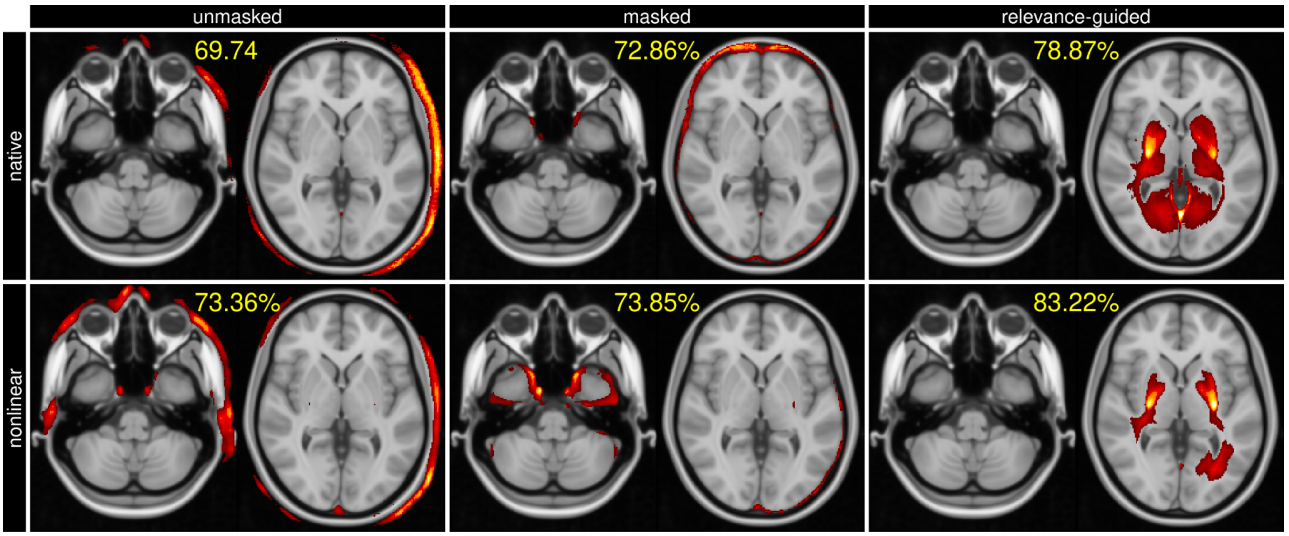

Figure 2: Mean relevance maps (highest relevances in yellow) overlaid on MNI152 template and balanced classification accuracy (percentage) obtained for all six models. Unmasked and masked MRI classifiers obtain relevant image features overwhelmingly from volumetric information (left and center columns). In contrast, the proposed relevance-guided method bases the classifier's decision on deep brain image features, virtually independently of the registration method (right column).

Table 1: Performance (in %) for the different models on the test set. Highest values per column are highlighted in bold.

Class., Classifier; BET, brain extraction; Reg., registration; Bal. acc.; balanced accuracy; Sens, sensitivity; Spec., specificity; AUC, area under the curve of the receiver operating characteristics; CNN, convolutional neural network; RG, relevance-guided

Class.	BET	Reg.	Bal. acc.	Sens.	Spec.	AUC
CNN	no	-	70%	89%	50%	0.70
CNN	yes	-	73%	89%	56%	0.79
CNN	no	nlin	73%	84%	63%	0.77
CNN	yes	nlin	74%	79%	69%	0.79
CNN+ RG	no	-	79%	**92%**	66%	0.80
CNN+ RG	no	nlin	**83%**	79%	**88%**	**0.85**

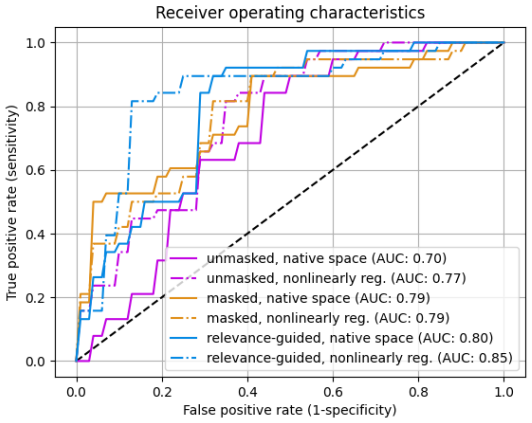

Figure 3: Comparison of receiver operating characteristics for all six configurations. The relevance-guided models (blue) show higher values for the area under the curve (AUC in legend) compared to unmasked (purple) and masked (orange) configurations.

Discussion and Conclusion

In this explorative study we demonstrate that the preprocessing of MR images is crucial for the feature identification by DNNs. While previous work has shown that skull stripping is necessary to avoid identification of features outside the brain, this introduces new edges by the brain mask, which are subsequently used by the DNN for classification. In this context, it was demonstrated that the outcome of brain extraction algorithms can be biased by the patient cohort [13]. In contrast, when using the proposed relevance-guided approach and independently of preprocessing, the regions of highest relevance were found in the basal ganglia. R2* is considered as a measure of iron content [14]. Histological and in-vivo studies [15], [16] have shown that brain iron concentration is higher in these regions in AD patients compared to normal controls. In conclusion, our results are in good agreement with findings from iron mapping studies and strongly support the hypothesis that the relevance-guided approach is minimizing the impact of preprocessing steps such as skull stripping and registration. Additionally,

Published by Verlag der TU Graz
Graz University of Technology

DOI: 10.3217/978-3-85125-826-4-16

relevance-guiding forces the feature identification to focus on the parenchyma only and therefore provides more plausible results with higher classification accuracy.

Acknowledgements

This study was funded by the Austrian Science Fund (FWF grant numbers: KLI523, P30134). This research was supported by NVIDIA GPU hardware grants.

References

[1] K. Hammernik *et al.*, “Learning a variational network for reconstruction of accelerated MRI data,” *Magn Reson Med*, vol. 79, no. 6, pp. 3055–3071, Jun. 2018, doi: 10.1002/mrm.26977.

[2] J. Kleesiek *et al.*, “Deep MRI brain extraction: A 3D convolutional neural network for skull stripping,” *Neuroimage*, vol. 129, pp. 460–469, Apr. 2016, doi: 10.1016/j.neuroimage.2016.01.024.

[3] A. Esteva *et al.*, “Dermatologist-level classification of skin cancer with deep neural networks,” *Nature*, vol. 542, no. 7639, Art. no. 7639, Feb. 2017, doi: 10.1038/nature21056.

[4] E. Hosseini-Asl *et al.*, “Alzheimer’s disease diagnostics by a 3D deeply supervised adaptable convolutional network,” *Front Biosci (Landmark Ed)*, vol. 23, pp. 584–596, Jan. 2018, doi: 10.2741/4606.

[5] W. Samek, T. Wiegand, and K.-R. Müller, “Explainable Artificial Intelligence: Understanding, Visualizing and Interpreting Deep Learning Models,” *ITU Journal: ICT Discoveries*, vol. 1, no. 1, pp. 39–48, 2018.

[6] C. Davatzikos, “Machine learning in neuroimaging: Progress and challenges,” *NeuroImage*, vol. 197, pp. 652–656, Aug. 2019, doi: 10.1016/j.neuroimage.2018.10.003.

[7] C. Tinauer *et al.*, “Relevance-guided Feature Extraction for Alzheimer’s Disease Classification,” presented at the ISMRM 27th Annual Meeting & Exhibition, Montréal, CANADA, May 2019.

[8] S. M. Smith *et al.*, “Accurate, robust, and automated longitudinal and cross-sectional brain change analysis,” *Neuroimage*, vol. 17, no. 1, pp. 479–489, Sep. 2002, doi: 10.1006/nimg.2002.1040.

[9] M. Soellradl *et al.*, “Assessment and correction of macroscopic field variations in 2D spoiled gradient-echo sequences,” *Magn Reson Med*, vol. 84, no. 2, pp. 620–633, Aug. 2020, doi: 10.1002/mrm.28139.

[10] S. M. Smith *et al.*, “Advances in functional and structural MR image analysis and implementation as FSL,” *Neuroimage*, vol. 23 Suppl 1, pp. S208-219, 2004, doi: 10.1016/j.neuroimage.2004.07.051.

[11] G. Montavon, S. Lapuschkin, A. Binder, W. Samek, and K.-R. Müller, “Explaining nonlinear classification decisions with deep Taylor decomposition,” *Pattern Recognition*, vol. 65, pp. 211–222, May 2017, doi: 10.1016/j.patcog.2016.11.008.

[12] D. P. Kingma and J. Ba, “Adam: A Method for Stochastic Optimization,” *ICLR*, 2015.

[13] C. Fennema-Notestine *et al.*, “Quantitative evaluation of automated skull-stripping methods applied to contemporary and legacy images: effects of diagnosis, bias correction, and slice location,” *Hum Brain Mapp*, vol. 27, no. 2, pp. 99–113, Feb. 2006, doi: 10.1002/hbm.20161.

[14] S. Ropele and C. Langkammer, “Iron quantification with susceptibility,” *NMR Biomed*, vol. 30, no. 4, Apr. 2017, doi: 10.1002/nbm.3534.

[15] N. Schröder, L. S. Figueiredo, and M. N. M. de Lima, “Role of brain iron accumulation in cognitive dysfunction: evidence from animal models and human studies,” *J Alzheimers Dis*, vol. 34, no. 4, pp. 797–812, 2013, doi: 10.3233/JAD-121996.

[16] C. Ghadery *et al.*, “R2* mapping for brain iron: associations with cognition in normal aging,” *Neurobiol Aging*, vol. 36, no. 2, pp. 925–932, Feb. 2015, doi: 10.1016/j.neurobiolaging.2014.09.013.

Published by Verlag der TU Graz
Graz University of Technology

Proc. Annual Meeting of the Austrian Society for Biomedical Engineering 2021
DOI: 10.3217/978-3-85125-826-4-17

A NEW CLASS OF ROBUST RF PULSES BY OPTIMAL CONTROL

C. Graf[1], M. Soellradl[1], C.S. Aigner[2], A. Rund[3], R. Stollberger[1]

[1]Institute of Medical Engineering, Graz University of Technology, Graz, Austria
[2]Physikalisch-Technische Bundesanstalt (PTB), Braunschweig and Berlin, Germany
[3]Institute of Mathematics and Scientific Computing, University of Graz, Graz, Austria

c.graf@tugraz.at

Abstract— *This work aimed to design and investigate inversion pulses that are robust among B_0 and B_1 inhomogeneities with a minimized pulse duration by optimal control. The optimized RF pulse was compared numerically to a state-of-the-art adiabatic RF pulse and a customized adiabatic one. All three RF pulses were investigated in extensive measurements on a 3T MRI system. Phantom measurements were performed to examine robustness with respect to B_0 and B_1. In vivo measurements of the knee emphasized the practicability of the proposed RF pulse which is shown to be robust among variations within B_0 and B_1.*

Keywords— *RF pulses, optimal control, robustness, B_0 inhomogeneities, B_1 inhomogeneities*

Introduction

Different MRI application experiments require inversion radio frequency pulses, i.e. pulses with a flip angle of 180°. However, for many applications, inhomogeneities within the B_0 and B_1 field are an issue, [1-9]. For special applications such as arterial spin labeling, even small deviations from the required exact inversion are unsatisfactory, [10]. Strong improvements regarding inversion efficiency could be achieved by using composite [6] or adiabatic [3] RF pulses, but at the cost of higher pulse energy and prolonged pulse duration. The design of RF pulses by optimal control has shown in the past that even conflicting requirements such as best pulse performance, short pulse duration, and limited pulse energy can be combined and fulfilled by using the entire parameter space [11-15]. This approach was already extended to account for B_0 and B_1 inhomogeneities, [4,16,17]. In [18], an ensemble-based optimal control formalism was used to include a time-minimal formalism and optimize for B_0 and B_1 robust inversion pulses. This work aims to compare the optimized RF pulse to state-of-the-art adiabatic RF pulses in phantom and in vivo measurements on a 3T MR system.

Theory and Methods

The goal of the optimization is to design RF pulses with robustness over a wide range of B_0 and B_1 variations, [18]. Therefore, we include B_1 scalings of 70% to 130% (i.e. a scale of the amplitude of the RF pulse by those factors) and B_0 offsets of +/-5ppm at 3T into the optimization. The optimization itself uses exact discrete derivatives supplied by adjoint calculus within a trust-region, semi-smooth quasi-Newton framework [13]. We use a 10ms RF pulse with random magnitude and random phase as initial. During optimization, the relaxation times were chosen to coincide with those of our cylindrical MR phantom (plastic bottle with diameter 14cm, length 42,5cm, filled with H_20 and contrast agent resulting in T_1=102ms, T_2=81ms at 3T). The underlying Bloch equations were solved using a symmetric operator splitting allowing for the inclusion of the relaxation effects, [19].

To compare the optimized pulse, two adiabatic, hyperbolic secant pulses are introduced. The first one (**HS1**) is commonly implemented for arterial spin labeling applications [10] and has a long pulse duration of 15.36ms. The second one (**HS2**) was designed so that the pulse duration and bandwidth coincide with those of the optimized pulse.

An extensive numerical comparison of all three RF pulses is performed including a broad set of B_0 offsets and B_1 scalings. The inversion efficiency is calculated for long a long repetition time (TR) with negligible T_1 influence for each pair of B_0 and B_1 as

$$eff = -\frac{I_{(inv)}}{I_0} = -\frac{S(x)\, M_{z(inv)}(x) \sin\alpha(x)}{S(x)\, M_0(x) \sin\alpha(x)} = -\frac{M_{z(inv)}(x)}{M_0(x)} \quad (1)$$

with M_z being the z-magnetization at the end of the respective RF pulse. Furthermore, M_0 is the initial magnetization and S(x) describes the signal intensity. For measurement, a slice selective excitation pulse with flip angle α is necessary. This excitation pulse is affected by RF inhomogeneities as well.

In addition, all three RF pulses were investigated in vivo measurements of the knee. We used the knee coil and we set the sequence parameters repetition time (TR) and echo time (TE) to TR=8000ms and TE=2.7ms. Those experiments were performed with a fixed B_1 scale of 100% and without additional B_0 offset. The flip angle was set to 90°.

Published by Verlag der TU Graz
Graz University of Technology

DOI: 10.3217/978-3-85125-826-4-17

Results

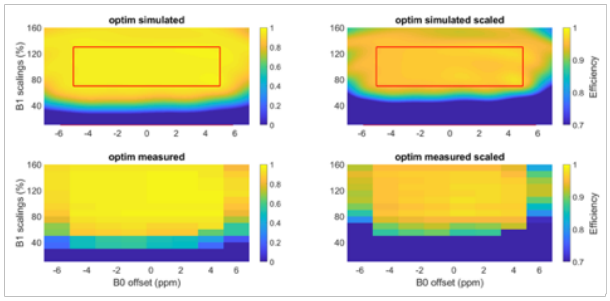

Figure 1: Simulated and measured inversion efficiencies of **optim** for B_1 scaled from 0% to 160% and ΔB_0 from -7ppm to 7ppm.

Figure 1 depicts the inversion efficiency of **optim** over a broad set of B_0 and B_1 variations. The red box indicates the area where the optimization was done (i.e. B_1 from 70% to 130% and B_0 from -5ppm to 5ppm). The pulse duration was reduced to T_p=3.25ms during optimization. The top figures show the numerical efficiencies which were calculated with the relaxation times of the phantom, while the bottom figures show the efficiencies measured on the MR scanner. The plots in the left column use an efficiency scale of 0% to 100% while in the right the plots are scaled from 70% to 100%. A very good inversion efficiency of more than 94.5% can be observed within the optimized area (red box). Furthermore, the figure shows strong accordance between numerical and measurement results.

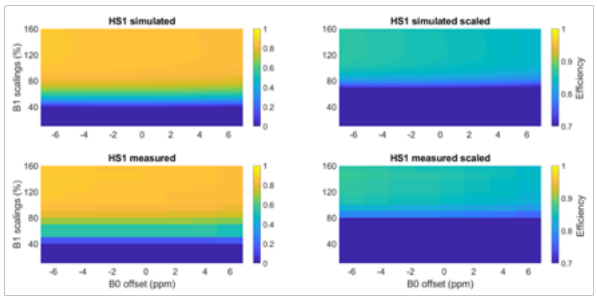

Figure 2: Simulated and measured inversion efficiencies of **HS1** for B_1 scaled from 0 % to 160% and ΔB_0 from -7ppm to 7ppm.

In Figures 2 and 3 we observe the inversion efficiencies of **HS1** and **HS2**. Again, a good accordance between simulated and measured inversion efficiencies can be observed. In both cases, the efficiency of **HS1** does not reach top values. There is strong robustness among changes within B_0, but for B_1 the efficiency is only acceptable for a scale of 100% and more. Below, the efficiency is less than 70%. In contrast, **HS2** shows a good inversion efficiency in the center of the plot (B_1 of 100% and B_0 at 0ppm). Only for a larger offset of B_0 the efficiency significantly decreases.

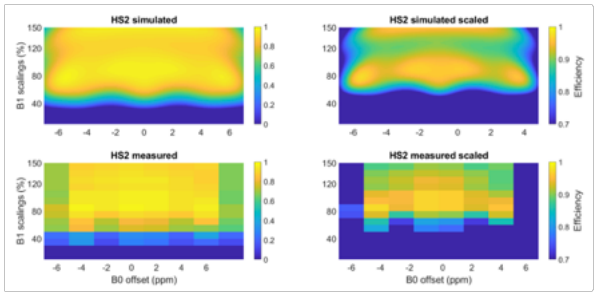

Figure 3: Simulated and measured inversion efficiencies of **HS2** for B_1 scaled from 0 % to 150% and ΔB_0 from -7ppm to 7ppm.

Figure 4 displays a sagittal cross-section of the knee using no pulse in the gradient echo sequence (top) and the **optim** inversion pulse (bottom). Figure 5 depicts the inversion profile measured with **optim**, a B_1-scale of 100% and without an additional B_0 offset. Between water and fat, bound protons at a resonance offset of 3.4ppm exist. Some chemical shift artifacts occur at tissue boundaries. We observe a severe decrease in signal intensity towards the proximal and distal parts in the image where the coil sensitivity and RF field strength drops to very low values. In Figure 5, the measured inversion efficiencies are depicted for all 3 RF pulses. Similarly to the phantom measurements, **optim** shows the best inversion efficiency among those 3 pulses within the defined field range. **HS1** has a decreased inversion efficiency even in the center of the knee with a fast loss in efficiency towards the coil edge. **HS2** shows a rather broad inversion capability, but with general lower inversion efficiency, in particular within the fatty bone marrow.

Discussion

During the optimization, the pulse duration of **optim** was reduced to 3.25ms, which is substantially shorter than the long duration of 15.36ms of **HS1**. **HS2** has the same pulse duration as **optim** by design. However, the maximum amplitude is increased by 25% which makes the pulse unsuitable for many applications due to the amplitude limitations of the MR scanner. Here, optimization for **optim** was started with random initialization. If existing for the application at hand, a sophisticated initialization is in general helpful for an optimizer, and also our optimizer can be used in this classical setup. However, optimizers that robustly converge from random initialization to a competitive minimizer, are rare, and open new perspectives (e.g. finding new – possibly better - local minimizers or even quasi-global optimization by multi-random initialization).

Published by Verlag der TU Graz
Graz University of Technology

DOI: 10.3217/978-3-85125-826-4-17

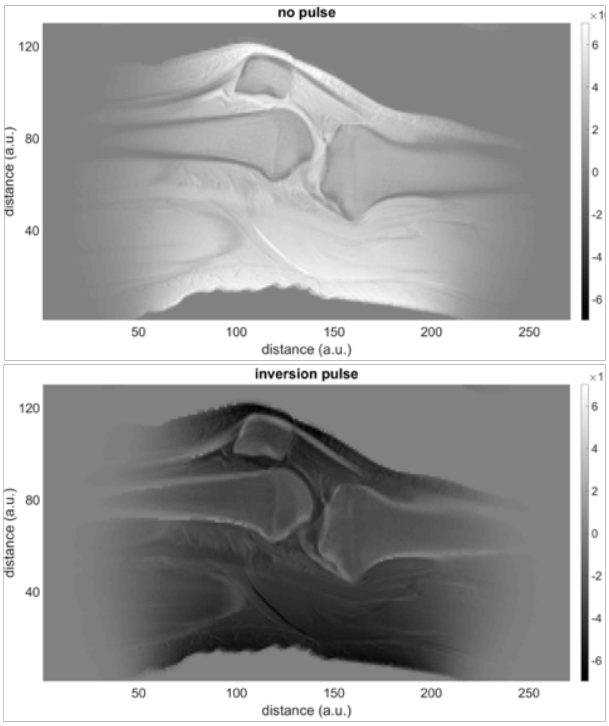

Figure 4: Sagittal cross-section of the knee. The top picture displays the image without an inversion pulse ($S(\mathbf{x}) \cdot M_0(\mathbf{x}) \cdot \sin\alpha(\mathbf{x})$), the bottom picture with an inversion pulse ($S(\mathbf{x}) \cdot M_{z(inv)}(\mathbf{x}) \cdot \sin\alpha(\mathbf{x})$) using **optim**. The inhomogeneous signal intensity represents the inhomogeneous RF field and coil sensitivity of the knee coil.

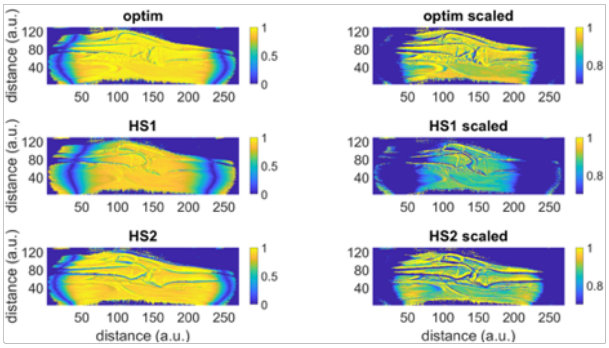

Figure 5: Inversion efficiencies for measurements of the knee. **Optim** (left), **HS1** (middle) and **HS2** (bottom). Efficiency scale of 0% to 100% (left) and 70% to 100% (right).

Figure 5 displayed the comparison of the three inversion pulses for in vivo applications. Similar to the phantom results, **optim** showed the best behaviour in terms of inversion efficiency. The long adiabatic pulse **HS1** showed already in simulation and phantom measurement only a moderate inversion efficiency which was validated in the in vivo measurement. One reason for that is its rather long pulse duration which results in relaxation effects affecting the efficiency. The short adiabatic pulse **HS2** could underline its behaviour in the in vivo experiments yielding a good efficiency. However, the main drawback is the higher amplitude required. Furthermore, in Figure 5, we depict line artifacts due to chemical shift behaviour.

A consequent future improvement of this work would be to jointly control the slice-selective gradient for slice-selective applications. Furthermore, an extension to optimize for excitation pulses, i.e. RF pulses with a flip angle less than 180° would be desired.

Conclusion

Inversion pulses were optimized within an optimal control framework with the aim of B_0- and B_1-robustness and a reduced pulse duration. The numerical and measured comparison to state-of-the-art adiabatic pulses revealed a significant improvement in terms of inversion efficiency while being short and fulfilling all physical limitations.

References

[1] Wang, J., Mao, W. et al.: *Factors influencing flip angle mapping in MRI: Pulse shape, slice-select gradients, off-resonance excitation and B0 inhomogeneities*, Magn Reson Med 2006;56:463-468.

[2] de Graaf, R.A.: *In Vivo NMR Spectroscopy*, John Wiley & Sons, 2007.

[3] Bernstein, M.A., King, K.F. et al.: *Handbook of MRI Pulse Sequences*, Elsevier Academic Press, 2004.

[4] Kobzar, K., Skinner, T.E. et al.: *Exploring the limits of broadband excitation and inversion: II. RF-power optimized pulses.* J Magn Reson 2008;194:58-66.

[5] Hurley, A.C., Al-Radaideh, A. et al.: *Tailored RF pulse for magnetization inversion at ultrahigh field*, Magn Reson Med 2010;63:51-58.

[6] Moore J., Jankiewicz, M. et al.: *Composite RF pulses for B_1^+-insensitive volume excitation at 7 Tesla*, J Magn Reson 2010;205:50-62.

[7] Warnking, J.M., Pike, G.B.: *Bandwidth-modulated adiabatic RF pulses for uniform selective saturation and inversion,* Magn Reson Med 2004;52:1190-1199.

[8] Alsop, D.C., Detre, J.A. et *al.*: *Recommended Implementation of Arterial Spin-Labeled Perfusion MRI for Clinical Applications: A Consensus of the ISMRM Perfusion Study Group and the European Consortium for ASL in Dementia*, Magn Reson Med 2014.

[9] Wang, K., Shao, X. et al.: *Optimization of adiabatic pulses for pulsed arterial spin labeling at 7 Tesla: Comparison with pseudo-continuous arterial spin labeling,* Magn Reson Med 2021;6:3277-3240.

[10] Garcia, D.M., Duhamel, G. et al.: *Efficiency of Inversion Pulses for Background Suppressed Arterial Spin Labeling,* Magn Reson Med 2005;54:366-372.

Published by Verlag der TU Graz
Graz University of Technology

DOI: 10.3217/978-3-85125-826-4-17

[11] Conolly, S., Nishimura, D. et al.: *Optimal control solutions to the magnetic resonance selective excitation problem,* IEEE Trans Med Imaging 1986;5:106-115.
[12] Aigner, C.S., Clason, C. et al.: *Efficient high-resolution RF pulse design applied to simultaneous-multislice excitation*, J Magn Reson 2016;263:33-44.
[13] Rund, A., Aigner, C.S. et al.: *Magnetic Resonance RF Pulse Design by Optimal Control with Physical Constraints*, IEEE Trans Med Imaging 2018;37:461-472.
[14] Rund, A., Aigner, C.S. et al.: *Simultaneous multislice refocusing via time optimal control,* Magn Reson Med 2018;80:1416-1428.
[15] Aigner, C.S., Rund, A. et al.: *Time optimal control-based RF pulse design under gradient imperfections*, Magn Reson Med 2020;2:561-574.
[16] van Reeth, E., Ratiney, H. et al.: *Optimal control design of preparation pulses for contrast preparation in MRI,* J Magn Reson 2017;279:39-50.
[17] Graf, C., Aigner, C.S. et al.: *Inversion pulses with B1-robustness and reduced energy by optimal control,* In Proceedings of the ISMRM, 2020.
[18] Graf, C., Soellradl, M. et al.: *Time optimal control based design of robust inversion pulses,* In Proceedings of the ISMRM, 2021.
[19] Graf, C., Rund, A. et al.: *Accuracy and performance analysis for Bloch and Bloch-McConnell simulation methods,* J Magn Reson, 2021.

Published by Verlag der TU Graz
Graz University of Technology

Proc. Annual Meeting of the Austrian Society for Biomedical Engineering 2021
DOI: 10.3217/978-3-85125-826-4-18

DEEP LEARNING BASED IMAGE REGISTRATION IN DYNAMIC CARDIAC CT USING A RECURSIVE CASCADE NETWORK APPROACH

K.A. Lara[1,2], I.A. Juárez[2], M.A. Perez[2], T. Rienmüller[1], C. Baumgartner[1]

[1]Institute of Health Care Engineering with European Testing Center of Medical Devices, Graz University of Technology, Austria
[2]Department of Biomedical Engineering, Galileo University, Guatemala

andrealh@galileo.edu

Abstract— *Registration of dynamic CT image sequences is a necessary preprocessing step for accurate assessment of multiple (patho)physiological determinants in the heart such as myocardial perfusion. In this work we present a recursive-cascade-network approach for deformable image registration using data from myocardial perfusion CT studies. A contrast-agent dependent loss function was introduced which enabled us to further improve the accuracy of sequence registration. In addition, different network configurations were evaluated, showing a good trade-off between spatial registration accuracy and image quality.*

Keywords— *myocardial perfusion, dynamic cardiac computed tomography, deep learning, sequence registration, recursive cascade network.*

Introduction

Deformable image registration (DIR) is essential for clinical applications where spatial alignment of anatomical structures is required. Such applications include image-guided procedures in diagnostics and therapy [1]. In cardiac image analysis, DIR is used in image-guided interventions, perfusion studies and procedures that requires myocardial motion tracking [2]–[4]

Cardiac perfusion studies in dynamic computed tomography (CT) are performed to qualitatively or quantitatively assess myocardial perfusion after contrast agent administration. Such studies evaluate the distribution of contrast agent in the heart and aim to identify and detect ischemic areas in the ventricle characterized by hypo attenuation (reduced CT values) in the image [5]. During a patient examination, an image sequence of the heart is obtained by using an ECG-gated protocol that usually acquires image data at the end-systolic phase. However, due to cardiac stressing, respiratory- and patient motion, spatial misalignment can be present. Hence, the registration of the whole ventricle or a selected ROI over the whole 2D/3D sequence is necessary for an accurate measurement of the time-attenuation curves. Such task has some unique challenges because of the non-rigid dynamic nature of the heart, the motion of the thorax and the lack of anatomical landmarks. Moreover, the dynamic information of the changing contrast agent introduces another degree of complexity to the problem.

Recent advances in image registration have demonstrated the potential of deep learning techniques in applications for multi-modal and inter-patient registration, and motion tracking [1], [6]. Furthermore, approaches using supervised and unsupervised learning have been introduced, however, supervised methods are hardly to be implemented due to the need of ground-truth flow-fields. In contrast, unsupervised methods do not require flow-field labels and perform image registration using a similarity measure between the fixed and the warped moving image [6]. Current state-of-the-art methods on DIR, however, use an unsupervised approach [7], [8], [9].

In this work, we further developed and evaluated the performance of a so-called Recursive-Cascade-Network [9], an established method for DIR using datasets of myocardial perfusion CT sequences. Here, we introduced a contrast-agent dependent loss function to improve the accuracy of sequence registration and evaluated the results using different network configurations. Finally, we evaluated the effects of the number of selected cascades and modified the loss function in terms of optimizing spatial alignment and image quality.

Methods

Recursive Cascade Network. Let $S = \{I_{m_i}\}_{i=0}^{N}$ denote a sequence of images, where $I_{m_i} \in \Omega \subset R^2$ and let $I_f \in S$ denote a fixed image. We want to predict a flow field $\varphi: \Omega \to \Omega$ that aligns the sequence S. The Recursive Cascade Network [9] generates a flow prediction function F which takes a fixed image I_f a moving image I_m and predicts φ This field is by the composition of flows (see Eq. 1)

$$\varphi = \varphi_1 \circ \varphi_2 \circ \cdots \circ \varphi_n \quad (1)$$

where φ_k for $k = 1,2,\dots,n$ is predicted by the k-th cascade which is a base subnetwork such as [7], [8]. The motivation of using a cascade-based-registration

Published by Verlag der TU Graz
Graz University of Technology

DOI: 10.3217/978-3-85125-826-4-18

concept is to decompose large displacements performed by φ into progressively small displacements generated by the flows $\varphi_1, \varphi_2, \ldots, \varphi_n$. The final image is obtained by successively warping of the moving image along all cascades (see Eq. 2).

$$\varphi \circ I_m = (\varphi_1 \circ \varphi_2 \circ \cdots \circ \varphi_n) \circ I_m \quad (2)$$

Loss function. As suggested in [8], the loss function in image registration often consist of a similarity loss L_{sim} for the fixed and warped image, and a regularization loss L_{reg} to smooth the terms of the field as presented in Eq. 3.

$$L_{nc}(I_f, I_m, \varphi) = L_{sim}(I_f, \varphi \circ I_m) + L_{reg}(\varphi) \quad (3)$$

However, for this application, we found that considering the loss as denoted in Eq. 3, affects negatively to regions of high contrast agent concentrations (right/left atrium or ventricle) in the image sequence. Specifically, for cases in which the contrast regions from the fixed image differ from the moving image. In these cases, contrast regions are introduced or removed from the moving image to make the warped image more similar to the fixed one. Therefore, to address this problem, we added a loss term that penalizes such changes and formulated the loss as presented in Eq. 4:

$$L_c(I_f, I_m, \varphi) = \alpha_1 L_{sim}(I_f, \varphi \circ I_m) + \alpha_2 L_{cont}(I_f, \varphi \circ I_m, C) + L_{reg}(\varphi) \quad (4)$$

The term L_{sim} is used to reduce the misalignment between I_m and I_f, and the introduced term L_{cont} is used to penalize the changes of the contrast regions in the warped image. Here, we included the parameters α_1 and α_2 to weight the losses. We experimentally found that α_1 has to be lower than 0.5 to reduce the changes in contrast regions. If $C_i \subset I_{mi}$ is a contrast region in the *i*-th moving image of the sequence *S*, we want to preserve as much information about C_i in the warped image, therefore, we want φ to modify this region only the necessary to reduce the misalignment. For this purpose, masks of the contrast agent were used and the regions generated as shown in Eq. 5

$$C_i = I_{m_i} \odot M_{m_i} \quad (5)$$

where *M* is the mask. Hence, the L_{cont} loss is defined as denoted in Eq. 6

$$L_{cont}(I_f, I_m, \varphi) = d(I_m \odot M_m, (\varphi \circ I_m) \odot M_m) + d(I_f \odot M_f, (\varphi \circ I_m) \odot M_f) \quad (6)$$

The first term penalizes the loss of contrast from the moving image in the warped image, and the second term penalizes the introduction of contrast regions into the warped image. Both cases are equally relevant for this application, therefore, we used the same weight factor, α_2, for both terms. Moreover the operator $\odot$ is the Hadamard product and *d* is a similarity metric such as correlation coefficient, mutual information or mean squares. For this application we used the *Pearson correlation coefficient*. We ran several experiments with different configurations for L_{cont}, to determine the parameters α_1 and α_2 .

Dataset. We used a dataset comprising 247 CT sequences of 2D myocardial perfusion images. The data was acquired from 19 patients undergoing regular CT examination with a Philips-iCT 256 scanner. All patients gave informed consent. The sequences where obtained from a 13 slices volume stack of slice thickness of 5 mm and matrix size of 512x512, containing 23 – 45 frames over time. However, from each volume stack only 4 to 5 slices representing the ventricular chambers were considered. For each of the frames, masks of the contrast agent (regions with high contrast agent concentrations) were obtained using a CT window of W:450 L:130. For training and validation, we used the default CT window W:750 L:90. Subsequently, we split the data on subject level, 17 for training and 2 for validation. I_f of each sequence was set to the frame with the maximum amount of contrast-agent.

Implementation. Our proposed configuration was implemented in PyTorch using a modified 2D version of the original implementation (for 3D volumes) as published in [9]. We also used the same hyper parameters and selected a VTN [7] for the base subnetworks. Our model was trained using a batch size of 32 on 2 TITAN RTX 25GB.

Experiments. The registration of the sequence was performed using different numbers of cascades and loss functions. The aim was to assess how the network configuration influences the image alignment and quality. Hence, we implemented several networks using 3, 5, 7, 10, 15 and 20 cascades, and trained them based on the loss function according to Eq. 3 and Eq. 4, respectively. The *Pearson correlation coefficient* was used as the similarity metric for L_{sim} and L_{cont}, L_{reg} is the total variation loss as used in [7] and the parameters α_1 and α_2 were set to 0.4 and 0.3, respectively. Finally, we assessed the registration performed by the networks by calculating the evaluation measures.

Evaluation Metrics. The performance of the registration was evaluated based on the accuracy of spatial alignment and the image quality. The spatial alignment was quantified using the Dice score [10] which measures the overlap between two regions and ranges between 0 and 1, where 1 means perfect

Published by Verlag der TU Graz
Graz University of Technology

DOI: 10.3217/978-3-85125-826-4-18

matching. In particular, we calculate the Dice score between the segmentations obtained from of the whole heart. Furthermore, the image similarity before and after registration was measured to assess the loss of information during the process, i.e. changes in contrast agent concentration over time. Next the Mutual Information (MI)[11] between the moving and the warped image is estimated. In addition, we included the Structural Similarity Index Measure (SSIM)[12] as an additional measure for estimating image quality, this was calculated between the moving and the warped image. The SSIM quantifies the quality between two images and ranges between 0 and 1, where 1 represents the highest quality.

Results

To demonstrate the effectiveness of the proposed model configurations, a qualitative and quantitative evaluation was performed. For qualitative evaluations we registered sequences and visualized them frame by frame by generating cines using the Graphic Interchange Format (GIF). Figure 1 shows the results of a CT perfusion sequence obtained from a 10-cascade model trained with L_{nc} (see Eq.3) and L_c (see Eq.4), respectively. The fixed (reference) image shows a good contrast between the LV cavity and myocardium, while the selected "moving" image represents a frame of the sequence before the contrast agent occurs in the LV (see first line: Fixed image shows perfect contrast between cavities and tissue. Moving image: no contrast agent appeared in the heart. Second line: Fixed image reveals perfect contrast. Moving image: agent already occurred in the right atrium and ventricle).

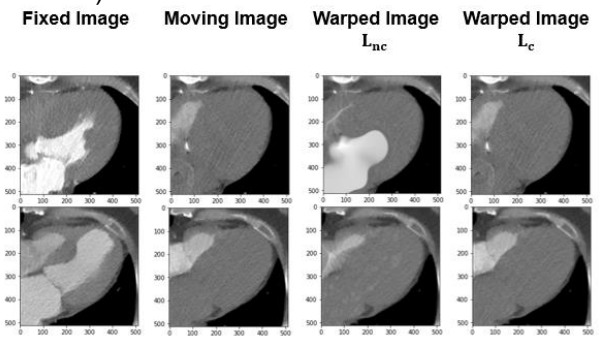

Figure 1: Results of sequence registration using a 10 cascade model with L_{nc} and L_c, respectively.

We also visualized the generated flow fields to assess the deformations performed by the models. Figure 2 shows the warped image and 10th flow field applied to the frames in the first row of Fig. 1. Here the norm of the vectors in the flow field is shown in a color scale, where red and blue represent large and small displacements, respectively. As expected, in the first column, L_{nc}, large displacements can be observed in the contrast regions while in the second column, $L_{c,}$, more uniform displacements can be seen in the contours.

The quantitative analysis was carried out using the evaluation metrics described above. We assessed the registration of the sequence by estimating the Dice score at frame level. Moreover, to investigate changes in the image quality, we calculated the MI between the moving and the warped image. The aim was to examine possible quality loss due to deformations. Figure 3 shows the mean Dice score and mean MI of one full CT perfusion sequence using a 10 cascade model trained with L_{nc} and L_c, respectively. The peak values are obtained at the frame selected as fixed.

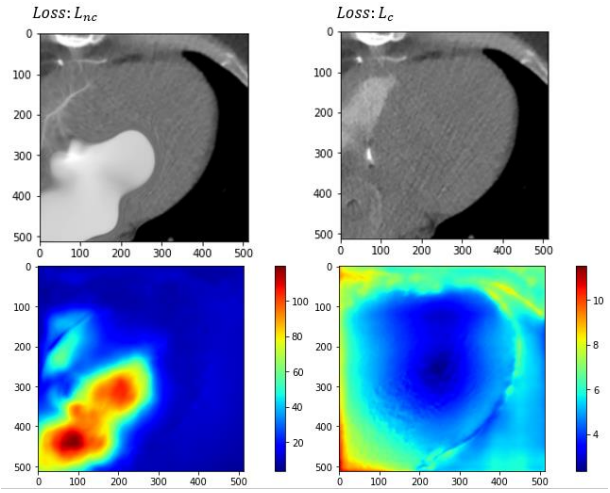

Figure 2: Warped images and flow field of two frames using a 10 cascade model.

Finally, to identify the optimal configuration in terms of the number of selected cascades we performed a quantitative analysis for all model configurations. Table 1 presents the means of the Dice score, MI and SSIM for the 3, 5, 7, 10, 15 and 20 cascade configurations obtained from the sequences in the validation set.

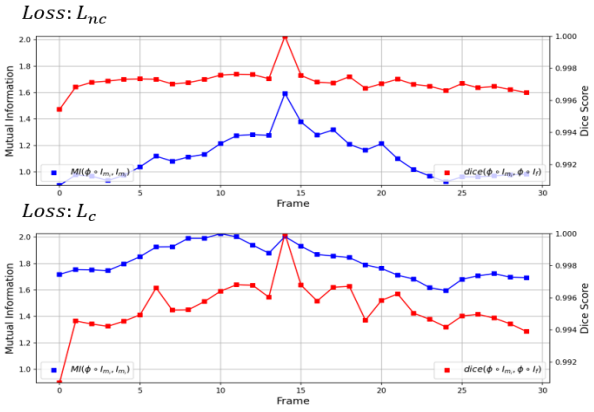

Figure 3: Evaluation metrics for one patient sequence using a 10 cascade-model

DOI: 10.3217/978-3-85125-826-4-18

Table 1: Evaluation metrics for different model configurations for the validation set.

N	Dice		MI		SSIM	
	L_{nc}	L_c	L_{nc}	L_c	L_{nc}	L_c
3	0.998	0.998	1.35	1.95	0.846	0.984
5	0.998	0.996	1.44	1.93	0.874	0.992
7	0.998	0.998	1.21	1.90	0.8	0.982
10	0.998	0.998	1.20	1.87	0.8	0.979
15	0.998	0.998	1.17	1.84	0.79	0.979
20	0.998	0.998	1.16	1.70	0.79	0.965

Discussion

In this work different model configurations of the Recursive-Cascade-Network were implemented and tested with the aim to identify the optimal configuration for the registration of myocardial perfusion CT sequences. Firstly, we evaluated the effect of the loss function at different cascade numbers. The results showed that training the model based on a loss function that does not penalizes the changes in the contrast regions negatively affects the quality of the warped image. Figure 1 shows an example of quality degradation of the warped image when the fixed and moving image have different contrast regions. It can be noted that the model deforms and introduces artifacts in these regions (see Fig 1 and Fig 2) that were observed for all investigated cascade configurations. Moreover, the models' performance was quantitatively assessed as shown in Fig 3 for a 10 cascade model as an example. Here, the quality metrics between the moving and the warped image were considerably lower in the L_{nc} model. Interestingly, the Dice score was higher than for the L_c model. However, considering only this measure as evaluation metric does not fully reflect the overall performance of the model. The latter can also be observed in Table 1, where despite achieving a high Dice score, all remaining quality measures (MI and SSMI) are lower. Finally, according to Table 1 and based on visual inspection, the best trade-off between spatial alignment and image quality can be achieved with a n=7 cascade model trained using the L_c loss function.

In summary, in this work we introduced a powerful loss function for optimizing the registration problem in cardiac CT perfusion imaging. Moreover, the effects of different model configurations were evaluated and they showed that considering the Dice score only as an evaluation metric does not fully represent the model performance of this approach in terms of spatial registration accuracy and image quality. In our future work we will investigate the effect of using other similarity metrics for the loss function and will evaluate the impact of feeding more contrast information into the network.

References

[1] Y. Fu, Y. Lei, T. Wang, W. J. Curran, T. Liu, and X. Yang, "Deep learning in medical image registration: a review," p. 48, 2020.

[2] T. Mäkelä, T. Katila, and I. E. Magnin, "A Review of Cardiac Image Registration Methods," *IEEE TRANSACTIONS ON MEDICAL IMAGING*, vol. 21, no. 9, p. 11, 2002.

[3] H. Wiputra, "Cardiac motion estimation from medical images: a regularisation framework applied on pairwise image registration displacement fields," *Scientific Reports*, p. 14, 2020.

[4] K. A. Lara Hernandez, T. Rienmüller, D. Baumgartner, and C. Baumgartner, "Deep learning in spatiotemporal cardiac imaging: A review of methodologies and clinical usability," *Computers in Biology and Medicine*, vol. 130, p. 104200, Mar. 2021, doi: 10.1016/j.compbiomed.2020.104200.

[5] D. Caruso *et al.*, "Dynamic CT myocardial perfusion imaging," *European Journal of Radiology*, vol. 85, no. 10, pp. 1893–1899, Oct. 2016, doi: 10.1016/j.ejrad.2016.07.017.

[6] G. Haskins, U. Kruger, and P. Yan, "Deep Learning in Medical Image Registration: A Survey," *Machine Vision and Applications*, vol. 31, no. 1–2, p. 8, Feb. 2020, doi: 10.1007/s00138-020-01060-x.

[7] S. Zhao, T. Lau, J. Luo, E. I.-C. Chang, and Y. Xu, "Unsupervised 3D End-to-End Medical Image Registration with Volume Tweening Network," *IEEE J. Biomed. Health Inform.*, vol. 24, no. 5, pp. 1394–1404, May 2020, doi: 10.1109/JBHI.2019.2951024.

[8] G. Balakrishnan, A. Zhao, M. R. Sabuncu, J. Guttag, and A. V. Dalca, "VoxelMorph: A Learning Framework for Deformable Medical Image Registration," *IEEE Trans. Med. Imaging*, vol. 38, no. 8, pp. 1788–1800, Aug. 2019, doi: 10.1109/TMI.2019.2897538.

[9] S. Zhao, Y. Dong, E. I.-C. Chang, and Y. Xu, "Recursive Cascaded Networks for Unsupervised Medical Image Registration," *2019 IEEE/CVF International Conference on Computer Vision (ICCV)*, pp. 10599–10609, Oct. 2019, doi: 10.1109/ICCV.2019.01070.

[10] L. R. Dice, "Measures of the Amount of Ecologic Association Between Species," *Ecology*, vol. 26, no. 3, pp. 297–302, Jul. 1945, doi: 10.2307/1932409.

[11] D. B. Russakoff, C. Tomasi, T. Rohlfing, and C. R. Maurer, "Image Similarity Using Mutual Information of Regions," in *Computer Vision - ECCV 2004*, vol. 3023, T. Pajdla and J. Matas, Eds. Berlin, Heidelberg: Springer Berlin Heidelberg, 2004, pp. 596–607. doi: 10.1007/978-3-540-24672-5_47.

[12] Z. Wang, A. C. Bovik, H. R. Sheikh, and E. P. Simoncelli, "Image Quality Assessment: From Error Visibility to Structural Similarity," *IEEE Trans. on Image Process.*, vol. 13, no. 4, pp. 600–612, Apr. 2004, doi: 10.1109/TIP.2003.819861.

Published by Verlag der TU Graz
Graz University of Technology

Proc. Annual Meeting of the Austrian Society for Biomedical Engineering 2021
DOI: 10.3217/978-3-85125-826-4-19

PREDICTING EMG ENVELOPES OF GRASPING MOVEMENTS FROM EEG RECORDINGS USING UNSCENTED KALMAN FILTERING

A.I. Sburlea[1,*], N. Butturini[2,*], G.R. Müller-Putz[1]

[1]Instituteof Neural Engineering, Graz University of Technology, Austria
[2]University of Padova, Italy
[*]these authors contributed equally

gernot.mueller@tugraz.at

Abstract—*Electromyographic (EMG) control of prosthetics is well established both in research and clinical settings. However, it remains unclear how much of the EMG information can be predicted from the electroencephalographic (EEG) signals, and used instead, for control. In this study, we used a dataset that contains simultaneously acquired EEG and EMG signals of 31 subjects performing 33 grasping conditions, and applied unscented Kalman filtering (UKF) to continuously predict the EMG grasping envelopes from the low-frequency (0.1-2 Hz) EEG. We achieved higher prediction accuracy for intermediate grasps compared to power or precision grasps. Our findings indicate the feasibility of continuously predicting EMG envelopes of grasping movements from EEG signals.*

Keywords—*EEG, EMG, grasping, UKF*

Introduction

Electromyographic (EMG)-based control of prosthetic devices has shown to be reliable in the detection of the initiation of movement, as well as in identifying the desired grasping type [1, 2]. Currently, the prosthetic control achieved with EMG signals looks promising and it is in daily use for many amputees. However, this type of control faces some limitations when the number of functional muscles or neuromuscular content in the EMG signal are not sufficient (e.g., in the case of high amputation, such as shoulder exarticulation, or severe paralysis). One way of increasing performance is by leveraging the information related to the movement from the brain activity, in addition to the muscle information. Electroencephalographic (EEG) signals contain global motor-related information that can be accessed to predict, instead of merely responding to the user's intention. Recent EEG-based brain-computer interfacing (BCI) studies have shown the feasibility of discriminating between several types of movements [3-5]. Movement covariates, such as velocity of hand movement, have also been decoded from low-frequency EEG activity [6]. Furthermore, we have shown in a previous study that EEG and EMG activity share similarities during different stages of grasping [7]. Adaptive approaches for sensorimotor control have attracted a lot of attention over the last decades [8, 9]. Recent studies that use Kalman filtering approaches show promising results in terms of movement covariates' prediction from EEG activity [10, 11].

In this study, we investigated the feasibility of predicting the EMG envelopes of extrinsic hand muscles in a wide range of grasping movements from EEG signals. We conducted this study on a previously recorded dataset [7]. EEG and EMG activity were recorded simultaneously. We studied the amplitude patterns of the EEG signals in the delta frequency band (0.1-2 Hz) and used an unscented Kalman filter for the prediction. Our findings show the feasibility of this approach and could be informative for more intuitive and reliable upper-limb neuroprosthetic control.

Methods

A. Dataset description

A previously recorded dataset [7] has been used in this study. The dataset contains simultaneously acquired neural (EEG) and behavioral (muscle and kinematic) data of 31 participants, in a task that involves observation and execution of 33 different grasping movements. Figure 1A illustrates the structure of the experimental protocol.

During the fixation period, participants were instructed to focus their gaze on a cross located in the middle of the screen and avoid eye movements for three seconds. Next, during the observation phase which lasted four seconds, participants were presented with a static image showing a hand in a final grasping position together with the grasped object as shown in Figure 1B. During the execution phase which was also four seconds long, participants were instructed to focus their gaze on the "x" symbol located in the middle of the screen and perform the grasping movement that they had observed during the previous phase. Figure 1C shows the pictograms of the 33 grasping movements with their ordinal numbers. The order of the grasping conditions (blocks) was randomized among subjects.

EEG and electrooculographic (EOG) data was recorded using a 64-channel ActiCap System with two BrainAmp amplifiers (BrainProducts, Germany). The ground sensor was placed on AFz and the reference sensor on the right mastoid. Muscle activity was recorded with a Myo armband (Thalmic Labs Inc., Ontario, Canada). The armband was located on the right arm close to the elbow, above the extrinsic hand muscles.

Published by Verlag der TU Graz
Graz University of Technology

 DOI: 10.3217/978-3-85125-826-4-19

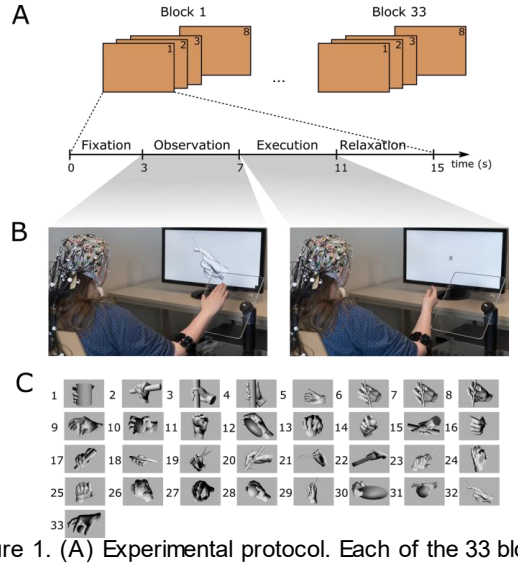

Figure 1. (A) Experimental protocol. Each of the 33 blocks contained eight consecutive repetitions (trials) of the same grasp. Each trial had four phases: fixation, observation, execution and relaxation. (B) Experimental setup. Photos of one participant during the observation and execution phases, and the materials used during recording. (C) Pictograms of the grasping conditions.

B. EEG and EMG data processing

For all data preprocessing and analyses, we used Matlab R2016b (Mathworks, Inc. USA). EEG data was first filtered using a Butterworth fourth-order, zero-phase, band-pass filter between 0.1–40 Hz and then downsampled to 100 Hz. We rejected the trials in which the task was incorrectly performed. From the EEG and EMG data we extracted 10-second long trials consisting of the last two seconds from the fixation period and the entire observation and execution periods. Next, we performed a similar cleaning processing pipeline as described in [7]. Then, we filtered the EEG data in the frequency range between 0.1–2 Hz using a zero-phase Butterworth band-pass filter of fourth-order. The eight EMG data channels were processed using Hilbert transform, standardized using z-score and, finally, the envelope of the data was computed. For both types of the data we reordered the groups of trials in a common order between subjects, as depicted in Figure 1C.

For each of the subjects we built an EEG-based measurement matrix by concatenating all the 10-second long trials, associated with different blocks of grasping conditions. In a similar way, the EMG data was concatenated across all trials to generate an EMG state vector (8 EMG channels by time samples for 264 trials, associated with 33 grasping conditions × 8 repetitions).

We used a hybrid approach similar to the one described in [12]. Like the standard Kalman filter, the n-th order unscented Kalman filter (UKF) [13] inferred the hidden state (the EMG envelope of the desired grasping) from the observations (low-frequency EEG amplitudes). The state transition model predicted the hidden state at the current time step given the state at the previous n time steps, where n is the order of the autoregressive model.

The standard Kalman filter is described by the following equations:

$$x_k = Fx_{k-1} + w_{k-1} \quad (1)$$

$$y_k = Hx_k + v_{k-1} \quad (2)$$

where the random variables w and v represent the process and measurement noise, respectively. They are assumed to be independent (of each other), white, and with normal probability distributions. The matrix F in (1) relates the state at the previous time step k-1 to the state at the current step k. The matrix H in (2) relates the state to the measurement. We choose a multivariate autoregression (MVAR) [14] to model the state transition equation because the trend of the EMG signal is assumed to be linear. The formula that describes the model is the following:

$$x_n = \sum_{i=1}^{m} x_{n-i} A_i(n) + e_n \quad (3)$$

where x_n is the nth sample of a d-dimensional time series, each $A_i(n)$ is a d-by-d matrix of coefficients (weights) and e_n is additive Gaussian noise. The neural tuning model relates the status of the system and the measures. To infer the relation between EEG and EMG signals we applied partial-least squares (PLS) as described in [15].

For each grasping condition, we performed an 8-fold cross validation (CV) among the EEG repetitions (7 trials for training and 1 trial for prediction). We used an n-th order UKF with a number of taps equal to the order of the fitted MVAR model (the model order was 3 or 4). For the PLS regression we have used the 10 previous lags of the EEG data to estimate the actual value of the EMG signal. Ten lags correspond to a time window equal to 0.4 s and we choose a fixed number of components (30), based on the level of explained variance (larger than 99%). Afterwards, we computed the mean over the different cross-validated predictions, for each trial and grasping condition.

C. Evaluation metrics

We define x_t as the measurement value and y_t as the prediction value at time t. We used Pearson correlation (r) and mean absolute error (MAE) to evaluate the quality of the EMG estimation with respect to the original EMG signal. Since MAE is a scale dependent metric, we expressed the prediction error in percentages and normalize it to the scale (the difference between maximum and minimum amplitudes) of the actual EMG envelope. We refer to the metric as normalized MAE (nMAE). The higher the r and the lower the nMAE values are, the better the prediction. Chance level values for our metrics were estimated by applying the 8-fold CV to shuffled data. We broke the association between x and y by randomly exchanging y across trials. The shuffling and 8-fold CV

Published by Verlag der TU Graz
Graz University of Technology

DOI: 10.3217/978-3-85125-826-4-19

procedure was repeated 100 times. Then, we then computed the α = 0.05 confidence interval for the r and nMAE distributions.
Next, we calculated the values of these two metrics for each EMG channel, grasp condition and subject. Finally, we present our prediction results for categories of grasps. Specifically, we group the 33 grasp conditions according to the more conventional grasping categorization into power, precision and intermediate grasp type, and according to the position of the thumb during grasping, adducted or abducted.

Results

A. Prediction accuracy of EMG envelopes

Figure 2 shows three cases of EMG envelope prediction. On the left plot we show an example of a good prediction (r = 0.65, nMAE = 20.4%), in which the overall shape of the predicted curve visually resembles the actual one. Similarly, the middle plot shows an average example of prediction (r = 0.41 and nMAE = 36.6%). In this case, the prediction is better during the grasping execution phase (from second 6 to 10) than in the other phases. Finally, the right plot shows an example of poor prediction (r = -0.13 and nMAE = 40%). In this example, the predicted signal captures the small EMG activation during the observation period, but fails to infer the muscle activation during the movement execution phase.

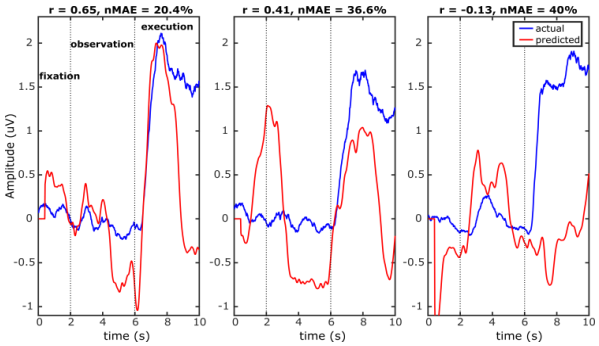

Figure 2. Examples of EMG single channel and single trial envelope estimation. Blue curves indicate actual EMG envelopes and red curves indicate predicted signals.

B. Correlation and normalized mean absolute error

Figure 3 shows median values of the two metrics for each grasping condition, across subjects. The highest r = 0.36 corresponds to grasp 11 (power sphere grasping), while the lowest nMAE value = 26% corresponds to grasp 16 (lateral grasping). We show the relation between all grasps relative to the two metrics of prediction. Dotted black lines indicate the overall median values for the two metrics. Dotted red lines show median chance level values across subjects and grasps. While it is informative to evaluate the prediction accuracy for each grasp, we believe that grouping the grasps into categories can be more interpretable and improve the general understanding of our findings. Hence, Figure 4 presents the results of the EMG envelope prediction for different categories of grasps. On the left side, the intermediate type of grasps has the lowest median nMAE = 27% compared to the power (nMAE = 28.7%) and precision (nMAE = 30.2%) types, and the highest correlation value r = 0.21, followed by r = 0.2 for power grasps and r = 0.18 for precision grasps. Regarding the categorization based on thumb's position, we found a better median prediction for the adducted grasps (r = 0.2, nMAE = 27.7%) than for the abducted grasps (r = 0.19, nMAE = 30%).

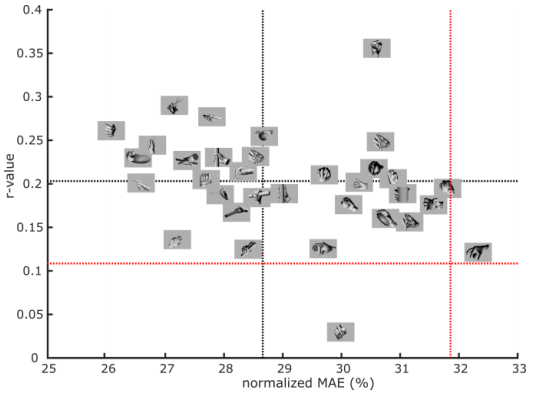

Figure 3. Scatter plot representation of all grasping conditions in terms of nMAE and r. The dotted black lines indicate the overall median values among grasping conditions for the two evaluation metrics: nMAE (vertical) and r (horizontal). The dotted red lines indicate the median chance level for the two metrics across subjects and grasps.

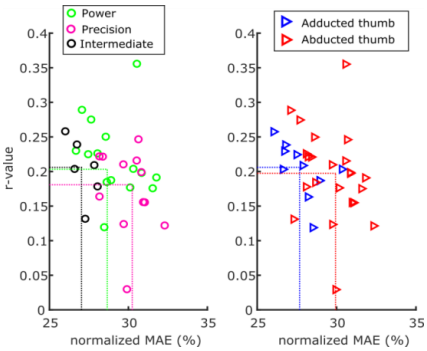

Figure 4. Prediction evaluation in terms of r and nMAE for two categorizations: Left. the type of grasp (power, precision and intermediate); Right. the position of the thumb (adducted and abducted). Dotted vertical and horizontal lines indicate median values for different groups of grasps.

Discussion

Our findings show the feasibility of predicting grasping EMG envelopes of extrinsic hand muscles from EEG signals using an UKF. In this study, we showed, for the first time, that EMG envelopes of a wide range of grasping conditions, involving periods of rest and movement, can be continuously predicted from low-frequency EEG amplitudes. Based on the presented categorizations of grasps we found a smaller predic-

Published by Verlag der TU Graz
Graz University of Technology

DOI: 10.3217/978-3-85125-826-4-19

tion error for the grasps in which the position of the thumb was adducted. Moreover, we observed that the EMG envelopes of intermediate grasps can be more successfully predicted from the brain activity, than power or precision grasps.

Previous studies have shown the ability of an UKF approach to infer EMG envelopes from low-frequency EEG amplitudes while performing a continuous ground walking task on different terrains [12, 16]. They obtained an overall r among subjects and muscles of 0.236, with an SNR of 0.8 dB. In the current study, we found a similar median r of 0.2 and an nMAE of 28.6%. However, a direct comparison between their findings and the ones of the current is not straightforward due to the differences in the performed task (other groups of muscles and different neural processes involved) and different number of movement repetitions.

Another study evaluated the prediction accuracy of grasping EMG envelopes of intrinsic hand muscles from firing rates in monkeys [17]. Their measurement consisted of more than 100 repetitions of each grasp leading to a better prediction and larger r than the ones reported in the current study. Nevertheless, comparison is again difficult due to further differences in signal acquisition modalities, measured hand muscles and signal processing.

Our findings show different levels of prediction accuracy among different grasps (Figure 3 and 4), as well as at single EMG channel level (Figure 2). We used median values to obtain robust global estimates in such cases of variability. Moreover, we employed r and nMAE as two complementary metrics for our prediction accuracy, evaluating both the phase and the amplitude similarity between the actual and the predicted values. Even though the number of grasps from each category is not the same, we observed that intermediate grasps have a lower median nMAE value than power or precision grasps. This observation could be due to the involvement of the wrist as an additional joint when performing intermediate grasp. Previous findings [3] have shown that EEG activity can be used to separate hand movements that involve different number of joints.

We have shown the feasibility of using UKF to predict grasping EMG envelopes from EEG activity; however, a better prediction could be achieved by increasing the number of movement repetitions for each grasp type, on which the model is trained. Moreover, the size of the prediction window plays also an important role, trading off precision to delay in the final prediction. In clinical setups, it is important to accommodate the delay between the EEG-based prediction and the actual triggering of the neuroprosthesis. Hence, different prediction windows could be evaluated in the future to enhance the control. These advances could lead to an intuitive and reliable interface that allows the user to reach autonomy in movement.

Acknowledgements

This research was supported by funding from the European Research Council (ERC-CoG 2015 681231 'Feel Your Reach').

References

[1] Ninu, A., *et al.* Closed-loop control of grasping with a myoelectric hand prosthesis: Which are the relevant feedback variables for force control?. *IEEE Transactions on Neural Systems and Rehabilitation Engineering, 22*(5), 1041-1052. (2014).

[2] Scheme, E. & Englehart, K. Electromyogram pattern recognition for control of powered upper-limb prostheses: state of the art and challenges for clinical use. *J. Rehabil. Res. Dev.* **48**, 643–659 (2011).

[3] Schwarz, A., *et al.* Decoding natural reach-and-grasp actions from human EEG. *J. Neural Eng.* **15**, 016005 (2018).

[4] Ofner, P., *et al.* Upper limb movements can be decoded from the time-domain of low-frequency EEG. *PLoS One* **12**, e0182578 (2017).

[5] Iturrate, I. *et al.* Human EEG reveals distinct neural correlates of power and precision grasping types. *Neuroimage* **181**, 635–644 (2018).

[6] Kobler, R. J., Sburlea, A. I. & Müller-Putz, G. R. Tuning characteristics of low-frequency EEG to positions and velocities in visuomotor and oculomotor tracking tasks. *Sci. Rep.* **8**, 17713 (2018).

[7] Sburlea, A. I. & Müller-Putz, G. R. Exploring representations of human grasping in neural, muscle and kinematic signals. *Sci. Rep.* **8**, 16669 (2018).

[8] Wolpert, D. M., Ghahramani, Z. & Jordan, M. I. An internal model for sensorimotor integration. *Science* **269**, 1880–1882 (1995).

[9] Antelis, J. M., *et al.* On the usage of linear regression models to reconstruct limb kinematics from low frequency EEG signals. *PLoS One* **8**, e61976 (2013).

[10] Schlögl, A., Vidaurre, C. & Müller, K.-R. Adaptive Methods in BCI Research - An Introductory Tutorial. *The Frontiers Collection* 331–355 (2009).

[11] Nakagome, S., *et al.* Prediction of EMG envelopes of multiple terrains over-ground walking from EEG signals using an unscented Kalman filter. in *2017 IEEE International Conference on Systems, Man, and Cybernetics (SMC)* (2017).

[12] Li, Z. *et al.* Unscented Kalman filter for brain-machine interfaces. *PLoS One* **4**, e6243 (2009).

[13] Wan, E. A. & Van Der Merwe, R. The unscented Kalman filter for nonlinear estimation. in *Proceedings of the IEEE 2000 Adaptive Systems for Signal Processing, Communications, and Control Symposium (Cat. No.00EX373)*

[14] Anderson, C. W., Stolz, E. A. & Shamsunder, S. Multivariate autoregressive models for classification of spontaneous electroencephalographic signals during mental tasks. *IEEE Transactions on Biomedical Engineering* **45**, 277–286 (1998).

[15] Ofner, P., & Müller-Putz, G.R. Using a noninvasive decoding method to classify rhythmic movement imaginations of the arm in two planes. *IEEE Transactions on Biomedical Engineering* 62.3 (2014): 972-981.

[16] He, Y. *et al.* An integrated neuro-robotic interface for stroke rehabilitation using the NASA X1 powered lower limb exoskeleton. *Conf. Proc. IEEE Eng. Med. Biol. Soc.* **2014**, 3985–3988 (2014).

[17] Ethier, C., *et al.* Restoration of grasp following paralysis through brain-controlled stimulation of muscles. *Nature* **485**, 368–371 (2012).

Published by Verlag der TU Graz
Graz University of Technology

Proc. Annual Meeting of the Austrian Society for Biomedical Engineering 2021
DOI: 10.3217/978-3-85125-826-4-20

DIRECTED CONNECTIVITY ANALYSIS IN PEOPLE WITH SPINAL CORD INJURY DURING ATTEMPTED ARM AND HAND MOVEMENTS

Kyriaki Kostoglou[1], Gernot Müller-Putz[1]

[1]Institute of Neural Engineering, Graz University of Technology, Austria

kkostoglou@tugraz.at

Abstract— *We investigated the cortical connectivity patterns that arise in subjects with spinal cord injury (SCI) during attempted hand and arm movements using multivariate autoregressive (MVAR) models and electroencephalographic (EEG) signals. The MVAR models were fitted using multiple trials from multiple subjects in order to capture general connectivity characteristics during different type of attempted movements. Based on the results we detected two main sources of information: the somatosensory and the primary motor area. Changes in directional connectivity between different regions before and after cue onset were found to be informative in terms of the type of movement attempted by the SCI participants.*

Keywords— *multivariate autoregressive model, directed coherence, EEG, spinal cord injury, attempted movement*

Introduction

Multivariate autoregressive (MVAR) models have been extensively used to capture couplings between different time-series [1]–[3]. They provide measures of interdependency but also causality in the frequency domain, which is an important aspect when investigating directional connectivity in the brain (i.e., how brain regions send and receive information).

Herein, we applied MVAR analysis in electroencephalographic (EEG) signals projected, however, on the source space for improved localization of brain sources. The EEG signals were acquired from spinal cord injury (SCI) subjects during attempted arm and hand movements. It has been previously suggested that motor cortex areas in SCI subjects can be activated during motor attempts of the paralyzed limbs [4]. This has enabled the use of EEG-based brain-computer interfaces (BCI) to enhance restoration of movements lost after SCI [5], [6]. Our analysis was mainly exploratory, and our main goal was to capture general oscillatory interactions between different cortex regions before and after cue onset. To our knowledge, there has been only one study by Astolfi et al. [7] that has investigated SCI connectivity during attempted foot movements using MVAR models. Herein, we focused on detecting possible connectivity patterns that can be linked to the different type of attempted hand/arm movements. This information is important in order to establish MVAR-based measures as possible features for BCI applications.

Methods

Data Acquisition

61-channel EEG signals were obtained from 10, originally right-handed, SCI participants (median age of 54±18.5) as described in [5] (available at https://doi.org/10.1038/s41598-019-43594-9). The neurological level of injury ranged from C1-C7. At the beginning of each trial, a fixation cross was initially presented on a black screen, along with a beep sound. The class cue was displayed 2s after the trial initialization. The participants were asked to attempt unilaterally one of the following arm/hand movements: pronation, supination, palmar grasp, lateral grasp or hand open. Each trial lasted for 5s.

Data Preprocessing

The recorded EEG signals were pre-processed using EEGLAB and Matlab. First, we bandpass-filtered the signals between 0.3 and 70 Hz using a 4th order, zero-phase, Butterworth filter. Trials with dominant impulsive noise characteristics were rejected using thresholding, as well as techniques based on abnormal joint probabilities and kurtosis [5]. Next, we performed independent component analysis (ICA) to remove stationary artefactual components such as blinks, saccades, and muscle movements. Source localization was carried out in Brainstorm [8] using minimum norm imaging and sLoreta. To examine connectivity related to motor function, we extracted 26 spatially segregated signals (13 for the left hemisphere and 13 for the right hemisphere) from anatomical regions defined by the Brodmann atlas (Fig. 1). These 26 anatomical regions correspond to the somatosensory area, the primary motor area, the pre-motor area, the Broca's area, the visual area and the perirhinal area (Fig.1). The extracted signals were then used to fit MVAR models using multiple trials from all participants for different attempted movements.

MVAR

In an MVAR model, each variable is predicted by the linear combination of its past values, as well as the history of all other variables. An M-dimensional MVAR of order p can be expressed as [9],

$$\boldsymbol{y}(n) = \sum_{k=1}^{p} \boldsymbol{A}_k \boldsymbol{y}(n-k) + \boldsymbol{\varepsilon}(n) \qquad [1]$$

Published by Verlag der TU Graz
Graz University of Technology

DOI: 10.3217/978-3-85125-826-4-20

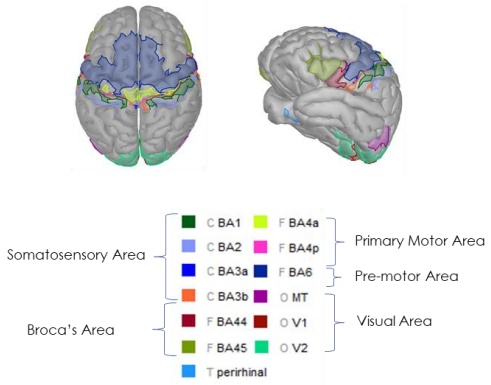

Somatosensory Area	BA1
	BA2
	BA3a
	BA3b
Primary Motor Area	BA4a (anterior)
	BA4p (posterior)
Pre-motor Area	BA6
Broca's Area	BA44 (pars opercularis)
	BA45 (pars triangularis)
Visual Area	MT (middle temporal)
	V1 (primary)
	V2 (secondary)
Perirhinal Area	BA35-BA36

Figure 1: Regions of Brodmann atlas

where $\boldsymbol{y}(n) = [y_1(n) \quad \dots \quad y_M(n)]^{\boldsymbol{T}} \in \boldsymbol{R}^{M\times 1}$ is a vector containing the values of M time-series at time n (i.e., the 26 source signals in our case). $\boldsymbol{A}_k$ is the so-called autoregressive matrix for $k = 1,..,p$ and $\boldsymbol{\varepsilon}(n)$ is the MVAR driving process noise which is assumed to be zero-mean and white. Equation 1 can be reformulated as,

$$\boldsymbol{y}(n) = \boldsymbol{A}\boldsymbol{\varphi}(n) + \boldsymbol{\varepsilon}(n) \qquad [2]$$

where $\boldsymbol{A} = [\boldsymbol{A}_1 \quad \dots \quad \boldsymbol{A}_p] \in \boldsymbol{R}^{M\times Mp}$ and $\boldsymbol{\varphi}(n) = [\boldsymbol{y}(n)^{\boldsymbol{T}} \quad \dots \quad \boldsymbol{y}(n-p)^{\boldsymbol{T}}]^{\boldsymbol{T}} \in \boldsymbol{R}^{Mp\times 1}$.
In this work, we used multiple trials from all participants to fit MVAR models that describe different type of attempted movements. Therefore, we expressed $\boldsymbol{y}(n)$ and $\boldsymbol{\varphi}(n)$ as,

$$\boldsymbol{y}(n) = [\boldsymbol{y}^1(n) \quad \dots \quad \boldsymbol{y}^K(n)]^{\boldsymbol{T}} \in \boldsymbol{R}^{M\times K} \qquad [3]$$

$$\boldsymbol{\varphi}(n) = \left[\boldsymbol{y}(n)^{\boldsymbol{T}} \quad \dots \quad \boldsymbol{y}(n-p)^{\boldsymbol{T}}\right] \in \boldsymbol{R}^{Mp\times K} \qquad [4]$$

where $\boldsymbol{y}(n)$ represents the M source signals concatenated from all K trials at time point n. The trial-based MVAR coefficients were computed using ordinary least-squares estimation.

MVAR model order selection

One important step in MVAR estimation is the selection of the model order p. Herein, we used the multivariate Akaike Information Criterion (AIC) defined as [10],

$$AIC(p) = N \cdot log\left(\left|\widehat{\boldsymbol{\Sigma}}\right|\right) + 2 \cdot d \qquad [5]$$

where N is the total number of samples, $\left|\widehat{\boldsymbol{\Sigma}}\right|$ is the determinant of the covariance of the residuals and $d = M^2p$ the total number of MVAR coefficients. The optimal p was selected by minimizing the AIC score described in Eq.(5).

MVAR coupling measures

To extract measures of coupling and directionality in the frequency domain, we applied the Fourier transform on Eq.2,

$$\boldsymbol{Y}(f) = \boldsymbol{H}(f)\boldsymbol{E}(f) = [\boldsymbol{I} - \boldsymbol{A}(f)]^{-1}\boldsymbol{E}(f) \qquad [6]$$

where $\boldsymbol{A}(f) = \sum_{k=1}^{p} \boldsymbol{A}_k\, e^{-i2\pi fkT}$ is the coefficient matrix and $\boldsymbol{H}(f) = [\boldsymbol{I} - \boldsymbol{A}(f)]^{-1} = \overline{\boldsymbol{A}}(f)^{-1}$ is the transfer matrix in the frequency domain. The relationship between $\boldsymbol{H}(f)$ and $\boldsymbol{A}(f)$ allows frequency domain measures of coupling to be derived easily using solely the coefficients of the MVAR model. The power spectral density matrix of the MVAR process can be written as,

$$\boldsymbol{S}(f) = \boldsymbol{H}(f)\boldsymbol{\Sigma}\boldsymbol{H}^{\boldsymbol{H}}(f) \qquad [7]$$

where $\boldsymbol{H}^{\boldsymbol{H}}(f)$ is the Hermitian of $\boldsymbol{H}(f)$ and $\boldsymbol{\Sigma} = diag([\sigma_1^2 \quad \dots \quad \sigma_M^2])$ is the covariance matrix of the process noise $\boldsymbol{\varepsilon}$. Based on the power spectral density matrix, we can generate smoothed versions of the power spectral density of the signals under consideration using the MVAR model as interpolating function.
The transfer matrix, the coefficient matrix as well as the power spectral density matrix can be also used to extract various coupling and causality measures such as coherence (COH) [11], directed coherence (DC) [12], partial coherence (PCOH) [13] and partial directed coherence (PDC) [14]. For the purposes of this work, we only considered DC, which describes causality as direct and indirect power contributions from one time-series to the other. DC from time-series D (i.e., driver) to time-series T (i.e., target) ($D \rightarrow T$) at frequency f is computed as [12],

$$DC_{TD}(f) = \frac{\sigma_D \cdot H_{TD}(f)}{\sqrt{\sum_{m=1}^{M} \sigma_m^2 \cdot |H_{Tm}(f)|^2}} \qquad [8]$$

The total information outflow from a particular region can be defined as the sum of statistically significant connections (e.g., DC values) towards all other cortical regions [1],

$$Outflow_D(f) = \sum_{T=1,T\neq D}^{M} DC_{TD}{}^{*}(f) \qquad [9]$$

where $DC_{TD}{}^{*}(f)$ refers to statistically significant DC values from time-series D to time-series T. To evaluate statistical significance, we permuted randomly 50 times the order of the source signals in each trial and estimated MVAR models based on the acquired trials. This way we destroyed possible

Published by Verlag der TU Graz
Graz University of Technology

DOI: 10.3217/978-3-85125-826-4-20

causal interactions between different regions and generated a reference DC distribution under the null hypothesis of no ''causality'' from time series D to T. The significance of the DC values evaluated from the actual data was then assessed using the reference DC distribution. The estimated DC and outflow values were finally averaged over different cortex areas. The 12 regions of interest (ROI) were the left and right hemisphere somatosensory, broca's, primary motor, pre-motor, visual and perirhinal areas.

Results

The MVAR framework was applied on two different time periods: before and after cue onset. The optimal model order (*p*) varied from 7-9 (for a sampling rate of 256Hz and for different MVAR models fitted on different attempted movements). The estimated DC values averaged over different type of attempted movements in the frequency range of [0.3 70] Hz can be found in Fig. 2. In the depicted matrices the columns and rows represent the driver and target ROIs, respectively. For example, the first column is the DC from left hemisphere (L) somatosensory area to all other regions (denoted in the y-axis of the matrix). Figure 3 illustrates the total information outflow (Eq. 9) from each ROI in different frequency bands (*delta* [0.3-4] Hz, *theta* [4-7] Hz, *alpha* [8-14] Hz, *beta* [14-32] Hz, *gamma* [32-60] and *broad* [0.3-70] Hz) and for different type of attempted movements before and after cue onset.

The obtained results were subjected to a three-way analysis of variance (ANOVA) examining the effect of attempted movement, frequency band and ROI on the DC changes before and after cue onset (i.e., the dependent variable was defined as $DC_{TD}(f)^{(after\ cue\ onset)} - DC_{TD}(f)^{(before\ cue\ onset)}$). The resulting *p*-values for the independent variables and their interactions can be found in Tab. 1.

Table 1: Three-way ANOVA examining the effect of attempted movement, frequency band and ROI on the DC changes after cue onset. $p < 0.05$ indicates strong effects.

Source	*p*-value
Attempted movement	0.086
Frequency band	0.011
ROI	0
Attempted movement ∗ Frequency band	0.984
Attempted movement ∗ ROI	0
Frequency band ∗ ROI	0

Discussion

Figs. 2 and 3 provide important information regarding the main sources/hubs of information. We detected overall increased outflow from the somatosensory and primary motor areas before and after cue onset. The outflow from the somatosensory area was elevated mainly in the beta and alpha band, whereas the outflow from the primary motor cortex was more pronounced in the delta band. The somatosensory area outflow was overall higher prior to cue onset. In contrast, the primary motor area outflow increased after cue onset, especially in the delta band. The main receivers of somatosensory information were the primary motor, the broca's, the perirhinal and the somatosensory area itself. On the other hand, the main receivers of primary motor information were the visual, the perirhinal and the somatosensory area. We also detected an ipsilateral pattern whereby dominant sources of information originated mainly from the right hemisphere.

Based on Fig.3, the outflow from different ROIs and for different type of attempted movements exhibited similar characteristics. However, we detected significant differences in DC changes before and after cue onset (Tab. 1). The three-way ANOVA returned a *p*-value of 0.086 (i.e., weak effect) for the factor 'attempted movement' and a *p*-value of 0 (i.e., strong effect) for the interactions between 'attempted movement' and 'ROI', indicating that the mean DC change can be explained better when considering both type of movement and driving ROI. An important aspect that should be pointed out here is that the exact attempt onset after the cue is not exactly known and this could also affect the results (i.e., the effect of the factor 'attempted movement' by itself could be more significant).

Conclusions

We estimated directional connectivity and information flow in SCI subjects during attempted hand and arm movements. Our results indicate that the most prominent sources of information were the somatosensory area prior to cue onset (in the beta/alpha band) and the primary motor area after cue onset (mainly in the delta band). DC and outflow measures exhibited the same patterns for different type of attempted movements. However, DC changes before and after cue onset in different ROIs were more informative in terms of the type of movement attempted by the SCI participant. This implies that the time- and spatial- varying aspects of DC could be used as features to improve decoding performance in BCI applications [5]. Future work involves DC estimation in a time-varying (TV) context using nonstationary MVAR models [2] and attempted movement classification using various TV-MVAR based connectivity measures.

References

[1] L. Astolfi *et al.*, "Comparison of different cortical connectivity estimators for high-resolution EEG recordings," *Hum. Brain Mapp.*, vol. 28, no. 2, pp. 143–157, 2007.

[2] K. Kostoglou *et al.*, "A novel framework for estimating time-varying multivariate autoregressive models and application to cardiovascular responses to acute exercise," *IEEE Trans. Biomed. Eng.*, pp. 1–1, 2019, doi: 10.1109/TBME.2019.2903012.

Published by Verlag der TU Graz
Graz University of Technology

DOI: 10.3217/978-3-85125-826-4-20

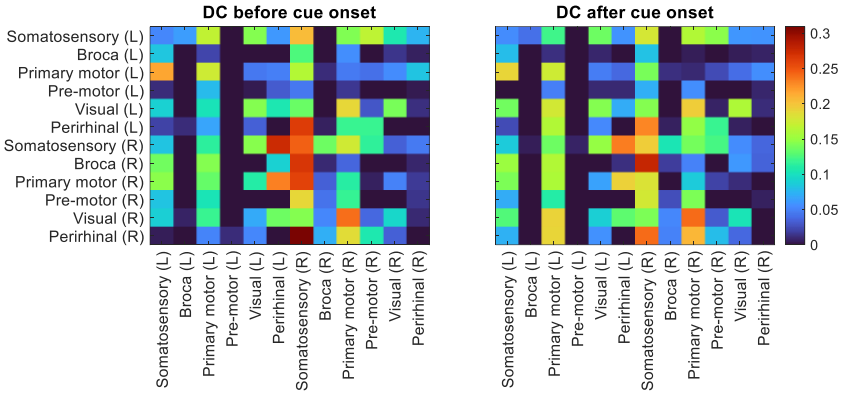

Figure 2: Averaged DC values over all attempted movements before (left panel) and after (right panel) cue onset in the frequency range of [0.3 70Hz]. The columns represent the drivers and the rows the targets. (L) and (R) refers to left and right hemisphere.

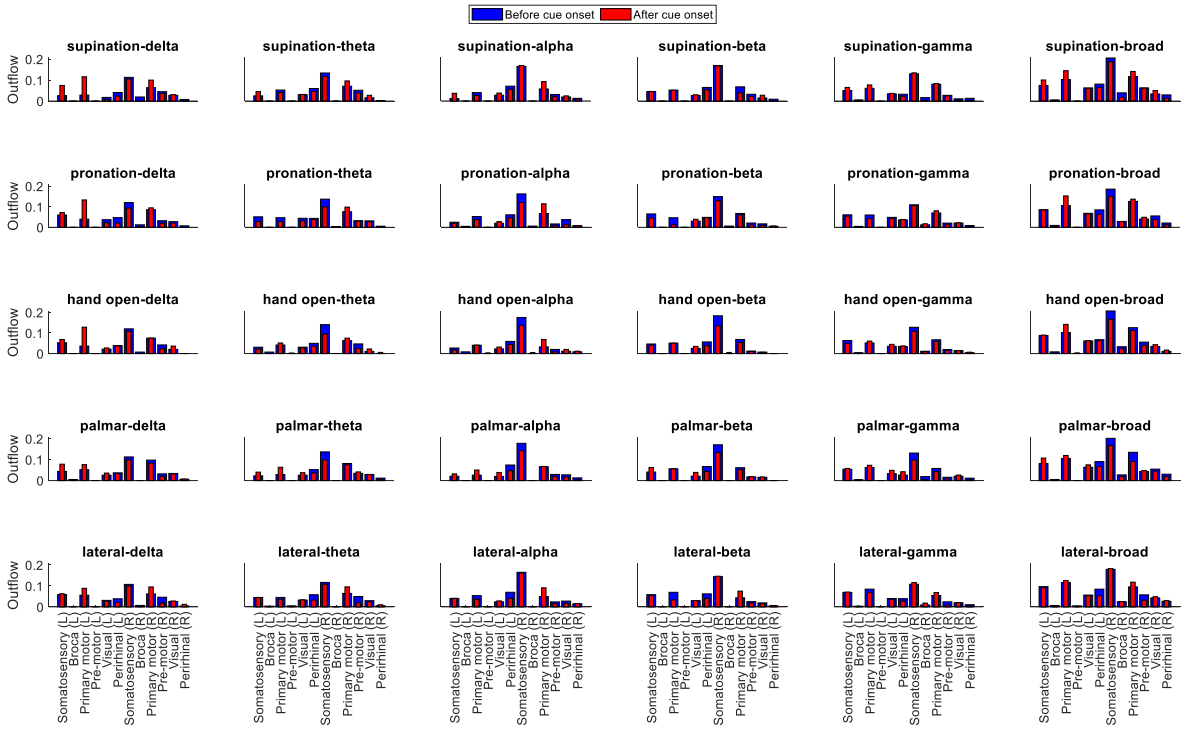

Figure 3: Total information outflow before (blue) and after (red) cue onset in the delta (first column), theta (second column), alpha (third column), beta (fourth column), gamma (fifth column) and broad (sixth column) and for different type of attempted movements i.e., supination (first row), pronation (second row), hand open (third row), palmar grasp (fourth row) and, lateral grasp (fifth row).

[3] L. Faes and G. Nollo, “Multivariate frequency domain analysis of causal interactions in physiological time series,” in *Biomedical Engineering, Trends in Electronics, Communications and Software*, InTech, 2011.
[4] S. Shoham *et al.*, “Motor-cortical activity in tetraplegics,” *Nature*, vol. 413, no. 6858, p. 793, 2001.
[5] P. Ofner *et al.*, “Attempted Arm and Hand Movements can be Decoded from Low-Frequency EEG from Persons with Spinal Cord Injury,” *Sci. Rep.*, vol. 9, no. 1, pp. 1–15, 2019.
[6] G. R. Müller-Putz *et al.*, “Towards non-invasive brain-computer interface for hand/arm control in users with spinal cord injury,” *2018 6th Int. Conf. Brain-Computer Interface, BCI 2018*, vol. 2018-Janua, pp. 1–4, 2018.
[7] L. Astolfi *et al.*, “Study of the time-varying cortical connectivity changes during the attempt of foot movements by spinal cord injured and healthy subjects,” *Proc. 31st Annu. Int. Conf. IEEE Eng. Med. Biol. Soc. Eng. Futur. Biomed. EMBC 2009*, pp. 2208–2211, 2009, doi: 10.1109/IEMBS.2009.5334878.
[8] F. Tadel *et al.*,, “Brainstorm: a user-friendly application for MEG/EEG analysis,” *Comput. Intell. Neurosci.*, vol. 2011, 2011.
[9] H. Lütkepohl, *New introduction to multiple time series analysis*. Springer Science & Business Media, 2005.
[10] L. Faes, S. Erla, and G. Nollo, “Measuring connectivity in linear multivariate processes: definitions, interpretation, and practical analysis,” *Comput. Math. Methods Med.*, vol. 2012, 2012.
[1 1] S. M. Kay, *Modern spectral estimation*. Pearson Education India, 1988.
[12] L. A. Baccala *et al.*, “Studying the interaction between brain structures via directed coherence and Granger causality,” *Appl. Signal Process.*, vol. 5, no. 1, p. 40, 1998.
[13] K. Yacoub, “Relationship between multiple and partial coherence functions,” *IEEE Trans. Inf. Theory*, vol. 16, no. 6, pp. 668–672, 1970.
[14] L. A. Baccalá, K. Sameshima, and D. Y. Takahashi, “Generalized partial directed coherence,” in *2007 15th International Conference on Digital Signal Processing*, 2007, pp. 163 –166.

Published by Verlag der TU Graz
Graz University of Technology

Proc. Annual Meeting of the Austrian Society for Biomedical Engineering 2021
DOI: 10.3217/978-3-85125-826-4-21

AN INVESTIGATION ON DIMENSIONALITY REDUCTION IN THE SOURCE-SPACE-BASED HAND TRAJECTORY DECODING

Nitikorn Srisrisawang[1], Gernot Müller-Putz[1]

[1] Institute of Neural Engineering, Graz University of Technology, Graz, Austria

E-mail: gernot.mueller@tugraz.at

Abstract— *In this work, the hand trajectory decoding was investigated in the source space. A couple of dimensionality reduction techniques were utilized to reduce the number of the source-space signals, namely, computing the mean, principle component analysis (PCA), locality preserving projection (LPP).*
The decoding performances from the source-space approaches were compared to the sensor-space approach. We found that every approach showed performance metrics in a similar range and only slight differences across approaches could be observed. The source-space approach with PCA with 8 components exhibited higher performance metrics than other approaches and slightly higher performance metrics than the sensor-space approach (improvement for correlation 0.01 to 0.09, SNR 0.05 to 0.1 dB). The results suggested that the source-space-based decoding is possible, and it can achieve comparable performance to the sensor-space approach.

Keywords— *EEG, BCI, source localization, PCA, LPP, PLS, UKF, hand trajectory decoding*

Introduction

The electroencephalogram (EEG) measures the electrical changes of the brain non-invasively. Since the actual underlying sources in the brain are inaccessible from EEG, source localization is utilized to estimate the underlying cortical sources. The source localization is rarely implemented in the processing steps but rather in the post-analysis because of the complexity of the problem.
Recently, some studies investigated this direction. They demonstrated the possibility of source-space classification in brain-computer interfacing (BCI) [1]–[4]. Still, only single literature [5] focused on the regression problem, so this work will explore the possibility of regression of hand trajectory in the source space.

Previously, a couple of works from our group [6]–[9] studied the decoding of hand movement trajectory for the pursuit tracking task (PTT) from EEG in an online setting. Group-level source localization analysis reveals the brain regions contributing to the decoding of the movement kinematics to be located between the medial part of the frontal and parietal area, which corresponds to the frontoparietal network [10]. This information could be used to restrict the signals in the source space, but the resulting number of signals is still in the range of thousands. Hence, different dimensionality reduction techniques widely used in different research fields were investigated, namely, principal component analysis (PCA), locality preserving projection (LPP) [11], and computing the mean.

Methods

Dataset description

The data from 2 studies [8], [9] was used. In total, there are 15 measurements from 14 different participants since one participant was in both studies while one participant was excluded due to the signal quality in some measurement runs.

Experimental setup

The task for the participant was to follow a target cursor ("snake") on the screen by controlling a robotic arm (JACO, Kinova Robotics Inc., Canada) via a mixed control between the hand movement, captured via the LeapMotion (LM) system (LeapMotion Inc., USA), and the decoded signal from EEG. The mixed percentage of the control was adjusted to the respective run from 100% LM and 0% EEG to 0% LM and 100% EEG. The EEG signals were simultaneously measured via 64 (in [8]) and 60 (in [9]) active EEG electrodes (actiCAP, Brain Products GmbH., Germany) recorded at 500 Hz with biosignal amplifiers (BrainAmp, Brain Products GmbH, Germany). The common EEG channels between both studies used in this analysis can be seen

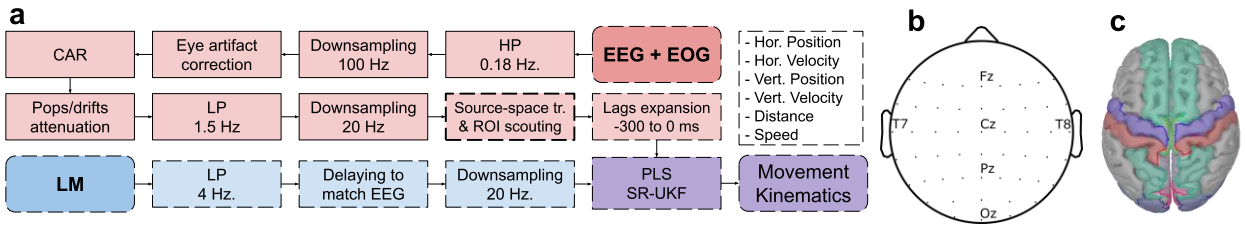

Figure 1: Overview of the experiment information a) common processing pipeline adapted from [7], [8] with additional source-space transformation and ROI scouting block, highlighted with dashed lines, b) common electrodes position used in the analysis, c) the predefined region-of-interest

Published by Verlag der TU Graz
Graz University of Technology

DOI: 10.3217/978-3-85125-826-4-21

in Fig. 1b. The data from the 100% LM was used to calibrate the decoding model. For a detailed explanation of the experimental setup, please refer to [8], [9]

Processing Pipeline

The overview of the processing was shown in Fig.1a. For a detailed description of the processing pipeline, please refer to [8], [9], on which the processing pipeline was based. The following changes were made in the processing pipeline. 1. an additional source-space transformation and ROI scouting block were added 2. criteria for choosing the retained number of components in the partial least square (PLS) model were to retain 95% of total variances components instead of fixing the same number of components across measurements. The combination between PLS and the square roots unscented Kalman filter (SR-UKF) [12] produces the following movement kinematics: horizontal position, vertical position, horizontal velocity, vertical velocity, speed, and distance.

Source-space transformation

Before the experiment, electrode positions were measured. This information was used to co-register with an ICBM152 template head model. The forward problem was modeled with a boundary element method (BEM) with 5000 unconstrained cortical dipole sources, meaning that each source was modeled with 3 components in XYZ directions. The conductivity of the scalp, skull, and brain was set to (0.41, 0.02, 0.47) [13], respectively. The inverse problem was solved with OpenMEEG [14] and sLORETA [15] using the Brainstorm package [16].

ROI scouting

Several regions-of-interests (ROIs) were defined according to the Mindboggle brain atlas [17] to reduce the number of signals in the source space. The predefined ROIs, which were based on the frontoparietal network [6], [10], are as follows: cuneus, lateral occipital, paracentral, postcentral, precentral, precuneus, superior frontal, and superior parietal in both hemispheres (Fig. 1c). Different dimensionality reduction techniques were employed for each directional component of sources in each ROI to reduce the number of signals further. These are PCA, LPP [11], and computing the mean signals. The optimum number of retained components for both PCA and LPP were chosen by comparing the correlation and the computational complexity of 1,2,4,8, and 16 components. For both PCA and LPP, 8 components were retained per each directional source component or equivalently 24 components per ROI. The processes of source-space transformation and ROI scouting can be summarized as matrix multiplications as:

$$\mathrm{Y} = SKX \tag{1}$$

where X is processed sensor-space EEG signals, K is a kernel matrix that transforms sensor-space signals into the source space, S is a scouting matrix that produces the representation signals Y from the source-space signals.

Decoding performance evaluation

The following metrics were chosen to compare among the different approaches. Namely, the correlation between the decoded and the actual trajectory, signal-to-noise (SNR) ratio defined as:

$$\mathrm{SNR}(\mathrm{z_t}, \widehat{\mathrm{z_t}}) = 10 \log_{10} \frac{\mathrm{var}(\mathrm{z_t})}{mse(\mathrm{z_t}, \widehat{\mathrm{z_t}})} \tag{2}$$

and decoded-signals-to-signal (DSSR) ratio defined as [7]:

$$\mathrm{DSSR}(\mathrm{z_t}, \widehat{\mathrm{z_t}}) = 10 \log_{10} \frac{\mathrm{var}(\mathrm{z_t})}{\mathrm{var}(\widehat{\mathrm{z_t}})} \tag{3}$$

where $\mathrm{z_t}, \widehat{\mathrm{z_t}}$ indicate the true and the decoded kinematics, $\mathrm{var}(x)$ means the variance of x and $mse(x, y)$ means the mean squared error (MSE) between x and y. The DSSR [7] could be interpreted as the amplitude mismatch between the decoded and the actual movement kinematics. The best case is that the amplitude of kinematics matches with a DSSR at 0 dB. The horizontal and vertical components were grouped by computing the mean and distance and speed into position, velocity, and magnitude. The 3 kinematics will be called 'simplified' kinematics, and they were meant only for visualization purposes, while the 'full' kinematics contain the original 6 kinematics. The metrics differences between 'Se' and the best source-space approach for each of the 'full' kinematics were computed by subtracting the best source-space approach to 'Se' from the same measurement and then computing the mean across measurements.

Statistical evaluation

The experiment was repeated in a simulated manner that closely resembles the online processing pipeline with different approaches: sensor-based approach *'Se'*, computing the mean *'Mean'*, *'PCA8'*, and *'LPP8'*. The subject-level average metrics were computed. Multiway repeated-measures ANOVA was used to compare the following factors: 1. control percentage (100% LM – 0% LM), 2. movement kinematics, and 3. different approaches ('Se', 'Mean', 'PCA8', 'LPP8'), using Greenhouse-Geisser correction. For the DSSR, the absolute value was used in the statistical test (aDSSR). Tukey's HSD test was used as a post-hoc test for multiple comparisons. These statistical tests were performed on the 'full' kinematics.

Results

The results from the 'simplified' kinematics were summarized in Fig. 2. Overall, the boxplots revealed the trends where the directional kinematics indicated higher performance than the non-directional ones.
From Fig. 2., every approach showed the median correlations in a similar range at around 0.30, 0.32, 0.12

Published by Verlag der TU Graz
Graz University of Technology

DOI: 10.3217/978-3-85125-826-4-21

for the position, velocity, and magnitude. 'PCA8' exhibited a higher median correlation in velocity and magnitude than 'Se'.

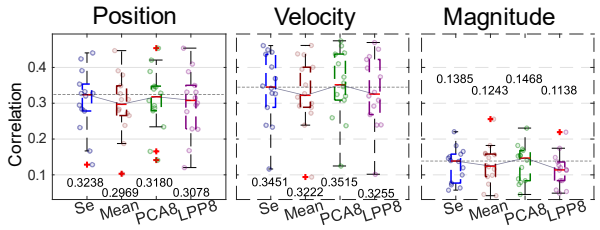

Figure 2: The subject-level boxplot correlation of different approaches, *'Se', 'Mean', 'PCA8', 'LPP8'*. For visualization purposes, the 'simplified' kinematics were used, and the mean of the correlations was computed across 100%LM to 0%LM runs. The numbers indicate the corresponding median values. The dashed lines indicate the median value of 'Se'.

Multiway repeated-measures ANOVA revealed statistically significant differences between approaches in terms of correlation ($F(3,39)=5.5$, $p=0.010$), SNR ($F(3,39)=5.1$, $p=4.15\times10^{-5}$), but not in the case of absolute DSSR ($F(3,39)=2.47$, $p=0.101$).
Post-hoc tests revealed that 'Mean' and 'LPP8' showed lower performance than 'Se' and that 'PCA8' indicated slightly higher performance than the rest. The only statistically significant results were between a pair of 'LPP8' to 'PCA8' ($p=0.018$), while the other comparison between pairs was not statistically significant. The performance's ranking is as follows: 'PCA8' > 'Se' > 'Mean' > 'LPP8'. The group-level differences between 'PCA8' and 'Se' of the 'full' kinematics can be found in Tab. 1. In most cases for correlation and SNR, 'PCA8' showed slightly higher performance than 'Se'.

Table 1: Group-level differences of 'PCA8' and 'Se' from 'full' kinematics

	Corr.	**SNR**	**aDSSR**
Pos. X	0.0009	0.1084	-0.0121
Vel. X	0.0049	-0.0165	-0.04
Pos. Y	0.0035	0.0938	-0.0454
Vel. Y	0.0084	-0.02	-0.0588
Distance	-0.0015	0.0704	0.0282
Speed	0.0096	0.0499	0.0503

Discussion

Several works had proven that the decoding of hand movement trajectory in humans based on the sensor-space EEG signals could be done with an actual hand movement [8], [9], or imagined hand movement [18]. However, an open question was whether it is possible to perform decoding of hand movement trajectory based on the source-space signals.
To answer that, we tried several approaches to overcome the problem of a high number of signals in the source space, namely, 'Mean', 'PCA8', 'LPP8'.
The processing pipeline of 'Se' is the same as in [9], and the results indicated the correlations of 'Se' to be in a similar range. Comparing 'Se' to the source space approaches ('Mean', 'PCA8', 'LPP8'), we see the performance in a similar range as in 'Se' with some slight differences. It is indicated via post-hoc tests that among all approaches, 'PCA8' could perform slightly better than 'Se', but the differences were not statistically significant. The results showed that the decoding in the source space is possible with comparable performance, and the best candidate out of all could be 'PCA8'.
We have the following assumptions to explain the cause of the lower performance of 'Mean'. First, the number of signals from 'Mean' was reduced from each ROI with the original number of signals in a range between hundreds to thousands of signals per ROI, to just 3 signals (1 for each direction of the source components), and this could retain very little information. Second, by using the mean function, we assumed the distribution of the signals in each ROI to be normally distributed, which was hardly the case in this situation. In LPP, it was introduced as a dimensionality reduction technique that tries to retain the local network structure in the lower dimension [11]. This technique was successfully applied in the computer vision field and the BCI field [19]. However, the results suggested the performance of LPP to be the worse among the candidates. The worse performance could be due to the difference between classification problems (as LPP was typically used) and the regression.
Some works [1]–[4] that utilized the source-space information in the classification problem indicated some improvement over the sensor space. However, Sosnik and Zheng 2021 [5], who investigated the decoding of joints kinematics with signals in the source space, showed slightly lower performance than the sensor space. Their approach was comparable with our 'Mean' approach, which also showed slightly lower performance than 'Se'.
There are some interesting points to further explore for the source-space-based decoding: the benefits of incorporating the individualized anatomical information from the magnetic resonance imaging (MRI) and how the decoding behaves in the actual online experiment.

Conclusion

Different reduction techniques were implemented to overcome the problem of a high number of signals. By comparing the performance metrics from the sensor-space approach, 'Se', to the source-space approaches, 'Mean', 'PCA8', 'LPP8', we found that only the 'PCA8' could perform better than 'Se'. However, the differences were only marginal and not statistically significant. The results suggested that the source-space-based decoding of hand movement trajectory is possible with comparable performance to 'Se'.

Published by Verlag der TU Graz
Graz University of Technology

DOI: 10.3217/978-3-85125-826-4-21

Acknowledgements

Research supported by funding from the European Research Council (ERC-CoG-2015 681231 'Feel Your Reach'), the author N.S. received funding from the Royal Thai Government.

References

[1] L. Qin, L. Ding, and B. He, “Motor imagery classification by means of source analysis for brain–computer interface applications,” *J. Neural Eng.*, vol. 1, no. 3, pp. 135–141, Sep. 2004, doi: 10.1088/1741-2560/1/3/002.

[2] B. J. Edelman *et al.*, “Noninvasive neuroimaging enhances continuous neural tracking for robotic device control,” *Sci. Robot.*, vol. 4, no. 31, p. eaaw6844, Jun. 2019, doi: 10.1126/scirobotics.aaw6844.

[3] C. Li, H. Guan, Z. Huang, W. Chen, J. Li, and S. Zhang, “Improving Movement-Related Cortical Potential Detection at the EEG Source Domain,” in *2021 10th International IEEE/EMBS Conference on Neural Engineering (NER)*, Italy, May 2021, pp. 214–217. doi: 10.1109/NER49283.2021.9441169.

[4] V. Shenoy Handiru, A. P. Vinod, and C. Guan, “EEG source space analysis of the supervised factor analytic approach for the classification of multi-directional arm movement,” *J. Neural Eng.*, vol. 14, no. 4, p. 046008, Aug. 2017, doi: 10.1088/1741-2552/aa6baf.

[5] R. Sosnik and L. Zheng, “Reconstruction of hand, elbow and shoulder actual and imagined trajectories in 3D space using EEG current source dipoles,” *J. Neural Eng.*, vol. 18, no. 5, p. 056011, Oct. 2021, doi: 10.1088/1741-2552/abf0d7.

[6] R. J. Kobler, A. I. Sburlea, and G. R. Müller-Putz, “Tuning characteristics of low-frequency EEG to positions and velocities in visuomotor and oculomotor tracking tasks,” *Sci. Rep.*, vol. 8, no. 1, p. 17713, Dec. 2018, doi: 10.1038/s41598-018-36326-y.

[7] R. J. Kobler, A. I. Sburlea, V. Mondini, M. Hirata, and G. R. Müller-Putz, “Distance- and speed-informed kinematics decoding improves M/EEG based upper-limb movement decoder accuracy,” *J. Neural Eng.*, Aug. 2020, doi: 10.1088/1741-2552/abb3b3.

[8] V. Mondini, R. J. Kobler, A. I. Sburlea, and G. R. Müller-Putz, “Continuous low-frequency EEG decoding of arm movement for closed-loop, natural control of a robotic arm,” *J. Neural Eng.*, Jul. 2020, doi: 10.1088/1741-2552/aba6f7.

[9] V. Martınez-Cagigal, R. J. Kobler, V. Mondini, R. Hornero, and G. R. Muller-Putz, “Non-Linear Online Low-Frequency EEG Decoding of Arm Movements During a Pursuit Tracking Task,” *2020 42nd Annu. Int. Conf. IEEE Eng. Med. Biol. Soc. EMBC*, p. 5, doi: 10.1109/EMBC44109.2020.9175723.

[10] J. C. Culham and K. F. Valyear, “Human parietal cortex in action,” *Curr. Opin. Neurobiol.*, vol. 16, no. 2, pp. 205–212, Apr. 2006, doi: 10.1016/j.conb.2006.03.005.

[11] X. He and P. Niyogi, “Locality Preserving Projections,” in *Advances in Neural Information Processing Systems 16*, 2004, p. 8.

[12] R. Van der Merwe and E. A. Wan, “The square-root unscented Kalman filter for state and parameter-estimation,” in *2001 IEEE International Conference on Acoustics, Speech, and Signal Processing. Proceedings (Cat. No.01CH37221)*, Salt Lake City, UT, USA, 2001, vol. 6, pp. 3461–3464. doi: 10.1109/ICASSP.2001.940586.

[13] H. McCann, G. Pisano, and L. Beltrachini, “Variation in Reported Human Head Tissue Electrical Conductivity Values,” *Brain Topogr.*, vol. 32, no. 5, pp. 825–858, Sep. 2019, doi: 10.1007/s10548-019-00710-2.

[14] A. Gramfort, T. Papadopoulo, E. Olivi, and M. Clerc, “OpenMEEG: opensource software for quasistatic bioelectromagnetics,” *Biomed. Eng. OnLine*, vol. 9, no. 1, p. 45, 2010, doi: 10.1186/1475-925X-9-45.

[15] R. D. Pascual-Marqui, “Standardized low-resolution brain electromagnetic tomography (sLORETA): technical details,” *Methods Find. Exp. Clin. Pharmacol.*, p. 16, 2002.

[16] F. Tadel, S. Baillet, J. C. Mosher, D. Pantazis, and R. M. Leahy, “Brainstorm: A User-Friendly Application for MEG/EEG Analysis,” *Comput. Intell. Neurosci.*, vol. 2011, pp. 1–13, 2011, doi: 10.1155/2011/879716.

[17] A. Klein *et al.*, “Mindboggling morphometry of human brains,” *PLOS Comput. Biol.*, vol. 13, no. 2, p. e1005350, Feb. 2017, doi: 10.1371/journal.pcbi.1005350.

[18] A. Korik, “Decoding Imagined 3D Hand Movement Trajectories From EEG: Evidence to Support the Use of Mu, Beta, and Low Gamma Oscillations,” *Front. Neurosci.*, vol. 12, p. 16, 2018, doi: 10.3389/fnins.2018.00130. PMID: 29615848.

[19] Ren Xu, Ning Jiang, Chuang Lin, N. Mrachacz-Kersting, K. Dremstrup, and D. Farina, “Enhanced Low-Latency Detection of Motor Intention From EEG for Closed-Loop Brain-Computer Interface Applications,” *IEEE Trans. Biomed. Eng.*, vol. 61, no. 2, pp. 288–296, Feb. 2014, doi: 10.1109/TBME.2013.2294203.

Published by Verlag der TU Graz
Graz University of Technology

Proc. Annual Meeting of the Austrian Society for Biomedical Engineering 2021
DOI: 10.3217/978-3-85125-826-4-22

LEARNING EFFECTS IN 2D TRAJECTORY INFERENCE FROM LOW-FREQUENCY EEG SIGNALS OVER MULTIPLE FEEDBACK SESSIONS

H.S. Pulferer[1], B. Ásgeirsdóttir, V. Mondini[1], A.I. Sburlea[1], G.R. Müller-Putz[1]
[1]Institute of Neural Engineering, Graz University of Technology, Graz, Austria
gernot.mueller@tugraz.at

Abstract— *Recent research from our group has shown that non-invasive continuous online decoding of executed movement from non-invasive low-frequency brain signals is feasible. In order to cater the setup to actual end users, we proposed a new paradigm based on attempted movement and after conducting a pilot study, we hypothesize that user control in this setup may be improved by learning over multiple sessions. Over three sessions within five days, we acquired 60-channel electroencephalographic (EEG) signals from nine able-bodied participants while having them track a moving target / trace depicted shapes on a screen. Though no global learning effect could be identified, increases in correlations between target and decoded trajectories for approximately half of the participants could be observed.*

Keywords— *Electroencephalography, trajectory decoding, learning effects.*

Introduction

Brain-computer interfaces (BCIs) [1, 2] are characterized by offering a user direct control over an interface without prior muscular activity. For years, a goal of our group has been the restoration of arm and hand movement respectively in people with cervical spinal cord injury (SCI) [3, 4, 5]. Through a BCI, these persons should be enabled to control an end-effector, e.g., a neuroprosthesis or a robotic limb. Starting from identifying different movement directions [6, 7, 8], the focus has advanced to continuous movement decoding.
Recently, it was shown that movement information (positions and velocities) in a plane is contained in low-frequency EEG signals, making it possible to infer executed movement trajectories in an online target tracking task with correlations between decoded and actual trajectories well above chance [9, 10]. However, the used paradigms were tailored to able-bodied participants, making their application to end users with limited motor output impossible.
As a possible solution to this, we conducted a pilot study based [11] on attempted instead of executed movement [12]. Feedback from the participant on the perceived level of control at the beginning and the end of the experiment lead to the assumption that the decoder accuracy may be improved through training. This implies that the decoding performance may not only be optimized through utilization of increasingly powerful signal processing and machine learning algorithms, but also via neuroplasticity with respect to the BCI users themselves. Considering this assessment, we hypothesized that any visible learning effects would take place within a short time span already. For this reason, we chose to investigate possible increases in BCI user performance over three sessions within five days. This timeframe was selected to keep the experience fresh in the participants' minds while allowing them to recuperate from the mental workload between the sessions.
In this work, we evaluate the two different paradigms we presented the participants with regarding an increase in performance over the sessions. Further, we evaluate whether neuroplasticity can play a role in 2D trajectory inference.

Methods

Participants and setup— EEG of nine able-bodied participants (24.2 ± 5.0ys) have been recorded three times each within five days. The participants sat in front of a TV screen with their dominant arm strapped to the chair (see Fig. 1, C), enabling minimal movement but largely restricting the motor output in order to mimic attempted movement [12]. Each participant (four female, five male) was assessed as right-handed according to the Edinburgh Handedness Inventory [13] and had normal or corrected-to-normal vision. Data of one specific participant was excluded from further analysis due to erroneous marker-labelling during the recording. The experiment was conducted as part of the Feel Your Reach project and as such was approved by the ethics committee of the Medical University of Graz.

Paradigm— In each of the three sessions, the participant was presented with two different paradigms: the *snakeruns* (Fig. 1, A) and the *freeruns* (Fig. 1, B). For the snakeruns, a target (called '*snake*') was shown on the screen, moving according to specifically designed trajectories that ensured decorrelation between x and y coordinate. The participant was asked to visually track the snake while attempting movement with the strapped lower arm and hand as if wielding a cursor.
In the freeruns, three different static shapes were shown on the screen: two diagonals (from top or bottom left, respectively), and a circle. In this paradigm, the participants had to trace the shape following their own pace without stopping, again visually as well as with attempted movement.
Each session was roughly divided into an offline calibration and an online feedback part.

Published by Verlag der TU Graz
Graz University of Technology

DOI: 10.3217/978-3-85125-826-4-22

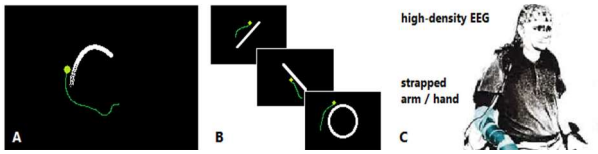

Figure 1: Experimental setup and paradigm. A) depicted moving target (snake, white) with green feedback dot, B) freerun shapes */*, \ and O to be followed at the participant's own pace, C) experimental setup with the participant's dominant hand/arm strapped to the chair.

During the calibration phase, two *eyeruns* (including resting gaze, blinks, horizontal and vertical eye movement) and four snakeruns (12 trials of 23s each) were recorded. For the calibration snakeruns, fake feedback in form of a green dot corresponding to the delayed snake trajectory was shown on the screen to accustom the participants to the additional visual information. After recording the data for the calibration, the eye data were used to train our sparse generalized eye artifact subspace subtraction (SGEYESUB) algorithm [14], while the snakeruns were used to fit the partial least squares regression unscented Kalman filter (PLSUKF) decoder discussed in [10].
In the online phase, the feedback condition was successively increased first to 50% EEG feedback, corresponding to the mean between actual and decoded snake position (three snakeruns: 36 trials of 23s duration), and then to 100% EEG decoded feedback (three snakeruns, three freeruns: 36 trials of 23s duration each).

Recording and preprocessing— Data from 64 channels was recorded, corresponding to a 60 channel EEG according to the 10-10 system and four electrooculographic (EOG) electrodes placed at the outer canthi of both eyes as well as above and below the left eye. Ground and reference electrodes were placed at Fpz and the right mastoid. The initial sampling rate of 200Hz was first reduced to 100Hz after high pass filtering at 0.18Hz and anti-aliasing filtering at 25Hz; the bad channels were then interpolated, the eye artifacts attenuated using the SGEYESUB algorithm [14], and the EOG and AF channels were removed. The data were then re-referenced to common average reference, and pops and drifts in the signals were attenuated using the HEAR algorithm [15]. After low pass filtering at 3Hz and further downsampling to 20Hz, the signals were fed to the PLSUKF decoder [10, 16], yielding the feedback output shown as a green dot on screen.

Results

Snakeruns—An accurate assessment of the decoder performance was accomplished by evaluating the Pearson's correlation coefficient *r* between actual snake trajectory (ground truth) and decoded EEG signals for each trial. The correlations for each feedback condition (50% and 100% EEG), directional movement parameters (pos_x, vel_x, pos_y, vel_y), session and participant are presented in Fig. 2. The correlations for single trials (36 per session and condition, notwithstanding trial rejection) are displayed as small dots, mean and 25th resp. 75th percentiles as big dots and whiskers. For each session, the chance levels were calculated using a shuffling approach [9], in which EEG data and corresponding snake trajectories were randomly interchanged, a new PLS model fitted, and *r* evaluated, for 100 times. The upper confidence intervals of the chance level correlations (with alpha = 0.05) were then found as the 95th percentile of the correlation moduli and are depicted as horizontal lines. For all participants, sessions and feedback conditions, mean correlations (approx. 0.3) lie well above chance levels (approx. 0.15).

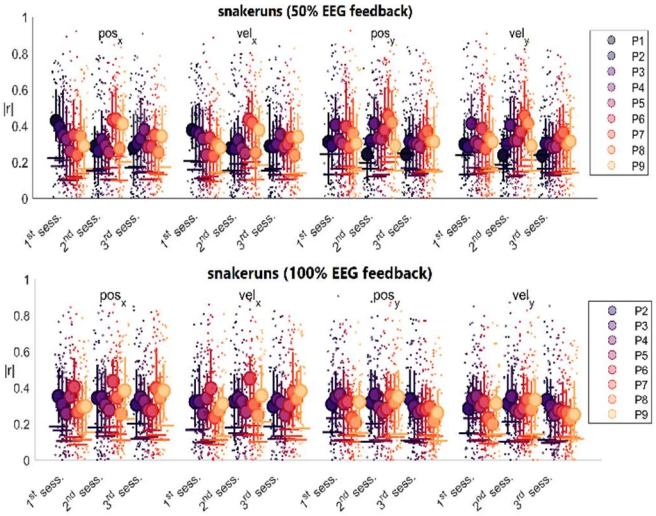

Figure 2: Correlations for all trials (small dots) with mean (big dots), 25th and 75th percentiles (whiskers) and chance levels (horizontal lines, see [9]) for each participant, directional movement parameter (pos_x, vel_x, pos_y, vel_y), session and feedback condition (top: 50% EEG, bottom: 100% EEG).

After evaluating the data of the first participant (P1), the initial recording sequence of three 50% EEG snakeruns and three 100% EEG freeruns was adapted, and snakeruns with 100% EEG feedback condition were added for quantitative performance analysis due to the lack of a ground truth for the self-paced freeruns. As a result, P1 could not be included in the 100% EEG feedback snakerun analysis (Fig. 2, bottom).
For both feedback conditions, single trial correlations are found to be spread over the whole range (0,1), with no global trend for the means over each session. A downward tendency from first to third session for approximately half of the participants can be observed, while the other half improved, often accompanied with a performance peak in the second session. Further, improvements in performance in one movement direction (x or y) are not necessarily seen in the other direction as well, implying varying decoder performance across movement directions over multiple sessions. Further measurements with additional participants will

Published by Verlag der TU Graz
Graz University of Technology

DOI: 10.3217/978-3-85125-826-4-22

allow for statistical evaluation of the correlations over all individuals.

Freeruns— Because of the self-paced character of the freerun task, target positions as in the snakeruns are not available as a ground truth in the freeruns. As a workaround, the expected target position on screen at each point in time was assumed as the point the participant was visually focusing on. The ground truth trajectories were inferred via horizontal and vertical bipolar derivates of the EOG signals. After lowpass filtering at 3Hz and downsampling to 20Hz of the raw EOG data, the correlation between the trajectory inferred via horizontal and vertical EOG derivates and the decoded trajectory was used as an evaluation metric.

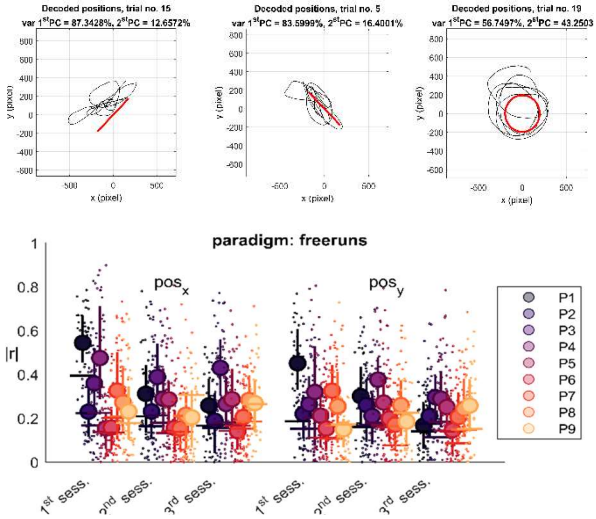

Figure 3: *Top*— Depicted shapes (red) and three corresponding EEG-decoded freerun trajectories (black) from P4, session 2. *Bottom*— Correlation between EOG-inferred and decoded trajectory for each trial (small dots), with mean (big dot), 25th resp. 75th percentiles (whiskers) and chance levels (horizontal lines) for each participant and session.

Three single freerun trials taken from P4, session 2 are shown in Fig. 3 for demonstration. The static shape shown to the participant on the screen is depicted in red, the EEG-decoded trajectory corresponding to the tracing task is overlaid in black. Pearson's correlation r between EOG-inferred trajectory (ground truth) and decoded trajectory for each participant, session and trial is shown in Fig. 3 (bottom). Small dots correspond to single trials, big dots and whiskers again to mean and 25th/75th percentiles of the correlations in each session. No distinction between the different depicted shapes (*I*, \, O) was made yet. The chance levels were again calculated using a shuffling approach.
As can be seen, the mean correlation lies below chance level for some sessions in contrast to the mean correlations during the snakeruns. Again, no global trend can be observed in terms of improvement or degradation of performance over all participants. However, a steady increase in performance can be observed in approximately half of the participants. Additionally, any trend from first to third session observed in one movement direction can be also seen in the other direction in two thirds of the participants, in contrast to the correlations in the snakeruns.

Discussion

Over three consecutive sessions in nine participants, no global learning effect could be observed for both presented paradigms (snakeruns, freeruns).
For each feedback condition, participant and session, the mean correlation in the snakeruns lay above chance level, though different decoding accuracies in x and y direction could be observed, implying a favored decoding direction. Approximately half of the participants showed an increase in performance from first to third session, which was often paired with a performance peak during the second session, while the other half exhibited a steady decrease in performance. Following a preliminary assessment, this does not directly correlate with the decoder performances observed on the calibration data. This implies underlying causes that are not strictly related to the varying decoder performance from session to session, even though the decoder was fitted anew for each session. Decreasing motivation and engagement of the participants due to the long experiment (3-4 hours per session) must be mentioned as influencing factors, along with a varying frustration tolerance between the participants. Although we did not ask the participants to fill a questionnaire, there seemed to be a consensus that higher learning rates were expected. This may have led to frustration and can explain the decrease in correlations from second to third session in participants with a performance peak in the second session.
For the freeruns, approximately half of the participants showed improvement from first to third session, whereas the performance decreased for the other half. Mean correlations did not lie above chance for all sessions, which in part can be attributed to the EOG trajectories that were used as a ground truth in the freeruns. In part, this may also imply that the self-paced freerun task was harder to fulfill than the tracking task during the snakeruns. Detailed investigations on correlations per specific shape (*I*, \, O), as well as on changes in correlation from session to session, remain to be done.
Detailed analysis regarding the grand average over all participants remains to be done and cannot be presented within the preliminary results yet.

Acknowledgements

This research was supported by funding from the European Research Council (ERC-CoG 2015 681231 'Feel Your Reach') and NTU-TUG joint PhD program.

Published by Verlag der TU Graz
Graz University of Technology

DOI: 10.3217/978-3-85125-826-4-22

References

[1] G. Müller-Putz und S. Wriessnegger, Neuroprosthetics and Brain-Computer Interfaces in Spinal Cord Injury, A Guide for Clinicians and End Users, Chapter 3: Electroencephalography and Brain-Computer Interfaces, Springer, 2021.

[2] J. d. R. Millán, Introduction to Neural Engineering for Motor Rehabilitation, Chapter 12: Brain-Computer Interfaces, Wiley-IEEE Press, 2013.

[3] G. Müller-Putz, J. Pereira, P. Ofner, A. Schwarz, C. L. Dias, R. Kobler, L. Hehenberger und A. I. Sburlea, „Towards non-invasive brain-computer interface for hand/arm-control in users with high spinal cord injury," in *In Proceedings of the 6th International Winter Conference on Brain-Computer Interface (BCI 2018)*, South Korea, 2018.

[4] G. Müller-Putz, P. Ofner, A.Schwarz, J. Pereira, A. Pinegger, C. Lopes-Dias, L. Hehenberger, R. Kobler und A. Sburlea, „Towards non-invasive EEG-based arm/handcontrol in users with spinal cord injury," in *5th International Winter Conference on Brain-Computer Interfaces*, 2017.

[5] A. Schwarz, P. Ofner, J. Pereira, A. Sburlea und G. Müller-Putz, „Decoding natural reach-and-grasp actions from human EEG," *Journal of Neural Engineering,* Bd. 15, Nr. 1, 2018.

[6] J.-S. Woo, K.-R. Müller und S.-W. Lee, „Classifying directions in continuous arm movements from EEG signals," *Conference Paper, The 3rd International Winter Conference on Brain-Computer Interface, IEEE,* 2015.

[7] Y. Li, Y. Sun, F. Taya, H. Yu, N. Thakor und A. Bezerianos, „Single Trial EEG Classification of lower-limb Movements Using Improved Regularized Common Spatial Pattern," *Conference Paper, IEEE EMBS Conference on Neural Engineering,* 2015.

[8] N. Robinson und A. Vinod, „Noninvasive Brain-Computer Interface: Decoding Arm Movement Kinematics and Motor Control," *IEEE Systems, Man & Cybernetics Magazine,* Oct. 2016.

[9] V. Mondini, R. Kobler, A. Sburlea und G. Müller-Putz, „Continuous low-frequency EEG decoding of arm movement for closed-loop, natural control of a robotic arm," *Journal of Neural Engineering, vol. 17, 046031,* 2020.

[10] R. Kobler, A. Sburlea, V. Mondini, M. Hirata und G. Müller-Putz, „Distance- and speed-informed kinematics decoding improves M/EEG based upper-limb movement decoder accuracy," *Journal of Neural Engineering, vol. 17, 056027,* 2020.

[11] G. Müller-Putz, V. Mondini, V. Martínez-Cagigal, R. Kobler, J. Pereira, C. Lopes-Dias, L. Hehenberger und A. Sburlea, „Decoding of continuous movement attempt in 2-dimensions from non-invasive low frequency brain signals," *Conference paper, IEEE EMBS Conference on Neural Engineering,* 2021.

[12] P. Ofner, A. Schwarz, J. Pereira, D. Wyss, R. Wildburger und G. Müller-Putz, „Attempted Arm and Hand Movements can be Decoded from Low-Frequency EEG from Persons with Spinal Cord Injury," *Scientific Reports, vol. 9,* 2019.

[13] R. Oldfield, „The assessment and analysis of handedness: The Edinburgh inventory," *Neuropsychologia, vol. 9/l,* pp. 97-113, 1971.

[14] R. Kobler, A. Sburlea, C. Lopes-Dias, A. Schwarz, M. Hirata und G. Müller-Putz, „Corneo-retinal-dipole and eyelid-related eye artifacts can be corrected offline and online in electroencephalographic and magnetoencephalographic signals," *NeuroImage, vol. 218, 117000,* 2020.

[15] R. Kobler, A. Sburlea, V. Mondini und G. Müller-Putz, „HEAR to remove pops and drifts: the high-variance electrode artifact removal (HEAR) algorithm," *Conference paper, IEEE EMBC,* 2019.

[16] V. Martínez-Cagigal und e. al., „Non-linear online low-frequency EEG decoding of arm movements during a pursuit tracking task," in *42nd Annual International Conference of the IEEE Engineering in Medicine & Biology Society (EMBC). IEEE*, 2020.

Published by Verlag der TU Graz
Graz University of Technology

Proc. Annual Meeting of the Austrian Society for Biomedical Engineering 2021
DOI: 10.3217/978-3-85125-826-4-23

PREDICTING THE CUMULATIVE FLUID INTAKE IN CARDIAC INTENSIVE CARE PATIENTS

K. Bergmoser[1,2], F. Wagner[1,2], L. Pflanzl-Knizacek[2,3], G. Schilcher[2,4], M. Schörghuber[5], M. Hafner[2], C. Baumgartner[1]

[1]Institute of Health Care Engineering with European Testing Center of Medical Devices, Graz University of Technology, Austria

[2]CBmed GmbH Center for Biomarker Research in Medicine, Graz, Austria

[3]Division of Endocrinology and Diabetology, Department of Internal Medicine, Medical University of Graz, Austria

[4]Intensive care unit, Department of Internal Medicine, Medical University of Graz, Austria

[5]Anaesthesiology for Cardiovascular Surgery and Intensive Care Medicine, Department of Anaesthesiology and Intensive Care Medicine, Medical University of Graz, Austria

katharina.bergmoser@tugraz.at

Abstract— *Fluid balance can be considered a valuable biomarker of critical illness. Administering the right dosage over time of fluids, thereby avoiding fluid overload, remains a challenge in intensive care. As a first step towards a fluid management decision support system, this work compared four models for predicting the course of the cumulative fluid intake in 30 cardiac intensive care patients. Analyses of the root mean squared error (RMSE) showed the lowest prediction error for an extrapolation model using a piecewise regression-approach.*

Keywords— *Cumulative fluid intake, prediction, fluid overload, fluid balance, intensive care*

Introduction

Fluid balance can be considered a valuable biomarker of critical illness [1]–[4]. It is calculated by subtracting the fluid outputs from the fluid intakes and documented routinely during a patient's stay in the intensive care unit (ICU). During fluid management in the ICU, fluid overload represents a serious side effect being associated with various comorbidities such as edema, cardiovascular dysfunction or respiratory complications [5]. In addition, fluid overload is an independent risk factor for morbidity and mortality when referring to critically ill surgical patients [6]–[11]. Hence, cumulative fluid balance (CFB), defined as the sum of daily fluid balances over a certain period of time, may provide important information for clinical decision making with respect to fluid management.
The clinical course of a patient's CFB in sepsis has been described by various hit models, such as the "ROSE model" which comprises the resuscitation-, optimisation-, stabilisation- and evacuation-phase [5], [12], [13]. Typical patient trajectories for CFB and cumulative fluid intake (CFI) [5], [12]–[15] with respect to the ROSE model are outlined in Fig. 1. Despite the necessity of administering large amounts of fluids in the resuscitation phase, fluids need to be considered as drugs, emphasising the administration of the right dosage over time within the subsequent phases to meet patient's needs and to avoid fluid overload. However, identifying the transition of a patient from the resuscitation phase to the optimisation phase (and subsequently to the stabilisation phase) is crucial in order to control adequate administration of fluids. Therefore, predicting CFI trajectories might pose the first step towards a fluid management decision support system and could prove beneficial in support intensivists in daily clinical practice. We therefore evaluated and compared four different approaches for estimating the CFI course in cardiac intensive care patients over a clinically reasonable timespan.

Methods

Patient cohort: 30 patients from the FLUIDATEX study (vote EK 30-076 ex 17/18 by the Ethics Committee of Medical University of Graz) were randomly chosen for analysis. The study includes patients in intensive care after cardiac surgery (20 males, 10 females). The mean age of the patients was 68.99 years (sd = 8.38 years). The mean length of stay at the ICU was 5 days (± 1 day). Twelve patients had a coronary artery bypass grafting, 12 patients had heart valve replacement and the remaining 6 patients underwent both interventions.

Materials: Fluid intake for all patients comprised all administered fluids (oral, enteral, parenteral) that were registered in the electronic patient records. For each patient, all intakes were added up cumulatively, resulting in a monotonous time series (expressed by

Published by Verlag der TU Graz
Graz University of Technology

DOI: 10.3217/978-3-85125-826-4-23

the CFI) describing the patient's intake since admission. Data of the first 48 hours of ICU stay was used for generating the model for CFI and data of the subsequent 24 hours were considered to estimate the extrapolation error of prediction.

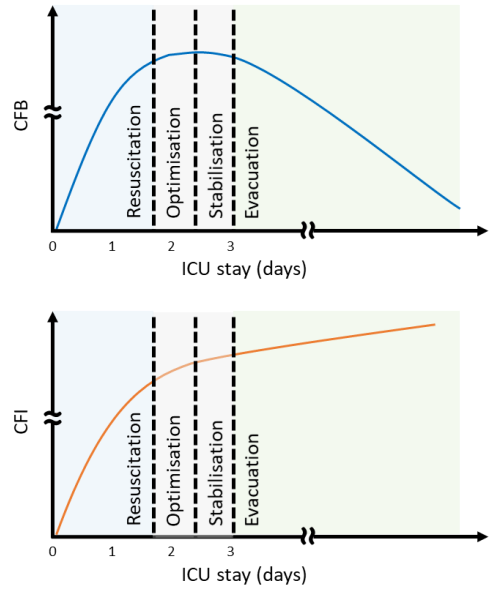

Figure 1: Clinical courses of the cumulative fluid balance (CFB) and the cumulative fluid intake (CFI) throughout a patient's stay at the intensive care unit (ICU) according to the ROSE model.

Statistical modelling and extrapolation: We used the statistical programming language R for Windows 10 (version 4.0.5) [16] for data modelling and analysis. The CFI was modelled using four different methods. As a benchmark we selected linear regression analysis (lm() in base R) as simplest method. Linear models are commonly used to describe and predict a target variable based on one or more independent variables. The general equation of the simple linear regression used in this work is shown in Eq. 1 where y is the observed variable, x is the explanatory variable, β_1 describes the slope and β_0 the intercept. The term e subsumes an unobserved random error.

$$y = \beta_1 x + \beta_0 + e \quad (1)$$

The fitted line can easily be extrapolated using the regression equation provided by the model. Second, we selected a "broken stick" approach, which adds two multiple linear regression lines together [17]. This method provides more freedom after a possible change in patient treatment over time. Based on this approach two subsequent simple linear regression models were fitted to the data. The breakpoint is determined as described in Eq. 2 [17]. The piecewise.linear() function from the R package SiZer was applied to model this approach. Extrapolation was performed using the "predict" function in R.

$$y_i = \begin{cases} \beta_0 + \beta_1 x_i + e_i & for\ x_i \le \alpha \\ \beta_0 + \beta_1 x_i + \beta_2 (x_i - \alpha) + e_i & for\ x_i > \alpha \end{cases} \quad (2)$$

The third method was a time series-based analysis, carried out automatically using the auto.arima() function [18], [19] from the forecast package in R. Time series analysis employs past time-discrete data to predict prospective data points by decomposing patient data into level, trend, seasonality and noise components. This approach may result in a spectrum of models of different degrees of complexity. Note that for prediction we applied the forecast() function from the forecast package as well. The fourth method was a non-linear regression approach, however using polynomial terms of power 2. Adding a polynomial term of this power, such as $\beta_2 * x^2$ to Eq. 1 as can be seen in Eq. 3, describes the final polynomial model.

$$y = \beta_2 x^2 + \beta_1 x + \beta_0 + e \quad (3)$$

Extrapolation was again performed with the predict() function. All model extrapolations were compared against the true course of the CFI using the root mean squared error (RMSE) as evaluation metrics.

Statistical comparison: A within-subjects ANOVA was calculated, comparing the four methods of modelling and extrapolation. The RMSE (in the unit milliliters) over the prediction timespan was entered as the dependent variable, selecting the modelling methods as independent variable (within-subjects factor).

Results

The four different extrapolation methods are depicted exemplarily for a selected patient in Fig. 2. The vertical dotted lines separate the modelling (48h) and prediction (24h) timespans. In this patient linear (2A) and piecewise linear (2B) regressions show a better fit compared to time series analysis (2C) or polynomial regression (2D). The distributions of extrapolation error of the CFI model over all patients is shown in Fig. 3. Piecewise linear modelling ("pw") revealed fewer extreme deviations compared to the other modelling approaches, in particular compared to regression analysis with polynomial terms ("poly") and time series analysis ("tsa"). The methods of modelling were found to be statistically significantly different, $F(2.3,66.71) = 5.51$, $p = 0.004$, generalized eta square = 0.11 (details in Fig. 4). Post-hoc analyses with Bonferroni adjustment revealed that the piecewise linear regression model showed stastically significant reduced extrapolation errors compared to all other models, while there was no difference in-between the three remaining models ($mean_{pw}$ = 631ml, $mean_{linearmodel}$ = 984ml, $mean_{tsa}$ = 1184ml, $mean_{poly}$ =1265ml, $p < 0.05$).

Published by Verlag der TU Graz
Graz University of Technology

DOI: 10.3217/978-3-85125-826-4-23

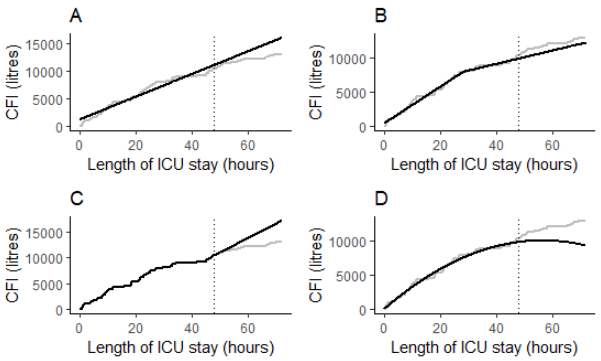

Figure 2: Linear (A), piecewise linear (B), time series analysis (C) and polynomial (D) regression of the cumulative fluid intake (CFI) in an exemplary patient using the first 48h of stay for modelling and the subsequent 24h for prediction.

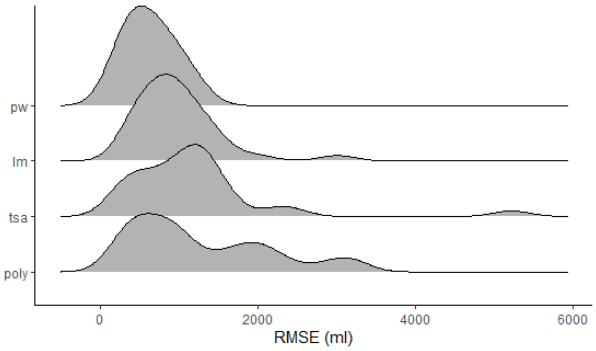

Figure 3: Whole sample extrapolation error of the cumulative fluid intake (48h of modelling, 24h of prediction). Piecewise linear modelling (pw), linear modeling (lm), time series analysis (tsa), polynomial terms (poly), root mean squared error (RMSE).

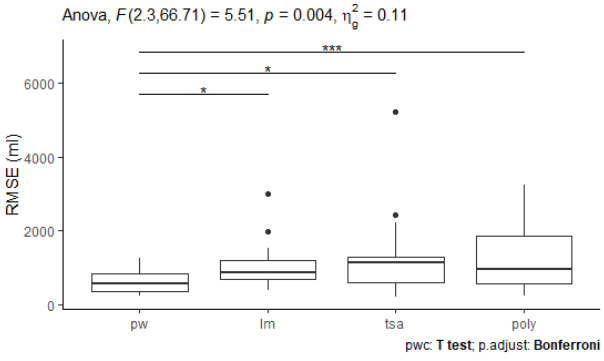

Figure 4: Variance analysis of the cumulative fluid intake extrapolation errors. Piecewise linear modelling (pw), linear modeling (lm), time series analysis (tsa), polynomial terms (poly), root mean squared error (RMSE).

Discussion

In this study we aimed to find a viable model for CFI estimation in cardiac intensive care patients and compared four different statistical methods. Our analysis demonstrated that a piecewise regression model seems to be the most promising model for estimating the CFI trajectory for the 24 hours – which is in good accordance with the common horizon for setting CFB goals – subsequent to the first 48 hours after admission to the ICU.

In this work, the orders of the applied models were restricted. Extrapolations using simple linear regression might be biased too much by the past trajectory, while polynomial regression of power 2 showed large deviations increasing with prediction time. A piecewise regression model using more than two straight lines or a polynomial regression of power 3 or more might outperform our models by allowing a higher degree of freedom. However, this may lead to complicated and overfitted models. Too much complexity might also be a reason for the underperformance of the time series-based model. The applied algorithm compares models of different complexity and chooses based on the best fit. Piecewise linear regression with one breakpoint might just be within a goldilock zone, where the method shows enough freedom to respond to changes in the CFI but not so much as to overestimate small changes. Still, we cannot assume that other statistical models may not perform better at other times of ICU stay or in other patient cohorts.

Although the applicated amount of fluids is usually documented by utilizing either paper-based or computer-assisted tools, especially small amounts of administered fluids (e.g. diluents, fluids used for flushing) are not able to be recorded [20]. Furthermore H. Asfour reported that documentation errors occur in 35% of reported CFBs [21]. These effects might negatively influence the prediction performance of CFI estimation models.

Setting and prescription of fluids to maintain microcirculation, to avoid hypoperfusion respectively, is a major challenge in critically ill patients. In this context fluid overload is common and associated with worse outcomes [5]–[11]. Decision support tools to display the history and prediction of the CFI and CFB might influence the clinical decision at bedside to assist the intensivist when prescribing fluids during the different phases of fluid resuscitation and evacuation.

In summary, predicting the CFI course using a piecewise linear regression model might assist clinicians in guiding fluid therapy, especially when incorporated in future decision support tools. The proposed approach needs to be verified in a larger patient cohort to determine the individual fluid transfer characteristics for CFB prediction.

Acknowledgements and Funding

The COMET Center CBmed is funded within COMET – Competence Centers for Excellent Technologies by

Published by Verlag der TU Graz
Graz University of Technology

DOI: 10.3217/978-3-85125-826-4-23

the Federal Ministry of Climate Action, Environment, Energy, Mobility, Innovation and Technology (BMK), the Federal Ministry for Digital and Economic Affairs (BMDW), Land Steiermark (Styrian Business Promotion Agency – SFG) and Land Wien (Vienna Business Agency – WAW). The COMET program is executed by the Austrian Research Promotion Agency (FFG).

References

[1] S. M. Bagshaw, P. D. Brophy, D. Cruz, and C. Ronco, “Fluid balance as a biomarker: Impact of fluid overload on outcome in critically ill patients with acute kidney injury,” *Crit. Care*, vol. 12, no. 4, 2008, doi: 10.1186/cc6948.

[2] E. Brotfain *et al.*, “Positive fluid balance as a major predictor of clinical outcome of patients with sepsis/septic shock after ICU discharge,” *Am. J. Emerg. Med.*, vol. 34, no. 11, pp. 2122–2126, 2016, doi: 10.1016/j.ajem.2016.07.058.

[3] L. Codes, Y. G. de Souza, R. A. C. D´Oliveira, J. L. A. Bastos, and P. L. Bittencourt, “Cumulative positive fluid balance is a risk factor for acute kidney injury and requirement for renal replacement therapy after liver transplantation,” *World J. Transplant.*, vol. 8, no. 2, pp. 44–51, 2018, doi: 10.5500/wjt.v8.i2.44.

[4] A. Acheampong and J. L. Vincent, “A positive fluid balance is an independent prognostic factor in patients with sepsis,” *Crit. Care*, vol. 19, no. 1, 2015, doi: 10.1186/s13054-015-0970-1.

[5] M. L. N. G. Malbrain *et al.*, “Principles of fluid management and stewardship in septic shock: it is time to consider the four D’s and the four phases of fluid therapy,” *Ann. Intensive Care*, vol. 8, no. 66, 2018, doi: 10.1186/s13613-018-0402-x.

[6] C. Li *et al.*, “Early negative fluid balance is associated with lower mortality after cardiovascular surgery,” *Perfusion*, vol. 33, no. 8, pp. 630–637, 2018, doi: 10.1177/0267659118780103.

[7] J. Lee *et al.*, “Association between fluid balance and survival in critically ill patients,” *J. Intern. Med.*, vol. 277, no. 4, pp. 468–477, 2015, doi: 10.1111/joim.12274.

[8] F. S. V. de Oliveira *et al.*, “Positive fluid balance as a prognostic factor for mortality and acute kidney injury in severe sepsis and septic shock,” *J. Crit. Care*, vol. 30, no. 1, pp. 97–101, 2015, doi: 10.1016/j.jcrc.2014.09.002.

[9] J. Bouchard *et al.*, “Fluid accumulation, survival and recovery of kidney function in critically ill patients with acute kidney injury,” *Kidney Int.*, vol. 76, no. 4, pp. 422–427, 2009, doi: 10.1038/ki.2009.159.

[10] M. C. Bellamy, “Wet, dry or something else?,” *Br. J. Anaesth.*, vol. 97, no. 6, pp. 755–757, 2006, doi: 10.1093/bja/ael290.

[11] J. L. Vincent and M. H. Weil, “Fluid challenge revisited,” *Crit. Care Med.*, vol. 34, no. 5, pp. 1333–1337, 2006, doi: 10.1097/01.CCM.0000214677.76535.A5.

[12] M. L. N. G. Malbrain *et al.*, “Fluid overload, de-resuscitation, and outcomes in critically ill or injured patients: A systematic review with suggestions for clinical practice,” *Anaesthesiol. Intensive Ther.*, vol. 46, no. 5, pp. 361–380, 2014, doi: 10.5603/AIT.2014.0060.

[13] M. L. N. G. Malbrain *et al.*, “Intravenous fluid therapy in the perioperative and critical care setting: Executive summary of the International Fluid Academy (IFA),” *Ann. Intensive Care*, vol. 10, no. 1, 2020, doi: 10.1186/s13613-020-00679-3.

[14] A. G. Hill and G. L. Hill, “Metabolic response to severe injury,” *Br. J. Surg.*, vol. 85, no. 7, pp. 884–890, 1998, doi: 10.1046/j.1365-2168.1998.00779.x.

[15] J. P. Desborough, “The stress response to trauma and surgery,” *Br. J. Anaesth.*, vol. 85, no. 1, pp. 109–117, 2000, doi: 10.1093/bja/85.1.109.

[16] R Core Team, “R: A Language and Environment for Statistical Computing,” Vienna, Austria. [Online]. Available: https://www.r-project.org.

[17] J. D. Toms and M. L. Lesperance, “Piecewise Regression: A Tool for Identifying Ecological Thresholds,” *Ecology*, vol. 84, no. 8, pp. 2034–2041, 2003, doi: 10.1890/02-0472.

[18] Rob J. Hyndman and Yeasmin Khandakar, “Automatic Time Series Forecasting: The forecast Package for R,” *J. Stat. Softw.*, vol. 27, no. 3, 2008, [Online]. Available: http://www.jstatsoft.org/v27/i03/paper.

[19] X. Wang, K. Smith-Miles, and R. Hyndman, “Characteristic-based clustering for time series data,” *Data Min. Knowl. Discov.*, vol. 13, no. 3, pp. 335–364, 2006, doi: 10.1007/s10618-005-0039-x.

[20] M. U. Bashir, A. Tawil, V. R. Mani, U. Farooq, and M. DeVita, “Hidden Obligatory Fluid Intake in Critical Care Patients,” *J. Intensive Care Med.*, vol. 32, no. 3, pp. 223–227, 2017, doi: 10.1177/0885066615625181.

[21] H. I. Asfour, “Fluid Balance Monitoring Accuracy in Intensive Care Units,” *IOSR J. Nurs. Heal. Sci.*, vol. 05, no. 04, pp. 53–62, 2016, doi: 10.9790/1959-0504015362.

Published by Verlag der TU Graz
Graz University of Technology

Proc. Annual Meeting of the Austrian Society for Biomedical Engineering 2021
DOI: 10.3217/978-3-85125-826-4-24

ANALYSIS OF A MATHEMATICAL MODEL OF THE SPREAD OF THE SARS-COV-2 PANDEMIC DETERMINED BY THE TRANSFER MATRIX

J. Lozanović Šajić[1,2], S. Langthaler[1], S. Stoppacher[1], C. Baumgartner[1]

[1] Institute of Health Care Engineering with European Testing Center of Medical Devices, Graz University of Technology, Austria

[2] Innovation Center of the Faculty of Mechanical Engineering, University of Belgrade, Serbia

j.lozanovicsajic@tugraz.at

Abstract— *This paper presents the development of a system theory-based model of the COVID-19 pandemic spread based on weekly reports available on the EU Open Data Portal (EUODP). The considered mathematical model will be represented in the S complex domain as a transfer matrix. System identification methodology, well known in control system theory, was applied. Stability analysis with possibilities of controllability and observability was considered. The spread of a pandemic can be controlled by proportional (P) action in an open loop.*

Keywords— *SARS-CoV-2, transfer matrix, transfer function, mathematical modeling, system identification*

Introduction

The spread of the SARS-Cov-2 pandemic can be described as a mathematical model of a system that is a unique function that maps the input vector to the output vector according to the mathematical law. The system model is an idealized, imaginary system, which retains the properties of the real system essential for system analysis [1]. Having in mind the definitions of the system [1], [2], the spread of the coronavirus pandemic can be considered as a dynamic model.

A large number of mathematical models of disease spread can be found in [3-8] with the aim to predict the pandemic's next moves. However, available models [9-14] are based on data representing the output function.

Mathematical modeling of a biological system based on system theory and control system engineering concepts however enable to determine and characterize the system model of the spreading pandemic by considering various aspects of the system including stability, observability, and controllability.

Methods

As known from systems dynamics and control theory, a dynamic system can be described by a behavioral differential equation which can be stochastic and deterministic [1]. The assumption is introduced that the spread of a pandemic system can be described as a dynamic system.

In previous considerations [15], a so-called SISO (single input – single output) system was considered. A similar approach is applied in this work, however, the system here will be defined as a multiple transfer system. Such a system is described by one input and two outputs (SIMO – single input – multiple outputs), that is why it is necessary to define the transfer matrix of the system instead of the transfer function.

The behavioral differential equation of the system with multiple inputs and multiple outputs is defined according to [16], [17]

$$\sum_{k=0}^{l} \mathbf{A}_k \mathbf{Y}(t) = \sum_{k=0}^{m} \mathbf{B}_k \mathbf{U}(t), m \leq l \qquad (1)$$

where $A \in R^{N\times N}$ and $B \in R^{N\times M}$ are matrices with constant coefficients, and l, m the highest derivations that occur between output and input variables. Based on the ordinary differential equation of the system behavior, the transfer matrix of a system is defined as

$$\mathbf{G}(s) = \begin{pmatrix} G_{11} & \cdots & G_{1M} \\ \vdots & \ddots & \vdots \\ G_{N1} & \cdots & G_{NM} \end{pmatrix} \qquad (2)$$

where N is the dimension of the output vector and M is the dimension of the input vector.

For the considered system describing the spread SARS-CoV-2 virus we assumed a system with one input and two outputs. The general transfer matrix is:

$$\mathbf{G}(s) = \begin{pmatrix} G_{11}(s) \\ G_{21}(s) \end{pmatrix} \qquad (3)$$

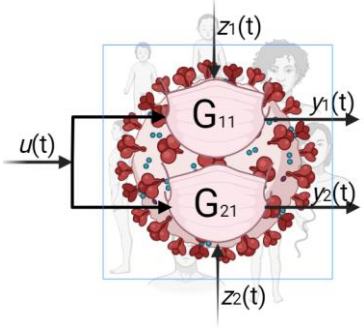

Figure 1. Illustrated block diagram of the system.

A block diagram of the system is given in Figure 1 based on Equation 3. Following Figure 1, $u(t)$ is the input variable, $\mathbf{y}(t) = (y_1(t) \quad y_2(t))^T$ is the output

Published by Verlag der TU Graz
Graz University of Technology

DOI: 10.3217/978-3-85125-826-4-24

vector and $\boldsymbol{z}(t) = (z_1(t) \quad z_2(t))^T$ is the disturbance vector. The disturbance vector can also be defined as an input vector, but can also be considered separately. Note that the disturbance vector is needed to be defined according to the definition of the input of a system [16]. For modeling the spreading pandemic, disturbances were not taken into consideration.

To determine the transfer matrix of the system, the concept of system identification that has been widely used in the field of control system engineering was applied. If it is not possible to determine a mathematical model based on physical laws, e.g. Newton's law, Bernoulli's equation, Kirchhoff's law, etc. the system identification methodology can be subsequently applied in case of a known response of the system, represented by the input and output vectors.

However, there are different approaches for system identification including parametric, nonparametric, linear, nonlinear, stochastic or deterministic modeling concepts. In general, the identification of a system is performed according to a flow chart with multiple key elements in the system identification cycle as defined in [18]. An adapted flow chart for this process is given in Figure 2.

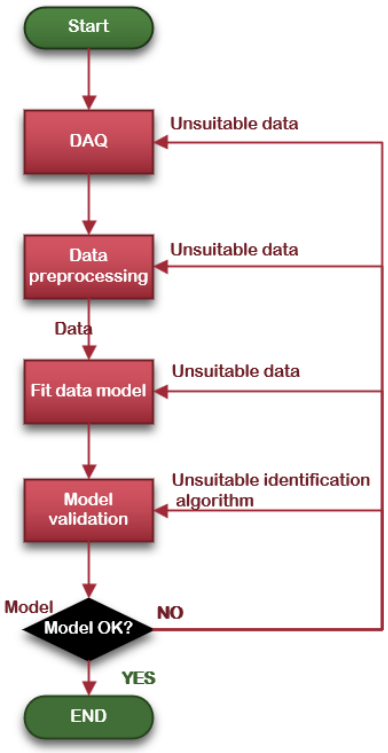

Figure 2. Adapted flow chart in system identification of the spread of SARS-CoV-2.

To determine the mathematical model of the system (spread of SARS-CoV-2) we used publicly collected data available on the EU Open Data Portal [19]. In a previous study pre-published in [15], mathematical models were provided based on data collected daily. It should be noted that in one period (14.12.2020 to 11.03.2021), the availability of data changed from a daily to weekly periods, as countries have begun to adopt anti-pandemic strategies on a two-week basis. Therefore, in this paper we present models based on the number of infected and dead persons weekly. Observed from the aspect of control theory, the sampling time was finally defined to be one week.

The basic hypothesis of this work was to define and predict the input vector, i.e. the number of new cases on a weekly level based on the output variable. In our recent work [15] we were able to demonstrate that the methodology can be applied similarly for different countries when the sampling time is daily. Model validation therein was performed for multiple countries such as Austria, Italy, Germany and Serbia. In this work, vectors were defined on a weekly basis, sample rate was set to one week, and results for Austria and Germany are presented in more detail.

Results

Models for Austria and Germany were exemplarily developed and evaluated in order to determine whether the used methodology can be applied with regard to a diminished (weekly) sampling time by maintaining a sufficient prediction accuracy.

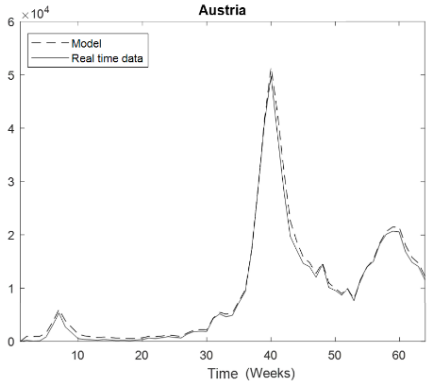

Figure 3. Identified transfer function model in relation to the number of new cases in Austria

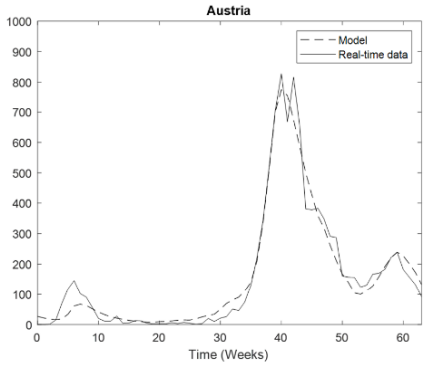

Figure 4. Identified transfer function model in relation to the number of deaths in Austria

In accordance with the definition of a behavioral differential equation, the ordinary differential equation (ODE) should be of lowest order, fully describing the

Published by Verlag der TU Graz
Graz University of Technology

DOI: 10.3217/978-3-85125-826-4-24

dynamic characteristics of the system. Therefore, we decided to adopt a second-order system based on the conducted analysis for systems from 1st to 5th order.

The spread of pandemic was assumed as a continuous-time model, and therefore a continuous-time transfer matrix was identified. Parameterization of the model included that each transfer function has two poles and one zero, the number of free coefficients is 4. The transfer matrix of the system $\mathbf{G}(s)$, which responses are shown in Figures 3 and 4, is:

$$\mathbf{G}(s) = \begin{pmatrix} G_{11}(s) \\ G_{21}(s) \end{pmatrix} = \begin{pmatrix} \frac{17{,}53s+17{,}71}{s^2+10{,}59s+18{,}85} \\ \frac{0.007816s-0.0001566}{s^2+0{,}3026s+0{,}000003505} \end{pmatrix} \quad (4)$$

Transfer matrices for other countries can be determined similarly. Figures 5 and 6 show that the transfer matrix for Germany with a ten times higher population than Austria can also be defined as a system of second-order in relation to the number of new cases and deaths.

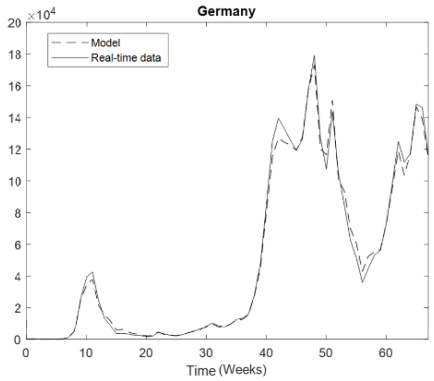

Figure 5. Identified transfer function model in relation to the number of new cases in Germany.

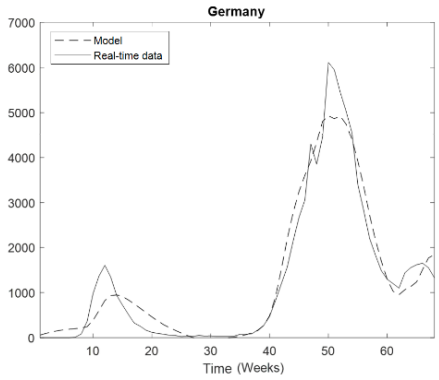

Figure 6. Identified transfer function model in relation to the number of deaths in Germany.

The transfer matrix determined for Germany, in relation to the number of new infected and the number of deaths as shown in Figures 5 and 6, is given by Eq. 5.

$$\mathbf{G}(s) = \begin{pmatrix} G_{11}(s) \\ G_{21}(s) \end{pmatrix} = \begin{pmatrix} \frac{6{,}397s+8{,}704}{s^2+2{,}787s+9{,}023} \\ \frac{0.007961s+0.0001296}{s^2+0{,}1518s+0{,}01323} \end{pmatrix} \quad (5)$$

The slight time delay of the model simulations observed in Figures 4 and 6 can be explained by effects of the disturbance and input vector. It should be noted that for both countries the spread of the pandemic can be determined by the transfer matrix which transfer functions are of second order. Note that the coefficients are different as a consequence of different values of the input and output vectors. If other countries were analyzed similarly, transfer matrices would be determined with appropriate transmission functions of second order.

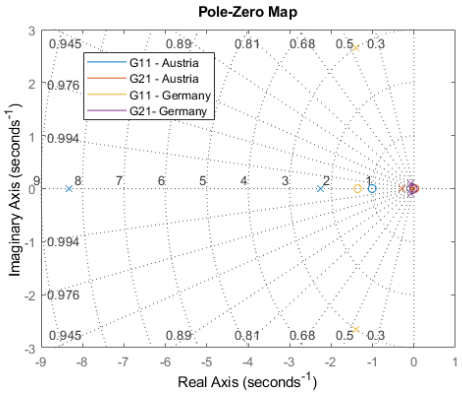

Figure 7. Pole-Zero Map for Austria and Germany.

Based on the pole distribution of transfer matrices for both systems as shown in Figure 7, it is reasonable to evaluate controllability and observability, because the systems of both countries are concluded to be stable. The same conclusion about stability can be made from the analysis of transient responses of the systems. For both systems, controllability and observability matrices were determined, and pandemics in both countries were observable and controllable, which could also be confirmed for the other countries.

When transfer matrices are known, behavioral differential equations are also known. By applying the inverse Laplace transform, the time responses of the systems are obtained, which also represent the solutions of the behavioral differential equations of those systems.

Discussion

By applying the system identification methodology from control theory, it is possible to determine a mathematical model of pandemic spread, as demonstrated on the example of SARS-CoV-2. Linear models of a second-order system at a satisfying level can be used to describe mathematical models representing a dynamic system. Deviations of the actual values from the model can be explained by the effect of disturbance on the system.

Theoretically it is possible to consider different types of control algorithms, e.g., predictive control model,

Published by Verlag der TU Graz
Graz University of Technology

DOI: 10.3217/978-3-85125-826-4-24

natural tracking control, exponential tracking control or fuzzy control so that in the future, in the case of similar epidemics, epidemic control can be exerted.
The models which are applied for both countries from the aspect of system control theory are represented by an application which contains a proportional gain of the control system. The system is considered as an open-loop control system without compensation of the effects of disturbances. A lockdown represents the application of a P (proportional) action in the open loop of controlling the spreading of the disease (see Figure 8).

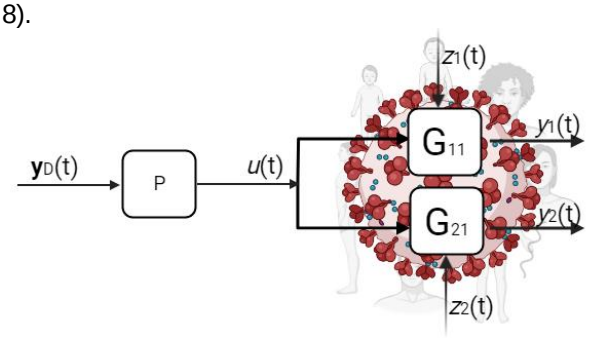

Figure 8. Control in open-loop with P-action.

Models were able to be determined even though the diminished weekly sampling time and provide sufficient information "on the basis of which" it is possible to predict the further spread of the pandemic since the mathematical model of the system is known. One of the conditions that need to be considered in further research is the impact of the number of vaccinated persons and the determination of mathematical models of pandemic spread, considering the data of the population.

References

[1] Lazic D. Nelinearni sistemi (Nonlinear systems), Faculty of Mechanical Engineering, University of Belgrade, 2005
[2] Sayama H. Introduction to the Modeling and Analysis of Complex Systems, Binghamton University, State University of New York, OpenSUNY, 2019
[3] Giordano G, Blanchini F, Bruno R. et al. Modelling the COVID-19 epidemic and implementation of population-wide interventions in Italy. Nat Med 26, 855–860, 2020 https://doi.org/10.1038/s41591-020-0883-7
[4] Chang SL, Harding N, Zachreson C. et al. Modelling transmission and control of the COVID-19 pandemic in Australia. Nat Commun 11, 5710 2020, doi.org/10.1038/s41467-020-19393-6
[5] Kyrychko YN, Blyuss KB & Brovchenko I. Mathematical modelling of the dynamics and containment of COVID-19 in Ukraine. Sci Rep 10, 19662, 2020, doi.org/10.1038/s41598-020-76710-1
[6] Ahmed I, Modu GU, Yusuf A, Kumam P, Yusuf I. A mathematical model of Coronavirus Disease (COVID-19) containing asymptomatic and symptomatic classes. Results Phys. 2021, doi: 10.1016/j.rinp.2020.103776
[7] Zeb A, Alzahrani E, Suat Erturk V, Zaman G, Mathematical Model for Coronavirus Disease 2019 (COVID-19) Containing Isolation Class, BioMed Research International, vol. 2020, Article ID 3452402, 7 pages, 2020 https://doi.org/10.1155/2020/3452402
[8] Logeswari K, Ravichandran C, Sooppy Nisar K, Mathematical model for spreading of COVID-19 virus with the Mittag–Leffler kernel, Numerical Methods for Partial Differential equations, ISSN:1098-2426, 2020, doi.org/10.1002/num.22652
[9] Ivorra B, Ferrández MR, Vela-Pérez M, Ramos AM. Mathematical modeling of the spread of the coronavirus disease 2019 (COVID-19) taking into account the undetected infections. The case of China. Communications in Nonlinear Science and Numerical Simulation, 2020
[10] Gostic K, Gomez ACR, Mummah RO, Kucharski AJ, Lloyd-Smith JO. Estimated effectiveness of symptom and risk screening to prevent the spread of COVID-19, Gostic et al. eLife 2020, doi: doi.org/10.7554/eLife.55570
[11] Pal D, Ghosh D, Santra PK, Mahapatra GS. Mathematical Analysis of a COVID-19 Epidemic Model by using Data Driven Epidemiological Parameters of Diseases Spread in India, doi.org/10.1101/2020.04.25.20079111, Preprint
[12] Din A, Li Y, Khan T, Zaman G. Mathematical analysis of spread and control of the novel corona virus (COVID-19) in China, Chaos, Solitons & Fractals Volume 141, December 2020
[13] Atangana A & Araz SI. Mathematical model of COVID-19 spread in Turkey and South Africa: theory, methods, and applications, Advances in Difference Equations volume 2020, Article number: 659, 2020
[14] Dehning J, Zierenberg J, Spitzner FP, Wibral M, Neto JP, Wilczek M, Priesemann V, Inferring change points in the spread of COVID-19 reveals the effectiveness of interventions. Science 369, 160, 2020
[15] Lozanovic Sajic J, Langthaler S, Stoppacher S, Baumgartner C. The Transfer Function of the SARS-CoV-2 Spread in Different Countries with Stability, Observability, and Controllability Analysis, doi.org/10.21203–/rs.3.rs-514785/v1, May 2021, Preprint
[16] Lazic D. Osnove automatskog upravljama, Univerzitet u Beogradu, Masinski fakultet, 2015
[17] Ogata K. Modern Control Engineering, Prentice Hall, NJ, 2009
[18] Verhaegen M and Verdult V. Filtering and System Identification: A Least Squares Approach, ISBN:9780511618888, 2007
[19] EU Open Data Portal, data.europa.eu, accessed on 24.05.2021

Published by Verlag der TU Graz
Graz University of Technology

Proc. Annual Meeting of the Austrian Society for Biomedical Engineering 2021
DOI: 10.3217/978-3-85125-826-4-25

T3E: TRANSPOSABLE ELEMENT ENRICHMENT ESTIMATOR

Michelle Almeida da Paz and Leila Taher

Institute of Biomedical Informatics, TU Graz, Austria

michelle.almeidadapaz@tugraz.at

Because of their repetitive nature, short sequencing reads derived from transposable elements (TEs) cannot be unambiguously mapped to the reference genome. As a result, most genomic analyses neglect over 50% of the human genome. Here, we present T3E, an algorithm to characterize the histone modifications associated with TEs from Chromatin Immunoprecipitation Sequencing (ChIP-seq) data. T3E relies on the structure of the ChIP-seq control experiment to assess enrichment. When applying T3E to five ChIP-seq libraries we found consistently fewer enrichments compared to a strategy that assumes a random distribution of the reads across the genome, suggesting that the latter has a high false positive rate. This provides a framework for the functional analysis of TEs.

Keywords— *Transposable element, enrichment, ChIP-seq, histone modifications*

Introduction

Over half of the human genome consists of repetitive sequences, including transposable elements (TEs) [1]. Based on their sequence and transposition mechanisms, TEs have been hierarchically classified into several groups/subgroups [2]. TEs are contributors to regulatory network evolution, playing role as host promoters, enhancers, and forming silencer/insulator regions [3]. To study the exaptation of TEs as cis-regulatory elements, we aim to quantitatively investigate the relationship between epigenetic histone modifications and TE groups/subgroups.

Repetitive sequences pose several analytical challenges to current short-read sequencing technologies. Specifically, reads originating from repetitive sequences will often map to multiple loci (multi-mappers) and cannot be unambiguously assigned to any region of the genome. The problem has been tackled in different ways. For example, some strategies simply use one random mapping, increasing the number of mapped reads, but reducing the precision of the mapping [4]. Others discard multi-mappers from the analysis and use only uniquely mapped reads [5].

Here, we present T3E, an algorithm that identifies TE groups featuring enrichment for specific histone modifications using chromatin immunoprecipitation followed by sequencing (ChIP-seq) data.

Methods

Selection of ChIP-seq datasets

We selected five ChIP-seq samples for the H9 cell line from the ENCODE Project data repository [6]: H3K4me1 and H3K4me3 (active euchromatin), H3K9me3 and H3K27me3 (repressed heterochromatin), and H4K8ac (both euchromatin and heterochromatin). All single-ended sequencing libraries were generated by the laboratory of Zhiping Weng, UMass Medical School.

ChIP-seq reads quality control and mapping

The raw data quality of all samples and their respective "input" controls (FASTQ files) were assessed using FASTQC [7]. Sequencing adapters were removed and low-quality reads (minimum Phred score of 10) were filtered out/or trimmed. Mapping was performed using BWA mem [8] against the GRCh37/hg19 assembly of the human genome with the parameter "-a*",* which outputs all found alignments for the single-end reads. The resulting mappings (BAM files) were processed with SAMtools [9] and BEDtools [10] to filter out unmapped reads, non-chromosomal scaffolds, and reads mapping to the mitochondrial chromosome (Tab. 1). The "input" controls were processed in the same manner.

Table 1. ENCODE Project ChIP-seq libraries considered in this study. * Number of processed reads. ENCFF969KKW has 9,862,491 reads and a read length of 30 base pairs (bp). ENCFF416GCS has 16,845,808 reads and a read length of 36 bp. The read length considered for the sample is the same for the corresponding "input" control.

Histone modifications	File accession	* Read count	Input file accession
H4K8ac	ENCFF974MOD	5508640	ENCFF969KKW
H3K9me3	ENCFF776JLA	7054172	ENCFF969KKW
H3K4me3	ENCFF909NXO	9771318	ENCFF416GCS
H3K27me3	ENCFF212TLT	12002119	ENCFF416GCS
H3K4me1	ENCFF210BMG	16779354	ENCFF416GCS

TE groups/subgroups

Repeat annotation for the GRCh37/hg19 assembly of the human genome was obtained from the RepeatMasker track of the UCSC Genome Browser [11]. Repeat annotation was processed to filter out simple repeats (micro-satellites), low complex repeats, satellite DNA, RNA repeats (including RNA, tRNA, rRNA, snRNA, scRNA, srpRNA, non-TE elements and uncommon repeats (less than 100 instances). Adjacent and overlapping TE instances of the same group/subgroup were merged.

Published by Verlag der TU Graz
Graz University of Technology

DOI: 10.3217/978-3-85125-826-4-25

Reads associated with a TE group/subgroup
The contribution of a read to a TE group/subgroup considers the fraction of a read mapping to a given TE instance and the total number of mappings for the read in the genome:

$$C_K = \sum_{k \in K} \sum_{r \in S} \sum_{i=1}^{N_r} \frac{l_{k\,r_i}}{N_r\, L_r} \quad (1)$$

where K is the set of all instances of a TE group/subgroup in the genome, S is the set of all reads in the sample, N_r is the number of mappings of read r, L_r is the length of read r, and $l_{k\,r_i}$ is the number of nucleotides of the ith mapping of read r overlapping with TE instance k, where $\{l_{k\,r_i} \in \mathbb{Z}_0^+ : 0 \leq l_{k\,r_i} \leq L_r\}$.

Input-based background probability distribution
The estimated probability of a mapping starting at position n on chromosome $c \in \{1, 2, \ldots, 22, X, Y\}$ of the genome is calculated based on the reads in the "input" library and defined by:

$$p_n = \frac{\sum_{r \in K} \frac{1}{N_r}}{\sum_{r \in M} \frac{L_r}{N_r}} \quad (2)$$

where L_r is the length of read r, N_r is the number of mappings of read r, K is the set of all read mappings on chromosome c overlapping n, and M is the set of all read mappings on chromosome c. Note that nucleotides with zero coverage have no probability assigned and are consequently excluded from the analysis.
We sample genomic positions from the corresponding empirical cumulative distribution for a given chromosome using discrete sample. Then, among the reads mapping to that position, we randomly select one. Finally, we identify all other mappings of the selected read (if any). The process is repeated as many times as there are reads in the ChIP-seq library of interest, resulting in a simulated "input" library of the same size of the ChIP-seq library.

TE group enrichment analysis
For each ChIP-seq library, we simulated *N*=100 "input" libraries. For each of them, we computed the number of reads associated with a TE group/subgroup as described above.
For each TE group/subgroup, the number of reads in the ChIP-seq library was compared to the number in the simulated "input" libraries using a permutation test. A P-value was calculated as the number of simulated "input" libraries with a number of reads higher than or equal to the number of reads associated with the TE group/subgroup in the ChIP-seq library divided by *N*. A fold-change (FC) was computed as the ratio between the number of reads associated with the TE group/subgroup in the ChIP-seq library divided by the average of the number of reads associated with the TE group/subgroup across all *N* simulated "input" libraries.
Note that enrichment was calculated for TE groups/subgroups, not for individual TE instances.

Uniform background distribution
A more traditional method to define a background distribution assumes a uniform distribution of the sequencing reads across the genome. Thereby, the reads of a ChIP-seq library are randomly shuffled across the entire genome.

Computational specifications and execution time
The algorithm is written in Python 3 and was executed in two machines using Python 3.8.5. Three samples were processed on a computer with AMD Ryzen 9 3900X, 12 cores, with in total 128 GB of RAM and running Linux version 5.8.0-41-generic (machine 1). Two samples were processed using a computer with AMD Ryzen Threadripper 3970X, 32 cores, with in total 128 GB of RAM and running Linux version 5.8.0-44-generic (machine 2). The execution time increased approximately linearly with the library size (Fig. 1).

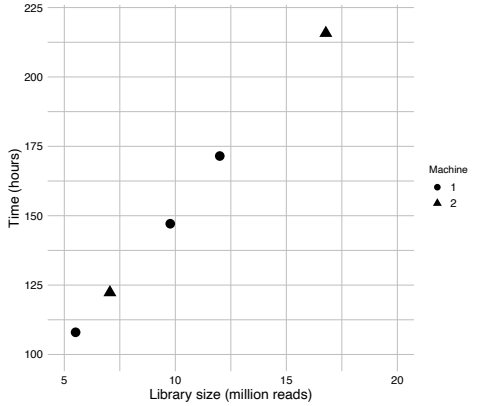

Figure 1. Execution time as a function of the ChIP-seq library size. Note that the times correspond to two different machines.

Results

In T3E the number of mappings observed for a given read is taken into account to quantify the contribution of a read to a TE group/subgroup. By doing this, every single nucleotide mapping onto a TE instance is counted and weighted by the uncertainty of where multi-mapper reads come from. As background for the enrichment analysis, the algorithm constructs a probability distribution of read mappings based on the read mappings in the ChIP-seq control experiment (Fig. 2).
In total, the repeat annotation comprises 860 different TE groups/subgroups covering 44.83% of the human genome. Read mapping statistics evaluation shows a substantial percentage of alignments uniquely mapping on TE regions (Fig. 3), indicating that although different instances of the same TE group/subgroup have repetitive sequences, they are not identical. Multi-mapper reads also mapped to non-TE regions, indicating the presence of other genomic repetitive sequences or non-annotated TEs.
The number of reads that are expected to be mapped by chance to TE groups/subgroups computed based

Published by Verlag der TU Graz
Graz University of Technology

DOI: 10.3217/978-3-85125-826-4-25

on the reads in the "input" library is strongly correlated with that computed assuming a uniform distribution (Fig. 4). However, LINE and SINE major groups exhibit clear deviations, in particular for LINEs using the ENCFF416GCS "input" library (Fig. 4).

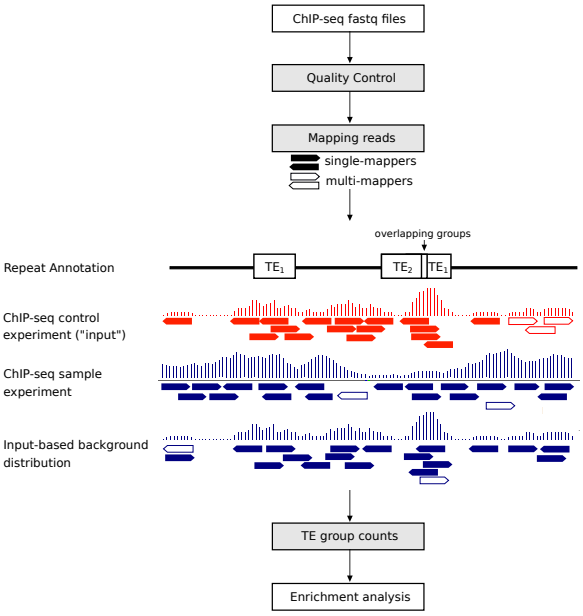

Figure 2. T3E algorithm strategy. The structure of the "input" control is used to construct the background. Overlapping of different TE groups are shown and reads mapping on this region contribute partially to both groups.

Consistently, T3E identified fewer TE groups/subgroups featuring histone modification enrichments. On average, T3E found only 11.11% of the TE groups/subgroups identified based on the uniform background distribution (Fig. 5). In total, 11 TE groups/subgroups showed enrichment: 4 to H3K4me3 (including LTRs, MER57E3 and HERVH-int, all classified into ERV1 - endogenous retroviruses group) and 7 to H3K9me3 (LTR12E and 6 SVA retrotransposons).

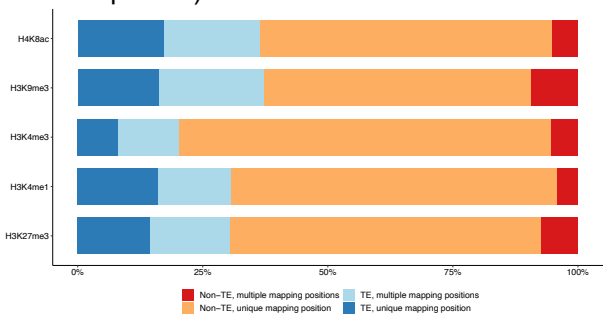

Figure 3. Read mapping statistics. On average, 10,223,121 reads comprised 64.04% uniquely mapped on non-TE, 15.77% multiple mapped on TE regions, 14.32% uniquely mapped on TEs, and 5.88% multiple mapped on non-TEs.

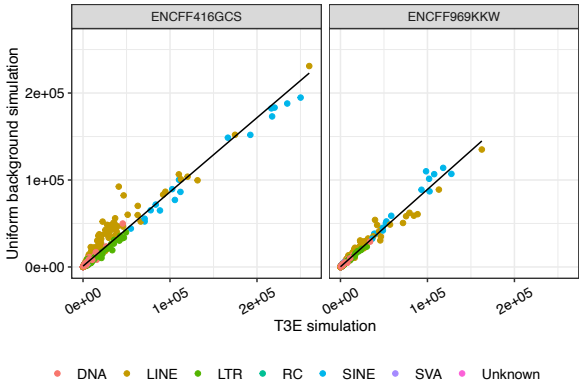

Figure 4. "Input" control simulations. Comparison of T3E input-based background and uniform background distribution counts as the average of 10 iterations. Each dot represents one TE group/subgroup. Unknown represents ancient TE not yet classified [12].

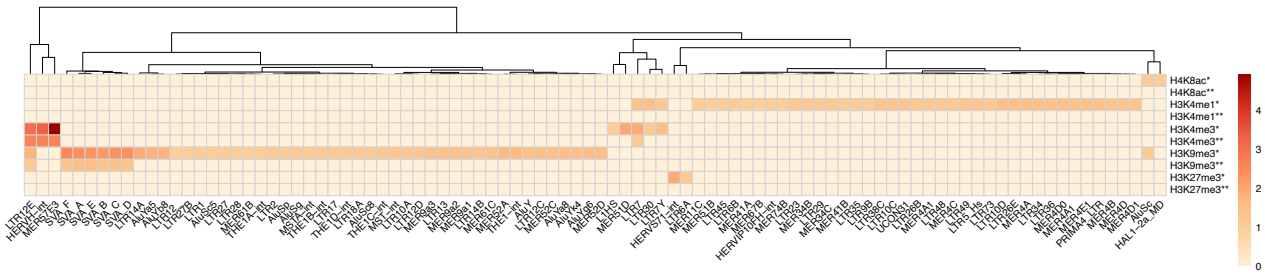

Figure 5. TE group/subgroups enrichment for different histone modifications. Only TE group/subgroups exhibiting a P-value ≤ 0.05 and a $\log_2$ FC ≥ 1 were considered enriched. Light-coloured cells indicate no enrichment. Red intensity varies according to $\log_2$ FC values, from 1.0 to the maximum found ($\log_2$ FC = 4.99). (*) Uniform background distribution. (**) T3E. Columns were clustered using Euclidean distance and complete linkage.

Discussion

Although a considerable effort has been done to study TEs in an integrative manner, several challenges are faced when mapping TE-derived sequences and predicting the enrichment of TEs in high-throughput sequencing, such as ChIP-seq data. Long reads increase the uniqueness of sequenced fragments and

Published by Verlag der TU Graz
Graz University of Technology

DOI: 10.3217/978-3-85125-826-4-25

also help in the mapping step, but still, it is a limiting factor in ChIP-seq and many other applications.

Like the repEnrich [13] method, T3E accounts for the uncertainty in the mapping of multi-mapper reads by dividing by the total number of mappings. In addition, T3E was developed to use the structure of the "input" library to estimate TE enrichments. Thus, the probability of observing a mapping at a given genomic position reflects the read distribution of the "input" control. Our approach avoids the bias of a uniform background, which does not reflect the read mappings, since TEs are not uniformly distributed across the genome [14] and the read mappings in the "input" control have a specific distribution. This is reflected in the decrease in the number of TE groups/subgroups showing enrichment. Furthermore, T3E's strategy of randomly sampling read mappings based on the "input" library takes into account potential library preparation biases. It also eliminates the need for normalization in enrichment computations, preventing the removal of true biological variations.

In summary, T3E is more conservative compared to other current approaches and has the benefit of estimating TE enrichment of groups/subgroups at a nucleotide resolution, without the need of further normalizations. Although this study is a proof of principle, it provides a framework for the analysis of the regulatory functions of TEs.

Acknowledgements

This research was funded by the Austrian Science Fund (FWF) [P33437-B].

References

[1] International Human Genome Sequencing Consortium. Initial sequencing and analysis of the human genome. Nature. 2001 Feb 15;409(6822):860–921.

[2] Wicker T, Sabot F, Hua-Van A, Bennetzen JL, Capy P, Chalhoub B, et al. A unified classification system for eukaryotic transposable elements. Nat Rev Genet. 2007 Dec;8(12):973–82.

[3] Etchegaray E, Naville M, Volff J-N, Haftek-Terreau Z. Transposable element-derived sequences in vertebrate development. Mob DNA. 2021 Dec;12(1):1.

[4] Teissandier A, Servant N, Barillot E, Bourc'his D. Tools and best practices for retrotransposon analysis using high-throughput sequencing data. Mob DNA. 2019 Dec;10(1):52.

[5] Jin Y, Tam OH, Paniagua E, Hammell M. TEtranscripts: a package for including transposable elements in differential expression analysis of RNA-seq datasets. Bioinformatics. 2015 Nov 15;31(22):3593–9.

[6] Davis CA, Hitz BC, Sloan CA, Chan ET, Davidson JM, Gabdank I, et al. The Encyclopedia of DNA elements (ENCODE): data portal update. Nucleic Acids Res. 2018 Jan 4;46(D1):D794–801.

[7] Andrews S. FastQC: A Quality Control Tool for High Throughput Sequence Data [Internet]. 2010. Available from: http://www.bioinformatics.babraham.ac.uk/projects/fastqc/

[8] Li H, Durbin R. Fast and accurate short read alignment with Burrows-Wheeler transform. Bioinformatics. 2009 Jul 15;25(14):1754–60.

[9] Li H, Handsaker B, Wysoker A, Fennell T, Ruan J, Homer N, et al. The Sequence Alignment/Map format and SAMtools. Bioinformatics. 2009 Aug 15;25(16):2078–9.

[10] Quinlan AR, Hall IM. BEDTools: a flexible suite of utilities for comparing genomic features. Bioinformatics. 2010 Mar 15;26(6):841–2.

[11] Kent WJ, Sugnet CW, Furey TS, Roskin KM, Pringle TH, Zahler AM, et al. The Human Genome Browser at UCSC. Genome Res. 2002 May 16;12(6):996–1006.

[12] Kojima KK. Human transposable elements in Repbase: genomic footprints from fish to humans. Mob DNA. 2018 Dec;9(1):2.

[13] Criscione SW, Zhang Y, Thompson W, Sedivy JM, Neretti N. Transcriptional landscape of repetitive elements in normal and cancer human cells. BMC Genomics. 2014 Dec;15(1):583.

[14] Ahmed M, Liang P. Transposable Elements Are a Significant Contributor to Tandem Repeats in the Human Genome. Comp Funct Genomics. 2012;2012:1–7.

Published by Verlag der TU Graz
Graz University of Technology

Proc. Annual Meeting of the Austrian Society for Biomedical Engineering 2021
DOI: 10.3217/978-3-85125-826-4-26

Purely Sequence based prediction of contact maps and classification of chromosomal compartments with DDA-DNA

X. F. D. Lainscsek[1] and L. Taher[1]

[1]Institute of Biomedical Informatics, Graz University of Technology, Austria

xenia.lainscsek@tugraz.at

Abstract *- The emergence of genome wide chromosome conformation capturing techniques such as HiC has enabled researchers to investigate the crucial role of chromatin folding in gene regulation. DNA folding forms distinct multiscale patterns which become visible in contact maps generated by such experiments. The abundance of information about chromatin architecture contained in the nucleotide sequence alone is still not well understood. Here we present a purely sequence based computational approach DDA-DNA that sifts out the sequence dependencies of genome architecture at 1Mb resolution.*

Keywords— *Hi-C, A/B Compartments, delay differential analysis, nonlinear dynamics*

Introduction

Advances in high-throughput chromosome conformation capture assays such as Hi-C has enabled the cataloging of genome-wide interaction maps in various cell types. How strongly DNA sequence signatures alone and at which scales they reflect this hierarchical organization remains unknown. The genome has various levels of organization. At megabase (Mb) resolution, chromosomes are organized into two types of chromatin called A and B compartments which correspond to open and closed chromatin [1]. The A/B compartments have been found to be cell-type specific and contribute to cell-type-specific gene expression [2].

Here we applied Delay Differential Analysis (DDA) [3] to extract dynamical properties of the DNA sequence that contribute to its conformation in 3D space. This method has been shown to achieve excellent classification and prediction performance in various data types [4, 5, 6]. The key difference to machine learning (ML) is that DDA uses a sparse feature set of only 4 terms compared to the typically huge parameter sets in ML. DDA does not utilize a typical training/testing approach, but rather a structure selection step where the model and the two fixed parameters that best represent the overall dynamics of the system are searched for. This makes DDA robust to overfitting and easily generalizable to new data [3].

We hypothesize that a substantial contribution of chromatin organization, at least at the 1Mb scale, arises from the sequence itself.

Methods

Background

Genome-wide chromosome conformation capturing techniques (Hi-C) is a type of next generation sequencing (NGS) method which produce contact frequency maps that depict the degree of interaction between two loci in the genome. The contact matrix is highly self-similar, a hallmark for a chaotic process, and can thus be understood as a recurrence map. It has been found that the contact frequency between two genomic regions i and j follows the power scaling law as

$$p(|i-j|) \sim |i-j|^{-\beta} \quad (1)$$

The scaling exponent β has been typically found to be slightly below 1. This is in good agreement with the predictions made by the so called “fractal” globule model of DNA [1, 7, 8].

Construction of contact maps from HiC-assay data

The Hi-C contact maps were derived using the publicly available Hi-C raw sequencing data set of a fetal lung fibroblast cell-line (GEO accession GSM862724). The reads were mapped using bowtie2 [9] and contact maps were generated with hicexplorer [10].

Construction of contact maps from nucleotide sequence

The DDA-contact maps were generated in a three-step process: 1) conversion of the nucleotide sequence into a numerically differentiable signal; 2) structure selection on chr14; and 3) testing on chr13,15,16, 17. A crucial fact of DDA ist that its functional form and parameters are never updated as in traditional ML methods. DDA does not learn but rather captures the important underlying macroscopic features of a dynamical system. A DDA model associates the numerical derivative of a signal, in this case a spatial sequence, with its delayed versions [3]. We used a cubic 3-term DDA model with two parameters τ_1 and τ_2

$$\dot{x}(t) = a_1 x_{\tau_1}^2 + a_2 x_{\tau_1}^2 x_{\tau_2} + a_3 x_{\tau_2}^3 + \rho \quad (2)$$

where $x_{\tau_i} = x(t-\tau_i)$ is the converted version of the DNA sequence delayed by τ_i. The coefficients a_1, a_2, a_3 and the least squares error ρ are estimated from the over-determined system of

Published by Verlag der TU Graz
Graz University of Technology

DOI: 10.3217/978-3-85125-826-4-26

equations with singular value decomposition (SVD) [11] and used as classifying features.

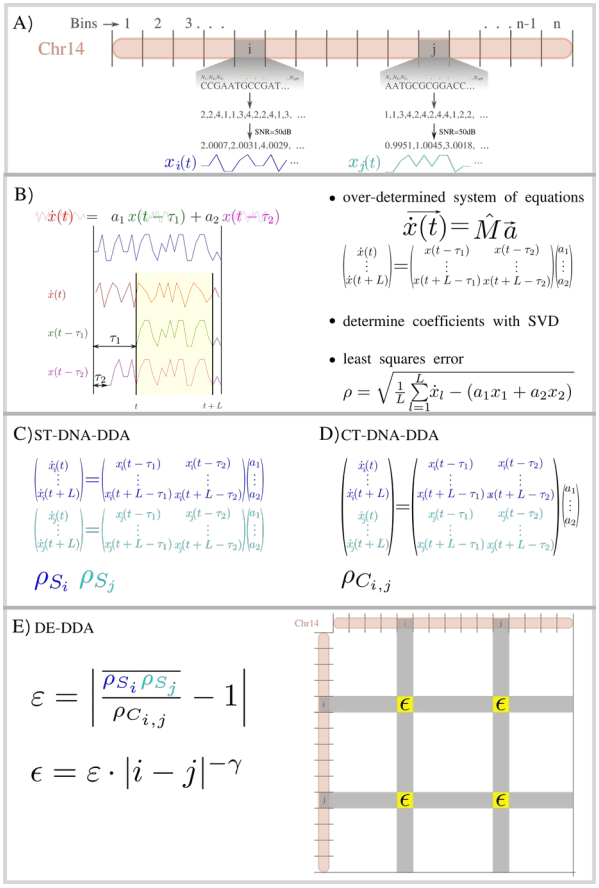

Figure 1: A) conversion of the nucleotide sequence B) DDA (example for a simple linear 2-term DDA model) C) ST DDA D) CT DDA E) DE-DDA

1) conversion of the nucleotide sequence

For DNA-DDA (see Fig. 1 B)), each nucleotide A, C, T and G in the sequence of the human genome (hg38 assembly) was encoded as 1, 2, 3 and 4 respectively, and the entire sequence was split into 1Mb long bins. To make the signal suitable for DDA, a small amount of signal-to-noise ratio (SNR) of 50 dB Gaussian noise was overlain to the signal of each bin $x_n = s + cN$ where s is the encoded DNA sequence, N are numbers drawn from the standard normal distribution and $c = \sqrt{var(s) \cdot 10^{-(SNR/10)}}$.

2) structure selection

The converted DNA signal x_n of each bin was inputted into Eq. (2) and the features a_1, a_2, a_3 and ρ were calculated for each delay pair (τ_1, τ_2) in a probe list consisting of 870 delays between 1 and 30.

The individual calculation of DDA features is called single-trial(ST) DDA. Data windows of multiple time series can be combined in cross-trial(CT) DDA where features are computed simultaneously by including them in the over-determined system of equations given by Eq. (2) [6, 12].

Each feature may be considered separately or combined. For instance for two 1Mb genomic regions i and j, we can compute the ST DDA features ρ_{S_i}, ρ_{S_j} as well as the CT DDA feature $\rho_{C_{i,j}}$. The CT errors and mean of the ST errors should be similar if the analyzed time series have similar dynamics and their quotient will be close to one.

The dynamical ergodicity (DE) DDA ε [12] is defined by the quotient

$$\varepsilon = \left| \frac{\overline{\rho_{S_i} \rho_{S_j}}}{\rho_{C_{i,j}}} - 1 \right| \quad (3)$$

Thus the lower ε, the more dynamically similar these two 1Mb stretches of sequence are to one another. Motivation of this feature comes from ergodic theory [13] which is concerned with the statistical properties of a dynamical system.

We hypothesize that DE DDA is correlated with the proximity of two 1Mb stretches of sequence in 3D space. Hence, we predict the contact probability between two DNA sequences i and j as

$$\epsilon = \varepsilon |i - j|^{-\gamma} \quad (4)$$

Where $|i - j|$ is the distance between genomic bin i and bin j and γ is the scaling exponent and was set to -0.77.

Calling A/B Compartments

We generated the pearson correlation matrices from the contact matrices to call A/B compartments. The HiC- and DDA-contact maps (Fig. 2 A) were normalized with Toeplitz normalization using the 4D nucleome Analysis toolbox [14] before being converted to a correlation matrix as described by [1]. The principal components which determine A/B compartments were derived using matlabs [15] pca function. The A and B compartments correspond arbitrarily to PC>0 or PC<0 respectively.

3) testing

Model performance was assessed with the stratum-adjusted correlation coefficient (SCC) given by HiCRep [19], the mean square error (MSE), Pearson's R of the resulting first or second PCs of the Pearson correlation matrices (r_{PC}), and lastly the area under the ROC curve of the compartment classification (AUC). Before calculating testing measures, both matrices were normalized to 0 and 1 whilst ignoring the main diagonal which was subsequently set to 1.

It is worth noting that the ordinary Pearson correlation coefficient is not sufficient for comparison of matrices of such type. The SCC statistic [19] takes spatial features such as domain structure and distance dependence into account. An averaging filter of size 2 was applied to HiC and

Published by Verlag der TU Graz
Graz University of Technology

DOI: 10.3217/978-3-85125-826-4-26

DDA maps using matlabs fspecial function before calculating the SCC (smoothing parameter=0) .

Results

The interaction probability between two genomic regions is not simply a matter of linear distance (Fig. 2A). Each chromosome has a unique and characteristic structure. Chr14 was arbitrarily chosen for the structure selection process. Based on the aforementioned performance measures the feature/delay pair combination that resulted in the highest performance was found to be ρ and the mean of the DDA-maps for $\tau_{1,2} = (5,3);(26,12)$. We tested this model-parameter combination on chr13,15, 16, 17 on which DNA-DDA shows promising performances (Tab. 1).

Table1: Performance of DNA-DDA for delays $\tau_{1,2} = (5,3);(26,12)$ on chr13-17

ChrNr	SCC	r_{PC}	AUC	MSE
13	0.74	0.78	0.84	0.06
14	0.62	0.74	0.80	0.02
15	0.68	0.61	0.78	0.06
16	0.74	0.71	0.82	0.06
17	0.73	0.71	0.82	0.06

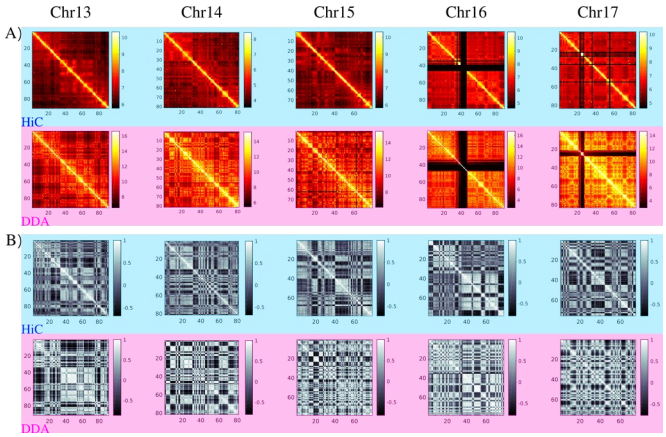

Figure 2: A) log-transformed HiC- and DDA-contact maps (ϵ^{-1}) for chromosomes 13-17. One value in the map corresponds to a genomic region of 1Mbp. B) Corresponding Pearson correlation HiC- and DDA-maps for chromosomes 13-17.

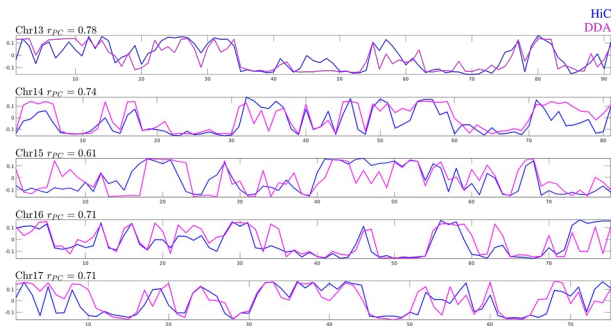

Figure 3: PCs of HiC (blue) and DDA (magenta) correlation maps (Fig 2 B))

Highly interacting regions predicted by DNA-DDA match very well those of the HiC-contact maps achieving a mean SCC of 0.72 on hold out chromosome contact maps (Fig. 2B). DNA-DDA-based compartment prediction was also remarkably accurate (Fig. 3) achieving a mean AUC of 0.82 on hold out chromosomes.

Discussion

We present DDA-DNA, a novel method based in nonlinear dynamics and ergodic theory that predicts the folding of chromatin inside the nucleus using the nucleotide sequence alone. Being able to infer structural changes in the genome could immensly aid in understanding disease pathology and be of clinical use in the long run. Hierarchial organization of the genome is crucial for nuclear activity such as transcription, DNA replication as well as for cellular processes and development.

Current approaches for modeling genome organization are based on machine learning or polymer chemistry and physics. The former typically rely on epigenomic information as input (eg [2, 16]), which are not able to model the effects of genetic variation. However recently, some deep learning sequence based multi-scale models including DeepC, Akita, and Orca for chromatin architecture have emerged [17, 18, 20]. DeepC is a transfer-learning based neural network which like Akita, predict interactions within Mb-scale loci. The training/testing and validation sets were split based on chromosomes. DeepC uses two training procedures the first of which used chr11 and chr12 for validation and chr15-17 for testing, the second used tha same validation chromosomes but only chr16 and chr17 for testing. GPU support was needed for training and the final models had ~60M parameters. DeepC models were trained on seven human and one mouse data sets and cross-validation accross all chromosomes acheived an average distance stratified Pearson's R of ~0.36 on raw skeleton data and ~0.57 when applying a smoothing filter to the discrete and noisy skeleton [17]. Akita uses a convolutional neural network that predicts interaction contacts up to 1Mbp. They divided the human genome into ~1Mb sequences and used a 80/10/10 random split for training, testing and validation sets (~262kb in the training set and ~524kb for the validation and test sets). The resulting model has 746,149 trainable parameters. Training and prediction were conducted on 5 high quality Hi-C and Micro-C data sets and acheived performances of MSE=0.14 and distance stratified Pearson's R=0.61. Akita currently makes predictions for 1Mb long windows and will need to be extended to make prediction on more distal pairs of genomic loci to obtain chromatin features such as A/B compartmentalization [18]. Currently in preprint, Orca is the first sequence

Published by Verlag der TU Graz
Graz University of Technology

DOI: 10.3217/978-3-85125-826-4-26

based model that predicts chromatin architecture from kp to whole-chromosome scale. The model takes 1Mb-256Mb as input and predicts interactions from 4kb-256Mb. On holdout test chromosomes 9 and 10, the model achieves a Pearson correlation of 0.78-0.84 and 0.72-0.79 consistently across all scales for the two micro-C datasets. Based upon additional analysis on sequence effects on A/B compartments, they proposed that compartment A formation is driven by TSS sequences whereas compartment B requires sequences of > 6-12kp without compartment A activity, is AT-enriched, and may be the “default” state established on all sequences not belonging to compartment A [20].

DNA-DDA’s performance measures do very well when compared with these recent publications achieving a mean of SCC=0.72, MSE=0.06, AUC=0.82 and r_{PC}=0.70 across the test chromosomes. What sets this method apart from the others, is the vastly lower number of parameters and distinguishing features. Opposed to other methods, we use merely one chromosome (chr14) to fix the DDA-model and parameters ($\tau_{1,2} = (5, 3); (26, 12)$) and subsequently test it on four others (chr13, 14, 15, 16, 17). Furthermore, the final fixed DNA-DDA can be computed on CPUs on new chromosomes in minutes (chr13: ~23 minutes on 6 AMD Ryzen 9 3950X CPUs). There remain many possibilities of adjusting our analysis such as: conversion of the sequence to a time series signal and using a different DDA functional form.

Additional analysis is still needed to assess DNA-DDA’s robustness on all remaining human chromosomes and on the sub-megabase scale.

We hypothesize that DNA-DDA has the potential to detect cell-type specific structural differences. DDA applied to other systems such as the human brain is able to classify various disease states defined by a certain delay pair and thus we hypothesize that also here, a different delay pair will best characterize DNA structure in another cell type.

We believe tha DNA-DDA has high potential in helping to understand the mechanisms by which derangement in the hierarchial architecture of the genome causes diesease pehotypes. Implementing DNA-DDA to perturbed sequences could help predict the effects of various genetic mutations. This is of particular interest for understanding disease progression such as in cancer. Similarly, removal of certain sequence motifs can give us insight into the highest contributing sequence signatures and biological mechanisms of genome folding at various scales.

Acknowledgments

We would like to express our gratitude to Dr. Claudia Lainscsek (Salk Institute) for the valuable discussions and insight into novel DDA methods.

References

[1] Lieberman-Aiden, Erez et al., Comprehensive mapping of long range interactions reveals folding principles of the human genome, 2009
[2] Fortin, Jean-Philippe and Hansen, Kasper, Reconstructing A/B compartments as revealed by Hi-C using long-range correlations in epigenetic data, 2015
[3] Lainscsek, Claudia and Sejnowski, Terrence J., Delay differential analysis of time series., 2015
[4] Lainscsek, Claudia and Sejnowski, Terrence J., Electrocardiogram classification using delay differential equations, 2013
[5] Lainscsek, Claudia et al. , Delay Differential Analysis of Seizures in Multichannel Electrocorticography Data, 2017
[6] Lainscsek, Claudia et al., Nonlinear dynamics underlying sensory processing dysfunction in schizophrenia, 2019
[7] Grosberg, Alexander et al., The role of topological constraints in the kinetics of collapse of macromolecules, 1988
[8] Grosberg, Alexander et al., Crumpled Globule Model of the Three-Dimensional Structure of DNA, 1993
[9] Langmead, Ben and Salzberg, Steven L, Fast gapped-read alignment with Bowtie 2, 2012
[10] Wolff, Joachim et al. , Galaxy HiCExplorer 3: a web server for reproducible Hi-C, capture Hi-C and single-cell Hi-C data analysis, quality control and visualization, 2020
[11] Golub, Gene H. and Reinsch, Christian, Singular value decomposition and least squares solutions, 1970
[12] Lainscsek, Claudia , Dynamical Ergodicity, Soon to be submitted for publication
[13] Boltzmann, Ludwig, Vorlesungen über Gastheorie , 1898
[14] Seaman, Laura and Rajapakse, Indika, 4D nucleome Analysis Toolbox: analysis of Hi-C data with abnormal karyotype and time series capabilities , 2018
[15] The MathWorks, MATLAB and Statistics Toolbox Release 2018a,
[16] Mourad, Raphaël and Cuvier, Olivier , Predicting the spatial organization of chromosomes using epigenetic data, 2015
[17] Schwessinger, Ron et al. , DeepC: predicting 3D genome folding using megabase-scale transfer learning, 2020
[18] Fudenberg, Geoff et al., Predicting 3D genome folding from DNA sequence with Akita, 2020
[19] Yang, Tao et al., HiCRep: assessing the reproducibility of Hi-C data using a stratum-adjusted correlation coefficient, 2017
[20] Zhou, Jian, Sequence-based modeling of genome 3D architecture from kilobase to chromosome-scale, 2021

Published by Verlag der TU Graz
Graz University of Technology